TU Delft

Delft University of Technology

Document Version
Final published version

Citation (APA)
Fazzi, L. (2024). *Minimal Intrusive Multi-parameter Optical Fibre Sensor for Aerospace Structures and Adhesives*. [Dissertation (TU Delft), Delft University of Technology]. https://doi.org/10.4233/uuid:6bbb0c33-97b7-415e-9649-9e0d7f4117de

Important note
To cite this publication, please use the final published version (if applicable).
Please check the document version above.

Copyright
In case the licence states “Dutch Copyright Act (Article 25fa)”, this publication was made available Green Open Access via the TU Delft Institutional Repository pursuant to Dutch Copyright Act (Article 25fa, the Taverne amendment). This provision does not affect copyright ownership.
Unless copyright is transferred by contract or statute, it remains with the copyright holder.

Sharing and reuse
Other than for strictly personal use, it is not permitted to download, forward or distribute the text or part of it, without the consent of the author(s) and/or copyright holder(s), unless the work is under an open content license such as Creative Commons.

Takedown policy
Please contact us and provide details if you believe this document breaches copyrights.
We will remove access to the work immediately and investigate your claim.

This work is downloaded from Delft University of Technology.

Minimal Intrusive Multi-parameter Optical Fibre Sensor for Aerospace Structures and Adhesives

Minimal Intrusive Multi-Parameter Optical Fibre Sensor for Aerospace Structures and Adhesives

Proefschrift

ter verkrijging van de graad van doctor
aan de Technische Universiteit Delft,
op gezag van de Rector Magnificus prof. dr. ir. T.H.J.J. van der Hagen,
voorzitter van het College voor Promoties,
in het openbaar te verdedigen op dinsdag 8 November 2024 om 10:00 uur
door

Luigi Fazzi

Master of Aerospace Engineering,
Università degli studi di Palermo, Palermo, Italië,
geboren te Enna, Italië.

The dissertation has been approved by the promotors

Composition of the doctoral committee:

Rector Magnificus	Chairman
Prof. Dr. R.M. Groves	Delft University of Technology, Promotor
Prof. C. Dransfeld	Delft University of Technology, Promotor

Independent members:

Prof. Dr. L.L.A. Vermeersen	Delft University of Technology
Prof. Dr. G. Pitarresi	University of Palermo
Prof. Dr. S. Valvano	University of Derby
Prof. Dr. C. Caucheteur	University of Mons
Dr. M. Holynska	European Space Agency/ESTEC TEC-QEE

Reserve lid:

Prof. Dr. F. Scarano	Delft University of Technology

The research carried out in this thesis was funded by the Operationeel Programma Zuid-Nederland (Op-Zuid) Project as part of the Dutch Composite Maintenance Centre (DCMC), supported by the Europees Fonds voor Regionale Ontwikkeling (EFRO) and by the European Space Agency (ESA)/ESTEC visiting researcher programme.









Keywords:	FBG, sensing, composite, silicone, aerospace
Printed by:	Ipskamp
Cover:	Fabia Mustica, Comic Book Artist

Copyright © 2024 by Luigi Fazzi
ISBN 978-94-6366-957-3
An electronic version of this dissertation is available at
http://repository.tudelft.nl

A Laura , mia indispensabile compagna di vita.

Grazie alla mia famiglia , Angelo , Tania , Roberta e Lola ,
perché senza di loro non ce l'avrei fatta.

Un pensiero va anche a chi è rimasto ,
a chi c'è sempre stato e a chi ci sarà.

Contents

Abbreviations » xiii

Preface » xvi

1. Introduction » 1

1.1 Aerospace materials: composites and silicone adhesives » 2

1.1.1 Composite materials » 2

1.1.1a Classification and materials » 2

1.1.1b History » 3

1.1.1c Manufacturing processes and issues » 4

1.1.2 Silicone adhesives » 5

1.1.2a Silicone operational issues in space environment » 6

1.2 Optical fibre sensors for SHM of composites and silicones » 7

1.3 FBG sensing technology gap and solution » 8

1.4 Thesis outline, contributions and motivations » 10

References » 12

2. TFBG: fundamentals and sensing properties » 18

2.1 TFBG spectrum » 20

2.1.1 Tilt angle influence » 20

2.2 Weakly TFBG spectrum » 22
2.3 Transfer matrix method for TFBG spectrum simulation » 22
2.4 Weakly TFBG multi-parameter sensing » 27
2.4.1 Thermomechanical effects and demodulation technique » 27
2.4.1a TFBG mechanical calibration and setup » 29
2.4.1b TFBG thermal calibration » 31
2.4.2 External Refractive Index effects on TFBG spectrum » 34
2.5 Conclusions » 35
References » 36
3. Delaunay triangulation demodulation technique and TFBG refractometric sensing » 39
3.1 Delaunay triangulation » 40
3.1.1 D-T approach for TFBG spectrum » 41
3.2 Refractometric calibration of the TFBG sensor » 43
3.2.1 Correlation normalised envelope area-external RI » 44
3.2.2 Fitting function of the RI correlation curve » 47
3.2.3 Methodology of the D-T demodulation algorithm » 48
3.3 Comparison of D-T approach with previous techniques » 49
3.4 α-shape parameter influence on the correlation curve » 50

3.5 Strain cross-sensitivity on RI measurements » 52
3.5.1 Experimental setup and equipment » 52
3.5.2 Strain cross-sensitivity quantification on the RI measures » 52
3.6 Measurement performance of the D-T technique » 54
3.6.1 Stability of the α-shape modified D-T technique » 54
3.6.2 Influence of the α-parameter on the measures stability » 57
3.6.3 Refractometric resolution and influence of the α-parameter » 58
3.7 Partial immersion of the TFBG sensor » 61
3.8 Conclusions » 67
References » 69

4. Thermomechanical evaluation of a composite plate with an embedded dual-parameter TFBG sensor » 71
4.1 Introduction » 72
4.2 TFBG sensorised composite plate sample » 73
4.3 Finite Element Model and simulation » 74
4.4 Experiment » 78
4.5 Strain-Temperature measurements: TFBG and classical approach comparison » 79
4.6 FEA results and comparison with experimental measures » 81
4.6.1 Error analysis » 82

4.7 Discussion and conclusions » 83
References » 86

5. Monitoring of the composite manufacturing process with three-parameter TFBG sensors » 88
5.1 Introduction » 89
5.2 Experimental procedure » 90
5.2.1 Materials and sensors » 90
5.2.2 Cure kinetics and T_g characterisation of the resin » 90
5.2.3 VARTM process » 92
5.3 Results and discussion for 2 mm sensorised composite » 94
5.3.1 TFBG measurements during pre-curing stages » 94
5.3.2 TFBG detection during resin infusion » 95
5.3.3 TFBG three-parameter monitoring during composite curing 95
5.4 Final considerations on the 2 mm thick composite monitoring » 99
5.5 Monitoring of thicker composites during VARTM » 100
5.5.1 Design, materials, embedded sensors and VARTM equipment » 100
5.5.2 Strain detection during vacuum imposition » 100
5.5.3 Resin flow detection » 101
5.6 Monitoring of thicker composite during the curing stage » 103

5.6.1 TFBG three-parameter monitoring during composite curing » 103
5.7 Conclusions » 108
References » 110

6. Silicone adhesive degradation detection via TFBG sensor in a simulated space environment » 113

6.1 Vacuum compatibility of the TFBG components » 114
6.2 Importance of silicone monitoring in space applications » 117
6.3 Methodology » 118
6.3.1 TFBG specifications and calibration » 118
6.3.2 Sensorised cover glass sandwich and testing facility » 119
6.3.3 High vacuum thermal cycling test parameters » 120
6.4 Results » 121
6.4.1 Strain measurements with classical TC compensation approach » 121
6.4.2 Strain-temperature measurements with self-compensated TFBG » 122
6.4.3 Silicone RI measurements detected by the TFBG » 123
6.5 Conclusions » 125
References » 126

7. Multi-parameter single sensor for space silicone adhesive monitoring under hi-vacuum ultra-violet exposure » 128

7.1 Predicting UV degradation of polymers for space applications through embedded TFBGs » 129

7.2 Samples » 130

7.3 Equipment » 132

7.4 UV effects on the TFBG sensors » 133

7.5 UV effects in silicone adhesive monitored via TFBG sensor » 136

7.6 Sensorised silicone adhesive directly exposed to UV radiation » 140

7.7 Conclusions » 143

References » 145

8. Conclusions and future developments » 148

8.1 Final considerations on TFBG sensing technology and future perspective » 152

Appendix A » 154

Abbreviations

2D, 3D: 2-Dimensions, 3-Dimensions

ATOX: Atomic-Oxygen

CEV: Crew Exploration Vehicle

CMX:

CMT:

CTE: Coefficient of Thermal Expansion

CVCM: Collected Volatile Condensable Material

DAQ: Data Acquisition

DEMO:

DSC: Differential Scanning Calorimetry

D_T: Delaunay Triangulation

ECSS: European Cooperation for Space Standardization

EFPI: Extrinsic Fabry-Pérot Interferometric

EM: Electro-Magnetic

ERI: External Refractive Index

ESA: European Space Agency

ESTEC: European Space Research and Technology Centre

FBG: Fibre Bragg Gratings

FC-APC: Fiber Connector-Angled Physical Contact

FEA: Finite Element Analysis

FEM: Finite Element Model

FML: Fiber-Metal Laminates

FTIR: Fourier-Transform Infrared

ISS: International Space Station

LCM: Liquid Composite Moulding

LED: Light Emitting Diod

LEO: Low Earth Orbit

LIDS: Low Impact Docking System

LPG: Long-Period grating

MDSC: Modulated Differential Scanning Calorimetry

NASA: National Aeronautics and Space Administration

NDT: Non-Destructive-Testing

NDET: Non-Destructive Evaluation Technique

NI: National Instruments

NIR: Near Infrared

OF: Optical Fibre

PC: Polycarbonate

RI: Refractive Index

RML: Recovered Mass Loss

RTM: Resin Transfer Moulding

SCRIMP™: Seeman Composites Resin Infusion Moulding Process

SHM: Structural Health Monitoring

SOFO: Surveillance d'Ouvrages par Fibres Optiques

TC: Thermocouple

TEC-QEE: Technology, Engineering and Quality – Quality Engineering Evaluation

TFBG: Tilted Fibre Bragg Gratings

TML: Total Mass Loss

TMM: Transfer Matrix Method

TR: Thermal Resolution

UD: Unidirectional

UV: Ultra-Violet

UVA, UVB, UVC: Ultra-Violet A, Ultra-Violet B, Ultra-Violet C

VARTM: Vacuum Assisted Resin Transfer Moulding

VCM: Vacuum

VI: Vacuum Infusion

VUV: Vacuum Ultra-Vacuum

WWII: World War II

Preface

Since the dawn of time, human beings have been always fascinated and envious of the flight of birds and human's desire to fly has become stronger and stronger over the centuries. What child looking at a bird does not wish that they could take flight to chase it and view the at the landscape from above? The dream to fly is inside the human being since tender age, although the physical possibility does not belong to their nature. Nevertheless, humans have exploited the power of their brain and hands to get closer this dream.

Leonardo Da Vinci (1452-1519)[1] was the first one that effectively studied the flight dynamics of the birds, developing several technical drawings and building flying machines between the XV and XVI century. However, for almost 400 years, no tangible developments occurred until the Wright brother's famous flight (in 1903)[2], which is the major milestone of the aeronautical world. From that far away event, enormous technological developments have been made so that a large number of apparatuses able to fly in the atmosphere and travel in Space have been developed.

One of the key technological sectors that has allowed the large growth of the aerospace industry is that of the materials. Specifically, the large use of composites materials and adhesives has allowed the design and building of modern airplanes, spacecraft and devices which are increasingly lighter, faster, stronger and tougher. Nevertheless, at the same time, the increase of aerospace performance by using new materials has raised the necessity to develop a technology which is able to provide information on the health state of the materials that composed the structures. This need is not only linked to the necessity to increase the safety but also to two other factors: to optimize the maintenance schedule of the aircrafts so that to save economical resources, and to increase our knowledge about the mechanical, damage and fracture behavior of the materials.

Although, during the decades, a number of inspection and monitoring technologies have been developed as such as piezoelectric, acoustic and ultrasound sensing, electrical gauges, fibre optic sensors, eddy current, comparative vacuum, interferometry, penetrating liquids, thermography, radiography (x-rays) and others, not one of these has proved to be applicable for the entire life cycle of the material (from the manufacturing, operating phase to the end of life) which provides in real-time enough information to effectively evaluate its health state.

Therefore, the here presented thesis aims to demonstrate the multi-sensing abilities and monitoring benefits of tilted Fibre Bragg gratings sensors (TFBGs) in order to fill a current technological gap in the previous technologies and to improve the state-of-art of the Structural Health Monitoring field. The research focused initially on the fundamentals, mathematical and numerical modelling, methodology and demodulation techniques of the TFBG sensors, successively the treatment is dedicated to the TFBG applications for

[1] https://www.treccani.it/enciclopedia/leonardo-da-vinci/.
[2] G. D. Padfield and B. Lawrence, The Aeronautical Journal, Vol. 107, Issue 1078, 2016.

simultaneous three-parameter monitoring embedded in composite material and silicone adhesive, respectively for aeronautical and space use. This selection of these materials was made from those commonly used in the aerospace industry. The application of TFBGs can be, from the very beginning, have a great impact in the scientific community and, also maybe, in industry.

Therefore, taking into account what was reported previously, the research presented in the following thesis was confronted with the aim to demonstrate that TFBG can be a promising sensor for structural health monitoring of aerospace materials, and are able to provide reliable and simultaneous multi-parameter measurements. The treatment begins with the first introduction chapter where composite materials, silicone adhesive and TFBG sensors are presented fro a historical perspective, and their current state-of-art regarding applications, issues and technological gaps in relation with the working load and environment, are reported. Then, the research questions and reasons that motivated the scientific investigation are introduced in the last part of chapter 1.

The starting point of the research can be considered chapter 2, where, first of all, the realization of a TFBG sensor customized for the desired application is confronted by providing a numerical model to simulate the spectrum based on the values of the parameters of the sensor Bragg structure. This is important to obtain TFBGs with a spectral signal usable for the simultaneous and separated measurements of different parameters before the manufacturing of the same sensor. It can be noted that, the simulation of the TFBG spectrum may bring other several benefits such as production time and costs savings. In fact, the determination, a priori, of the Bragg structure, and hence, the parameters of the TFBG manufacturing setup, allows the TFBG sensor to be obtained with the desired measuring characteristics without the waste of materials, testing and manpower time.

In chapter 3, the demodulation of the TFBG spectrum for refractometric measures was improved by developing a new technique based on the Delaunay triangulation of the datapoints that compose the spectral signal, which was demonstrated to be faster and more accurate than previous techniques. This technique is also compatible with the method to extract the strain-temperature variation from the spectrum, so that the methodology for multi-parameter measurement performed with a single TFBG is completed.

At this point, chapter 4 starts the beginning of the second part of the thesis, where the simultaneous thermomechanical measurements of the TFBG were used to determine the deformation effects of a thermal load profile on a glass-fibre/epoxy composite plate induced by heating lamps. A further step achieved in this chapter, was to compare the TFBG measurements with a classical strain sensing technique based on the use of a TFBG as standard strain gauge thermally compensated by a thermocouple. Furthermore, another comparison was performed between the experimental results and the Finite Element Model (FEM) analysis results obtained by modeling the composite sample with and without the embedded TFBG and applying a Gaussian thermal profile.

These comparisons show that the strains measured with the single TFBG are very close to the values obtained by using the classical approach and the full FEM model. The improvement regarding the single TFBG sensor can be obtained by increasing its thermal resolution which is the weak point of the simultaneous thermomechanical measurements. Nevertheless, it can be further improved by using an interrogation system with a finer wavelength scanning resolution or by designing a TFBG whose resonance peaks move in the spectrum much more with the temperature variation. The comparison of the empirical measured deformations with the strain values extracted by the FEMs analysis have highlighted the importance to model the optical fibre inside the composite to increase the accuracy of the model. In conclusion, the single TFBG sensor was able to monitor the thermomechanical trend inside the composite during the heating lamp exposure with a good accuracy as the values were close to those measured with the classical approach and full FEM simulation.

The conclusions drawn from the first and second part of the thesis are that the investigation on the multi-parameter sensing abilities of the TFBG sensors, also embedded in composite materials for a complete monitoring of their state from their manufacturing to the operating life, has given positive and promising results. Especially regarding the embedding of the sensor, each single TFBG sensor can be used in order to measure simultaneously thermomechanical and refractometric variations of the composite material where the sensor is embedded and in any step of the material life.

The second part of the thesis continues with chapter 5. Here, the TFBG sensors are embedded inside glass-fibre/epoxy resin composite material to monitor simultaneously the strain-temperature variations, the resin refractive index (RI) during the manufacturing process and the application of a thermal load profile. Regarding the TFBG monitoring performed during the composite manufacturing, several samples of different thickness were tested and sensorised. In these samples, the sensors were able to measure, simultaneously, the strain state induced in the material due to the manufacturing steps, the temperature profile, and the resin RI variations due to the crosslinking occurring during the curing. This allowed the evaluation, not only of the possible state of stress in the material during the production, but, even more interesting, the cure degree of the resin. Indeed, as anticipated already in previous research, the resin RI measured with the TFBG can indicate the curing degree matrix of the composites. The TFBGs were able to provide the entire RI profile of the resin during the curing in which three different behavior ranges were identified in combination with the temperature trend. The expected typical plateau was reached in the RI curve when the resin was considered fully cured. Furthermore, the refractometric sensing abilities of the TFBGs were also used to monitor the resin flow and speed during its infusion.

From chapter 6 on, the treatment is focused on the TFBG application study on the space qualified silicone adhesive, which regards the third part of the thesis. Silicones are strategic and widely used materials in many engineering fields, but mainly their use finds great importance in space industries, especially for electronic and structural components. Nevertheless, some parts of the spacecraft where silicone elements and

adhesives are used undergo a direct exposure to the space environment, which represents harsh operating conditions and is strongly degrading for any material. In fact, perturbations as severe temperature gradients, ultra-high-vacuum, Ultra-Violet (UV) and ionizing radiations (x-rays, γ-rays, etc…), extreme thermal range and cycles, thermal shock, micro-gravity, atomic oxygen (ATOX), high accelerations, vibrations and space debris are characteristic of the space operating environment. Furthermore, it has to be also considered that these elastomers have to maintain their original mechanical and physical properties during their operational life in space, which is a challenging target. In this context, TFBG sensors embedded inside silicone adhesives, through their simultaneous thermomechanical and refractometric measuring abilities, may offer fundamental information to evaluate the internal mechanical and chemical state of the elastomers during the use in space environment. This would offer the possibility to have a technology able to provide a general view on the degradation state of the adhesive in real-time during the laboratory testing or operational life, which may improve the evaluation of its health and performance trend along the exposure time. Nevertheless, as for the composite, the monitoring technology should be always minimally intrusive, light and not affecting the material performance and properties. Hence, in order to match these requirements, each embedded TFBG sensor has to be able to perform the thermomechanical-refractometric measurements as single sensor without to be affected by the exposure to the space environment. The demonstration of a working TFBG sensor in a simulated space environment may be an interesting and promising starting point for the future development of a sensing technology able to real-time detect degradation and damages in spacecraft structures and components during the space missions.

In chapter 6, since studies in literature about the compatibility of optical fibre sensor layers in vacuum were not found, initially, the waveguide containing the TFBG was subjected to an outgassing test. Once the compatibility was verified, a TFBG was then embedded inside a space qualified silicone used as adhesive to join two micro-sheet cover glasses in order to compose a sandwich. This TFBG sensorised glass sandwich was tested inside a vacuum chamber and exposed to high-vacuum (around 10^{-6} mbar) and loaded with a thermal cycling profile. Hence, in this first approach, the experiment was planned to simulate the degradation on the silicone adhesive of the TFBG sensorised sample generated by outgassing (due to high-vacuum) and thermal cycling loads, which are perturbations constantly present in space environment.
The measurements of the single multi-parameter TFBG sensor, acquired during the experiment, were compared with the values obtained by using the classical sensing approach consisting in the thermal compensation of the TFBG (used as strain-gauge) through a thermocouple. The comparison highlighted the inaccuracy of the classical sensing method due to the different location of the sensors in the silicone which brings serious mistakes in the measurements. In fact, due to the absence of an atmosphere in the space environment, the transfer of heat inside a body depends only from the thermal conductivity of the material which accentuates the issue of the classical sensing approach linked to the different location of the sensors. While, the self-compensated TFBG can overcome this gap as it is thermally self-compensated.

Furthermore, for a complete evaluation of the health state of an organic material such as a silicone adhesive, temperature and deformations may be not sufficient as it is not easy to obtain information on the chemical state of the material, such as the variations of the silicone RI. The embedded TFBG sensor, simultaneously sensitive to temperature and deformations, was able to provide measurements of the silicone RI that was changing due to hardening and chemical evolution induced by the thermal cycles in high vacuum environment. The chemical variations were checked also by testing a sample of pure cured silicone adhesive via the Differential Scanning Calorimetry, which showed chemical variations due to the realising of volatiles during the heating-up and cooling-down phases of the test. These results make the TFBG a promising sensor able to provide a complete evaluation of the silicone state that comprises the thermomechanical and refractometric measurements while working in space environment.

By exploiting the experiences achieved in the previous chapters, chapter 7 treats of the research focused on the detection of the UV effects induced in the silicone adhesive working in space simulated environment. This topic may be interesting for polymers used in a space working environment as long exposure to UV radiation in vacuum can cause severe damages and bring the component to failure together with the structures of a spacecraft. The reason lies in the absorption of these light wavelengths by the silicone, whose organic chemical composition is photochemically susceptible to these light wavelengths. As a consequence, the photochemical reactions cause severe degradation of the material with deterioration of the original properties and efficiency and shorter working life. Then, it is easy to understand that a sensing technology able to monitor the degradation of the silicone working in the previously described conditions, may be really useful to evaluate the state of the material during its use, but also, in the phase of laboratory testing to better detect the material behaviour and its changes. Therefore, several and different TFBG sensorised samples were tested in a high vacuum chamber provided of UV lamps which emitted a high radiation level for a certain exposure time. Hence, the acquired spectra were demodulated and used to measure the thermomechanical and refractometric variations induced by the UV exposure inside the silicone in correlation with the equivalent exposure solar hours. This allowed an analysis of the different degrees of degradation of the silicone based on the sample configuration and exposure time. In conclusion, the achievement of this research was the demonstration of a minimal intrusive sensor as the TFBG is not only compatible with operating in a space environment, but is also able to provide in-situ reliable multi-parameter sensing for the monitoring of the thermomechanical and refractometric state of the material during its operations in space environment.

The conclusions of the thesis are reported in chapter 8 where the outcomes of the conducted researches highlighted the potentiality of the TFBG as a single three-parameter sensor to monitor the state of materials for aerospace industry. As consequence, these results may induce the raising-up of the SHM concept by developing a sensing technology based on the TFBGs that are able to provide an overall view of the material

state, from the manufacturing to the operational life, also working in harsh environmental conditions as those in space.

1

Introduction

"Get a good idea and stay with it. Do it, and work at it until it's done right."
Walt Disney

Tilted Fibre Bragg Gratings (TFBG) are a specific kind of Fibre Bragg Gratings (FBG) sensors with promising and advanced sensing properties. They have the same embedding features and physical benefits as FBGs such as low weight, minimal intrusiveness, electromagnetic interferences immunity, mechanical and chemical resistance and long-distance interrogation capability, but unlike standard FBGs, they can be used to perform simultaneous multi-parameter measurements [1]. In fact, the spectrum of each single TFBG can be demodulated to obtain information regarding the thermomechanical variation [2] and the refractometric condition of the material where the sensor is embedded [3]. These important properties allow the concept of Structural Health Monitoring (SHM) to be brought to a higher level through remote in-situ simultaneous multi-parameter measurements with a single minimally intrusive apparatus. The main advantages are substantially a leaner and less expensive equipment, easy handling and embedding procedure, and minimal influence of the monitored material performance with a more efficient and accurate monitoring system. However, so far, the scientific community has not sufficiently investigated the full potential of these TFBG sensors for in-situ monitoring of the health state of high performance engineering materials such as composite materials and silicone adhesives. During literature review, it has been noted that, currently, studies about TFBGs are mostly related to their mathematical treatment, intrinsic measurement features and some biochemical sensing approaches. While, the multi-parameter TFBG abilities have not yet been examined in detail when the sensors are embedded in materials of high technological interest. Therefore, the research described in this thesis aims to demonstrate the unique sensing abilities of the TFBG sensor when embedded in materials used in aerospace applications, such as composites and silicone adhesives. The reason why these materials are the best candidates and have been selected for these studies can be better understood from information given later in this introduction chapter. Briefly, some of these are: 1) their internal composition is very compatible for optical fibre sensors embedding, 2) due to their nature, operating environmental and load conditions their health state and behaviour should be monitored especially in space applications, and 3) their use to exploit their mechanical performance and properties in high technology and aerospace engineering or related fields is expected to increase with the growth of the space and aeronautic industry.

Nevertheless, for the above-mentioned reasons, the aim of the work is not only related to the TFBG sensing aspect, but also to raise up the bar of the SHM concept by proving that this three-parameter sensor provides enough information to monitor the overall state of advanced materials for aerospace applications from the manufacturing process to their operational life, even in adverse environmental conditions. The final aim of the work is to present the TFBG as a single and complete multi-parameter sensor able to perform advanced SHM tasks in any operational condition. The research activities were conducted at the Delft Aerospace Structures & Materials Laboratories (DASML) of the Aerospace Engineering faculty of Delft University of Technology and at the Materials and Electrical lab and the TEC-QEE section of the European Space Agency (ESA), European Space Research and Technology Centre (ESTEC) site.

1

1.1 Aerospace materials: composites and silicone adhesives

In this section some historical background and basic information about composite materials and silicone adhesives are provided to the reader so that the reasons behind the selection of these materials for the study, in combination with the TFBG sensors, are more perceptible.

1.1.1 Composite materials

The definition of a composite material derives from the word *composite* that is meant as a combination, in macroscopic scale, of two or more materials to produce a third component with physical and chemical properties profoundly different from those of the starting materials [4].

1.1.1a Classification and materials

There are many classification metods for composite materials, however, a first distinction can be made between natural materials (human bone and teeth, wood, pearls, mother of pearl, and related shell structures) [5], artificial materials (made usually with a polymeric and natural/synthetic reinforcement fibres) and hybrid composites (where different reinforcement fibres are embedded in a unique or combined matrix mixture) [6]. Composites can be also classified by considering the nature of the matrix (polymeric, metallic, ceramic) or the type of reinforcement (whisker, particles, fibres), and sub-classifications can be made based on the reversibility of polymeric matrix hardening or the type of particle and fibre reinforcement [7,8]. A complete overview is provided in Fig.1-1.

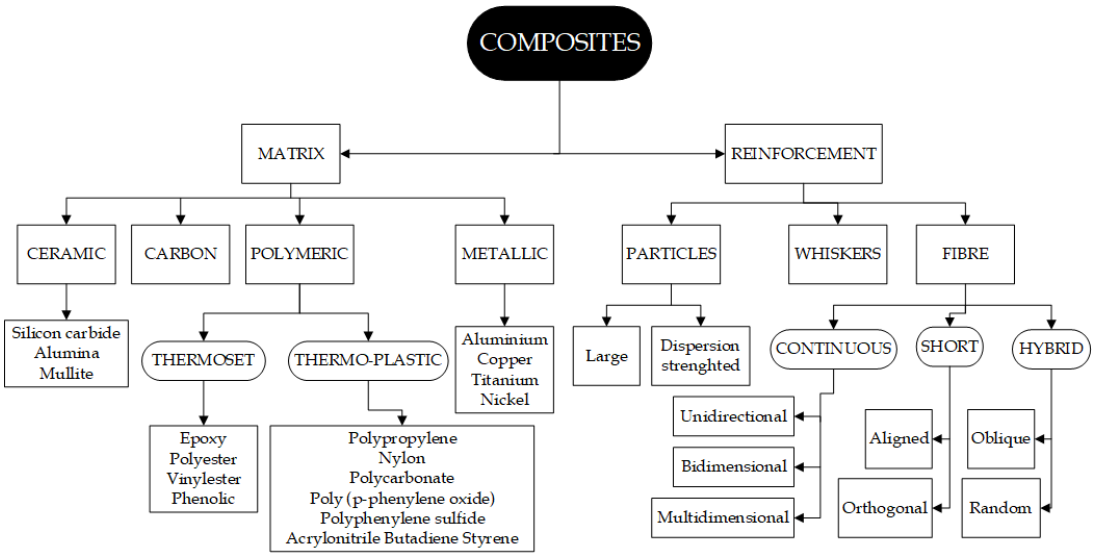


Fig.1-1. General classification of matrix and reinforcement components for composites.

The opportunity to combine several kinds of reinforcements and matrices, offers a broad range of opportunities to create a material with special characteristics, properties and costs. However, although nowadays various material combinations are used in the technological fields, such as railways, marine, wind turbine, civil infrastructures and constructions, automotive, orthopaedic prosthesis, sport equipment, appliances and electrical components [9], in aerospace, the main combination for structural parts is a polymeric matrix reinforced with synthetic continuous-fibres. Fig.1-1 reports also the most commonly used matrices. Regarding the fibre reinforcement, these can be natural (flax, jute, hemp, sisal, ramie, kenaf, abaca, pineapple leaf, coir, oil palm, bagasse, bamboo, wheat straw, curaua and andrice [10]) or synthetic which are principally made of carbon, glass, aramid or Kevlar®, boron (Br) (or graphite)/aluminium (Al), graphite/magnesium (Mg) and silicon carbide (SiC). Specifically, for aerospace applications, carbon and glass fibres are fabricated and interlaced in bidimensional or multidimensional plies called laminas, many of these are stacked and immersed in the matrix to compose a laminate which is the structural component. However, each macroscopic fibre is formed from thousands of microscopic fibres (as 5k,10k,15k), and based on the production process they can

have different mechanical properties such as high strength or high Young's modulus. Other special classes of structural elements are represented by sandwich-structured composite and fibre-metal laminates (FMLs) [11]. The first class is fabricated by bonding two thin and stiff skins to a thick and lightweight core made by open-/closed-cell-structured foams like polyether-sulfone polyvinylchloride, polyurethane, polyethylene or polystyrene foams, balsa wood, syntactic foams, metal foams or honeycombs. The skins can be made with glass- or carbon fibre-reinforced thermoset (sometimes thermoplastic) composites or metal sheet as Aluminium. FMLs follow the same concept of sandwiches but, here, two skins of Aluminium and/or titanium alloys are bonded with glass-, or carbon-, or aramid-epoxy bismaleimide resin prepregs to obtain a five layers laminate.

1.1.1b History

Although some kind of natural composite materials made with wood, cob, cow tendons, clays and mud, slaked lime and limestone, soft and hard steel, have been used since ancient times by the Greeks, Romans, Egyptians, Mongols, and Japaneses for buildings, mortars and concretes or weapons [4,12], World War II (WWII) gave the greatest initial impulse for the development of the modern composites for aerospace applications. If wood was the main structural material at the dawn of the aviation era (famous is the Wright Flyer in 1903), the increasing aerodynamic loads, performance and efficiency requirements during 1920's and 1930's due to the airplane racing competitions induced by World War I, pushed engineers and designers to use metals such as Al making wood obsolete. With the advent of WWII, new extreme requirements were desired for military airplanes, which brought the new chemical discoveries of the first decades of the 1900's in plastics and artificial resins from laboratories to be used for aviation production [13]. In this same way, from the 1960's, the experience left from the war and the new space programs raised the speed of development, research and the use of composites for the aerospace industry, and their use slowly became more and more intensive supplanting metallic materials such as steel, aluminium and titanium. In this period, an important contribution to the integration of the composites in the aerospace industries was given by the race for the space where extensive energy was invested in new structures, components and technologies that were able to work safety in the harsh environment of space. Here, metal-matrix composites were developed based on aluminium-boron carbide, graphite/aluminium or graphite/magnesium continuous-fibre reinforcement immersed in an aluminium alloy matrix [14] and carbon-carbon [15] composites for the Space Shuttle Orbiter and the Hubble Space Telescope.

As is easily understood, the main reason behind the growing demand of composites, was the needs for the performance and efficiency, which required materials with a higher specific tensile modulus and strength but also materials that were economically competitive. In Fig.1-2, a graph showing the composite percentage for some models of military and civil airplanes is presented [16-18]. Composites satisfy perfectly these requirements though, in general, they are more expensive than steel and aluminium alloys, but cheaper than titanium which has amazing mechanical properties and also the highest price. The same reasons attracted composites in the aircraft industry, however if military airplanes exploited these properties to increase the weapons weight and mission time, civil aviation was interested in saving weight for fuel consumption reduction, payload increase, but also for low

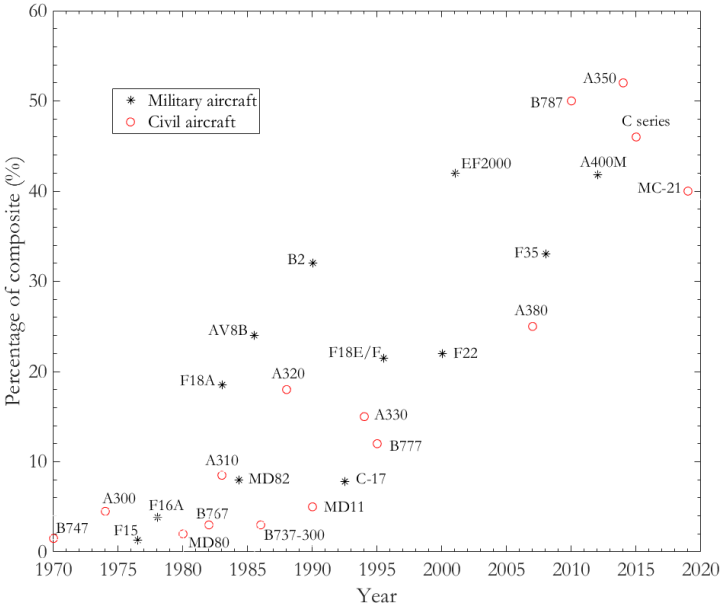


Fig.1-2. Percentage of composites in military and civil aviation [16-18].

maintenance costs and commercial reliability [16]. Nowadays, modern airplanes are constructed by using a high composite percentage to maximize the benefit from their features, as in the case of the Boing 787 with 50% of composite over the total weight and Airbus 350 with ~55%.

1.1.1c Manufacturing processes and issues

Since, as described previously, thermosetting composites are the main materials used in the aerospace industry and the here studied TFBGs have been embedded inside these composites, from now on, the treatment is only on thermoset composite structural parts as laminates composed of continuous-fibre reinforcements and a polymeric matrix. Thermosets are the most used composites for primary structures in aerospace industry and in other fields. They have to be able to resist high loads and be light, but also satisfy several requirements such as chemical and fatigue resistance, but also have a good toughness. Considering all these factors, this research wants to demonstrate a sensing technology able to provide a continuous monitoring of the state of these materials, from the manufacturing to their operational life. The starting materials are usually dry fibres reinforcement injected with a thermosetting resin mixed with a hardener (or curing agent) for layup or as plies of fibres pre-impregnated with resin (prepregs) ready to be stacked. The prepreg lamina are plies of fibre reinforcement already pre-impregnated with the resin mix only partially cross-linked, hence these need to be stored in a refrigerated environment (usually -18°C) to strongly reduce the crosslinking reactions rate. During the decades, several manufacturing techniques and processes have been developed to turn the starting components into composites and a single technique can include two or more processes [19]. The choice of technique is based on the required type of fibre or matrix, quality, performance, application and cost of the final product. Some techniques such as hand layup, spray layup and filament winding comprise an open moulding, while a bag moulding is used for vacuum bag moulding, vacuum infusion, or a closed moulding in resin transfer moulding, compression moulding, pultrusion and reinforced reaction injection moulding [20]. For years, usually in combination with prepregs, vacuum bagging techniques exploited autoclave curing process to thermoset the resin [21]. This allowed composites with the highest fibre volume fraction, quality and performance to be produced ensuring the best standards and repeatability (especially with prepregs) with respect to other processes. However, autoclave processing requires high capital and time investments for operating and maintenance costs, especially for large production volumes as a series of autoclaves of large dimensions are required [22]. Therefore, Liquid Composite Moulding (LCM) processes have raised an interest as an acceptable alternative to the autoclave to obtain composite parts. Resin Transfer Moulding (RTM), Vacuum Infusion (VI), Vacuum Assisted Resin Infusion Moulding (VARTM) and Seeman Composites Resin Infusion Moulding Process (SCRIMP™) are part of the LCM family processes. These are united in having the same process steps, whose the sequence is mould conditioning (cleaning & release agent application), bag placement, plies preforming, layup, draping & vacuum, resin injection, curing & post-curing, and demoulding. The product can undergo successive machining processes such as drilling and/or milling to be prepared for the installation of sensing and monitoring technology. The quality obtained using these processes is quite good compared with the operating costs; a high fibre volume fraction can be achieved and, especially VARTM and SCRIMP™ allow the production to be made flexibly so that large structures and variable production volumes are easily obtainable [20]. The manufacturing process of a composite is the most important step to obtain a valid component with the best mechanical performance and operational requirements [23]. Defects induced in the material during the production are often the first reason for dangerous premature and unexpected failures [24]. Typical defects caused by LCM processes are voids, dry post or resin-rich areas, non-uniform or incomplete curing, uneven stress distribution and residual stresses, fibres reinforcement misalignment and contamination, volatiles and, especially for thicker composites, temperature overshoots due to dominant exothermal reaction phenomena and low thermal conductivity. A reduction of mechanical performance is not the only consequence of the defects, indeed, fibre-matrix bonding failure, micro- and macro-cracking, delamination and deformations can occur in the product causing premature failure, assembly issues for sizing distortions, buckling, waviness and broken fibres and irregularities of fibre distribution in the matrix [25-26].

1.1.2 Silicone adhesives

With the development of polymers during WWII, also the research on silicone chemistry and their production recorded a considerable increase. Silicones are semi-organic high molecular weight chains of silicon and oxygen atoms modified with side groups composed by organic molecules which are cross-linked through primary chains with the silicon atoms [27]. The great interest for these materials, especially for space applications, is related to their attractive properties which make them technologically versatile, flexible, adaptable and indispensable. Furthermore, through a given chemical formulation, the silicone properties can be customised depending the application. Among their numerous features [28], they have:

- Excellent elastomeric capacities such as high flexibility, elastic recovery, low creep and fatigue resistance
- High operating temperature range and cold temperature flexibility (up to 300°C, and down to -90/-115°C based on the chemical formulation)
- Environmental stability in the presence of ultraviolet, moisture, oxygen, ozone, low outgassing, chemical and fire resistance
- High optical transparency customisation (from opaque to clear)
- High gas permeability
- Excellent sealant for a large variety of fluids, in micro- and macro-gaps
- High electrical resistivity/conductivity with the addition of electrically conductive fillers [29-32]
- Low toxicity, easy handling and wet-out
- Low residual stress and shrinkage once cured
- Adhesion to several materials and many different surfaces.

A remarkable advantage of silicones is the option to modify their physical properties through the addition of specific molecules to their chemical composition, as reported in the bulleted list for the electrical conductivity, but also, for example, for the thermal conductivity. Indeed, usually these adhesives have very low thermal conductivity coefficients, which can be increased by adding a conductive filler network (usually ceramic or metal oxides particles as aluminium, beryllium, silver oxide) able to favourite heat conduction [33-35]. Considering the special properties of silicones, this allows them to be used as structural and semi-structural adhesives in several technological fields such as aerospace, automotive, medical, electronic and electric, construction and domestic appliances. Specifically, these result in excellent specifications in bonding applications of different components which are difficult (or almost impossible) to join, where high flexibility is required to absorb movements due to thermal expansion, vibration and external loads. Furthermore, their functionalities are maintained for a wide temperature range, a long time period and in harsh environmental conditions. In aviation, these polymers are applied for semi-structural bonds of materials hard to bond together, in jet engines to prevent bimetallic corrosion at high temperatures, and in optical, electronic and electrical (resistors, connectors) assemblies and components. While, the space sector benefits from silicone's properties and resistance to thermal vacuum outgassing, thermal shock, radiation and high humidity to protect technological components of the spacecraft, to dampen launch vibrations and absorb stresses generated by different thermal expansion [36]. A large structural use is found in photovoltaic arrays, specifically for the bonding sequence of protective cover glasses to solar cells and optical solar reflectors to the substructures [28,37]. Silicones are applied as adhesives, sealants and encapsulants also for LED's, electronic and optical sub-components and assemblies, sensors, detectors, modules, connectors and relays. Although, polymers are usually reactive to atomic oxygen (ATOX) which causes their erosion, some chemical formulations of silicones allow a good level of resistance to be obtained to this form of degradation [38]. However, usually the silicone adhesive is encapsulated between two surfaces to avoid direct exposure to ATOX. Silicones have been used as sealant also for larger parts of spacecraft systems, a specific example is the Low Impact Docking System (LIDS) of the Crew Exploration Vehicle (CEV) developed by NASA Johnson Space Centre to contain cabin air during docking operations of the CEV with the International Space Station (ISS) [39]. For this application, only silicone seals were considered as they were the only class of space qualified elastomers able to work across the mission temperature range, exposed to space environment (vacuum, radiation, ATOX) conditions. Some

examples of commercial available space qualified silicone adhesives are: Nusil® by Avantor, Elastosil® by Wacher, Dowsil™ by Dow and AS1707 by CHT.

1.1.2a Silicone operational issues in space environment

Focusing on space applications, here the operational conditions are the most severe for which a material must guarantee its performance/properties and satisfy the determined mission requirements. Silicones, though possess high environmental resistance properties, and they must coexist with ultra-high-vacuum, ultra-violet (UV) and ionizing radiations, extreme thermal range and cycles, thermal shock, micro-gravity, ATOX, high accelerations, vibrations and space debris for their entire functional life [39,40]. Each harsh perturbation or a combination of these may influence the original material state and induce a modification of its properties [40]. For example, ultra-high-vacuum can affect the original dimensional stability and composition of the polymer as it induces silicone outgassing of additives and low-molecular weight residues [39-42]. In this way, contaminant layers may deposit on nearby cold surfaces and their interaction with UV or ionizing radiation, thermal cycles and ATOX can induce their fixation compromising quality, efficiency and causing severe issues such as failure or permanent damages [41]. Silicone deposited fragments released with outgassing, when interacting with ATOX, undergo oxidation processes with loss of hydrocarbons converting the polymer into a silica-based surface layer. This coating is resistant to ATOX erosion and transparent enough, however in combination with hydrocarbon deposition, its absorbance increases a lot. After years of accumulation, these microscopic contaminant layers form a rough optically absorbing coating which is absolutely undesired on solar arrays (which is, among other things, the spacecraft part where silicone adhesives are extensively used) [42]. A further effect to consider on a spacecraft is thermal variations. Satellites in Low Earth Orbit (LEO) missions, such as European Radar Observatory Sentinel of Global Monitoring for Environment and Security Space programme by ESA [43], experience thermal cycling with significant temperature variations (-170°C:130°C) depending on sunlight/shadow intensity and duration, materials thermo-optical properties such as solar absorbance and thermal emittance, orbit and exposure position/angles respect with Sun and Earth. While, space missions in deep space (Voyager [44], Rosetta [45], Juice [46]) or closer to Sun (BepiColombo [47]) can reach temperatures down to -190°C and up to 400°C, with possible thermal shocks and abrupt gradients. In these conditions, qualified silicone adhesives must be able to maintain their bonding strength and ductility within the determined acceptable margins and absorb possible stress generated by bonded materials with different coefficients of thermal expansion (CTE). Furthermore, chemical stability is also necessary to avoid chemical reactions of organic molecules that might involve undesirable post-curing/aging, decomposition and rupture of chemical bonds [48], with a change of the silicone thermo-optical properties. The entities causing the temperature increase are the incident Solar radiation (UV, Infrared and visible light) and, in much more part, the kinetic energy of ions and molecules impacting the spacecraft. UV beams are particularly dangerous for polymers (silicones included) as the organic chemical composition is photochemically susceptible to these light wavelengths between 200 and 400 nm [49]. Indeed, organic molecules absorb UV light initiating photochemical reactions which cause the rupture of the original bonds. The radical reactions released due to the cleavage of homolytic bonds induce colouration of the transparent silicones with the consequence of a much stronger solar absorbance capability. This effect is especially high when volatiles are released and non-saturated bonds are present in the remaining material, or if impurities are contained in the polymer increase the absorption of UVs contributing to the photochemical reactions [50-52]. The discoloration/colouration indicates a degradation process that means a loss of the original thermo-optical properties and efficiency, and a decrease of the silicone mechanical performance and durability. Even worse consequences may occur when UV effects are combined concurrently with other space phenomena, in particular micro-cracking, loss of property efficiency and premature failures [49-53].
Therefore, taking into account the harsh phenomena and the consequences of their combined actions on the materials, these materials and the components undergo rigid development, qualification, acceptance and protoflight test campaign (as European Cooperation for Space Standardization regulates) to certificate their suitability for space applications, to evaluate their degradation state after the space environment exposure, and to minimise the risk to obtain premature failures [54]. However,

testing campaigns are very time consuming and expensive in terms of resources, equipment, apparatuses and personnel, as intermediate verification methods are necessary to estimate the sample condition. Hence, with the evolution of the space industry, several non-destructive evaluation techniques (NDET) have been developed to monitor the health state of the materials during ground testing and in service [55-60]. However, although many technologies might be used for in-situ evaluation/remote/real-time monitoring [61], the sensors and the support apparatus must match the space compatibility [62] and the embedding requirements [63]. Another issue regards the need to perform multi-parameter measurements to evaluate the overall state of a material or for simple cross-sensitivity compensation of some sensors to a determined parameter (as in the case of temperature for strain-gauges). This involves the integration of more sensors inside the materials and apparatuses in the spacecraft, with a consequent increase of the weight and complexity of the overall system, costs and payload reduction.

1.2 Optical fibre sensors for SHM of composites and silicones

As mentioned in the previous section, composite materials and silicone adhesives, for some common and different reasons, would both benefit from an embedded minimal intrusive and lightweight detection system. The engineering dream to monitor the health and degradation state of the materials from their manufacturing process and during their operational life, with the need to quantify accurately their properties, have motivated, for many years, engineers, researchers and scientists to develop several sensing technologies (Piezoelectric, Acoustic and ultrasound sensing, Electrical gauges, Fibre optic sensors, Eddy current, Comparative Vacuum, Interferometry) [61,64]. These motivations became still stronger specifically with the advent of composite materials, as their anisotropy and physics composition make their behaviour and failure modes different from the "traditional" metallic materials [65]. For their nature, when loaded, the composite internal stress distribution is strictly influenced by its dimensions, lay-up design and manufacturing quality [66], independently from the matrix and fibre reinforcement from which it is made. While, as anticipated in section 1.1.1a, although silicone adhesives for space applications possess highly resistant properties, they are forced to work in harsh environmental conditions for a long time which may degrade, break or reduce the performance of the same elastomeric adhesive. Hence, an embedded technology able to provide information on the material internal state (as such strain levels and temperature) would be appreciable in these circumstances. However, although many sensors can be easily applied externally, a device has to address specific requirements to be embedded inside the element. Since the first applications [67], optical fibre (OF) sensors have been demonstrated to be the perfect candidate for such a task, guaranteeing, at the same time, minimal intrusiveness and addition of weight to the structure. There are substantially three types of these sensors, point-, long-gauge and distributed sensors [68]. This classification is reported in Fig.1-3.

In particular, FBGs (red box in Fig.1-3) possess attractive and interesting features which makes them widely used in SHM and sensing applications. Relevant operational properties are insensitivity to electromagnetic (EM) disturbances, low signal loss and interrogation power, multiplexing on a single OF, accurate and reliable multi-parameter measurements. Furthermore, they satisfy the essential embedding requirements of being light (~70 gr/km) and of tiny dimensions, but of high installation flexibility [69]. Another advantage is the opportunity to adapt the FBG to its specific use through the customisation of the internal Bragg structure, OF glasses and external layers. Therefore, as reported in Fig.1-3, several types of FBGs with specific peculiarities can be obtained.

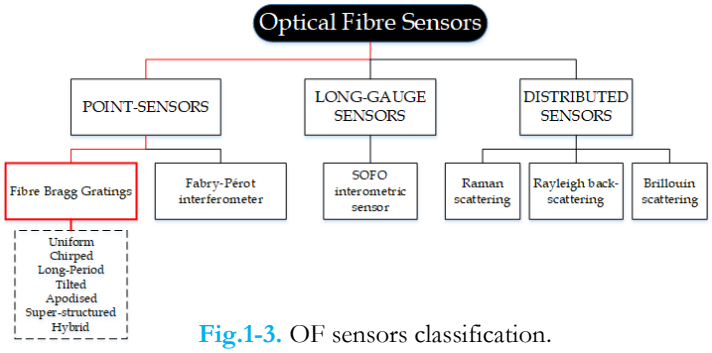


Fig.1-3. OF sensors classification.

Since the first damage detection with an FBG sensor reported by Crane *et al* in 1984 [70], FBGs important benefits have been largely exploited in the composites world from their manufacturing

processes [71-76] to the operational phase for several detection purposes [66,77-80]. Also the space industry has raised an interest for FBGs as the integration of these sensors into spacecraft structures or components allows defect detection to be performed during production, testing and orbit operation [81-83]. Specifically, the FBG diagnostic system helps to detect damage during curing/gluing of polymers and optimisation of the manufacturing process, while damage from debris impact (strain wave) and thermal cycle loads (abnormal and no uniform temperature distribution and strain) are the main monitoring tasks during the orbit or missions in deep space. However, the most relevant benefits are obtained for the environmental testing step as FBGs allow the need and number of conventional sensors (thermocouples, strain gauges, accelerometers, acoustic emission sensors) to be reduced, reducing the costs and lead-times of spacecraft. In this context, SHM through an embedded FBG network can be particularly useful during thermal vacuum, acoustic, vibration, static and dynamic load tests [55-62].

1.3 FBG sensing technology gap and solution

The key points of an SHM system are its lightness and, minimal intrusiveness/interference with the surrounding material, hence, as consequence, a minimum number of applied sensors is desirable. However, these requirements often collide with the need to measure multiple parameters to obtain a complete point of view on the state of the sensorised aerospace materials. Despite the numerous benefits, as for any sensor, FBGs have the weak point of cross-sensitivity for which the uncoupling of parameters affecting the same signal is not achievable with a single conventional OF sensor. Focusing on thermomechanical measurements (which is of great interest in the aerospace field), mechanical deformations and temperature variations affect the wavelength of the same signal in the FBG spectrum [69]. This makes it impossible to distinguish the entities of the two perturbations by knowing the sensitivity of a single signal to both the parameters. Hence, basically, a conventional FBG should be always supported by other techniques to achieve compensation towards a given effect. With the aim to overcome this issue, while maintaining the embedding benefits of the Bragg gratings, several FBG sensor-based techniques have been developed during the last decades. The oldest one proposed is to splice together two different waveguides where two FBGs were manufactured (Fig.1-4a), to obtain a single OF with double consecutive FBGs [84]. A variation of this technique contemplated to produce two consecutive FBGs working at different wavelengths in the same OF [85]. The basic principle of these previous techniques resides in the different sensitivities of the two sensors which allows the separation of the strain and temperature variation. Several techniques exploit the temperature compensation through a second sensor contained inside the same FBG's OF or externally. One of these is two FBGs in the same optical fibre, where one of the sensors is encapsulated in a metallic or plastic capsule (Fig.1-5) so that it works as an optical thermometer and thermally compensates the free FBG [86].

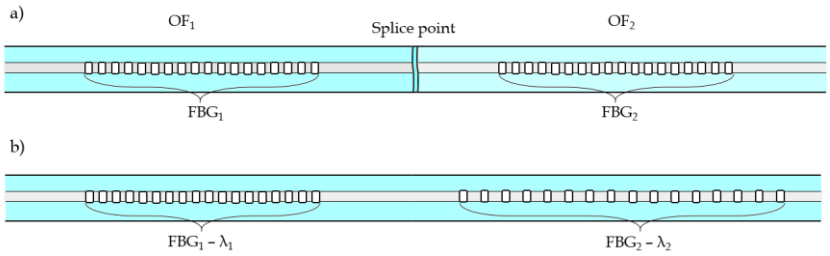


Fig.1-4. a) OFs splicing technique, b) double FBG in single OF.

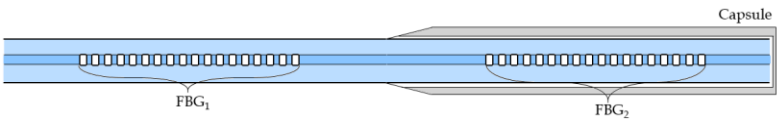


Fig.1-5. a) OFs splicing technique, b) double FBG in single OF.

The same concept was applied for the coupling of the FBG with a Fabry-Pérot interferometer in the same OF [87], or its hybrid variant called the FBG/extrinsic Fabry-Pérot interferometric (FBG/EFPI)

technique [88]. The discrimination has also been performed using a hybrid OF dual sensor composed of FBG and Long Period gratings (LPGs) in the same waveguide [89,90]. Although these solutions seem to solve the technological gap, they do not supply a point (or localized) measurement compromising the spatial resolution and accuracy of the measured parameter. Some techniques suffer from cross-sensitivity, such as to bending in the case of a hybrid FBG/LPGs sensor. Another issue regards the presence of the capsule that, being highly intrusive, can interfere with the surrounding material influencing its performance. The capsule or the splices are also weak points inside the structure as they can induce defects and/or generate points of stress concentration, from which micro-cracks may start and grow with operational fatigue or cycling loads. The use of different sensors implies also several interrogation systems; this fact increases the operational costs and the complexity of the overall monitoring system. Moreover, considering the special design of the sensors, their price is usually higher than standard FBGs and, further, they need time consuming pre-treatment steps (OF splicing, coating removing, encapsulating, joining, cutting) which may also weaken the waveguides.
A further strategy concerns the application of a different sensor, next to a standard FBG, to compensate the temperature effect from its signal. Thermocouples (TCs) are the most reliable option for this scope as they are easy to handle and use, though they are intrusive due to their large diameter (≥1 mm). Thin TCs (Ø≈30-50 μm) can be used to solve the intrusiveness issue, but as experienced during composite sample manufacturing, they are so delicate as to be easily breakable during the embedding and de-moulding step. Certainly, this is an undesirable occurrence since some impurities might be induced in the material which affect its integrity or performance. Moreover, the TCs should be always placed as close as possible to the OF sensors to avoid non-localized measurements, albeit the vicinity of the two sensors could create some disturbances in the measurement of the deformation by the FBG.

In conclusion, by taking into consideration the described techniques, even if FBG sensors match the embedding requirements, they suffer from some critical issues that make the state of art weak, obsolete and not ready for the technological innovation currently occurring in smart materials and SHM.
Therefore, with the aim to overcome the issues of the previous techniques and to raise-up the technological progress and state of art in the sensing field, here, a special and customised FBG sensor is, in this research, demonstrated to measure, simultaneously and separately, three parameters when embedded in non-metallic materials as composites and silicones. This sensor is called a Tilted FBG (TFBG), and it possesses all the features and embedding benefits of the standard FBGs such as low intrusiveness, weight and high resistance. However, unlike FBGs, each single TFBG sensor has been proved to be able to detect, at the same time, strain, temperature and refractive index (RI) variations of the surrounding medium with which the sensor is in contact [91] through the simultaneous demodulation of the Bragg, Ghost and cladding resonance peaks. These resonances compose the transmission spectrum of the TFBG sensors and change their resonance wavelength and amplitude based on the external perturbations that impact the TFBG. A full treatment of the TFBG spectrum and its characteristic resonance peaks, is specifically achieved in chapter 2. Despite that, the scientific literature is focused more on the TFBG as double-parameter discrimination sensor [92-95] or as a refractometer [96,97] using it in air or inside liquids. Indeed, during the literature review, it has been noted that only two researches present measurements performed with TFBGs embedded in composite materials, but using the sensor measuring strain-temperature [98] or RI [3] variations.

In this thesis, the embedding benefits and the special sensing features of the single TFBG are fully exploited when the sensor is embedded in composite materials or space qualified silicone adhesives, to demonstrate that it can provide suitable and reliable information, not only on the thermomechanical state of these materials, but also regarding their refractometric status which is strictly related to their chemical composition evolution. This makes each single TFBG a minimally intrusive multi-parameter sensor able to work individually inside advanced aerospace materials. Furthermore, this sensor has proved to be suitable in monitoring the health state of different materials from their manufacturing process to their operational life, even in harsh environmental conditions as in the case of a silicone adhesive for space applications. At the end, with respect other techniques, the monitoring system based on TFBGs results in lower expense, is compact and easier to set-up and handle, and is an integrated system. The sensor interrogation and the demodulation of the acquired spectra can be performed in

automated mode and optimised algorithms are able to reduce the computational power and the processing times of the computers, which are fundamental requirements and properties for a real-time measurement system. Real-time monitoring systems allow the detection of damage, defects or to verify the health state of a material during its operation without special procedures which could result in some drawbacks, for this reason they are highly desirable.

1.4 Thesis outline, contributions and motivations

The issues described previously for composite materials and silicone adhesives in aerospace applications and the limitations of the sensing technologies at the current state of art have motivated this research to focus on the single three-parameter TFBG sensor. Specifically, the research questions, which represent the milestones of the entire investigation process, are the following:

- *How can the customization of the Bragg gratings influence the capability of the sensor for measuring a certain parameter?*
- *How does the surrounding refractive index variation affect the cladding resonance peaks in the transmission signal of the TFBG sensor?*
- *How do the several steps of the VARTM process affect the resonance peaks in the transmission signal of the TFBG sensor in combination with the thickness of the composites?*
- *How do the space environmental conditions influence the transmission signal and the sensing abilities of the TFBG sensor even once this is embedded in a space qualified silicone adhesive?*

The previously listed research questions have motivated the investigation to obtain exhaustive responses and a complete characterisation of the monitoring technique. First of all, the customisation of the sensor's Bragg structure was analysed respect with its measurement performance. During this step, a novel demodulation technique for refractometric purposes was developed, which is based on the demodulation of the TFBG spectrum through a triangulation method. The interaction between the sensor and the different surrounding materials was addressed from a scientific point of view. Specifically, the investigation was directed towards the effects on the TFBG spectrum induced from: a partial immersion in a liquid with different RI, the several steps that occur during the VARTM composite manufacturing process (such as vacuum imposition, resin infusion, curing and cooling-down stage), thermal cycling loads, UV radiation and space environmental conditions. The VARTM manufacturing process for composites is selected as it is a flexible manufacturing method and available in the TU Delft laboratories. The embedding of this special OF sensor inside different materials was made to investigate its sensing behaviour and the influence of the different surroundings on its measurement performance and reliability. Through this scientific approach, knowledge regarding the fundamentals of the TFBG and its in-situ multi-measurements properties, were directed towards the study the advanced and engineering use of this sensor to monitor the thermomechanical and chemical state of composite and silicone materials at any step of their life and in any environmental condition. The methodology executed for the achievement of these challenging goals is reported in this thesis in six chapters, which are detailed in the scheme reported below in Fig.1-6. The last chapter of the thesis is dedicated to the conclusions and future work purposes.

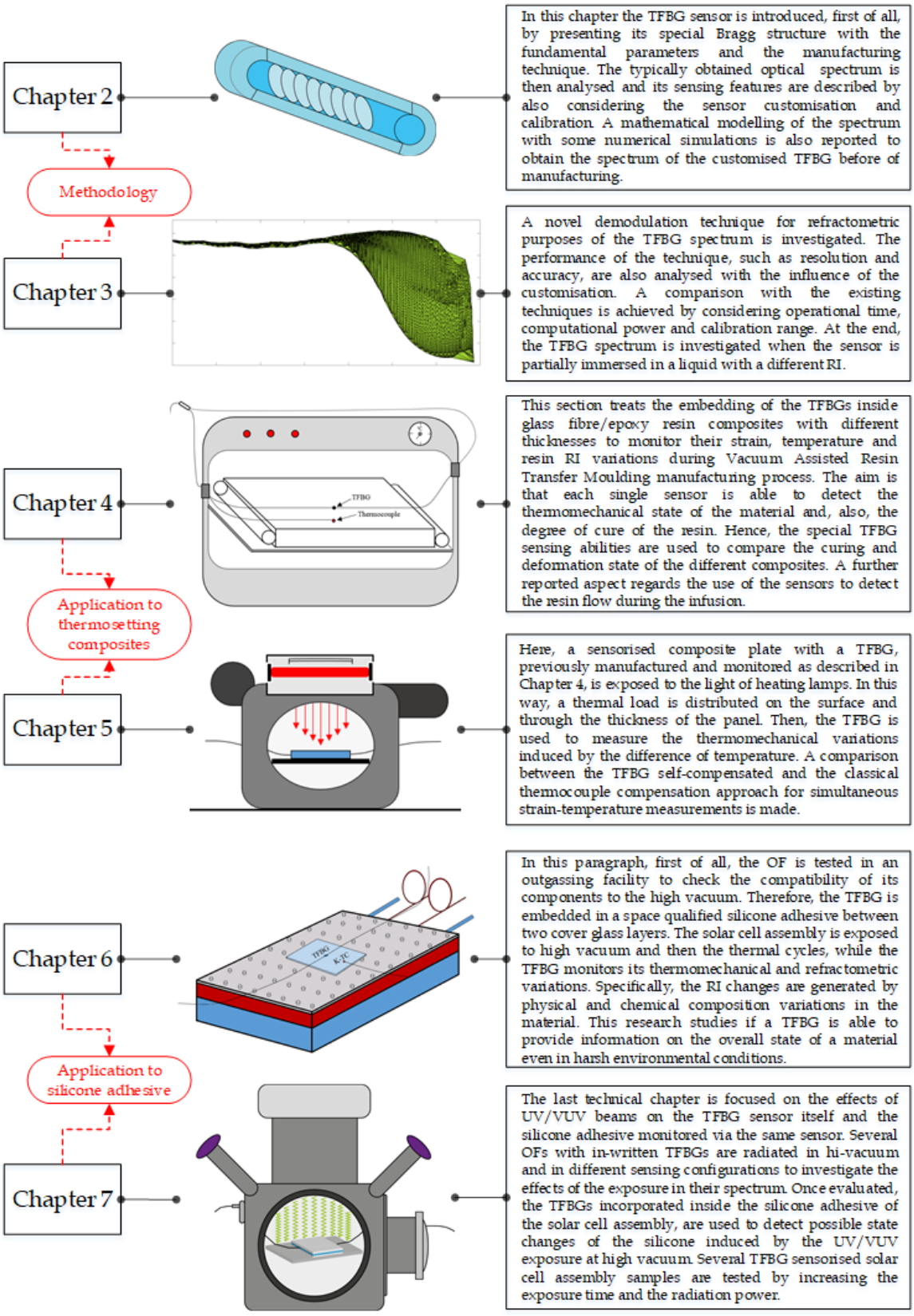


Fig.1-6. Main thesis' chapters outline

References

[1] N.J. Alberto, C.A Marques, J.L. Pinto, R.N. Nogueira, *Three-parameter optical fibre sensor based on a tilted fibre Bragg grating*, Applied Optics, 49 (31), p. 6085-6091, (2010).

[2] E. Chehura, S.W. James, R.P. Tatam, Temperature and strain discrimination using a single tilted fibre Bragg grating, Optics Communications, 275, p. 344-347, (2007).

[3] S.J. Buggy, E. Chehura, S.W. James and R.P. Tatam, *Optical fibre grating refractometers for resin cure monitoring*, J. Opt. A: Pure Appl. Opt., 9, p. S60-S65, (2007).

[4] D. Gay, S.V. Hoa, S.W. Tsai, *Composite materials: design and applications*, CRC Press, 2007.

[5] L. Murr, *Handbook of Materials Structures, Properties, Processing and Performance*, Springer, p. 425-449, 2015.

[6] M.R.M. Jamir, M.S.A. Majid, A. Khasri, *Natural lightweight hybrid composites for aircraft structural applications*, Woodhead Publishing Series in Composites Science and Engineering, p. 155-170, (2018).

[7] F.C. Campbell, *Manufacturing Processes for Advanced Composite*, Elsevier Advanced Technology, 2003.

[8] D.D.L. Chung, *Composite Materials: Science and Applications*, 2nd edition, Springer-Verlag London, 2010.

[9] D.K. Rajak, D.D. Pagar, R. Kumar, C.I. Pruncu, *Recent progress of reinforcement materials: a comprehensive overview of composite materials*, Journal of Mater. Res. Technology, 8 (6), p. 6354-6374, (2019).

[10] O. Faruk, A.K. Bledzki, H.P. Fink, M. Sain, *Progress Report on Natural Fiber Reinforced Composites*, Materials and Engineering, 299, p. 9-26, (2014).

[11] X.S. Yi, S. Du, L. Zhang, *Composite Materials Engineering, Volume 1*, Springer, 2018.

[12] A. Moropoulou, A. Bakolas, S. Anagnostopoulou, *Composite materials in ancient structures*, Cement & Concrete Composites, 27, p. 295–300, (2005).

[13] T.G. Ngo, *Composite and Nanocomposite Materials from knowledge to industrial applications*, IntechOpen, p.3-4, 2020.

[14] S. Rawal, *Metal-Matrix Composites for Space Applications*, The Journal of The Mineral, Metals & Materials Society, 53, p.14-17, (2001).

[15] J.D. Buckley, D.D. Edie, *Carbon-Carbon Materials and Composites*, Noyes Publications, 1993.

[16] R.M. Jones, *Mechanics of Composite Materials*, Taylor & Francis, 1999.

[17] L. Zhang, X. Wang, J. Pei, Y. Zhou, *Review of automated fibre placement and its prospects for advanced composites*, Journal of Material Science, 55, p. 7121-7155, (2020).

[18] R.S. Pierce, B.G Falzon, *Simulation Resin Infusion through Textile Reinforcement Materials for Manufacture of Complex Composite Structures*, Engineering, 3, p. 596-607, (2017).

[19] K.G. Swift, J.D. Booker, *Plastics and composites processing*, Manufacturing Precess Selection Handbook, p. 141-174, (2013).

[20] S.K. Mazumdar, *Composites manufacturing materials, product and Process Engineering*, CRC Press, p. 47-49, (2002).

[21] A. Vita, V. Castorani, M. Germani, M. Marconi, *Comparative life cycle assessment and cost analysis of autoclave and pressure bag molding for producing CFRP components*, The International Journal of Advanced Manufacturing Technology, 105, p. 1967-1982, (2019).

[22] S.H. Advani, K.T. Hsiao, *Manufacturing techniques for polymer matrix composites*, Woodhead Publishing, p. 4-11, (2012).

[23] A. Hambali, S.M. Sapuan, N. Ismail, Y. Nukman, *Composite Manufacturing Process Selection using Analytical Hierarchy Process*, International Journal of Materials and Engineering, 4 (1), p. 49-61, (2009).

[24] E.S. Greenhalgh, *Failure Analysis and fractography of polymer composites*, CRC Press, p. 11, 2009.

[25] P. Robinson, E. Greenhalgh, S. Pinho, *Failure mechanisms in polymer matrix composites*, Woodhead Publishing Limited, p. 26-52, (2012).

[26] P.E. Irving, C. Soutis, *Polymer Composites in the Aerospace Industry*, Woodhead Publishing Series in Composites Science and Engineering, p. 83-97, (2020).
[27] D.V. Rosato, R.T. Schwartz, *Environmental Effects on Polymeric Materials*, Interscience Publishers, John Wiley & Sons, p. 121, (1968).
[28] C. White, K. Tan, A. Wolf, L. Carbary, *Advances in structural silicone adhesives*, Advances in Structural Adhesive Bonding, Woodhead Publishing Series in Welding and Other Joining Technologies, p. 66-95, (2010).
[29] J.C. Getson, M.A. La Scola, *Electrically Conductive, Cured Silicone Rubber Compounds, Made from Storage-Stable Compositions Based on known Organopolysiloxane Composition containing Silver-Coated Mica and Carbon Black Stabilizer*, US Patent, 4, 777, 205, (1988).
[30] L.N. Kroupa, *Electrically Conductive Silicone Compositions Containing Carbon Particles, Have Disilazane Compound or Hydroxyl Endeblocked poly(methylphenyl) siloxane to Lower Resistivity*, European Patent EP 0, 352, 039-B1, (1990).
[31] H. Adachi, N. Suganuma, *Electrically Conductive, Moisture-Curable Silicone Rubber Sealants obtained by Blending Polyorganosiloxane with Silane or Siloxane Metal Oxide Filler*, European Patent, EP 0, 558, 044-B1, (1993).
[32] D.L. Kleyer, M.A. Lutz, *Silicone Composition and Electrically Conductive Silicone Adhesive Formed Therefrom*, US Patent, 6, 534, 581, (2003).
[33] R.C. Rogelhof, J.L. Throne, R.R. Ruetsch, *Methods for predicting the thermal conductivity of composite systems: a review*, Polymers Engineering Science, 16 (9), p. 615-625, (1976).
[34] J.C. Getson, M. Pate, *Thermally Conductive Room Temperature Vulcanizable Silicone-Elastomer Containing Silicon Nitride Filler*, US Patent, 4, 584, 336, (1986).
[35] L.N. Lewis, S.K. Gifford, S. Rubinsztajn, *Curable Silicone Compositions, Methods and Articles made Therefrom*, US Patent 6, 639, 008, (2003).
[36] L.H. Lee, *Adhesives, Sealants, and Coatings for Space and Harsh Environments*, Polymer Science and Technology, 37, Springer, (1988).
[37] C.O.A. Semprimoschnig, D. Pueyo, J.R. Williamson, C. Mooney, C. Zimmermann, M. V. Eesbeek, S. Taylor, *Elastosil S 690 – A Space Qualified European Silicone Material*, 11th International Symposium on Materials in a Space Environment, (2009).
[38] B.A. Banks, R. Damko, *Atomic Oxygen Protection of Materials in Low Earth Orbit*, NASA Technical Memorandum 211360, NASA, (2002).
[39] H.C. de Groh III, C.C. Daniels, J.A.Dever, S.K. Miller, D.L. Waters, J.R. Finbeiner, P.H. Dunlap Jr, B.M. Steinetz, *Space Environment Effects on Silicone Seal Materials*, NASA/TM-2010-216332, (2010).
[40] E. Grossman, I. Gouzman, *Space environment effects on polymers in low earth orbit*, Nuclear Instruments and Methods in Physics Research B, 208, 48-57, (2003).
[41] B.A. Banks, S.K. Rutledge, E. Sechkar, T. Stueber, A. Snyder, K.K. de Groh, C. Haytas, D. Brinker, *Issues Effects of Atomic Oxygen Interactions with Silicone Contamination on Spacecraft in Low Earth Orbit*, in: Proceedings of the 8th International Symposium on Materials in a Space Environment, 5th International Conference on Protection of Materials and Structures from the LEO Space Environment, France, (2000).
[42] B.A. Banks, K.K. de Groh, S.K. Rutledge, C.A. Haytas, *Consequences of Atomic Oxygen Interaction with Silicone and Silicone Contamination on Surface in Low Earth Orbit*, NASA TM-1999-209179, (1999).
[43] R. Torres, P. Snoeij, D. Geudtner, D. Bibby, M. Davidson, E. Attema, P. Potin, B. Rommen, N. Floury, M. Brown, I.N. Traver, P. Deghaye, Berthyl Duesmann, B. Rosich, N. Miranda, C. Bruno, M. L'Abbate, R. Croci, A. Pietropaolo, M. Huchlerc, F. Rostan, *GMES Sentinel-1 mission*, Remote Sensing of Environment, 120, p. 9-24, (2012).
[44] C.E. Kohlhase, P.A. Penzo, *Voyager Mssion Description*, Space Science Reviews, 21, p. 77-101, (1977).
[45] K. Glassmeier, H. Boehnhardt, D. Koschny, E. Kührt, I. Richter, *The Rosetta mission: flying towards the origin of the solar system*, Space Science Reviews, 128, p. 1-21, (2007).

[46] O. Grasset, M.K. Dougherty, A. Coustenis, E.J. Bunce, C. Erd, D. Titov, M. Blanc, A. Coates, P. Drossart, L.N. Fletcher, H. Hussmann, R. Jaumann, N. Krupp, J.-P. Lebreton, O. Prieto-Ballesteros, P. Tortora, F. Tosi, T. Van Hoolst, *Jupiter Icy moons Explorer (JUICE): An ESA mission to orbit Ganymede and to characterise the Jupiter system*, Planetary and Space Science, 78, p. 1-21, (2013).
[47] J. Benkhoff, J. Casteren, H. Hayakawa, M. Fujimoto, H. Laakso, M. Novara, P. Ferri, H.R. Middleton, R. Ziethe, *BepiColombo-Comprehensive exploration of Mercury: Mission overview and science goals*, Planetary and Space Science, 58, 1-2, p. 2-20, (2010).
[48] J.A. Dever, E.J Bruckner, D.A. Scheiman, C.R. Stidham, *Combined contamination and space environmental effects on solar cells and thermal control surfaces*, 18th Aerospace Ground Testing Conference, AIAA 94-2627, Colorado, (1994).
[49] C.G. Zimmermann, *On the kinetics of photodegradation in transparent silicones*, Journal of Applied Physics, 103, 083547, (2008).
[50] A.C. Tribble, *The Space Environment: Implications for Spacecraft Design*, Princeton University Press, (1995).
[51] H.R. Fischer, C. Semprimoschnig, C. Mooney, T. Rohr, E.R.H. van Eck, M.H.W. Verkuijlen, *Degradation mechanism of silicone glues under UV irradiation and options for designing materials with increased stability*, Polymer Degradation and Stability, 98, p. 720-726, (2013).
[52] W. Schnabel, *Polymer Degradation: Principles and Practical Applications*, Macmillan Publishing Co. Inc., Chapter 4, (1981).
[53] M. Kutz, *Handbook of Environmental Degradation of Materials*, William Andrew Publishing, Chapter 23, (2005).
[54] D.L. Edwards, A.P. Tighe, M. Van Eesbeek, Y. Kimoto, K.K. de Groh, *Overview of the Natural Space Environment and ESA, JAXA, and NASA Materials Flight Experiments*, MRS Bulletin, 35, p. 25–34, (2010).
[55] R.O. Claus, K.A. Murphy, K.D. Bennett, *Smart Skinks and Structures overview*, SEM Spring Conference on Experimental Mechanics, Proceedings A91-16751, 04-39, p. 528-533, (1989).
[56] R.S. Rogowski, J.S. Heyman, M.S. Holben Jr., *Sensor Technology for Smart Structures*, International Instrumentation Symposium, Proceedings A91-1965106-35, p. 177-181, (1989).
[57] R.S. Rogowski, *On-orbit Structural Health Monitoring*, Fiber Optic Smart Structures and Skins III, Proceedings of SPIE, 1370, (1990).
[58] M.D. Aggarwal, B.G. Penn, J. Miller, *Triboluminescent Materials for Smart Optical Damage Sensors for Space Applications*, NASA/TM-2008-215410, (2008).
[59] S.G. Hang, D.H. Kang, C.G. Kim, *Real-time monitoring of transverse thermal strain of carbon fiber reinforced composites under long-term space environment using fiber optic sensors*, NDT&E International, 42, p. 361-368, (2009).
[60] A.J. Osei, *Monitoring of Structural Integrity of Composite Structures by Embedded Optical Fiber Sensors*, Journal of Emerging Trends in Engineering and Applied Sciences, 5 (7), (2014).
[61] T. Savill, E. Jewell, *Techniques for In Situ Monitoring the Performance of Organic Coatings and Their Applicability to the Pre-Finished Steel Industry: A Review*, Sensors, 21, 6334, (2021).
[62] B. Hufenbach, S. Habinc, P. Vuilleumier, *Space Applications For Smart Sensors*, European Space Agency, Proceed. Eurosensors XIII, 13th European Conference On Solid-St. Transducers, (1999).
[63] G. Dumstorff, S. Paul, W. Lang, Integration Without Disruption: The Basic Challenge of Sensor Integration, IEEE Sensors Journal, 14 (7), (2014).
[64] D. Balageas, C.P. Fritzen, A. Güemes, *Structural Health Monitoring*, ISTE Ltd., p. 13-50, (2006).
[65] J.N. Reddy, *Mechanics of Laminated Composite Plates and Shells*, CRC Press, Second Edition, 2004.
[66] J.M. Balvares, *In situ strain & cure monitoring in liquid composite moulding by fibre Bragg grating sensors*, Doctoral thesis, TU Delft, 2014.
[67] B. Hofer, *Fibre optic damage detection in composite structures*, Composites, 18 (4), (1987).
[68] G. Di Branko, D. Inaudi, *Fiber Optic Metods for Structural Health Monitoring*, John Wiley & Sons Ltd., 2007.
[69] R. Kashyap, *Fiber Bragg gratings*, San Diego Academic Press, (1999).

[70] R.M. Crane, *A Fiber Optic System for Damage Assessment of FRP Composite Structures*, Naval Engineers Journal, 6 (96), p. 52-56, (1984).
[71] E. Chailleux, M. Salvia, N. Jaffrezic-Renault, V. Matejec, I. Kasik, *In situ study of the epoxy cure process using a fibre-optic sensor*, Smart Materials and Structures, 10(9), p. 194-202, (2001).
[72] P. Ferdinand, S. Magne, V. Dewynter-Marty, S. Rougeault, L. Maurin, *Applications of Fibre Bragg Grating Sensors in the Composite Industry*, Materials Research Society, 3, p. 400-407, (2002).
[73] E. Chehura, A.A. Skordos, C.C. Ye, S.W. James, I.K. Partridge, R.P. Tatam, *Strain development in curing epoxy resin and glass fibre/epoxy composites monitored by fibre Bragg grating sensors in birefringent optical fibre*, Smart Materials and Structures, 14 (9), p. 354-362, (2005).
[74] V. Antonucci, M. Giordano, A. Cusano, J. Nasseri, L. Nicolais, *Real time monitoring of cure and gelification of a thermoset matrix*, Composites Science and Technology, 66 (16), p. 3273-3280, (2006).
[75] G. Rajan, B.G. Prusty, *Structural Health Monitoring using Fiber Optic Methods*, CRC Press Taylor & Francis Group, p. 238-243, (2017).
[76] S. Khadka, M. Kumosa, *Determination of residual stresses in a single FBG fiber/epoxy composite system*, Composites Science and Technology, 109138, (2021).
[77] S. Takeda, S. Minakuchi, Y. Okabe, N. Takeda, *Delamination monitoring of laminated composites subjected to low-velocity impact using small-diameter FBG sensors*, Composites Part A: Applied Science and Manufacturing, 36 (7), p. 903-908, (2005).
[78] N. Takeda, Y. Okabe, T. Mizutani, *Damage detection in composites using optical fibre sensors*, Journal of Aerospace Engineering, 221 (4), p. 497-508, (2007).
[79] M. Mieloszyk, K. Majewska, W. Ostachowicz, *Application of embedded fibre Bragg grating sensors for structural health monitoring of complex composite structures for marine applications*, Marine Structures, 76, 102903, (2021).
[80] M.G.R. Sause, E. Jasiūnienė, *Structural Health Monitoring Damage Detection Systems for Aerospace*, Springer Aerospace Technology, (2021).
[81] S. Kabashima, T. Ozaki, N. Takeda, *Structural health monitoring using FBG sensor in space environment*, SPIE Proceedings, Smart Structures and Materials, 4332, (2001).
[82] E. Haddad, R. Kruzelecky, J. Zou, B. Wong, N. Mohammad, G. Thatte, W. Jamroz, S. Riendeau, *Innovative Embedded Fiber Sensor System for Spacecraft's Health in Situ Monitoring*, AIP Conference Proceedings, 1087, 463, (2009).
[83] G. Hegde, M.V.N. Prasad, S. Asokan, *Temperature compensated diaphragm based Fiber Bragg Grating (FBG) sensor for high pressure measurement for space applications*, Microelectronic Engineering, 248, 111615, (2021).
[84] P.M. Cavaleiro, F.M. Araujo, L.A. Ferreira, J.L. Santos, F. Farahi, *Simultaneous Measurement of Strain and Temperature Using Bragg Gratings Written in Germanosilicate and Boron-Codoped Germanosilicate Fibers*, IEEE Photonics Technology Letters, 11 (12), (1999).
[85] X. Shu, Y. Liu, D. Zhao, B. Gwandu, F. Floreani, L. Zhang, I. Bennion, *Dependence of temperature and strain coefficients on fiber grating type and its application to simultaneous temperature and strain measurement*, Optics Letters, 27 (9), (2002).
[86] R. Montanini, L. D'Acquisto, *Simultaneous measurement of temperature and strain in glass fibre/epoxy composites by embedded fibre optic sensors: I. Cure monitoring*, Smart Materials and Structures, 16, p. 1718-1726, (2007).
[87] R. de Olivera, C.A. Ramos, A.T. Marques, *Health monitoring of composite laminates using fibre optic sensors*, Smart Materials and Structures, 86 (3-5), p. 340-346, (2008).
[88] H.K. Kang, D.H. Kang, C.S. Hong, C.G. Kim, *Simultaneous monitoring of strain and temperature during and after cure of unsymmetric composite laminate using fibre-optic sensors*, Smart Materials and Structures, 12(1), p. 29-35, (2003).
[89] H.J. Patrick, G.M. Williams, A.D. Kersey, J.R. Pedrazzani, A.M. Vengsarkar, *Hybrid fibre Bragg grating/long period fibre grating sensor for strain/temperature discrimination,* Photonics Technology Letters, 8(9), p. 1223-1225, (1996).

[90] S. Triollet, L. Robert, E. Marin, Y. Ouerdane, *Discriminated measures of strain and temperature in metallic specimen with embedded superimposed long and short fibre Bragg Gratings*, Measurement Science and Technology, 22(1), 15202, (2011).
[91] N. J. Alberto, C. A. Marques, J. L. Pinto, R. N. Nogueira, *Three-parameter optical fiber sensor based on a tilted fiber Bragg grating*, Applied Optics, 49 (31), p. 6085–6091, (2010).
[92] M. S. D. Chun-Liu Zhao, Xiufeng Yang, W. Jin, *Simultaneous temperature and refractive index measurements using a 3° slanted multimode fiber bragg grating*, Journal of Lightwave Technology, 24 (2), p. 879–883, (2006).
[93] E. Chehura, S. W. James, R. P. Tatam, *Temperature and strain discrimination using a single tilted fibre Bragg grating*, Optics Communication, 275, p. 344–347, (2007).
[94] Y. Miao, B. Liu, C. Zhao, *Simultaneous measurement of strain and temperature using single titled fibre Bragg grating*, Electronics Letters, 44 (21), p. 1242–1243, (2008).
[95] Y.X. Jin, C.C. Chan, X.Y. Dong, Y.F. Zhang, *Temperature-independent bending sensor with sensor with tilted fiber Bragg grating interacting with multimode fiber*, Optics Communications, 282, p. 3905–3907, (2009).
[96] G. Laffont, P. Ferdinand, *Tilted short-period fibre-Bragg-grating-induced coupling to cladding modes for accurate refractometry*, Measurement Science & Technology, 12, p. 765–770, (2001).
[97] C. Chan, C. Chen, A. Jafari, A. Laronche, D. J. Thomson, J. Albert, *Optical fiber refractometer using narrowband cladding-mode resonance shifts*, Applied Optics, 46 (7), p. 1142–1149, (2007).
[98] G. Rajan, B.G. Prusty, *Structural Health Monitoring using Fiber Optic Methods*, CRC Press Taylor & Francis Group, p. 238-243, (2017).
[99] S. J. Buggy, E. Chehura, S. W. James, R. P. Tatam, *Optical fibre grating refractometers for resin cure monitoring*, Journal of Optics A: Pure and Applied Optics, 9, p. S60–S65, (2007).

1

2

TFBG: fundamentals and sensing properties

"If opportunity doesn't knock, build a door."
Milton Berle

The work presented in this chapter, is able to provide some responses regarding the first and (partially) the second research questions, which are reported here:

- *How can the customization of the Bragg gratings influence the capability of the sensor for measuring a certain parameter?*
- *How does the surrounding refractive index variation affect the cladding resonance peaks in the transmission signal of the TFBG sensor?*

Specifically, in order to obtain answers for the previous questions, the fundamentals regarding the Bragg gratings structure, spectrum and mode-coupling of the TFBG are treated in the first and second section, while the third section is dedicated to the numerical modelling and simulation of the resonance peaks in the spectrum by considering different TFBG customizations. Therefore, from the fourth section, the multi-parameter sensing abilities of the TFBG sensor are introduced along with the calibration procedures and the demodulation technique for thermomechanical measurements.

Part of the here reported work is the result of a collaboration with Dr. D. Klyukin, who gave a great contribution in the development of the mathematical model. The produced work has been published in AIP Congress Proceedings under "*Transfer matrix method for fundamental LP_{01} core mode coupling in a Tilted FBG sensor*" [1].

FBGs are also called short period Bragg gratings as they are created via a short (usually ~1 cm) and permanent modulation of the refractive index (RI) in the core layer of the OF used to manufacture the sensors. This modulation modifies the RI core of the OF and it is performed by using a well-defined profile (such as uniform, chirped, apodizing, super-structure) from which the sensor, and hence, its properties and features fully depend. Unlike standard FBGs, the Bragg structure for a TFBG with the core RI modulation, is tilted with respect to the OF optical axis, at an angle called the tilt angle and conventionally indicated with θ. Nowadays, the most used manufacturing technique to engrave the RI profile in the OF's core is the phase-mask technique [2]. The schematic of its manufacturing setup is reported below in Fig.2-1. Usually, the TFBG manufacturing setup consists of a UV excimer laser (or a femtosecond pulse laser, working between 193-266 nm) beam directed through a cylindrical lens. The beam is then expanded by the lens and forced to pass through several tiny slots of a rotational phase-mask. The interferences generated from passing through the mask's slots allow an interfering beam of 0^{th} order to be obtained by modifying locally the core RI of the OF. Across the length where the sensor is written, the external coating layer has been removed. In this way, at each pulse of the laser, the Bragg structure is increasingly engraved with a larger RI variation as the TFBG sensor is formed. The live spectrum can be observed during the TFBG inscription process by connecting the OF to the interrogator, as reported in Fig.2-2 for a TFBG used in this work. By viewing from the left side to the right and from the upper to the lower spectra, the evolution of the TFBG signal morphology can be

seen and enhanced with the increasing number of laser pulses. Specifically, in the first stages, the Bragg peak is the narrowest one that can be recognised (at approximately 1552 nm) and is the first to form.

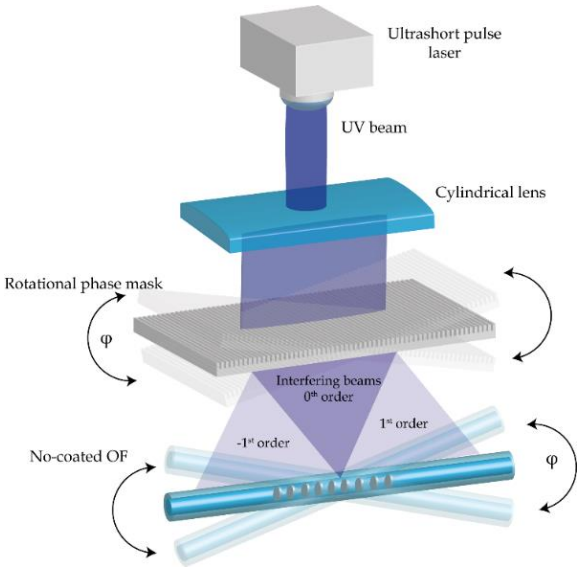


Fig.2-1. Schematic of the TFBG manufacturing setup.

Initially, the other peaks are too weak to distinguish, however, when the core RI modulation becomes deeper with the increment of pulses, these take their own shape in the spectrum. This process is the same for any FBG sensor, however, in the case of TFBGs, the phase-mask (or special mirrors placed below the mask) or the OF can rotate with respect to the optical axis at the angle indicated in Fig.2-1 by φ which is different from the tilt angle θ inside the TFBG.
More components of the writing setup can be rotated at the same time, during the TFBG inscription based on the manufacturing requirements of the sensor. The external rotational angles and the tilt internal angle θ are linked by several formulas depending from the manufacturing method [3]. As can be understood, the internal structure and the properties of the TFBG depend on the external angles, the phase-mask, the laser source and the OF used.

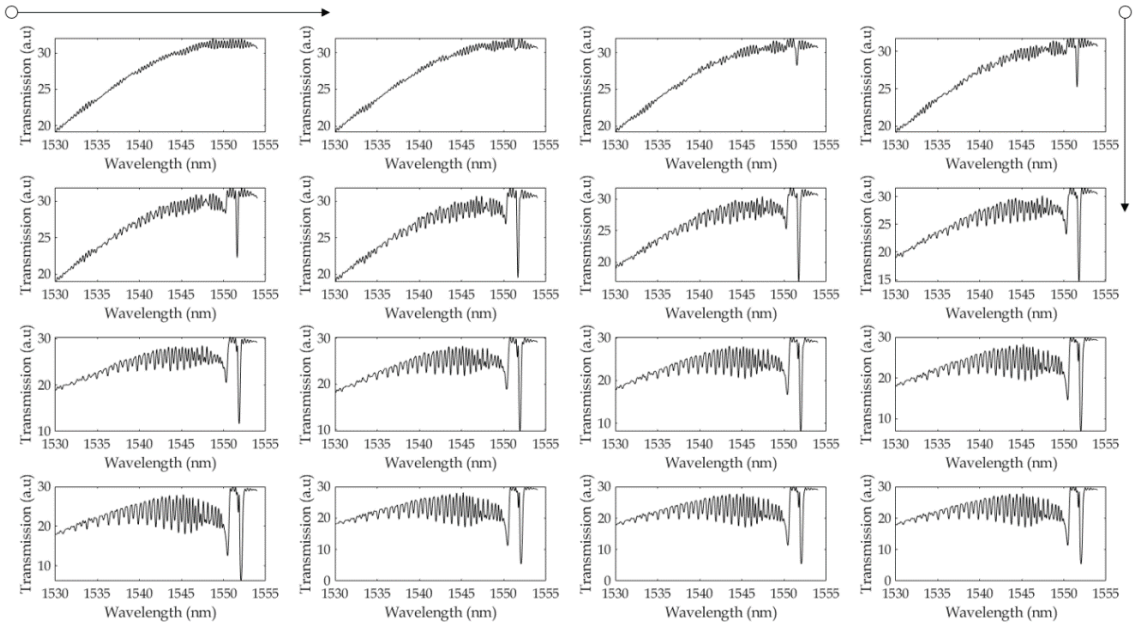


Fig.2-2. TFBG spectrum morphology evolution during the manufacturing (arrows indicate increasing time and energy).

The generic final result of the inscription is reported in Fig.2-3, where the tilt angle can be observed and Λ and Λ_G are defined as the nominal grating period and the period of the tilted grating, respectively.

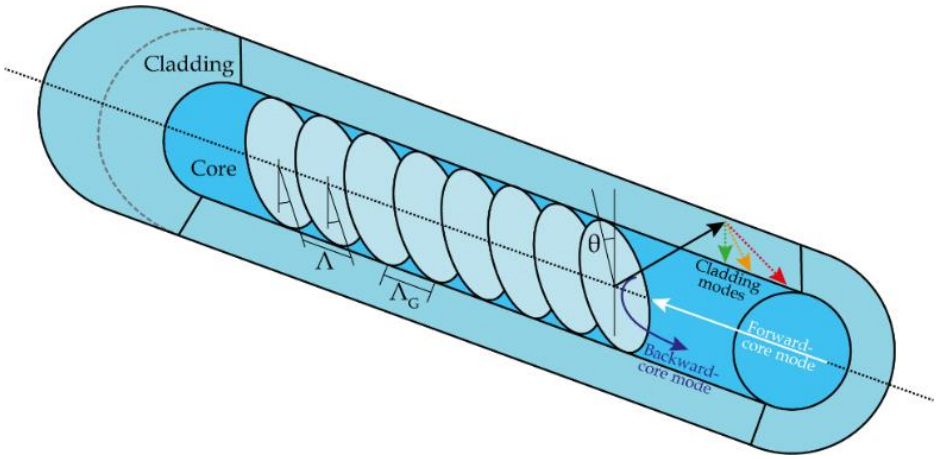


Fig.2-3. Schematic of the internal tilted Bragg grating structure and its fundamental parameters.

The tilted modulation allows a different mode coupling system to be generated inside the core of the OF. Specifically, as shown in Fig.2-3, the forward-propagating broad light inside the core (arrow in white) is reflected in two ways, a part is backward-propagated in the same direction and a second part is directed into the cladding layer. This last ray is reflected back into the core from the cladding layer according to the total internal reflection law, where it is coupled with the forward-propagating light. The described coupling-mode generates unique and special characteristics in the transmission spectrum of the TFBG, which, as consequence, can be demodulated to achieve multi-parameter measurement abilities.

In this chapter, the TFBG theory is treated by introducing the fundamentals regarding the spectrum properties and the sensing features. In the first section, the transmission spectrum is presented with its resonance peaks. Here, a novel technique is reported, based on the transfer matrix method to simulate the transmission signal in relation to the parameters of the OF and TFBG customisation. The second part of the chapter is dedicated to the calibration and demodulation technique used to measure the strain-temperature variations. The refractometric sensing theory is introduced in this chapter, however the demodulation is achieved in the next chapter.

2.1 TFBG spectrum

In the past, the TFBG sensor has been studied, modelled and analysed theoretically by several scientists [4-8] with the aim to develop mathematical models representing its coupling-mode theory, and hence, the spectrum. Specifically, three main kind of resonances can be identified in the transmission[1] spectrum of a TFBG: Bragg, claddings and Ghost. The Bragg peak comes from the coupling between the forward-propagating core light and the backward-propagating core light reflected by the slanted Bragg surfaces, and it is common in all FBG type sensors. The cladding resonance peaks are generated by the exchange of power between the modes reflected back from the cladding layer and the main propagation mode forward-flowing inside the core. These resonances are typical of the TFBGs, the Bragg structure of which enhances their reflection and, hence, power amplitude in the spectrum. The Ghost resonance is a special peak that can be found only in the transmitted signal of weakly tilted FBG sensors slightly away on the blue wavelength side of the Bragg peak, and it is the result of a group of low-order and strongly guided cladding modes coupling with the core light. Its presence in the spectrum of these peaks allows the multi-parameter sensing. However, their resonance amplitude and wavelength depend strongly on the tilt angle imposed to the sensor.

2.1.1 Tilt angle influence

An analysis of the phase-matching condition can be performed to understand how the tilt angle θ influences the coupling system between the in-fibre propagating modes. For this, the core mode,

[1]Cladding resonances might be noted also in the TFBG reflection spectrum, even in the case of standard FBGs as the core RI modulation is not perfectly perpendicular to the optical axis of the OF. However, the resonances amplitude is too attenuated to be well-defined and are confused with the noise of the interrogation system.

radiated and grating light wave vectors are introduced, respectively, as $\mathbf{K_{core}}$, $\mathbf{K_R}$ and $\mathbf{K_G}$, where the strongest mode coupling occurs when the phase-matching condition is satisfied, when $\mathbf{K_R = K_{core} + K_G}$. Furthermore, since in single-mode OF, the RI of the core and cladding are close, it is justified to suppose that the weakly guided OF approximation holds where $\mathbf{K_{core}}$ and $\mathbf{K_R}$ are assumed the same. At this point, three cases can be supposed [9-11], specifically, gratings with, $\theta<45°$, $\theta\approx45°$ and $\theta>45°$ tilt angles. In the first case ($\theta<45°$, Fig.2-4), the vector's composition allows a double coupling system of the core mode light, which is coupled to the backward-propagating core mode and cladding modes. The radiation angle indicated with δ is obtuse in this specific case, and the TFBG is called reflective.

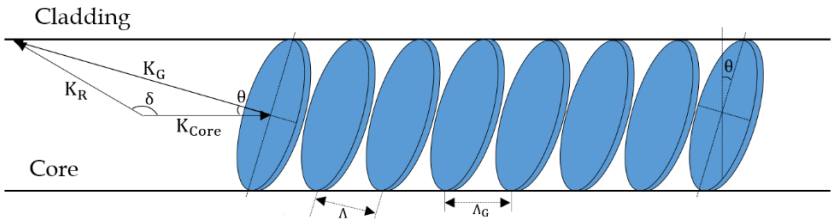


Fig.2-4. Light wave vectors composition for $\theta<45°$.

When θ is in an interval of values close to 45° (δ is around 90°), a phenomenon called radiation mode coupling occurs. In particular, a large amount of the light is reflected toward the cladding and irradiated out of the OF as shown in Fig.2-5. This range of angles where the light is irradiated out depends on a critical angle which can be calculated in the cladding and surrounding medium RIs [10]. As the cladding modes are no longer guided in the OF but are coupled outside, consequently the spectrum is characterised by a lack of resonances.

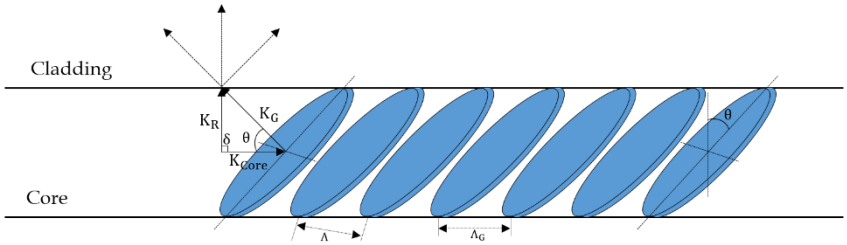


Fig.2-5. Light wave vectors composition for $\theta\approx45°$.

In case θ is greater than 45°, out of the radiation range, the radiation angle becomes acute and $\mathbf{K_R}$ heads from backward- towards a forward-propagation direction (Fig.2-6). This means the cladding modes are coupling with the core mode flowing inside the OF in the same direction. In this condition, the TFBG are called transmissive.

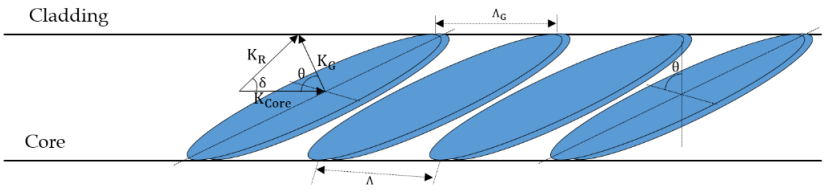


Fig.2-6. Light wave vectors composition for $\theta>45°$.

For the scope of this thesis, the only configuration able to provide a spectrum with three-parameter sensing abilities is the reflective TFBG ($\theta<45°$). Specifically, only weakly tilted FBGs ($\theta<10°$) allow only the Bragg, Ghost and cladding peaks to be present in the spectrum. Indeed, based on the OF type, after a certain tilt angle, the Ghost resonance (and even the Bragg peak) disappear from the spectrum [4,6]. For example, before the experimental campaign, during the definition of TFBG customisation it was noted during manufacturing by the supplier FORC-Photonics that using a Fibercore PS1250/1500 with $\theta>5°$, the Ghost mode was not anymore useful for measurements as its amplitude was too attenuated, while with Corning SMF-28e the same occurred with $\theta>6°$. Hence, the customisation, as the definition of the tilt angle and OF, is a crucial step and it depends on the specific use of the sensor.

2.2 Weakly TFBG spectrum

At this point, the treatment is referred to only weakly TFBGs. A full TFBG spectrum[2] is shown in Fig.2-7, which was obtained from transmitted light for a 3° TFBG in-written in Fibercore PS1250/1500 which was manufactured by FORC-Photonics.

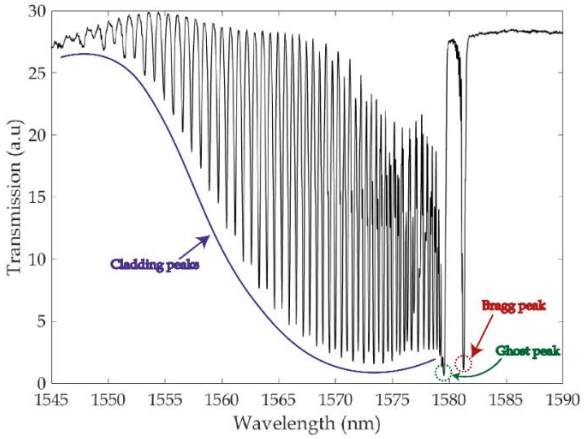


Fig.2-7. Transmission spectrum of a 3° tilted FBG with main resonance peaks indicated.

The Bragg peak is on the right side of the TFBG signal, while the cladding peaks are on the left hand side and consist of a series of close well-defined peaks. The wavelength of both these peak types can be calculated by considering the effective core RI of the OF and the periods Λ and Λ_G defined in Fig.2-3, as reported in the following equations [7]:

$$\lambda_{Bragg}=2n_{eff,core}\Lambda=2n_{eff,core}\frac{\Lambda_G}{\cos\theta}, \quad \text{(II.1)}$$

$$\lambda_{clad_i}=(n_{eff,core}+n_{eff,clad_i})\Lambda=(n_{eff,core}+n_{eff,clad_i})\frac{\Lambda_G}{\cos\theta}. \quad \text{(II.2)}$$

Where, λ_{Bragg} and λ_{clad_i} are the wavelengths of the Bragg and *i*-th cladding peak in the spectrum. The reason why the cladding peaks are placed at lower wavelengths is due to their lower effective RI $n_{eff,clad_i}$ compared to that of the Bragg mode $n_{eff,core}$. The high number of cladding resonances is caused by the different reflections that the modes undergo when reflected back into the core from the cladding in relation to their own n_{eff}. Hence, since each mode has its own n_{eff}, multiple and well-defined resonance peaks appear in the spectrum. Following this argumentation, the Ghost peak might seem an anomaly since, as described previously, although it comes from the coupling by the main core mode and a group of low order cladding modes strongly guided at the interface between core and cladding layer, it appears as a single peak in the spectrum. A possible explanation lies in the n_{eff} of the cladding modes, which are so similar that the resonance wavelength of each coupling is very close to each other. In this way, the contribution to the reflection of each mode in the spectrum makes the Ghost peak appear as a single peak but with a larger bandwidth than other peaks, as it can be observed in Fig.2-7. In other words, the Ghost peak may be assumed to be generated by a congregation of multiple peaks placed at, approximately, the same wavelength. Hence, the Ghost mode can be considered as a mode generated by the overlapping of several peaks. As these are confined and interacting at the interface of the internal OF layers, the modes generating the Ghost resonance are not influenced by surrounding RI variations. This is one of the key properties for multi-parameter sensing of the TFBGs presented successively. Meanwhile, the fundamentals regarding optics and FBG theory can be found by consulting [3,4,5,7,8].

2.3 Transfer matrix method for TFBG spectrum simulation

Since the customisation of the TFBG (as the choice of the tilt angle and OF) is of fundamental importance to obtain an optimal signal after the sensor manufacturing, a mathematical method able to

[2]The unit of measure used in the graph for the amplitude of the transmission spectra, presented in this thesis, is *a.u.* This is the acronym of auxiliary unit, a dimensionless unit widely used in FBG science. Indeed, theoretically and often instrumentally, the spectrum is obtained as ratio between input power and reflected/transmitted power. The dimensionless magnitude allows to the interrogator equipment to amplify the signal. Other measurement unit are Decibel and Watt.

provide in advance the forecast of the spectrum would be very useful. This will save time and the cost of production trials, while providing a better design for the TFBG parameters.

For example, it is required to achieve the maximum enhancement of the cladding resonance peaks in the spectrum with the constraint of keeping the Bragg peak at a good amplitude to allow multi-parameter measurements. Therefore, it is useful to know the Bragg peak amplitude in advance based on the TFBG customisation.

This is a typical query and issue during the design and, consequently, production of the TFBG sensor as the spectrum shape is function of many Bragg grating structure parameters. Indeed, as anticipated in the phase-match discussion reported in the previous section, although a higher θ generates the increasing of the cladding peaks, it can cause the disappear of the Bragg resonance peak.

Previous research has been carried out to investigate the problem of modelling and simulating mathematically the spectrum. The first and most intuitive approach applied also for tilted FBGs, is coupled-mode theory (CMT) [4,5,12], while alternative approaches are to use the antenna theory [13] or the volume current method [14]. CMT allows the amplitudes of the modes during their propagation in the tilted phase Bragg grating to be described through a system of differential equations. In these relations, the mode coupling is weighted with the energy exchange equations between the propagating modes in the TFBG [4]. Specifically, in addition to the core-core mode coupling, since the tilt angle enhances the exchange of energy between the fundamental core mode and the cladding backward-propagating modes, multiple coupling coefficients can be obtained from the energy exchange relations. The general CMT equations can be written to describe the interactions of any modes propagating in the OF when their coupling per unit length is not strong as in the case of FBGs. However, the relations reported below, are written by considering the fundamental core mode LP_{01} and the backward-propagating hybrid (*lm*, respectively azimuthal and radial number) cladding mode in a reflective tilted FBG [5]:

$$\frac{dR_{01}}{dz} = i f_{01\text{-}01}\, R_{01} + i\, g_{01\text{-}01} S_{01}\, \exp(-2i\, \delta_{01\text{-}01} z) + i \sum_{l,m} \left[S^{j}_{lm} g^{j}_{lm\text{-}01} \exp\left(2i\, \delta^{j\text{-}r}_{01\text{-}lm}\, z\right) \right], \tag{II.3}$$

$$\frac{dS_{01}}{dz} = -i\, R_{01\text{-}01}\, g_{01\text{-}01}\, \exp(2i\, \delta_{01\text{-}01} z) - i\, S_{01} f_{01\text{-}01}, \tag{II.4}$$

$$\sum_{l,m} \left[\frac{dS^{j}_{lm}}{dz} = -i\, g^{j}_{01\text{-}lm} R_{01} \exp\left(2i\, \delta^{j\text{-}r}_{01\text{-}lm}\, z\right) - i\, S^{j}_{lm} f^{j}_{lm\text{-}lm} \right], \tag{II.5}$$

where j=(co,cl) and:

$$2\delta^{j\text{-}r}_{01\text{-}lm} = \beta_{01} + \beta^{j}_{lm} - K_g \cos\theta, \tag{II.6}$$

$$\delta^{r}_{01\text{-}01} = \beta_{01} - K_g \cos\theta. \tag{II.7}$$

The terms R_{01} and S_{01} are the amplitude of the forward- and backward-propagating LP_{01} modes respectively, while S^{co}_{lm} and S^{cl}_{lm} are the amplitude of a generic backward-propagating LP_{lm} core mode and hybrid (*lm*) cladding mode. The wording 'hybrid' is used here to express the exact mode form rather than the weakly guiding approximation form indicated with 'LP' as the negligible core-cladding RI difference cannot be considered also between the RI of the cladding and surrounding (usually air) for the greater difference of these values. z is the length of the sensor, *i* is the imaginary number, r indicates the radial position in the OF radius. In II.6 and II.7, β_{01} and β^{j}_{lm} are, respectively, the propagating constants of the LP_{01} and LP_{lm} core modes or the hybrid cladding modes if *j*=cl. K_g is the wave number of the tilted Bragg grating, which can be calculated as $K_g = \pi/\Lambda_g$ or related to the wave-vector component along the OF axis $K = \pi/\Lambda$ as $K = K_g \cos\theta$. The propagating constants can be obtained via the relations:

$$\beta_{01} = 2\pi n^{LP_{01}}_{eff}/\lambda, \tag{II.8}$$

$$\beta^{j}_{lm} = 2\pi n^{j}_{eff}/\lambda, \tag{II.9}$$

where $n_{eff}^{LP_{01}}$ and n_{eff}^{j} are the effective RI of the LP_{01}, LP_{lm} and hybrid cladding modes, while λ is the working wavelength. The last terms to define in CMT are the coupling coefficients, which can be identified as components between the modes $g_{01\text{-}01}$, $g_{lm\text{-}01}^{j}$ and $g_{01\text{-}lm}^{j}$ and self-coupling coefficients $f_{01\text{-}01}$ and $f_{lm\text{-}lm}^{j}$. These self-coupling coefficients can be neglected as their contribution is very small for the Bragg gratings considered here. Next the coupling coefficients are introduced as conventionally treated in the CMT of the TFBGs:

$$g_{lm\text{-}01}^{cl}=A_g^{cl}\int_0^{a_1} r\,dr\; J_{l-1}\left(2r\,K_g\,\sin\theta\right) J_{l-1}(u_{lm}r)\,J_0(u_{01}r), \tag{II.10}$$

$$g_{lm\text{-}01}^{co}=A_g^{co}\int_0^{a_1} r\,dr\; J_{l}\left(2r\,K_g\,\sin\theta\right) J_{l}(u_{lm}r)\,J_0(u_{01}r), \tag{II.11}$$

where the initial coefficients A_g have different formulations for core and cladding modes:

$$A_g^{cl}=(\pm i)^{l-1}\,\pi^2\,n_1\,\Delta n\,u_{lm}\times\left(1+\sigma\,\zeta_0/n_1^2 l\right)E_{01}^{co}\,E_{lm}^{cl}/2\lambda Z_0, \tag{II.12}$$

$$A_g^{co}=(\pm i)^{l-1}\,\pi^2\,n_1\,\Delta n\,E_{01}^{co}\,E_{lm}^{co}/2\lambda Z_0. \tag{II.13}$$

The last parameters to introduce are:

$$u_{lm}=\left(\frac{2\pi}{\lambda}\right)^2\left(n_1^2-n_{eff,j,lm}^2\right)=\frac{V\sqrt{1-b_{lm}}}{a_1}, \tag{II.14}$$

$$b_{lm}=\left(n_{eff,lm}^2-n_2^2\right)/\left(n_1^2-n_2^2\right), \tag{II.15}$$

$$E_{lm}^{co}=\sqrt{\frac{4\,Z_0\,b_{lm}}{e_l\,\pi\,n\,a_1^2\left|J_{l-1}(u_{lm}a_1)\,J_{l+1}(u_{lm}a_1)\right|}}, \tag{II.16}$$

$$V=\frac{2\pi}{\lambda}\,a_1\sqrt{\left(n_1^2-n_2^2\right)}. \tag{II.17}$$

Specifically, b_{lm} is the normalised effective index of the *lm* mode, V is the number of the fibre and J is the Bessel function of the first kind. Here Z_0 is the electromagnetic impedance in air equal to 377Ω, n_1 and a_1 are the core RI and radius, while n_2 is the cladding RI and $\Delta n = 2n_1\sigma\upsilon$ (with $\sigma=il\,n_{eff,lm}Z_0$ and $\upsilon=1$) is the 'ac' index modulation. E_{lm}^{co} is the electromagnetic field of the *lm* mode propagating in the core. Usually, in the numerical simulations, only the modes interacting near to the main resonant wavelength are considered as the other terms oscillate too rapidly to contribute appreciably to the mode amplitude variation [15-16]. This means that the mathematical treatment is performed by considering the phase match condition (as used in section 2.1.1) which means $\delta_{01\text{-}lm}^{j\text{-}r}=0$. The electromagnetic field normalisation constant E_{lm}^{cl} and the parameter ζ_0 are related to the dispersion relation for the cladding modes. Their calculation is treated in detail, respectively, in [15] and [16]. Indeed, the mathematical treatment is based on the three-layer optical fibre theory and is extensive for both parameters.

At this point the CMT equations system might be numerically solved by using, for example, the Runge-Kutta solving method for differential equations system [17] to obtain the transmission spectrum of the TFBG. However, the resolution of these equations, even considering only the Bragg peak resonance, results an extremely long and computational expensive operation. Especially, if more combinations of sensor, manufacturing and waveguide parameters need to be tested. The process may be sped-up by reducing the wavelength span resolution, or in other words, by decreasing the number of points where the equations need to be solved. However, the obtained spectrum would appear devoid of important information, especially in the case of the cladding resonance peaks.

To overcome these issues, the transfer matrix method (TMM) is here proposed and adapted for tilted Bragg gratings to simplify and speed-up the numerical calculation. This is a piece-wise approach where the TFBG is divided in a certain number of sections and the wave is described by a transfer matrix 2×2 at each segment Δz. By solving this matrix, the transmitted or reflected spectrum can be obtained. This method has been used for the same reasons in the case of uniform, chirped and apodized FBGs [18-20], and even in case of birefringence [21]. Here, TMM is proposed for the case of a uniform tilted

FBG to analyse its Bragg resonance peak spectral behaviour in relation to the variation of the Bragg grating and OF parameters as tilt angle and OF core diameter. This procedure may allow solving, in an easy and fast computational way, the design issue about the Bragg structure parameters to impose during the TFBG production in order to obtain a customised spectrum, formulated at the beginning of this section. Considering the same hypothesis as introduced for the CMT, the Fibercore PS1250/1500 is assumed to act as a waveguide in which the TFBG is written. This OF has a core RI of 1.44973 and a cladding RI of 1.4402 both at 1550 nm [22], and a core and cladding diameter of 6.9 μm and 124.6 μm [23], respectively. The modulation depth imposed to the core RI is $\delta n=0.5\times10^{-3}$, the TFBG is L=4 mm long and has a resonant Bragg wavelength $\lambda_{Bragg}=1550$ nm. Starting from these parameters, the Bragg peak can be obtained for several values of the tilt angle θ by using the TMM. Specifically, the electric fields of the forward- and backword-propagating LP_{01} modes can be calculated after passing through each *i*-th segment with the following equation [1]:

$$\begin{bmatrix} R_{01\,i\text{-th}} \\ S_{01\,i\text{-th}} \end{bmatrix} = \begin{bmatrix} \cosh(\gamma_B \Delta z) - i\frac{\hat{\sigma}}{\gamma_B}\sinh(\gamma_B \Delta z) & -i\frac{\varkappa}{\gamma_B}\sinh(\gamma_B \Delta z) \\ i\frac{\varkappa}{\gamma_B}\sinh(\gamma_B \Delta z) & \cosh(\gamma_B \Delta z) + i\frac{\hat{\sigma}}{\gamma_B}\sinh(\gamma_B \Delta z) \end{bmatrix} \begin{bmatrix} R_{01\,(i\text{-th})-1} \\ S_{01\,(i\text{-th})-1} \end{bmatrix}, \quad \text{(II.18)}$$

where, in this specific case:

$$\gamma_B = \sqrt{\varkappa^2 - \hat{\sigma}}, \quad \text{(II.19)}$$

$$\hat{\sigma} = \pi\left(\frac{n_{eff_\lambda}}{\lambda} - \frac{n_{eff}^{LP_{01}}}{\lambda_{Bragg}}\right). \quad \text{(II.20)}$$

In eq. II.19, $\varkappa$ is the 'ac' coupling coefficient, which can be calculated by using the core mode propagating constant and the transverse coupling coefficient $g_{01\text{-}01}$ as follows:

$$\varkappa = \left(\frac{\delta n}{n_1+n_2}\right) g_{01\text{-}01}\beta_{01}. \quad \text{(II.21)}$$

In this specific case, for the LP_{01} mode, the mathematical expression of the coupling coefficient $g_{01\text{-}01}$ can be written as below:

$$g_{01\text{-}01} = 2\,\frac{b_{01}}{(u_{01}\,a_1)^2}\,J_1(u_{01}\,a_1)^2 \int_0^{u_{01}a_1} J_0(u)^2 J_0(\Omega u)^2 u\,du \quad \text{(II.22)}$$

in which $\Omega = 2K\,\tan\theta / u_{01}$.

Since the grating is uniform and no loads are applied on the sensor, the entire TFBG length can be considered as a single segment such that Δz=L, so a single matrix can describe globally the electric fields of the LP_{01} mode. Otherwise, the global matrix is calculated from the product of all the sub-matrices:

$$\begin{bmatrix} R_{01\,i\text{-th}} \\ S_{01\,i\text{-th}} \end{bmatrix} = \mathbf{F}\begin{bmatrix} R_{01\,(i\text{-th})-1} \\ S_{01\,(i\text{-th})-1} \end{bmatrix} = \boldsymbol{F_i} * \boldsymbol{F_{i-1}} * \ldots * \boldsymbol{F_1}\begin{bmatrix} R_{01\,(i\text{-th})-1} \\ S_{01\,(i\text{-th})-1} \end{bmatrix}. \quad \text{(II.23)}$$

Once the global matrix is obtained, the transmission or the reflection signal of the Bragg peak resonance can be obtained as functions of the working wavelength in the TFBG spectrum:

$$R(\lambda) = \left(\frac{F_{21}}{F_{11}}\right)^2, \quad \text{(II.24)}$$

$$T(\lambda) = \left(\frac{1}{F_{11}}\right)^2. \quad \text{(II.25)}$$

As expected, the Bragg peak in the spectra shown in Fig.2-8 decreases by increasingly tilting the Bragg gratings of the sensor. Specifically, the main peak transmission remains appreciable until around 5°, while after that it becomes quite attenuated with an amplitude comparable to those of the side lobes.

This trend reflects the experienced one (anticipated in section 2.1.1) during the manufacturing of the sensors when the Bragg peak was disappearing from the spectrum for tilt angles greater than 5°. This phenomenon is strongly connected with the trend of the $g_{01\text{-}01}$ coupling coefficient as its value is variable with θ as Fig.2-9a shows. However, through a variation of the core size, this trend can be managed. In particular, as reported in Fig.2-9b, a smaller core radius returns lower $g_{01\text{-}01}$ for small θ values but it allows good coefficient values for higher Bragg grating inclinations by pushing the zero-point forward. At the same time, a larger core diameter increases considerably the LP_{01} mode coupling but this is achievable in an increasingly stringent range of angles.

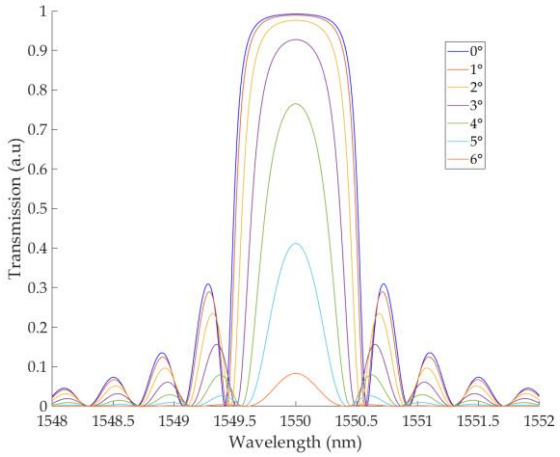


Fig.2-8. Transmission spectrum with the variation of the tilt angle.

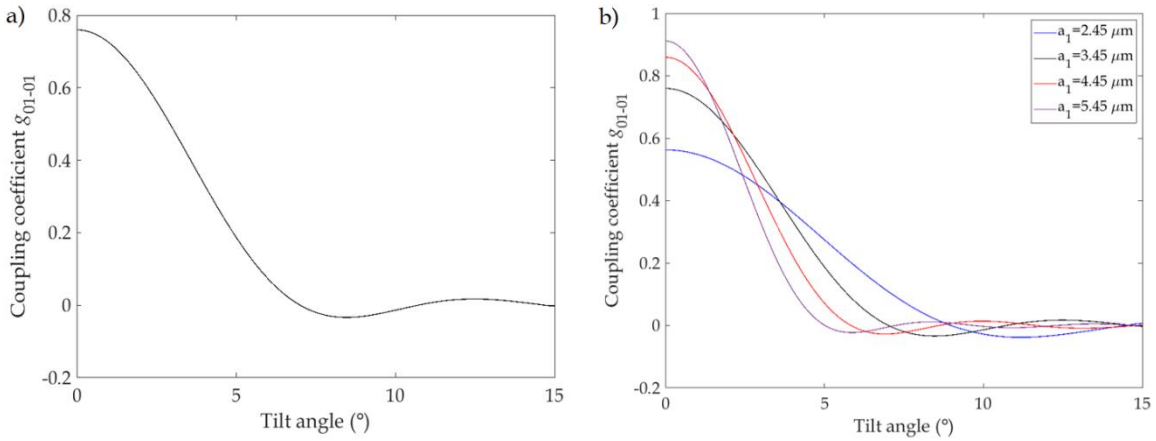


Fig.2-9. a) $g_{01\text{-}01}$ vs. θ trend for a_1=3.45 μm, b) $g_{01\text{-}01}$ vs. θ trend for several a_1 values.

Already these examples can demonstrate the importance of the customisation on the spectrum quality or features by considering the Bragg structure and OF. Of course, other parameters such as core and cladding RIs can play a role in optimising a defined peak resonance in the TFBG signal. It is easy to understand that to define all these parameters may involve performing many simulations to decide the right sensor configuration. This is easily and quickly feasible with the TMM.

Another possible issue could be to improve the amplitude of the Bragg peak when the tilt angle and the OF are constrained and not modifiable. In this case, the manufacturing parameter δn and the TFBG length L can be considered to achieve this goal. The TMM allows the evaluation of this spectra also in this case with the variation of these parameters. Fig.2.10 shows that the Bragg amplitude of a 6° tilted FBG can be enhanced with a deeper modulation δn of the core RI which can be set during the manufacturing process. However, a very deep RI modulation generates an over-saturation of the spectrum as is possible to note from the broad bandwidth of the Bragg peak obtained for $\delta n=6\times10^{-3}$. This effect is not desired as the wavelength shifting of the peak would be difficult to identify and

quantify. The TFBG length can be also another chance to improve the Bragg resonance amplitude, but also as it allows a well-defined peak to be present by decreasing the bandwidth as Fig.2-11 shows. Hence, the combination between a deeper RI modulation and longer sensor can improve the amplitude of the mode resonance while holding a well-defined peak.

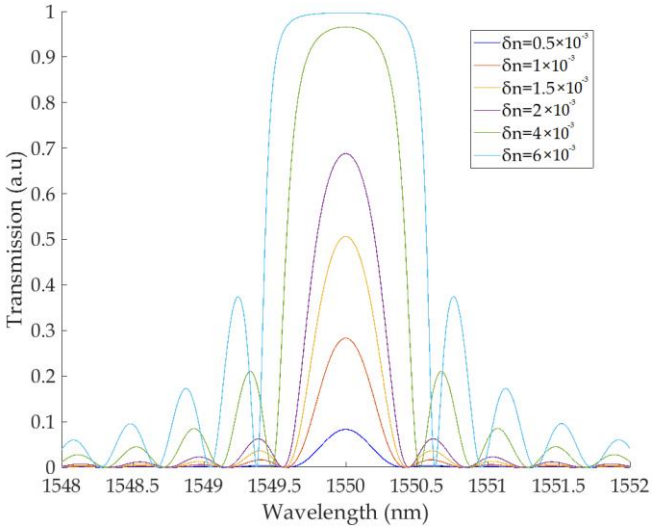


Fig.2-10. Transmission spectrum of 6° tilted and 4 mm long FBG with the increasing of δn.

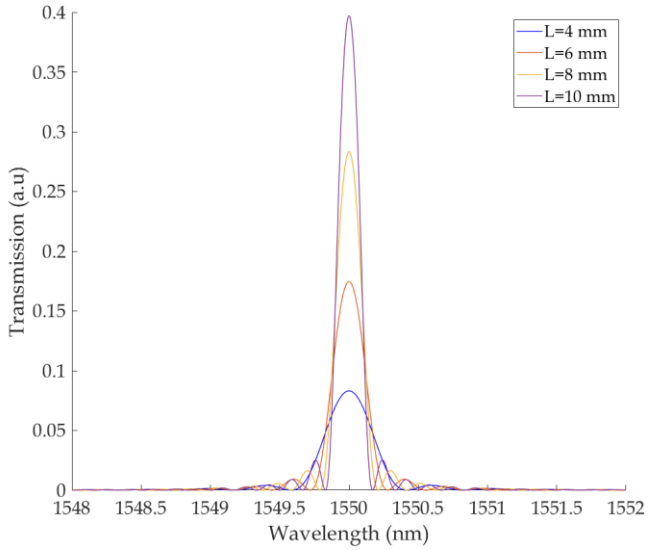


Fig.2-11. Transmission spectrum of 6° tilted FBG with δn=0.5e-3 for different lengths.

2.4 Weakly TFBG multi-parameter sensing

In this section the multi-sensing features of the weakly TFBG spectrum are described in relation to its different resonance peaks. In particular, all the resonance peaks undergo the shifting of their nominal wavelength when the TFBG thermomechanical condition changes. At the same time, only the cladding resonances are affected by the surrounding RI while the Bragg and Ghost peaks remains unperturbed. At the end, the sensor is demonstrated to be able to detect, simultaneously and separately, strain, temperature and surrounding RI variations.

2.4.1 Thermomechanical effects and demodulation technique

All the peaks in the spectrum are sensitive to thermomechanical perturbations as a variation of strain ($\Delta\varepsilon$) or temperature (ΔT) (or their combination) alters the effective RI of the propagating modes and

the periods of the grating due to its physical expansion or constriction. This can be expressed mathematically for any mode present in the TFBG signal by considering eq.II.2 in general and can be written in terms of wavelength variation as:

$$\Delta\lambda_{Bragg}=\left(\frac{2\Lambda_G}{\cos\theta}\frac{d\,n_{eff,core}}{d\varepsilon}+\frac{2n_{eff,core}}{\cos\theta}\frac{d\Lambda_G}{d\varepsilon}\right)\Delta\varepsilon+\left(\frac{2\Lambda_G}{\cos\theta}\frac{d\,n_{eff,core}}{dT}+\frac{2n_{eff,core}}{\cos\theta}\frac{d\Lambda_G}{dT}\right)\Delta T, \quad \text{(II.26)}$$

$$\Delta\lambda_{clad_i}=\left(\frac{\Lambda_G}{\cos\theta}\frac{d\left(n_{eff,core}+n_{eff_{cl_i}}\right)}{d\varepsilon}+\frac{n_{eff,core}+n_{eff_{cl_i}}}{\cos\theta}\frac{d\Lambda_G}{d\varepsilon}\right)\Delta\varepsilon+ \\ +\left(\frac{\Lambda_G}{\cos\theta}\frac{d\left(n_{eff,core}+n_{eff_{cl_i}}\right)}{dT}+\frac{n_{eff,core}+n_{eff_{cl_i}}}{\cos\theta}\frac{d\Lambda_G}{dT}\right)\Delta T. \quad \text{(II.27)}$$

In eqs. II.26 and II.27, the terms $\frac{d\,n_{eff,core}}{d\varepsilon}$ and $\frac{d\left(n_{eff,core}+n_{eff_{cl_i}}\right)}{d\varepsilon}$ represent the mode's effective RI alteration due to $\Delta\varepsilon$, the photoelastic effect, while the components generated by the temperature variation are due to the thermo-optic effect and are $\frac{d\,n_{eff,core}}{dT}$ and $\frac{d\left(n_{eff,core}+n_{eff_{cl_i}}\right)}{dT}$. Both these eqs. are conventionally written in a short format by introducing the so-called thermomechanical sensitivity coefficients:

$$\left(\frac{2\Lambda_G}{\cos\theta}\frac{d\,n_{eff,core}}{d\varepsilon}+\frac{2n_{eff,core}}{\cos\theta}\frac{d\Lambda_G}{d\varepsilon}\right)=k_{\varepsilon Bragg},$$

$$\left(\frac{2\Lambda_G}{\cos\theta}\frac{d\,n_{eff,core}}{dT}+\frac{2n_{eff,core}}{\cos\theta}\frac{d\Lambda_G}{dT}\right)=k_{T Bragg},$$

$$\left(\frac{\Lambda_G}{\cos\theta}\frac{d\left(n_{eff,core}+n_{eff_{cl_i}}\right)}{d\varepsilon}+\frac{n_{eff,core}+n_{eff_{cl_i}}}{\cos\theta}\frac{d\Lambda_G}{d\varepsilon}\right)=k_{\varepsilon clad_i},$$

$$\left(\frac{\Lambda_G}{\cos\theta}\frac{d\left(n_{eff,core}+n_{eff_{cl_i}}\right)}{dT}+\frac{n_{eff,core}+n_{eff_{cl_i}}}{\cos\theta}\frac{d\Lambda_G}{dT}\right)=k_{T clad_i t},$$

which can be substituted in II.26 and II.27 to obtain the general equation of the wavelength variation of the modes induced by thermomechanical loads:

$$\Delta\lambda_{Bragg}=k_{\varepsilon Bragg}\Delta\varepsilon+k_{T Bragg}\Delta T, \quad \text{(II.28)}$$

$$\Delta\lambda_{clad_i}=k_{\varepsilon clad_i}\Delta\varepsilon+k_{T clad_i}\Delta T. \quad \text{(II.29)}$$

Eqs. II.28 and II.29 represent a system of equations for the thermomechanical sensing determination. Indeed, this system is composed of two equations with the same number of unknown parameters ($\Delta\varepsilon$ and ΔT) which can be easily calculated. This means that by detecting the wavelength shifts of any two peaks in the TFBG spectrum, both the temperature and strain variations can be determined simultaneously and uniquely. This is the basis of the demodulation technique for thermomechanical measurements that is used in this thesis. This eqs. system can be written also in matrix form:

$$\begin{bmatrix}\Delta\lambda_{Bragg}\\ \Delta\lambda_{clad_i}\end{bmatrix}=\begin{bmatrix}k_{\varepsilon Bragg} & k_{T Bragg}\\ k_{\varepsilon clad_i} & k_{T clad_i}\end{bmatrix}\begin{bmatrix}\Delta\varepsilon\\ \Delta T\end{bmatrix}=[\mathbf{K}]\begin{bmatrix}\Delta\varepsilon\\ \Delta T\end{bmatrix}, \quad \text{(II.30)}$$

where the matrix **K**, which contains the coefficients, is the thermomechanical sensing matrix of the selected peaks. About the selection of the two peaks, there is no a general rule but any two resonance peaks in the spectrum can be taken in consideration. However, there are several considerations that should be taken into account during the selection. First of all, the kind of application in which the sensor should be applied plays an important role. In fact, as it is described in the next section, if the TFBG is used for refractometric purposes, the cladding peaks could be irradiated out and would not appear anymore in the spectrum for certain surrounding RIs. This means that if one or two cladding resonances were selected for thermomechanical measurements, these could stop being visible, and hence, their wavelength variation is not detectable. Moreover, an external RI (ERI) change induces a

mutation of the cladding modes effective RI (and electric field), which means a different resonance wavelength and amplitude. This effect on the wavelength should be necessarily uncoupled from the one due to the strain-temperature perturbations, which means the matrix relation II.30 is not sufficient any more. These considerations are the most important for three-parameter detection scopes. Another point, for a proper thermomechanical discrimination, regards the values of the coefficients of the sensing matrix which determine the measurement performance of the technique as accuracy and resolution. In this context an issue appears due to the fact that usually the strain sensitivity coefficients of the resonance peaks are very similar to each other, hence, to make the system computationally resolvable, the peaks should have sufficiently different k_T. Indeed, to solve the relation II.30 with respect to the perturbations, the inverse of **K** must be calculated which is not a possible operation if the thermal coefficients are the same. Moreover, since k_ε is approximately the same for all the peaks, the thermal resolution (*TR*) of the TFBG plays a fundamental role in the achievement of the measurements. This is linked to the k_T coefficients by the following formula:

$$TR = \frac{swR}{\left|k_{T\,clad_i} - k_{T\,Bragg}\right|}. \qquad \text{(II.31)}$$

In II.31, *swR* is the wavelength scanning resolution of the interrogator device used to record the TFBG signal. From this equation, with the increasing difference between the thermal coefficients, *TR* is finer and the measurements are improved. Another qualitative analysis on the performance of the strain-temperature discrimination technique can be done by using the condition number of the matrix [24]. However, this parameter does not give univocal information about the performance of the technique as it can be used only to compare different discrimination techniques by providing an indication on the matrix operation sensitivity based on the uncertainties in the matrix elements. Despite this, it is possible to assert that the closer the condition number is to unity the better its behaviour and that the calculation errors are expected to be small. Specifically, a finer strain and/or thermal resolution decrease the errors and the condition number [25].
Keeping in mind the previous considerations for the research conducted in this thesis, the embedded TFBG should be used not only to monitor material thermomechanical state, but also to measure its RI variation, the selection of the Bragg and Ghost peaks allows the three-parameter measurements to be performed without incurring the disappearance of the peak from the spectrum or compensation issues. Indeed, these two peaks, which are typical of weak TFBG, are not influenced by ERI changes such as those generated by the coupling of the modes propagating in the core (in the case of the Bragg resonance) or at the interface between core and cladding layers as for the Ghost peak.
About the coefficients values to improve the measurements performance, as it is reported in the section dedicated to the calibration, a proper customisation of the sensor can help to obtain a better resolution of the sensor, and hence, increase the measurement accuracy. The thermomechanical sensitivity coefficients can be easily determined through the strain and the thermal calibration of the TFBG (reported in section 2.4.1a). Once, these are obtained, the variation of the strain and temperature can be calculated by starting from the wavelength variations of the two peaks:

$$\begin{bmatrix}\Delta\varepsilon\\ \Delta T\end{bmatrix} = \begin{bmatrix}k_{\varepsilon Bragg} & k_{T Bragg}\\ k_{\varepsilon Ghost} & k_{T Ghost}\end{bmatrix}^{-1} \begin{bmatrix}\Delta\lambda_{Bragg}\\ \Delta\lambda_{Ghost}\end{bmatrix} = [\mathbf{K}]^{-1} \begin{bmatrix}\Delta\lambda_{Bragg}\\ \Delta\lambda_{Ghost}\end{bmatrix}. \qquad \text{(II.32)}$$

Eq. II.32 represents the thermomechanical demodulation technique to obtain $\Delta\varepsilon$ and ΔT from the TFBG signal by considering $\Delta\lambda_{Bragg}$ and $\Delta\lambda_{Ghost}$. This classical approach is used, in the successive chapters, in simultaneous combination with a novel demodulation technique for refractometric measurements, developed in this research, to allow the three-parameter measurements with a single TFBG to be performed.

2.4.1a TFBG mechanical calibration and setup

The mechanical and thermal calibration is a fundamental and necessary step to obtain the sensitivity coefficients needed in the **K** sensing matrix. Here, the methodology to perform the strain calibration

of the TFBG is presented. The base of the calibration setup for both the steps is a special linear translation stage designed for the single-mode OF dimensions. The drawings to manufacture the parts of the calibration setup with the views and dimensions are reported in Appendix A at the end of this thesis. These drawings were used by the DEMO lab at the Delft Aerospace Structures and Materials Laboratory (DASML), TU Delft to produce the parts. A complete 3D drawing is reported in Fig.2-11. This assembly is composed of several main components:

- a fixed block where the OF is constrained and cannot move,
- a bridge with a straight guide for the OF. This possesses two rails in one of the ends through which
- a moving element which can horizontally shift, in which the other end of the OF is encased.

Both the blocks are provided with a polycarbonate (PC) insert to ensure the continuity of the OF guideline across the bridge. Indeed, these PC elements have the function to receive the OF ends and create a clamp when the upper rubber strip when the closing element is screwed. This system demonstrated able to guarantee the best alignment of the components during the operations of calibration and to ensure no slipping of the clamped OF ends. The movement of the moving part is powered by a linear actuator placed below the bridge and pushing centrally the base of the moving part. The central pushing point is important to avoid possible false movement of the component when the displacement applied and friction influences the sliding through the rails. The actuator is a Zaber NA23C60-T4. All its details and performance can be found in [26]. It was controlled via a dedicated software developed by the manufacturer.

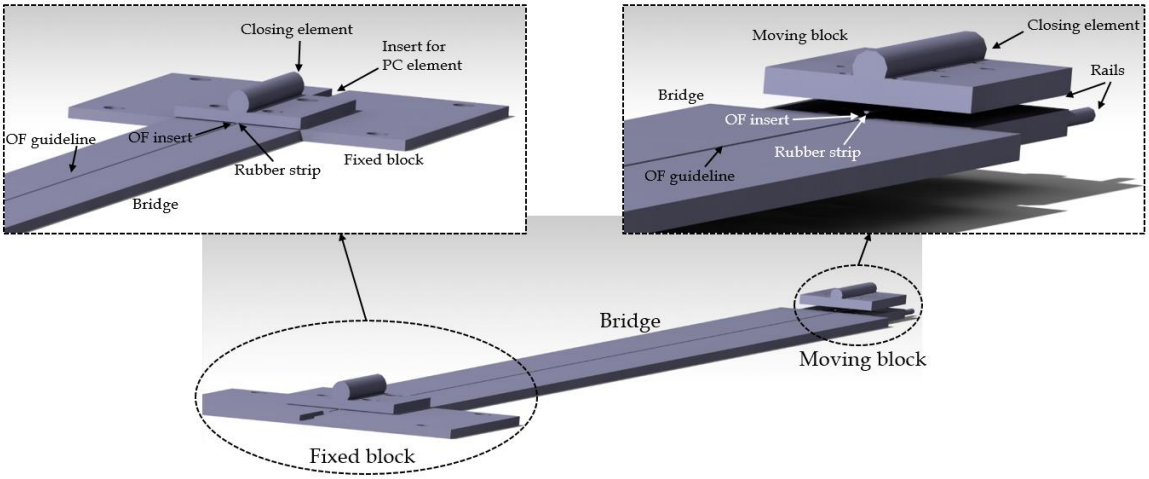


Fig.2-11. 3D drawing of the complete translation system for the OF.

The calibration of the TFBG sensors was performed by inducing displacements to the OF via the actuator, with a span of 100 µm until a maximum extension of 2000 µε. A small deformation was initially applied to the OF to have a pre-tensioning condition, which is considered the starting point $\Delta\varepsilon=0$. At each interval, the TFBG spectrum was acquired and analysed so that the wavelengths of the Bragg and Ghost peak were obtained at each new extension of the sensor. This entire process was repeated five times for each sensor. A k-TC (±1°C accuracy) was placed on the bridge close to the TFBG to monitor the room temperature, which was kept at 21.5°C for all the calibrations.

Once the medium points from the measurements have been calculated by correlating the medium wavelength variations of the peaks from the starting condition ($\Delta\varepsilon=0$) with the induced strain, a linear trend can be extracted from the graphs as shown in Fig.2-12 for the case of a 3° tilted FBG written in Fibercore PS1250/1500. Indeed, the square-error (R^2) obtained for the linear fitting is very close to unity (0.999962 for the Bragg peak and 0.999968 for the Ghost), and also the standard error is tiny in the 95% confidence interval. This means clearly that both the peaks then have a linear wavelength shift with an increase of the applied deformation. The strain sensitivity coefficients can be extracted by calculating the gradient of the linear trend for both the selected peaks. The values found are the

following: $k_{\varepsilon Bragg}$=1.255±0.004 pm/με and $k_{\varepsilon Ghost}$=1.255±0.006 pm/με. A curious aspect noted during the calibration of several different TFBGs, does not regard the linear trend (already demonstrated in several works [3,25]), but the fact that all the tested sensors had around the same coefficients with variable accuracy. This was validated by testing TFBGs manufactured with different tilt angles (2°,3° and 5°), in two kinds of OFs (Fibercore PS1250/1500 and Corning SMF-28e, coating layer in acrylate, no-recoated), with different cladding diameters (standard a_2=125μm, thin a_2=80μm) and produced by different manufacturer (FORC-Photonics and Technica). Taking all the calibrated sensors into account, a valid general $k_{\varepsilon Bragg}$=1.25±0.06 pm/με and $k_{\varepsilon Ghost}$=1.25±0.1 pm/με may be used without performing the calibration of each specific sensor, although always considering that the TFBGs are in the range of the above described specifications.

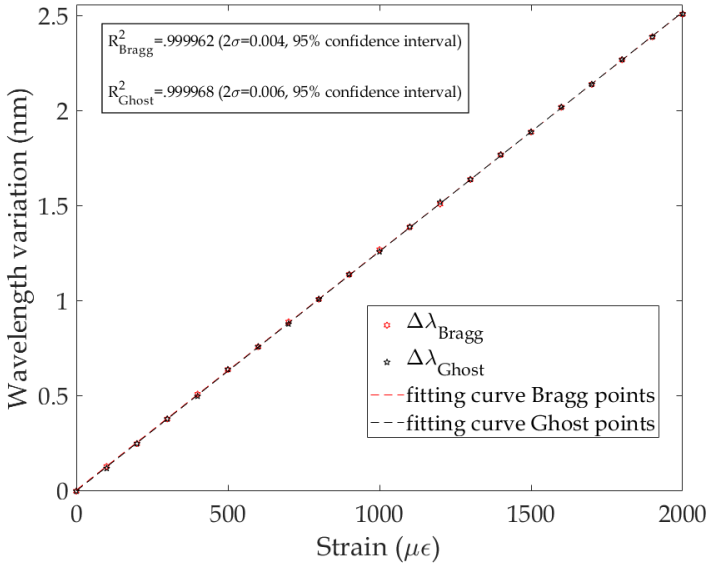


Fig.2-12. Strain calibration trend for 3° tilted FBG in-written Fibercore PS1250/1500 OF.

2.4.1b TFBG thermal calibration

To complete the sensitivity matrix, the thermal calibration of the sensor has to be performed. Also, as described in the previous section, the values of the coefficients are analysed in relation to the sensor customisation. This demonstrates how the TFBG customisation influences not only the spectrum, but also the sensitivity of the selected peaks.

The setup used for this calibration is based on the one shown in Fig.2-11. However, here, the bridge was removed and the translation stage has only the function to hold the OF straight and in tension. In addition, adjacent to the TFBG, a heating plate was placed horizontally on top of a vertical translation stage. This is used to adjust the height of the heating plate with respect to the position of the sensor. The heating system has its own TC fixed on the bottom surface of the plate. However, for a more accurate calibration, a second k-TC was mounted on the top of the heating plate, as close as possible to the TFBG but in a way not to interfere with it. The entire system is summarised in Fig.2-13. The surface of the plate hosting the TFBG and the TC was covered with insulation foam to create an isolated and thermal protected environment.

All the TFBG sensors were calibrated with a pre-tensioning of ~150 μm applied to the OF so that the OF was very straight at the considered equilibrium point (Δε=0). The temperature room was kept at 21.5°C and this was monitored by a k-TC placed close to the operational area. The first spectrum was acquired at a stable temperature of 30±0.25°C, which is the starting point of the calibration. From this point, 10 spectra were acquired at each stable 10°C until a maximum temperature of 80°C. The nominal temperatures were considered 'stable' when the oscillation was within ±0.25°C as measured by the TC.

As done for the strain case, the trend of the wavelength variation for the Bragg and Ghost peak for the thermal calibration is reported by considering the medium correlation points among the measurements in Fig.2-14.

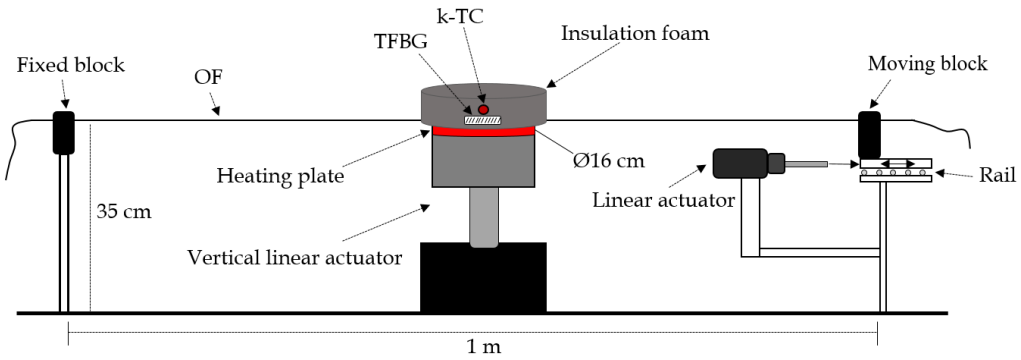


Fig.2-13. Setup used for thermal calibration campaign of TFBG sensors.

The results specifically discussed in Fig.2-14, referred to the same sensor as that calibrated for strain (Fig.2-12). Also in this case, both peaks show a linear behaviour with the increase of the temperature, although the square-errors and the standard deviations are slightly worse than the strain case. This is justifiable as, despite multiple precautions, it is much more difficult acquire many spectra at a precise temperature while avoiding its unavoidable oscillations.

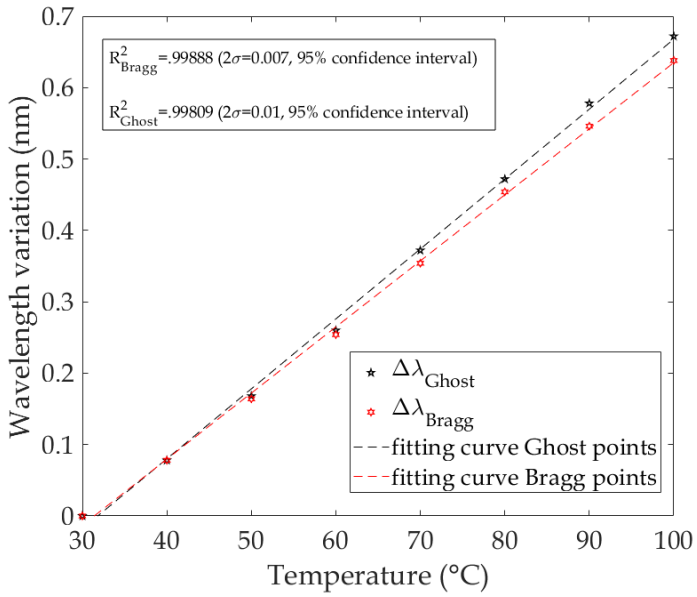


Fig.2-14. Thermal calibration trend for 3° tilted FBG in-written Fibercore PS1250/1500 OF.

Unlike those of Fig.2-12 which are practically overlapping the $\Delta\lambda_{Bragg}$ and $\Delta\lambda_{Ghost}$ calibration trend, of Fig.2-14, show a different slope. This means they have dissimilar thermal sensitivity coefficients, which can be calculated from the gradient of the linear trend. For this sensor, $k_{T_{Bragg}}$=9.117±0.007 pm/°C and $k_{T_{Ghost}}$=9.6±0.01 pm/°C. By using eq. II.31, the thermal resolution of this specific TFBG can be found. In particular, for a FBG interrogator NI PXIe-4844 with 4 pm of *swR* (the same as used in the experimental testing campaign), the *TR* of the sensing system is ≈8.23°C. This value can be improved in two strategies: by optimising the TFBG customisation to enhance the difference between $k_{T_{Bragg}}$ and $k_{T_{Ghost}}$, and/or simply by employing an interrogator with a finer *swR*.

About the first option, several TFBG samples were calibrated during the experimental campaign. The TFBGs used in the beginning, were produced in standard Corning SMF-28e and thin OF (dual acrylate coated) with θ=5° and 6°, not-recoated at the sensor location and 10 mm long. In Tab.2-1, the thermal

coefficients are reported with the TFBG customisation. These exhibited too close $k_{T_{Bragg}}$ and $k_{T_{Ghost}}$ values, resulting in high *TR* values that did not satisfy the measurement requirements for the next planned applications. Therefore, with the aim of improving the *TR* of the sensing system, different customisations of the TFBG were tested. The new sensors were manufactured by FORC-Photonics with the phase-mask technique and excimer laser at 248 nm, in standard Fibercore PS1250/1500 (a_2=125 µm, hydrogenated for 2 weeks at 100°C in order to obtain 2-3% of H_2 concentration in the glass of the OF) with tilt angle of 2° and 3° and length of 4 mm across 10 mm of no-recoated OF. In Tab.2-2, $k_{T_{Bragg}}$ and $k_{T_{Ghost}}$ are reported for several sensors. By comparing the values obtained by the old (Tab.2-1) and new (Tab.2-1) configurations, it is possible to appreciate the improvement deriving from a proper customisation. This demonstrates once again, the influence of the customisation of the TFBG on its sensing performance and how it can be exploited to improve the quality and accuracy of the measurement. Of course, in the chapters dedicated to the several applications, the TFBGs are present only in the preferred configuration.

Table.2-1. Thermal sensitivity coefficients and *TR* of several tested TFBGs.

OF	a_2	θ	$k_{T_{Bragg}}$ (pm/°C)	$k_{T_{Ghost}}$ (pm/°C)	*TR* (°C)
Corning SMF-28e	125 µm	5°	11.25	11.083	23.95
			11.41	11.13	14.28
			11.371	11.211	25
		6°	10.502	10.317	21.6
			10.512	10.351	24.84
			10.514	10.322	20.83
Corning RC SMF	80 µm	5°	11.416	11.75	11.97
			11.5	11.92	9.52
			11.519	11.882	11.02
		6°	12.625	12.455	23.53
			12.655	12.405	16
			12.621	12.198	9.45

Table.2-2. Thermal sensitivity coefficients and *TR* of several TFBGs produced with different customisations.

θ	$k_{T_{Bragg}}$ (pm/°C)	$k_{T_{Ghost}}$ (pm/°C)	*TR* (°C)
2°	8.6290	9.2000	7.01
	8.7143	9.5714	4.67
	8.2857	8.7143	9.3
	8.8857	9.4857	6.66
	8.8000	9.9100	3.60
3°	8.6571	9.600	4.24
	9.2860	9.9710	5.84
	9.0860	9.600	7.78
	9.1143	9.600	8.23
	8.7429	9.4571	5.6

Since many sensors were calibrated, the medium thermal sensitivity coefficients can be calculated for both the peaks with their standard deviation values in the 95% confidence interval. These are $k_{T_{Bragg}}$=8.667±0.197 pm/°C and $k_{T_{Ghost}}$=9.347±0.299 pm/°C for 2° TFBGs and $k_{T_{Bragg}}$=8.959±0.223 pm/°C and $k_{T_{Ghost}}$=9.531±0.272 for 3° TFBGs. If new TFBGs with the same customisation have to be used without performing the thermal calibration, then these coefficients may be considered.

2.4.2 External Refractive Index effects on the TFBG spectrum

Here, the third measuring ability of the TFBG sensor is treated theoretically. The cladding resonance peaks are the result of the coupling between the forward-propagating core mode and the back directed cladding modes coming from the cladding layer. Due to their nature, the cladding modes are strongly connected with the external surrounding medium conditions, especially to its RI. Specifically, each cladding mode propagates with a determined effective RI and electric field from the cladding to inside the core mode where they are coupled. However, these conditions are stable only until the external refractive index (ERI) is constant. If the refractometric condition outside of the OF changes, then the amplitude and the wavelength of the cladding resonances undergo a variation as their n_{eff}^{cl} and E_{lm}^{cl} are different with respect to before. The relation between ERI and effective RI and propagation electromagnetic field was also treated mathematically in [16,27]. This is the physical reason why the selection of the cladding peaks is not convenient for thermomechanical measurements when also the surrounding RI changes, as anticipated in section 2.4.1.

For ERI variations from air to slightly higher values, although altered, the cladding resonances continue to be present in the spectrum. However, with the gradual approaching of the surrounding RI to the effective one of the *i*-th mode, this last mode becomes less guided within the cladding and its resonance appears weak in the spectrum. While, when the ERI matches the effective RI of *i*-th mode then the mode is irradiated out and the relative resonance does not appear anymore in the spectrum. The total disappearance of the resonance peaks from the spectrum is a phenomenon linked to the missing of the internal reflection of the modes, which are radiated outside from the OF. Indeed, for $\theta<45°$ the cladding modes are reflected back to the OF core due to the internal reflection occurring at the interface between cladding layer and external medium. The internal reflection phenomenon is based, in this case, on the propagation angle, effective RI of the cladding modes and the medium surrounding RI. By supposing the propagation angle is not influencing the reflection as in the case of weakly TFBG, when the ERI is the same of a $n_{eff_{cl}}$, the relative mode is not any more reflected and continues its propagation outside of the OF. In other words, from the modes side, the two different media appear as a single continuous material without a physical boundary. This mechanism begins from the higher order modes until to the lower order modes with the increasing of the ERI as the sequence of spectra in Fig.2-15 shows.

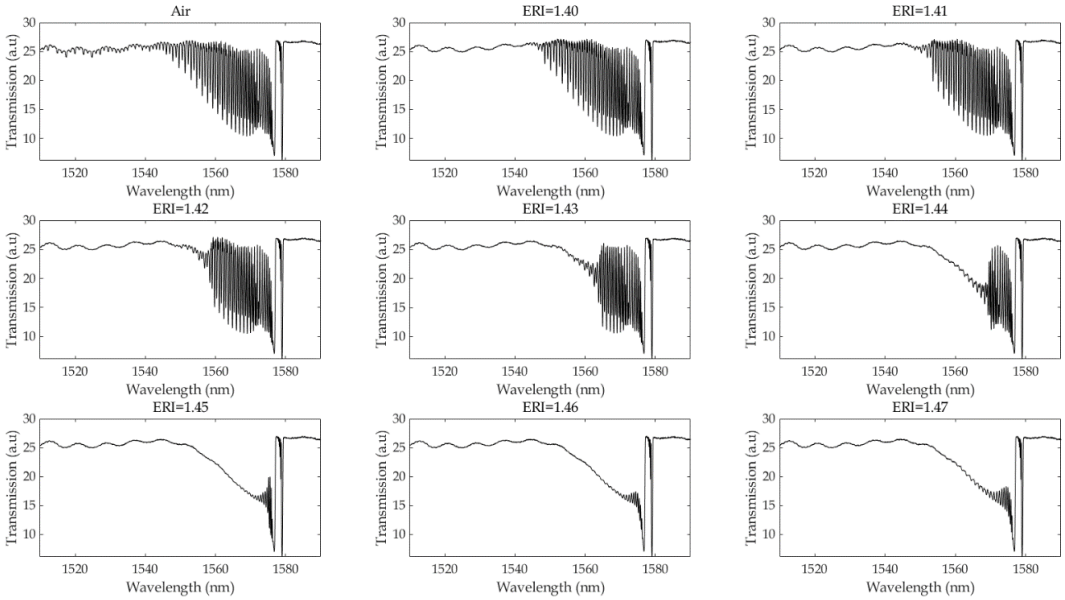


Fig.2-15. Cladding resonance peaks decay in 3° TFBG sensor with the ERI increasing.

These spectra were obtained by immersing a 3° TFBG in several Cargille oils with well-defined RI (accuracy $\pm 2\times10^{-5}$, produced by Cargille laboratories). From this picture, the spectrum in air is observed to possess all the cladding peaks appearing from the wavelengths near the Ghost mode to

those lower where small peaks are attributable to high order cladding modes. However, when the ERI reaches already 1.40, these last small resonance amplitudes disappear and the spectrum is an oscillating line. With the ERI increasing, more modes are involved in escaping from the OF, and their peaks becomes smaller and smaller as the subplot RI=1.46 shows. At certain point, there is a specific value for which the spectrum is totally empty of cladding peaks. However, between the figures at ERI=1.46 and 1.47 RI, the cladding peaks appear growing in the spectrum. This fact has two consequences. The first is the ERI for which all the cladding modes escape out from the OF is between 1.46 and 1.47. The second is that there exists a new confinement condition in the cladding layer which generates again the reflection of the modes from the cladding to the core. This means that the cladding resonance peaks appear again in the spectrum and may be exploited for measurements. Indeed, unlike asserted by several researchers such as in [28], in the next chapter the TFBG will be demonstrated to be a valid refractometric sensor even when surrounded by a RI greater than the cladding layer one. As consequence, each single TFBG can be used to detect the RI variation of any kind of resin or adhesive, from the manufacturing to during its operation life.

There are several demodulation techniques able to convert the spectrum in RI measure. These are treated in the next chapter where a novel advanced method with high performance based on the Delaunay triangulation (D-T) is presented.

2.5 Conclusions

The results obtained by solving the system of differential equations of the TFBG coupling mode theory (section 2.3) and the thermomechanical-refractometric calibration tests (section 2.4) demonstrated the significant influence of the TFBG customisation on the measurement of the same sensor. This is the investigation raised by the formulation of the first and second research question.
Initially, the TMM was introduced as a technique that is able to solve the fundamental equations that describe the exchange of energy between the modes propagating in the OF, also taking into account the Bragg structure of the sensor. Hence, it allows the quick verification of the goodness of the TFBG transmission spectrum in relation to the measurement that should be performed. The trends shown from Fig.2-8 to Fig.2-11 highlighted as the parameters that depend from the structure of the TFBG, can make the spectrum, ideal or not appropriate, for a certain measuring application of the sensor. Therefore, a preliminary evaluation of the TFBG spectrum, based on the manufacturing or effective Bragg structure parameter, by using the TMM, can provide information on the usability or optimisation of the sensor before the manufacturing.
Successively, the thermomechanical calibration of several TFBGs with different customisations, allowed the calculation of the sensitivity coefficients and, then, the thermal resolution of each sensor. Tables 2-1 and 2-2 report the data obtained after the calculation. It is possible to observe as, tilt angle, manufacturer's production methodology and OF characteristics (hydrogenation, doping concentrations, thin or standard fibre) the factors that greatly influence the measuring capability of the TFBG. From the research performed to provide a response to the first research question, it is easily understandable as the customisation of the TFBG is the first fundamental step for a successful measuring system based on these sensors.
In order to provide a response also to the second research question, the experiment presented in section 2.4.2 was carried out. As shown in Fig.2-15, the transmission spectrum of the TFBG is demonstrated to change when increasingly the sensor is immersed in a liquid with a refractive index different respect to that of the cladding layer. The results treated in this chapter, about the influence of the external refractive index on the TFBG spectrum, are only qualitative and demonstrate the radiation of the cladding modes outside the cladding of the OF due to the external RI value. This means a variation of the spectrum as presented in Fig.2-15 where it can be observed the continuous decay of the cladding peaks with the immersion of the sensor in the liquid. However, a deeper investigation is carried out in the next chapter where this topic is fully treated and the second question is fully achieved. In this way, as described in the next chapter, the phenomenon of the TFBG spectrum change can be exploited to perform the measurement of the surrounding refractive index.

References

[1] L. Fazzi, D. Klyukin and R.M. Groves, *Transfer matrix method for fundamental LP_{01} core mode coupling in a Tilted FBG sensor*, AIP Conference Proceedings, 2293, 200010 (2020).

[2] K.A. Konnova, E.A. Frolova, A.I. Gribaeva, V.V. Zakharova, A.A. Mikhnevaa, V.A. Novikovaa and S.V. Varzhela, *Inscription and Visualization of Tilted Fiber Bragg Gratings*, Optics and Spectroscopy, 125, p. 54–59, (2018).

[3] Y. Zhao, Q. Wang and H. Huang, *Characteristics And Applications Of Tilted Fiber Bragg Gratings*, Journal of Optoelectronics And Advanced Materials, 12 (12), p. 2343-2354, (2010).

[4] T. Erdogan and J. Sipe, *Tilted fibre phase gratings*, Journal of the Optical Society America A, 13 (2), p. 296-313, (1996).

[5] T. Erdogan, *Fiber grating spectra*, Journal of Lightwave Technology, 15 (8), p. 1277-1294, (1997).

[6] L. Dong, B. Ortega and L. Reekie, *Coupling characteristics of cladding modes in tilted optical fiber Bragg gratings*, Applied Optics, 37 (22), p. 5099-5105, (1998).

[7] K. S. Lee and T. Erdogan, *Fibre mode coupling in transmissive and reflective tilted fibre gratings*, Applied Optics, 39 (9), p. 1394-1404, (2000).

[8] Y. Li, Mark Froggatt and Turan Erdogan, *Volume Current Method for Analysis of Tilted Fiber Gratings*, Journal Of Lightwave Technology, 19 (10), p. 1580-1591, (2001).

[9] Z. Yan, C. Mou, K. Zhou, X. Chen, and L. Zhang, *UV-Inscription, Polarization-Dependant Loss Characteristics and Applications of 45° Tilted Fibre Gratings*, Journal of Lightwave Technology, 29 (18), p. 2715-2724, (2006).

[10] K. Zhou, L. Zhang, X. Chen, and I. Bennion, *Low Thermal Sensitivity Grating Devices Based on Ex-45° Tilting Structure Capable of Forward-Propagating Cladding Modes Coupling*, Journal of Lightwave Technology, 24 (12), p. 5087-5093, (2006).

[11] K. Zhou, L. Zhang, X. Chen, and I. Bennion, *Optic sensors of high refractive-index responsivity and low thermal cross sensitivity that use fibre Bragg gratings of <80° tilted structures*, Optics Letters, 31 (9), p. 1193-1195, (2006).

[12] C. Jáuregui and J. M. López-Higuera, *Near-field theoretical model of radiation from a uniform-tilted fiber-Bragg grating*, Microwave and Optical Technology Letters, 37, p. 124–127, (2003).

[13] M. J. Holmes, R. Kashyap and R. Wyatt, *Physical properties of optical fiber sidetap grating filters: free-space model*, IEEE Journal on Selected Topics in Quantum Electronics 5, p. 1353–1365, (1999).

[14] Y. Li, M. Froggatt and T. Erdogan, *Volume current method for analysis of tilted fiber gratings*, Journal of Lightwave Technology 19, p. 1580–1591, (2001).

[15] C. Tsao, *Optical Fibre Waveguide Analysis*, Oxford Science Publications, (1992).

[16] T. Erdogan, *Cladding-mode resonances in short- and long- period fiber grating filters*, Journal of Optical Society of America A, 14 (8), p. 1760-1773, (1997).

[17] Y.C. Lu, W.P. Huang and S.S. Jian, *Full vector complex coupled mode theory for tilted fiber gratings*, Optics Express, 18, p. 713, (2010).

[18] M. Yamada, K. Sakuda, *Analysis of almost-periodic distributed feedback slab waveguides via a fundamental matrix approach*, Optical Society of America, 26 (16), p. 3474-3478, (1987).

[19] G. J. Liu, Q. Li, G. L. Jin, B. M. Liang, *Transfer matrix method analysis of apodized grating coupler, Optics Communications*, 235, 321, (2004).

[20] A. Ikhlef, R. Hedara, M. Chikh-Bled, *Uniform Fibre Bragg Grating modeling and simulation used matrix transfer method*, IJCSI International Journal of Computer Science Issues, 9(1), (2012).

[21] L.Fazzi, A. Rajabzadeh, A. Milazzo and R.M. Groves, *Analysis of FBG reflection spectra under uniform and non-uniform transverse loads*, Proceedings of SPIE, 10970 (109701X), (2019).

[22] M. Smietana, W.J. Bock, P. Mikulic and J. Chen, *Pressure Sensing in High-Refractive-Index Liquids Using Long-Period Gratings Nanocoated with Silicon Nitride*, Sensors, 10, p. 11301-11310, (2010).

[23] F. Chiavaioli, D. Laneve, D. Farnesi, M.C. Falconi, G.N. Conti, F. Baldini and F. Prudenzano, *Long Period Grating-Based Fiber Coupling to WGM Microresonators*, Micromachines, 9(7), 366, (2018).

[24] W. Jin, W.C. Michie, G. Thursby, M. Konstantaki and B. Culshaw, *Geometric representation of errors in measurements of strain and temperature*, Optical Engineering, 36 (8), (1997).
[25] W. Jin, W.C. Michie, G. Thursby, M. Konstantaki and B. Culshaw, *Simultaneous measurement of strain and temperature: error analysis*, Optical Engineering, 36, 598, (1997).
[26] https://www.zaber.com/products/linear-actuators/NA/specs?part=NA23C60-T4A (20/03/2022).
[27] Z. Zhang and W. Shi, *Eigenvalue and field equations of three-layered uniaxial fibers and their applications to the characteristics of long-period fiber gratings with applied axial strain*, Journal of Optical Society of America A, 22 (11), p. 2516-2526, (2005).
[28] G. Rajan and B.G. Prusty, *Structural Health Monitoring using Fiber Optic Methods*, CRC Press Taylor & Francis Group, p. 225, (2017).

2

3

Delaunay triangulation demodulation technique and TFBG refractometric sensing

"The process of scientific discovery is, in effect, a continual flight from wonder."
Albert Einstein

This chapter is dedicated to the treatment of a new demodulation technique to obtain from the TFBG transmission spectrum the refractive index measurement of the media surrounding the OF sensor.
The development of this new approach occurred during the studies to solve the research question about the effects of the surrounding RI on the cladding resonance peaks. In fact, the need to analyse as soon as possible the TFBG spectrum, independently of its shape, motivated the formulation of the Delaunay demodulation technique, which improved the quality of the results and the investigation times and methodology with respect to the previous techniques.
At the same time, the ease of application and the shortening of the spectra processing times allowed the implementation of several measurements and experiments focused on how to study the customization of a TFBG to change the capability of the sensor in measuring the surrounding RI. Therefore, the arguments of the thesis with regards to the first and second research questions, which are the following:

- *How can the customization of the Bragg gratings influence the capability of the sensor for measuring a certain parameter?*
- *How does the surrounding refractive index variation affect the cladding resonance peaks in the transmission signal of the TFBG sensor?*

The here presented new technique is based on the Delaunay triangulation of part of the TFBG spectrum enclosed between the higher and lower cladding resonance peaks, whose amplitude depends on the RI media surrounding the cladding layer of the OF. The values of these areas are calculated and correlated to the external RIs in order to build a correlation function, which can be used to independently measure the surrounding RI from the TFBG spectrum. This work was published in the Journal of the International Measurement Confederation (IMEKO, "Measurement") under the title "*Demodulation of a tilted fibre Bragg grating transmission signal using a-shape modified Delaunay triangulation*" [1].

The spectral changes of the TFBG cladding resonances in amplitude and wavelength due to the ERI, promoted, during the last decades, the development of several techniques aiming to convert the TFBG spectrum response into a measurement of the surrounding RI. These methods are fundamentally divided between those using the wavelength-encoded information (wavelength shifting [2] and cutoff resonance [3]), and those using information contained in transmission spectral changes of the cladding resonances (envelope [4] and area method [5], standard deviation method [6], and contour length approach [7]). For these reasons, the two classes are respectively called wavelength shift and global methods. The first class of methods is easy to apply, as the techniques are based on the wavelength shifts of the cladding resonance peaks caused by ERI changes. However, this strategy suffers from

cross-sensitivity due to other parameters such as strain and temperature, which, in turn, affect the wavelength of the cladding peaks. Hence, the use of these techniques would require a preliminary calibration to obtain the temperature and RI sensitivities coefficients of some selected cladding resonances. Actually, in case of multi-parameter measurements, this operation is fundamental as the coefficients of the sensitivity matrix must be found to uncouple opportunely the different perturbations. The strategy and steps in this approach involve in some drawbacks which are not easy to overcome due to the large errors in the calculation for similar sensitivity coefficients or the impossibility to separate individual effects if the coefficients are the same. Moreover, the methods will only work until a certain RI as the peaks disappear or can be confused with the noise at the low amplitudes.

The second demodulation group is independent of thermo-mechanical perturbations as these techniques are focused on the transmission power carried by the upper and lower cladding peaks through the spectrum. This makes them more suitable for simultaneous multi-parameter measurements by offering also precise measurements in a certain surrounding RI range. Unfortunately, however, the demodulation procedures of these techniques must follow many steps which are time consuming. In fact, as the cladding resonances are not uniform in amplitude and wavelength distribution, the process of obtaining the envelope of the upper and lower peaks is not always straightforward to perform.
This induces researchers to use some mathematical artefacts like extra-smoothing of the envelope curves, and/or approximations of the integrals of the transmission signal to better adapt to the mathematical trend, the functions of which are often generated through piecewise-functions whose integration process is computationally heavy and slow. These gaps provide the necessity to develop a new demodulation technique for refractometric purposes without incurring the previously mentioned drawbacks.
Therefore, in this chapter, a novel global demodulation technique is introduced theoretically and practically with the aim to convert the cladding resonance peaks of the TFBG spectrum into RI measurements. The approach is based on Delaunay (also known as Delone) triangulation [8] which is used to create a triangles mesh of the upper and lower cladding resonance peaks. Therefore, the area of each triangle is summed to the other to calculate the global envelope area.
Once the technique has been introduced, it will be used to analyse the TFBG refractometric properties, as RI measurements performance, RI calibration of the sensor and double-surrounding effects.

The arguments treated in this chapter were published in scientific journals. The articles can be consulted at references [1] and [9].

3.1 Delaunay triangulation

Several triangulation methods can be used for the discretisation or partitioning of complex polygons into multiple triangles (in 2D) or polyhedrons into tetrahedrons (in 3D), with a final objective of computing the area, volume or discretizing a point set into a convex hull. Further applications find the triangulation useful for the creation of interpolation functions and the generation of a refined mesh for FEM analysis of complex body parts [10]. Several algorithms based on different triangulation strategies have been developed over the years: recursive diagonal insertion, ear cutting, prune and search, decomposition into monotone polygons, divide and conquer, sweep-line, Graham scan, randomized incremental, and using bounded integer coordinates [11]. However, all these algorithms have a common triangulation definition which is that the following mathematical conditions are satisfied:

$$\begin{cases} \forall\ t \in \mathbf{T} \Rightarrow \mathrm{conv}(\mathbf{S}) = \cup t_n, \\ \forall\ \mathbf{P}_i \in \{\mathbf{S}\} \equiv \mathbf{B}_i, \\ \mathrm{conv}(\mathbf{S}) \cap t_n \equiv \mathbf{V}_i \vee \mathbf{l}_m \vee \emptyset. \end{cases} \tag{III.1}$$

The elements in eq.III.1 are defined as: **S** is a set of points, **T** is the t_n triangles array or triangulation whole, $\mathbf{V}_i$ and $\mathbf{l}_m$ are the vertices and edges of triangles, while i, m and n are the indices of the relative elements. The first expression in eq.III.1 describes the convex hull of **S** which is defined as the union of all the triangles generated by the triangulation. The second condition of the same equation system

establishes that each point of **S** is a vertex of the generated triangles. The last condition of eq.III.1 implies that the intersection between the convolution of the point set and the triangles, generated by the triangulation, coincides with the vertices or the edges of the triangles, or it is empty.
Now, the previous mentioned triangulation strategies may result in a more or less efficient triangulation algorithm based on the shape of the element to analyse. However, the obtained triangles, after the triangulation, can sometimes appear skinny and with long edges, with the vertices of some of them tending to be spread out from each other or to not be connected properly to each other. These issues and inaccuracies are highly undesirable. The reason for this is that the triangulation becomes non-uniformly distributed, and consequently, the convex hull of the discretised point set may be different from the optimum one. Therefore, to avoid these issues, Delaunay triangulation (D-T) can be considered to obtain well-shaped and uniformly distributed triangles (Fig.3-1) [12]. Starting from eq.III.1, D-T can be defined by adding the so-called empty circumcircle property, let us suppose that:

- $\mathbf{S}=\{P_1(x_1,y_1),P_2(x_2,y_2),\ldots,P_i(x_i,y_i)\}$ point set in $\Re^2$,
- $\mathbf{T}=\{t_1, t_2,\ldots,t_i\}$ D-triangulation array of **S**,

$$\Rightarrow \forall\, \mathbf{l}_m \in \mathbf{T}\ \exists\ \mathbf{c}_n : \mathbf{l}_m \cap \mathbf{c}_n \equiv \mathbf{V}_i \wedge \mathbf{l}_m \wedge \mathbf{c}_n = \emptyset. \qquad \text{(III.2)}$$

(x_i,y_i) are the in-plane coordinates of the several points and $\mathbf{c}_n$ are the circles generated during the triangulation. Following, eq. III.2, for each edge of the triangles generated by the triangulation, a circle exists such that the end of the edges (vertices) are on the boundary of the circle. However, at the same time, no other vertex of **S** is in the interior of the same **c**. When D-T is not applicable then the constrained version can be used. In this version, two vertices of the same triangle of **T** must be coincident on the boundary of **c** and the third can be interior or outside of the circle $\mathbf{c}_n$ [11]. In Fig.3-1, a clear example of D-T is reported where a set of 7 points undergo the triangulation by following the above rules. Each point of the set is a vertex of one or more triangles generated on the circles, and simultaneously, each point is outside by any circle. Moreover, since for three points only one circle can intersect, therefore the written triangle, with vertices the same points, is unique.

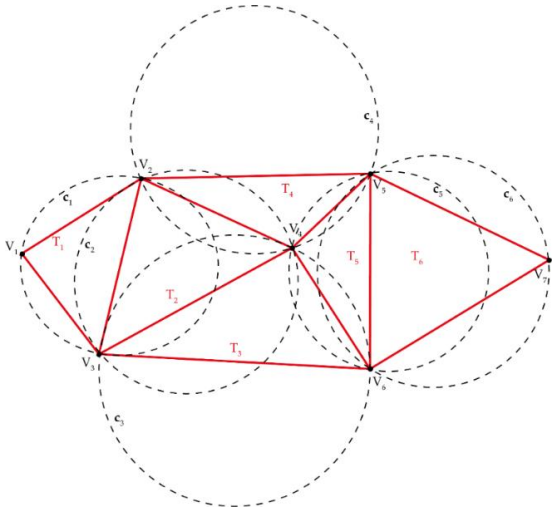


Fig.3-1. Delaunay triangulation of a 7 point set.

3.1.1 D-T approach for TFBG spectrum

The demodulation technique based on D-T aims to create a triangles mesh of the cladding resonances spectral region by using the data points of the transmission spectrum of the TFBG. Once the triangulation has been performed, the total envelope area can be easily calculated by summation of all the areas of the triangles. Hence, the area values can be correlated with the ERIs.
The first step regards the preparation of the spectrum for the triangulation. The TFBG signal acquired by the interrogation system is a set of points which have a certain spacing, in wavelength and amplitude, depending by the resolution of the interrogator's scanning detection system. Therefore, as reported in

Fig.3-2, the TFBG spectrum is processed as a sequence of points whose coordinates are known, and hence, these can be treated as a point set **S**.

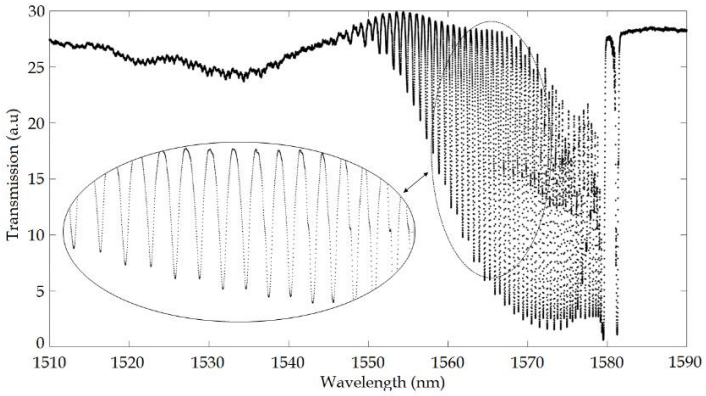


Fig.3-2. TFBG spectrum as a point set.

The demodulation technique can be applied to the entire spectrum or a part of it. Since only the envelope area of the cladding region can provide information on the ERI, it is convenient to apply the D-T only to the bandwidth referred to these peaks. In particular, here, the working spectrum is considered from the point corresponding to half of the Ghost peak to over the entire cladding resonance range. This choice allows the spectral variations that happen in the bandwidth between the Ghost and the first peak of the cladding resonances to be taken into account. Each data point of the set in the TFBG spectrum, is potentially a vertex of the Delaunay **T**. However, if the triangulation is performed globally to **S** then the resulting convex hull most likely could be different from the actual envelope of the cladding resonance peaks. Specifically, a parameter to control the proper connection distance between the vertices should be defined to avoid that the algorithm generates very long edges **l** between vertices placed in far bandwidths. Hence, the notion of α-shape in the algorithm of Delaunay triangulation [13,14] has been introduced to overcome this issue. Hence, substantially, **T** occurs based on the Delaunay definition, but simultaneously the triangulation is kept under control through the parameter α that represents the maximum r radius of the circles $\mathbf{c}_n$, which can be attributed under different conditions. Specifically, to yield a reliable D-T for the TFBGs spectra, the following should be considered:

- Delaunay triangulation $\mathbf{T}=\{t_1,t_2,\ldots,t_n\}$,
- from eq.III.2, $P_1(x_1,y_1),P_2(x_2,y_2),P_3(x_3,y_3)=V_i$,

$$\Rightarrow\sqrt{\left((x_1-x_r)^2+\left(y_1-y_r\right)^2\right)}=\sqrt{\left((x_2-x_r)^2+\left(y_2-y_r\right)^2\right)}=\sqrt{\left((x_3-x_r)^2+\left(y_3-y_r\right)^2\right)}=r\leq\alpha. \qquad \text{(III.3)}$$

The condition in eq.III.3 guarantees that the algorithm generates triangles inside circles with $r\leq\alpha$. This allows the algorithm to take into account small variations of the cladding resonances area through a smoother and more uniform meshing of the spectrum. During the demodulation phase, it was noted that the triangular mesh elements usually have smaller sizes when they are internally used in the convex hull of the spectrum (where the vertices concentration is higher), while longer edges **l** are used for the border elements. The resulting spectrum triangulation is strongly influenced by the α value. Hence, an optimized α value should be applied to perform the discretisation so that to calculate accurately the cladding peaks envelope area.

At this point, by taking as a sample the spectrum of Fig.3-2, the D-T of it is performed for several values of α. The triangulated spectra are reported in Fig.3-3. By observing Fig.3-3a and 3-3b, if values of α between 0.1 and 0.5 are used, the triangular elements formed during the mesh generation do not have enough dimensions to fill the entire set point. Indeed, a conspicuous number of empty regions are present. With an increase of the maximum permissible radius (α = 1), a solid convex hull of the spectrum is created without holes, but the borders do not match smoothly the peaks in some regions as observable in Fig.3-3c. Therefore, through a higher shape parameter (α = 2, 6), the triangles perfectly

discretized the spectrum in a fine convex hull which represents the peaks envelope. Due to the larger α, some regions of the spectrum external to the expected envelope shape are triangulated as well. These are indicated by the red arrows in Fig.3-3e) and 3-3d)). The triangulation of these areas could seem to be an issue for the calculation operations of the envelope area, however, as will afterwards be demonstrated, it does not influence the success of the correlation with the RI. Rather, since these external areas grow and wane congruently with the cladding resonance peaks, a better fitting function of RI correlation might be obtained resulting in a higher predictability and smoother trend of the curve. Obviously not all radii α allow a useful area measurement to be determined. In fact, a trade-off analysis should be performed to select the optimum α. However, it has been noted that a radii range exists where each α value returns an acceptable correlation.

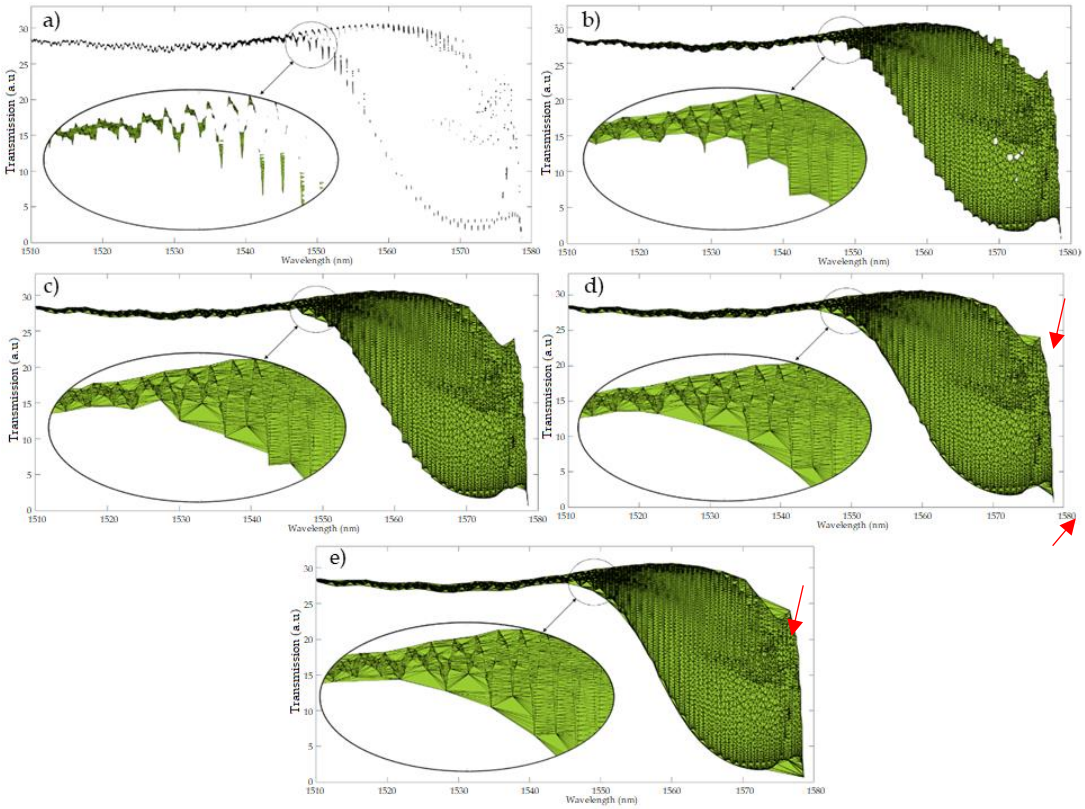


Fig.3-3. D-triangulation of the 5° tilted FBG transmission spectrum for: a) $a = 0.1$, b) $a = 0.5$, c) $a = 1$, d) $a = 2$ and e) $a = 6$. The red arrows, see text for a detailed description, indicate the triangulation outside the cladding peaks envelope.

3.2 Refractometric calibration of the TFBG sensor

Now, the D-T fundamentals have been introduced, in this section, D-T will be used to obtain the envelope areas of a TFBG sensor used for the testing campaign, when it is immersed in several oils with a specific RI. In this way, the refractometric process of a TFBG is shown and, the correlation between the normalised envelope areas and the ERIs can be obtained. Then, the sensor is ready to perform refractometric measurements.

Furthermore, considering that also thin OFs (cladding Ø 80 μm) are often used in embedded SHM applications as the sensors are even less intrusive than those written in standard OFs, the correlation curve obtained with the TFGB inside the standard OF was compared with a twin sensor but written in a thin OF. This offers an interesting point of view regarding the variation of the refractometric properties of a TFBG when the customisation changes. Specifically, the D-T demodulation was applied to the spectra of a tilted FBG written in Fibercore SM1500(9/125)P with (cladding Ø 125 μm) and thin-single mode OFs (thin-SMF, cladding diameter Ø 125 μm). Sensors were manufactured using a tilted phase mask technique by FORC-Photonics company. In this case, the kind of OF is different

from those announced in the previous chapter as Fibercore PS1250/1500 OF is not available in a thinner cladding diameter version. However, the use of these new OFs is reserved only for the topics of this section. Both the TFBGs have a tilt angle of 5°, length of 10 mm, and the coating layer was removed before the experiment to obtain a bare OF for the entire length of the TFBGs. The sensors were interrogated with a 4-Channel National Instruments NI PXI- 4844 Universal Input Module based on a scanning Fabry-Pérot tunable filter technology with 4 pm spectral resolution, a minimum power detection of 6.103×10^{-4} dBm and a working wavelength range between 1510 nm and 1590 nm. This means 20×10^{3} points are available for the triangulation of the spectrum. During calibration, the TFBG sensors were surrounded by a well-defined RI environment by using Cargille oils [15]. The set comprised RI liquids from 1.3 until 1.7 with 0.01 interval and accuracy of ± 0.0002 in the temperature range between 18 and 32 °C. During the calibration, the OFs were mounted on a translation stage so that the sensors were kept linear while dipping them in a polycarbonate bowl containing the RI liquid. This calibration setup is shown in Fig.3-4.

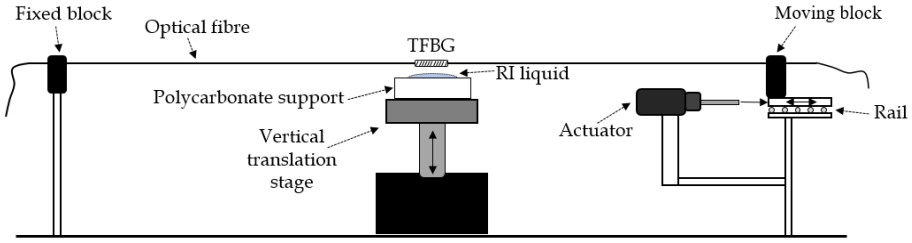


Fig.3-4. Schematic of the setup for the refractometric calibration of the TFBGs.

The temperature of the immersed sensor was monitored with a k-type TC and kept at 25 ± 2 °C. A digital microscope camera was used to check that no air bubbles remained at the interface between the oil and the cladding of the OF. Once the spectra were acquired via the DAQ system, they were processed by applying the D-triangulation through a dedicated algorithm.

3.2.1 Correlation normalised envelope area-external RI

Once the immersion of the TFBGs was performed and the spectra were acquired, the D-T method can be applied on the data point set. Fig.3-5 shows three overlapped spectra after that the meshing was performed with α=2 on the 5° TFBG sensor written in standard OF surrounded by three oils with different RIs. The spectrum in red is for the oil with RI = 1.47, in yellow and red when the TFBG is surrounded by a liquid with RI = 1.42, while in the case of RI = 1.33 the spectrum is composed of blue, yellow and red regions.

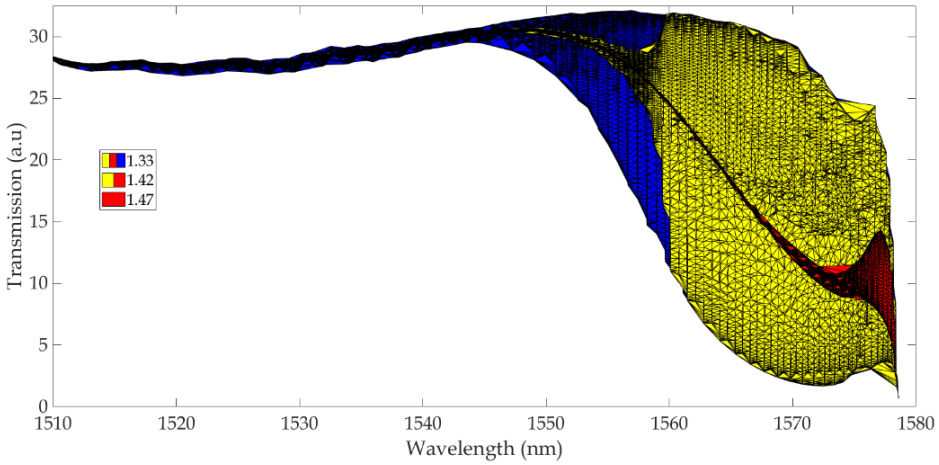


Fig.3-5. D-Triangulation of 5° TFBG (in-written standard SMF) spectra immersed in 3 different RI liquids, the imposed α value is 2.

As anticipated in section 2.4.2, it is possible to observe the reduction of the area formed by the D-triangulation of the upper and lower cladding resonance peaks as the surrounding RI increases. Specifically, the triangulated cladding area results are at their maximum (blue + red + yellow) when the sensor is immersed in the oil with RI=1.33 and incorporates all the cladding resonances. While, when the ERI grows, the upper and lower relative amplitude peaks fall, hence, for 1.42, the same blue region decreases to the yellow one and then to the red one for 1.47. This decay is such that between the several areas a 'funnel effect' happens. This effect is also visible for higher effective RI cladding modes after zooming into these parts of the spectrum as seen in Fig.3-6.

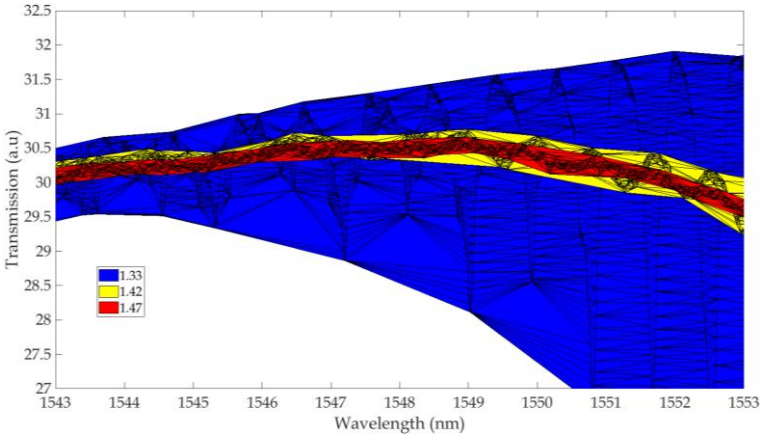


Fig.3-6. Triangulated area zoom of medium-high effective RI cladding modes peaks. Also here the 'funnel effect' is visible as smaller ERIs produce greater areas incorporating those obtained for lower RIs.

Once all the spectra have been acquired with the sensor immersed in each RI liquid set for the calibration, the area is discretised by following D-T and the total envelope area can be calculated as the summation of all the triangles areas (A_t):

$$A_T(RI)=\sum_{t=1}^{m} A_t. \qquad \text{(III.4)}$$

Of course, $A_T(RI)$ is function of the surrounding RI, hence, it assumes a different value with the variation of the RI. A correlation can be then performed between the RI and the relative A_T. By convention, this correlation is done by using the normalised area value $\mathscr{A}_i$:

$$\mathscr{A}_i(RI)=\frac{A_T(RI_i)}{A_T(RI_{ref})} \qquad \text{(III.5)}$$

As eq.III.5 reports, $\mathscr{A}_i$ is calculated as the ratio between the envelope area obtained for a given ERI and a reference area. The reference area is arbitrary, however, in this case it is taken when RI was 1.33 as for this value the maximum A_T was obtained and, hence, the resulting correlation graph y-axis is between 0 and 1. Fig.3-7 shows the correlation trends between surrounding the RI and normalised area for the 5° TFBGs written in standard and thin Fibercore SM1500(9/125)P. The two curves show a different trend although the only parameter that is changing between the TFBG customizations is the cladding diameter of the OF in which the sensors are engraved. From the correlation graph it is possible to deduce some features of the TFBGs spectra and behaviours. Starting from RI = 1, the trend is substantially linear around 1.33 where both curves reach their maximum value. This behaviour was reported also in previous work [4,16], so it was considered unnecessary to perform a finer calibration between 1 and 1.3. In this range, the curve referred to the TFBG inside the thin-OF (in red) is above the blue curve. Since, the normalisation condition is applied in same way for both the correlations, therefore the ratio A_i is bigger for the TFBG in thin-OF. Considering that a reduction of the cladding diameter generates an enhancement of cladding mode coupling in TFBG sensors [16], the transmitted resonance peaks of the highest cladding modes (Fig.3-8) have a much deeper loss than those recorded for the standard OF (Fig.3-2). A possible explanation, for low RI values is that the high cladding mode

peaks' contribution to building up the area is greater in the case of TFBG in-thin-OF written than standard waveguides so that the ratio with the maximum area is bigger. Furthermore, the two lines are not parallel. Especially, the red line has a more accentuated slope, this means the susceptibility of the cladding modes coupling to the surrounding RI is higher in a TFBG sensor written in a thin-OF. From RI = 1.33 the trend of both curves changes showing the maximum TFBGs sensitivity to the RI variations. Though the standard-OF TFBG is not very sensitive until 1.4, this sensor is highly susceptible to RI variation between 1.4 and 1.46, and its curve has a strong slope. Meanwhile the other sensor exhibits a smooth trend and good slant along the entire range 1.33–1.46. The above description demonstrates how the TFBG sensor customization can influence their sensing abilities. Particularly, in this case, the TFBG in the standard-OF is extremely sensitive between 1.42 and 1.46, while the second is susceptible to a broader range, although having a lower sensitivity. The last RI interval (1.46–1.7) in the wavelength working window shows substantially the same behaviour for both the sensors, which are both more or less sensitive to RI changes. Although, the purpose of this work was not to study this behaviour, it is possible to try to explain this phenomenon by considering the effect of the internal reflection and the refraction at the interface between cladding and surrounding. When the surrounding RI reaches that of the cladding material all the cladding modes are irradiated out of the OF because they propagate as if the two materials are optically the same material. However, by increasing the ERI, the two materials become optically different. In particular, part of the light continues to be irradiated externally, while some modes return to be reflected internally towards the core where they are coupled with the forward-propagating core mode. In fact, in the cladding of the OF, thousands of modes with different effective RIs are present for which the critical angle (or cut-off angle) is not the same, and in particular, when the RI is higher than the cladding RI, some modes are reflected back internally at the cladding-surrounding interface.

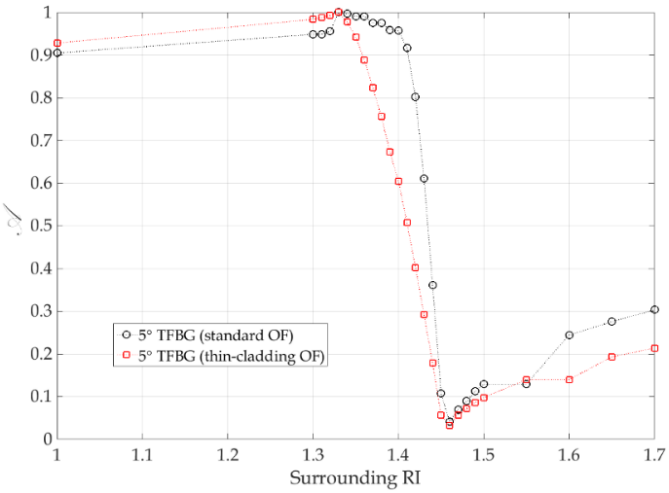


Fig.3-7. Correlation surrounding RI- $\mathscr{A}$ performed via D-T for 5° TFBGs written in standard (blue curve) and thin-cladding (red curve) OF, $\alpha = 2$.

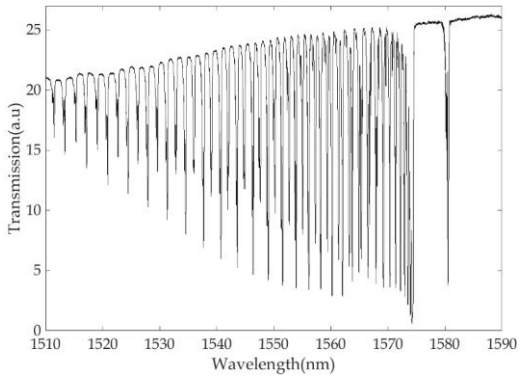


Fig.3-8. Transmission spectrum of a 5° tilted FBG written in Fibercore thin-SM1500(9/125)P optical fibre surrounded by air.

3.2.2 Fitting function of the RI correlation curve

For any sensor, once the correlation between the surrounding RI and $\mathscr{A}$ has been performed, the refractometric sensing capability of the TFBG sensor can be observed in order to find a suitable RI working range. In any case, for practicality, the correlation curve should be described analytically in the range of interest through an appropriate fitting function. This allows a direct calculation of the surrounding RI by solving the equation after the introduction of the envelope area value. However, as observed in Fig.3-7, usually the correlation curves are obtained for a broad RI range and their behaviour is different depending by the interval. This means also the optimum fitting can change along the RIs. Furthermore, if a single fitting function is supposed to exist for the entire RI range, then a single value of $\mathscr{A}$ could give two different RIs. This ambiguity may be solved by considering the two statistical parameters Skewness and Kurtosis as reported in [17], during the application of the D-T approach. However, since this ambiguity was not encountered during the post-processing of the data coming from the measurements for the applications in which the TFBGs were used, this topic was not addressed.

In this section, the fitting is performed only by considering the best sensitivity range between 1.41 and 1.45 RI. The goodness-of-fit is attributed to each function by using the R-square (R^2) statistical approach. R^2, also known as coefficient of determination, is the square of the correlation between the response values and the predicted response values, hence defined as the ratio between the deviation of the regression and the total deviation. R^2 is useful because, being constrained between 0 and 1, it provides an intuitive description of the goodness of the fit. The closer R^2 is to 1, the closer the data points are to the regression line. Here, the R-square values are attributed to the fitting functions only with the purpose of evaluating the quality of the calibration. Of course, for the same RI interval, several fitting functions can be found based on the polynomial degree considered. In Fig.3-9, the fitting functions are reported from the linear to the quartic polynomial degree for the TFBG inside the standard OF.

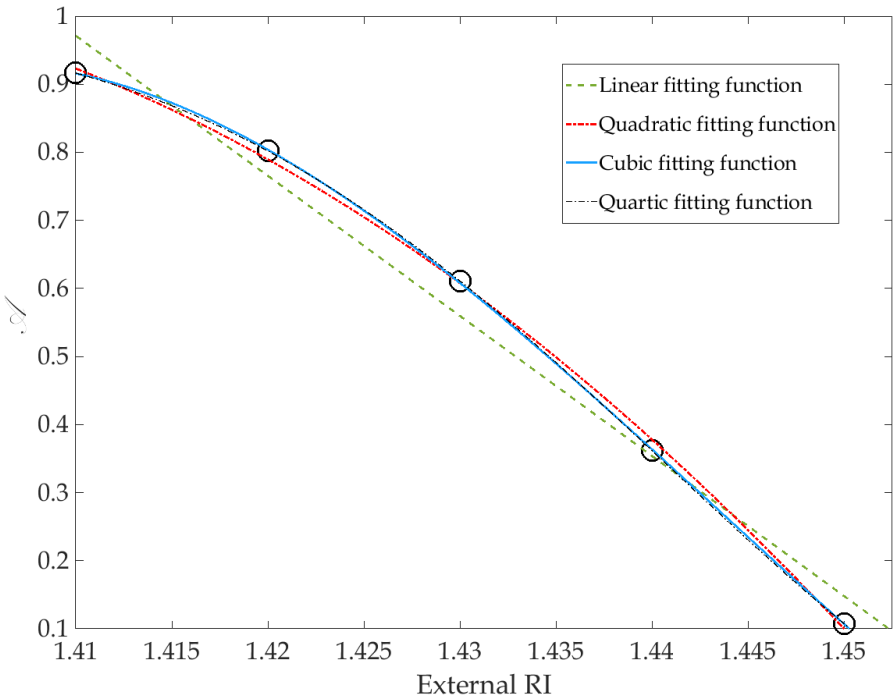


Fig.3-9. Fitting of correlation points with several polynomial degrees, standard-OF TFBG sensor.

The linear regression cannot properly represent the correlation trend as the points appear spread out with respect to the regression line. However, by already using a quadratic degree, the fitting function is such that the fitting curve is closer to the data points. The R^2 can be quantified for each fitting function generated. The values are reported in table 3-1 and 3-2 in both the cases of TFBG written in standard and thin OF.

Table.3-1. R^2 values of the fitting curves for defined RI intervals in the case of TFBG in standard OF.

RI range		Fitting function degree of $\mathscr{A}_i$(RI)			
		1	2	3	4
1.40-1.46	R^2	.9625	.9747	.9965	.9998
1.41-1.45		.9799	.9988	.9999	1
1.42-1.45		.9958	.9995	1	-

Table.3-2. R^2 values of the fitting curves for defined RI intervals in the case of TFBG in thin OF.

RI range		Fitting function degree of $\mathscr{A}_i$(RI)			
		1	2	3	4
1.33-1.46	R^2	.9757	.9953	.9977	.9985
1.40-1.46		.9882	.9913	.9973	.9994
1.41-1.45		.9991	.99997	.9999	1
1.42-1.45		.9994	.99997	1	-

From both the tables, it is possible to assert that the quadratic fitting function results sufficiently enough match the trend of $\mathscr{A}_i$(RI) as the R^2 value is already close to 1 (R^2>0.99).
For a complete characterisation of the approach, a specific study focused on the measurement performance of this technique should be performed. This is specifically reported in section 3.5.

3.2.3 Methodology of the D-T demodulation algorithm

The methodology is a fundamental to design the algorithm. A flow chart is provided below (Fig.3-10), as a summary and example of the methodology to follow to integrate the algorithms of the demodulation technique in a RI measurement system, also by considering a real-time application.

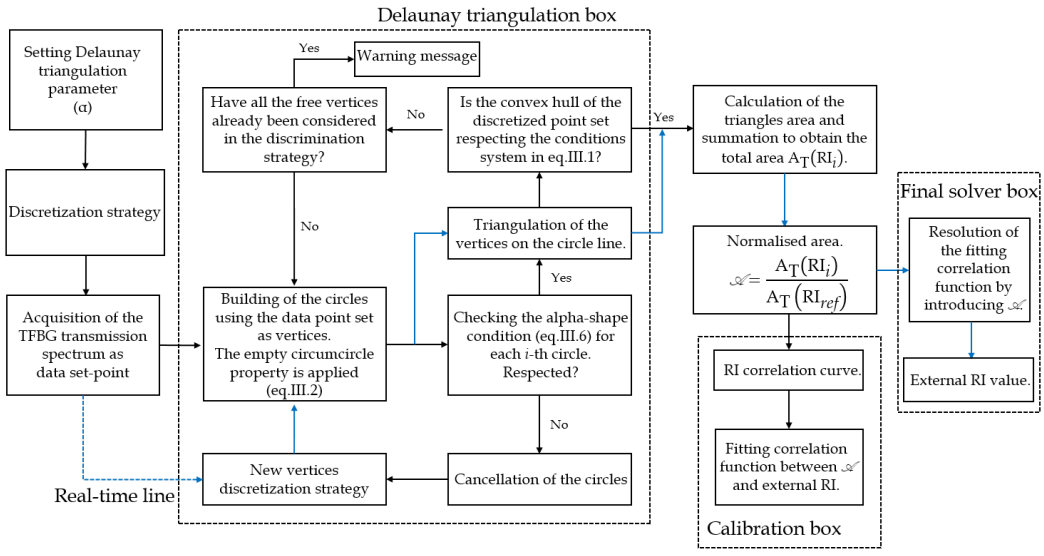


Fig.3-10. Flow chart representing the methodology of the D-T demodulation algorithm.

In the flow chart, the blue arrows show the way the analysis can be performed during real-time measurements, and it can be noted that this is composed of only 6 steps. The reduction is due to the

fact that the TFBG was calibrated in advance, hence, its measurement algorithm is already optimized for all of the RI range. Regarding the discretization or triangulation strategies, described in section 4, there are many possible options whose use depends substantially on the programmer; the here reported analysis were performed using the triangulation with the divide and conquer method. For real-time application, the discretization in triangles could be performed using a moving and adaptive mesh, as this would reduce the triangulation time and speed-up the calculation.

3.3 Comparison of D-T approach with previous techniques

In this section the benefits of the D-T technique are presented by comparing its refractometric correlation curve and the computational time with those of the other main methods. Therefore, the correlation curves obtained by applying the D-T and other demodulation techniques (envelope [4], wavelength shift separation [2] and area method [5]) are reported in a single graph, see Fig.3-11.

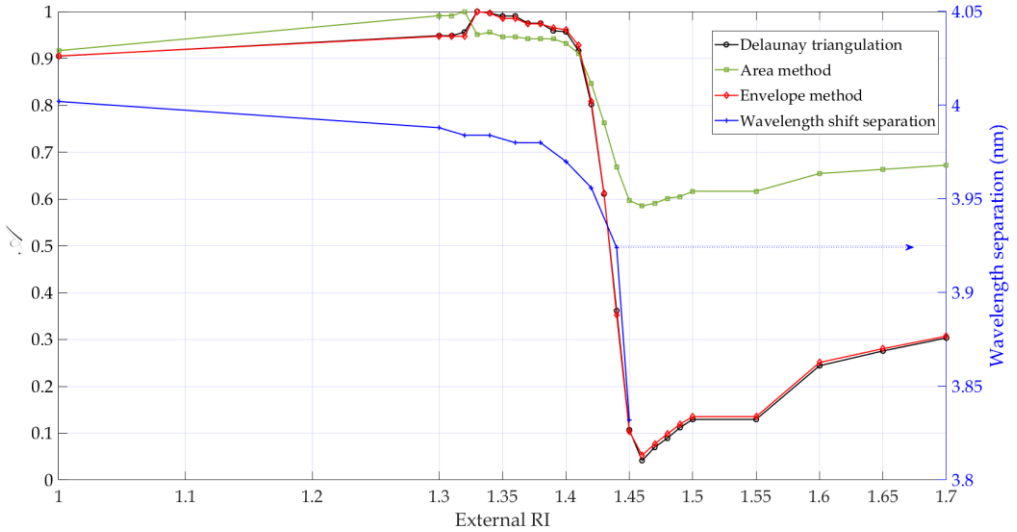


Fig.3-11. Comparison of the ERI correlation curves by using several demodulation techniques.

From Fig.3-11, the envelope and the D-T triangulation techniques provide very close correlation curves. While, the area method provides a correlation curve restricted in a smaller range, which makes the refractometric sensitivity of the TFBG lower than the previous techniques. The demodulation technique based on the wavelength shift separation develops a correlation curve until 1.45 as the selected peak was not recognizable anymore after this RI value due to the escaping effect of the cladding mode relative to the resonance in the spectrum.

A further result can be obtained by using the necessary times to demodulate a single TFBG transmission spectrum in an auxiliary parameter (normalised area or wavelength shift separation). The times are reported, for each used technique, in Table 3-3.

Table.3-3. Computational times of several demodulation techniques.

TFBG demodulation technique	Computational time [sec]
Delaunay triangulation	**0.120**
Wavelength shift separation [2]	0.095
Envelope method [4]	1.198
Area method [5]	1.998

The fastest demodulation technique, between the main methods here analysed, is the wavelength shift separation. However, the D-T technique is the fastest of the global demodulation methods, indeed the envelope and area method are, respectively, almost 10 and 17 times slower than the D-T. Although the difference in time between the global techniques may not appear to be relevant, when a high number of spectra have to be demodulated, the difference in processing with high temporal resolution between the techniques becomes important. It is enough to note that the necessary time to demodulate a TFBG

spectrum by using the envelope method is the same as needed by the D-T technique to process 10 TFBG spectra and more than 16 in comparison with the area method. Moreover, the computational time factor is fundamental during the real-time measurement because this value should be smaller than the detection rate of the interrogation system to perform appropriate real-time monitoring. Regarding the wavelength shifting method, this provides results faster than the global techniques due to its simplicity. However, if the several drawbacks described previously are considered, the difference in time-lapse is so small as not justify the use with respect to the benefits guaranteed by the D-T demodulation technique. Specifically, the computational time difference between the two techniques is 0.025 sec. By supposing to demodulate 1000 TFBG spectra, the total time difference between the two techniques is only 25 sec, which is a nice compromise if the enormous advantages of the D-T technique are considered.

3.4 α-shape parameter influence on the correlation curve

As mentioned in section 3.1, the success of the D-T approach depends strongly on the α value used to discretise the spectrum. For this reason, it is important to analyse how the RI-$\mathscr{A}$ correlation curve changes when the triangulation is applied with several α values. This is addressed in this section. With this aim, the first step is to identify valid intervals of α values in which the correlation curve has a physical meaning. Usually the RI correlation curve, as performed in this work and found in literature for any TFBG customization, has a trend characterized by a slightly increasing upward trend until a maximum point. From this peak, the best RI sensitivity range can be found with a strong but decreasing slope, until to a minimum point from which the trend is again to growth. Hence, there are substantially three trend intervals which can be physically explained and justified by taking into account the description regarding the interactions between cladding modes and surrounding RI described in chapter 2 (in particular, section 2.4.2) and section 3.2. These trend intervals are expected to remain constant if external disturbances (temperature fluctuations, bending) remain constant. Therefore, the first aim is to identify the values of α for which the correlation curves are valid from their physical meaning. Hence, by considering a range of α values, the correlation curves can be generated for both the TFBGs written in standard and thin-OF. Two different working α intervals were obtained: for the standard-OF TFBG, the suitable interval is $1.6 \leq \alpha \leq 6$, while in the case of the thin-OF TFBG any α greater than 0.8 is useful to perform the demodulation. At this point, since the correlation curves keep essentially their same trends, it is not possible to appreciate graphically in detail the differences of using different α values in Fig.3-12 and Fig.3-13.

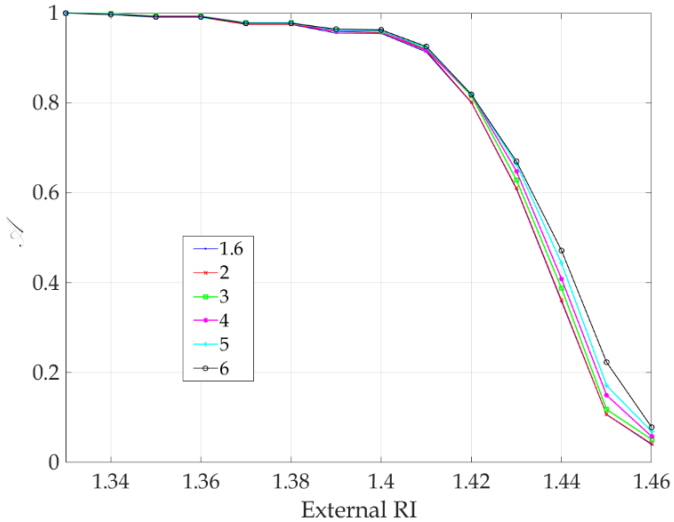


Fig.3-12. ERI-$\mathscr{A}$ correlation performed with several α values for the TFBG written in standard OF.

For this reason, to evaluate how the quality of the RI calibration of TFBGs changes, the variation of the R-square value of the fitting functions was considered. By taking into account some α radii, the same previous fitting function polynomial degrees, and the widest sensitivity RI range of the same TFBGs (in which the correlation curve has the better slope), the calculated R^2 values are reported in

Tables 3-4 and 3-5. From the R-square values, it is possible to suppose that any α value is suitable to obtain an acceptable fitted correlation curve. Nevertheless, by using a specific α, the fitting quality after calibration can be improved. Indeed, for example: by considering a TFBG in a standard-OF, the best fit for functions of 2-nd and 3-rd order can be obtained by using α = 6, while in the linear or 4-th order fitting function, the D-triangulation should be performed with α = 1.6. For a TFBG in a thin-OF, an α = 4 provides the best fit quality by considering until a 4-th polynomial fitting function. Although an optimum α value can be found when comparing the R-square values in Tables 3-4 and 3-5, as mentioned before, the use of another variable does not cause a serious drop in the goodness of the correlation.

Table.3-4. R^2 values of the fitting curves for defined RI intervals in the case of TFBG in standard OF.

α		Fitting function degree of $\mathcal{A}_i$(RI)			
		1	2	3	4
1.6	R^2	**.96254**	.97474	.99658	**.99985**
2		.96247	.97475	.99651	.99979
3		.95871	.97484	.99530	.99955
4		.958953	.98015	.99584	.99979
5		.95761	.98328	.99533	.99729
6		.96172	**.99166**	**.99800**	.99939

Table.3-5. R^2 values of the fitting curves for defined RI intervals in the case of TFBG in thin OF.

α		Fitting function degree of $\mathcal{A}_i$(RI)			
		1	2	3	4
0.8	R^2	.97364	.99526	.99719	.99859
2		.97567	.99533	.99770	.99855
3		.97887	.99607	.99798	.99874
4		**.97981**	**.99643**	**.99851**	**.99902**
5		.97844	.99606	.99821	.99887
6		.97976	.99596	.99818	.99886

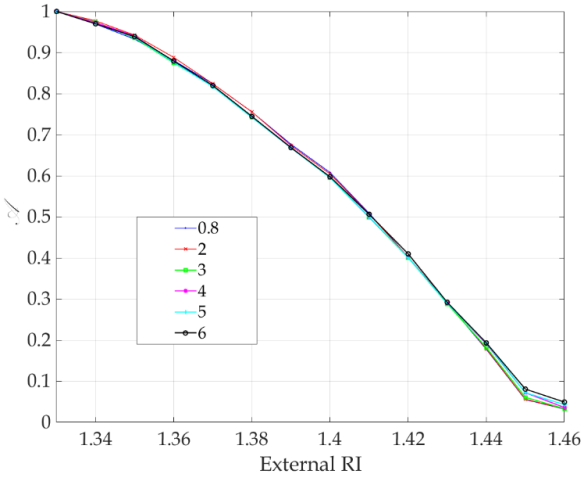


Fig.3-13. ERI-$\mathcal{A}$ correlation performed with several α values for the TFBG written in thin-OF.

3.5 Strain cross-sensitivity on RI measurements

As mentioned, the D-T technique is compatible to be used simultaneously with other techniques for multi-parameter measurements. Specifically, in the interest of the research conducted here, the TFBGs were calibrated for simultaneous thermo-mechanical-refractometric measurements. An important aspect is the inspection of the cross-sensitivity due to possible strain and temperature perturbations. From the literature, it is known that although a temperature variation induces a blue- or red-shift of the entire TFBG transmission spectrum and an amplitude change of the cladding peaks, it has been demonstrated this does not have a direct effect on the RI measurements using the global demodulation techniques [4,5]. This can be demonstrated also in the case of the D-T technique. However, for the novel approach presented in this chapter, the same cannot yet be asserted for the strain cross-sensitivity. Therefore, in this section, the variation of the cladding peaks envelope area is monitored when the sensor subjected to tensile strain while immersed in three different RI liquids. This is a fundamental step as it quantifies the cross-sensitivity influence due to a mechanical perturbation during TFBG multi-parameter measurements.

3.5.1 Experimental setup and equipment

For the investigation on the influence of the strain cross-sensitivity on the RI measurements, a 3° TFBG written in a PS1250/1500 Fibercore standard OF by FORC-Photonics was used. The test was conducted on a different sensor with (respect with the others used to introduce the D-T technique) as this customisation was preferred during the testing campaign on the aerospace materials. Also, this demonstrates as the D-T technique can be exploited on any kind of TFBG.

The experimental setup is the same as the one for the TFBG calibration presented in Fig.3-4. Specifically, this TFBG was placed centred in the linear translation stage, where, in the middle, the same previous set of Cargille labs oil liquids was used on top of a polycarbonate surface for the fibre optic sensor immersion. The linear translation stage has the double task of holding the OF straight, in position and inducing axial deformations. The accuracy of the induced displacements depends on the accuracy of the linear electric actuator, which is ±5 μm [18]. The sensor was interrogated by the same system and the vertical translation stage was used to perform the immersion in different liquids without removing the OF from the clamps.

3.5.2 Strain cross-sensitivity quantification on the RI measures

Before presenting the evolution of the envelope area with the increase of the induced displacement on the OF, the correlation curve is presented also for this sensor in Fig.3-14. Obviously, the TFBG spectra were demodulated by using the D-T with an $\alpha=2$ and the reference area at 1.33 RI. After the calibration, the mechanical cross-sensitivity on the refractometric measurements can be inspected. The TFBG was then pre-tensioned to ~30 μm, fully immersed in 1.33, 1.40 and 1.46 RI liquids and underwent several levels of axial deformation. The relative spectra were acquired every 50 με up to a maximum of 1000 με. The cladding resonance envelope areas obtained from these spectra via D-T, were normalised by using the same reference area of the calibration. The temperature detected during the experimental step was 22℃ with oscillations of ±2℃. For each RI liquid, once the TFBG was fully wetted, the actuator induced the strain to the TFBG by pushing the moving part of the translation stage where the OF end was clamped. The displacements were given as inputs to the linear actuator through its computer software provided by the manufacturer, while the spectra were acquired with a dedicated LabView code. Once the envelope areas have been calculated, these can be related to the axial strain as Fig.3-15 shows.

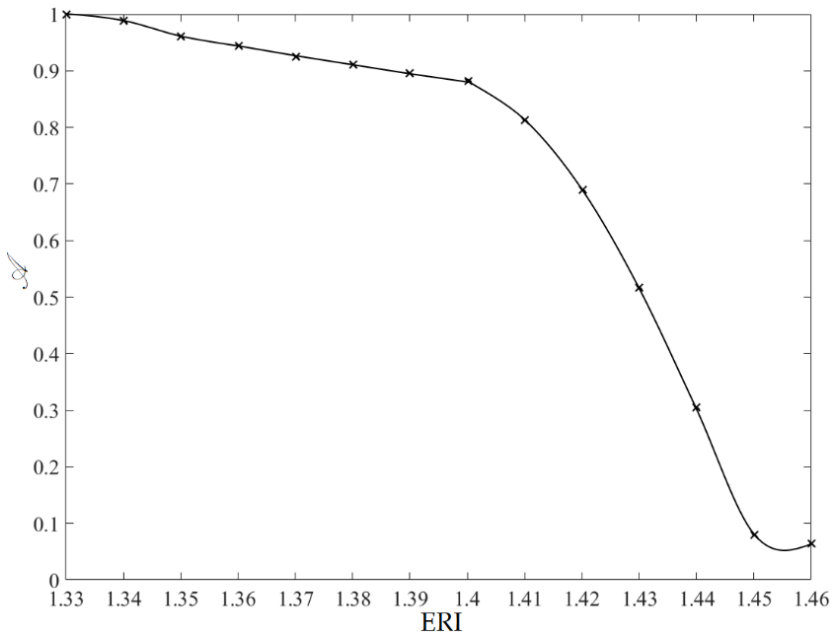


Fig.3-14. ERI-$\mathscr{A}$ correlation spline-curve for 3° TFBG written in Fibercore PS1250/1500.

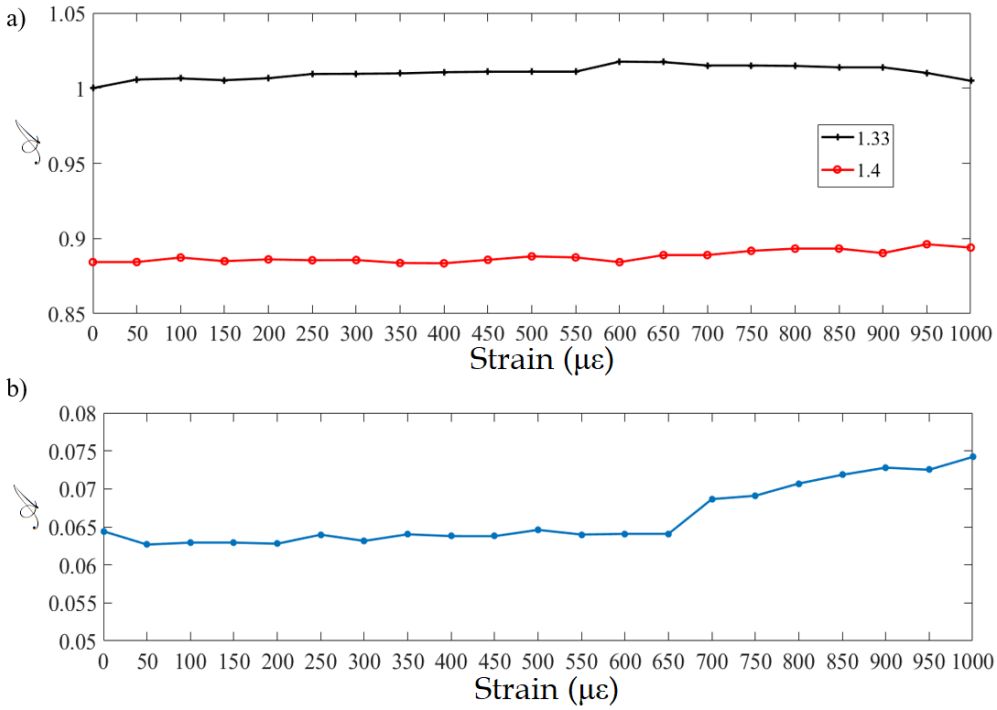


Fig.3-15. Normalised envelope area trends with strain increasing for immersion in a) 1.33 and 1.40 RI and b) 1.46 RI liquids.

From Fig.3-15, the variation of the normalised area with the strain increasing has a maximum value of 1.76% when considering $\alpha = 2$ for the 1.33 RI curve.

Now, by taking into account the TFGB worst sensitivity RI range between 1.33–1.40 RI (observable in Fig.3-14), and the linear fitting correlation function, the maximum RI error measurement caused by the strain perturbation is 0.0103. This value is calculated by considering the worst measurement condition without removing the influence of the temperature changes on the RI and the fitting error. Therefore, it is necessary to consider the temperature variation during the test and the dRI/dT thermal-refractometric variation coefficient of the immersion liquids, which is 4.5×10^{-4} RI °C^{-1}. Hence, by using the temperature variation at the maximum RI error (obtained at 600 με, with the TFBG immersed in

1.33 RI oil), the RI variation due to the temperature oscillation can be removed from the total error so that the new error value is 8.05×10^{-3}. For the same liquid, the RI shifting remains constant until 900 με, while for the total strain range, an average error value of 2.05×10^{-3} RI can be calculated. With the same procedure, the errors can be calculated also when immersing the TFBG in 1.40 and 1.46 RI oil. In this case the maximum errors are respectively 9.6×10^{-4} and 1.05×10^{-3} RI. Nevertheless, as Fig.5b shows, for each RI liquid, the trends are substantially flat between 0 and 600 με, where the RI variations due to the strain perturbation can be comparable with the coefficient dRI/dT of the immersion liquids (3.0×10^{-4} and 4.5×10^{-4} RI). If a general application of these sensors is considered, and looking at the operating temperature range of Bragg gratings written in silica OF without coating protection, which is broad (from -100 °C to 900 °C) [19,20], the temperature influence on the RI variation is expected to be far greater than the strain perturbation in a real measurement application. Moreover, all errors reported here include the possible deviations induced in the spectrum from the precision in amplitude and wavelength scanning of the interrogation system.

3.6 Measurement performance of the D-T technique

The novel technique introduced in the previous sections was demonstrated to be simple and fast to implement, saving time and reducing the computational power required, flexible, insensitive to variations in the spectrum shape and compatible for real-time measurements and simultaneous multiple measurements. However, until now the treatment has been focused more on the algorithm of the demodulation technique. Therefore, for a complete characterisation of the technique, a parametric analysis is achieved in this section regarding the refractometric measurement performance (stability, resolution and accuracy). Specifically, the robustness of the α-shape modified Delaunay triangulation in measuring the RI variation in a wide range by using the TFGB spectra when the sensor is fully immersed in the RI liquids, will be investigated. In this way, the performance of the technique is fully analysed based on the fundamental α-parameter used to perform the demodulation.

3.6.1 Stability of the α-shape modified D-T technique

The investigation of the measurement stability of the TFBG demodulated with D-T, starts by considering only a single value of α. The same experimental setup of Fig.3-4 was used, where the OF was fixed to the linear translation stage with a pre-tension of ~100 μm. The TFBG spectrum was recorded 10 times for each RI liquid, and more specifically the OF sensor was cleaned with acetone and allowed to dry after each immersion. In this way, each TFBG measurement was independent of the previous one, even in the case where the RI liquid was the same between two consecutive measurements. The envelope areas related to the RIs can be calculated as described previously and the correlation points are reported on a graph as blue circles (Fig.3-16). In this case, the selected RI range in which the analysis was conducted is from 1.40-1.60. This range includes the maximum refractometric sensitivity interval of the TFBG (1.40-1.46) and, furthermore, demonstrates that the sensor is able to work even at RIs higher than 1.46, where all the cladding modes should have been irradiated out of the OF. Usually, this last range is neglected during the analysis as it is considered erroneously not able to offer an appreciable detection of ERI. However, as described in chapter 2, part of the light is irradiated out from the cladding to the surrounding, while some cladding modes returns to be internally reflected toward the core of the OF where they are coupled [2,9]. This means the TFBG can be defined to be able to detect surrounding RIs even higher of the OF one.
Once the ten correlation points are related to the ERIs, the mean value μ of these can be calculated for each set of point placed at the same surrounding RI. At the same time, in order to determine the reliability and repeatability of the D-T demodulation technique, also the σ standard deviation is calculated for each points set, which estimates the spread of the measurements. In Fig.3-17, the cubic spline interpolation curve of the μ mean values (black line) is reported with the upper and lower σ cubic spline limits in red dashed-lines for both the RI ranges. In the maximum sensitivity range (Fig.3-17a), the σ value is greater for liquids with lower RIs, while, the measurements spreading tends to be less for higher RIs. Specifically, the σ limit curves approach closer to the black curve with the increase of the RI, up to points which almost coincide in some parts of the graph.

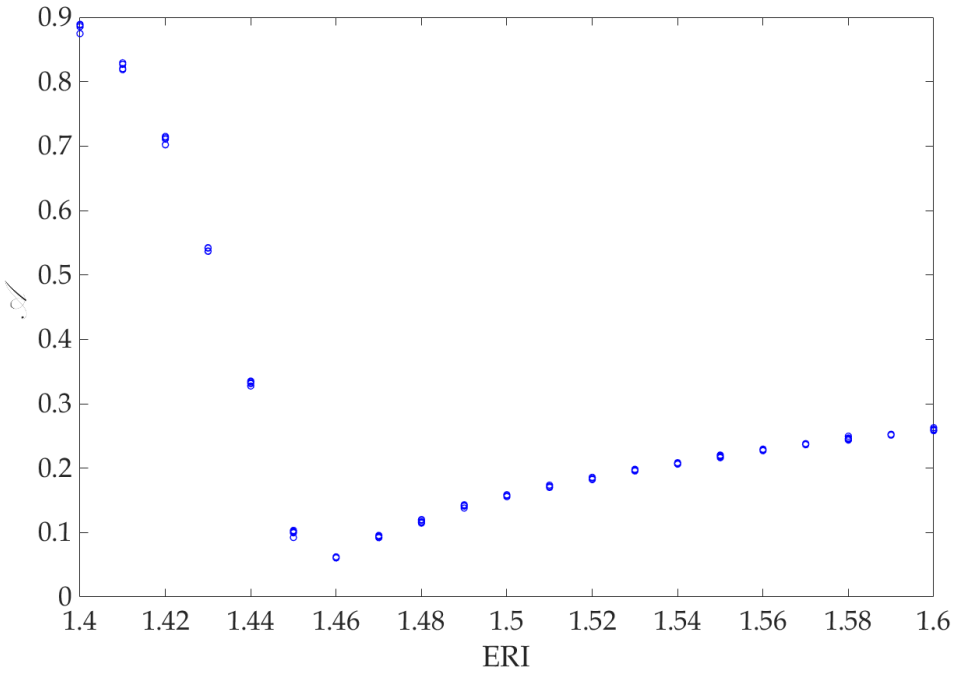


Fig.3-16. Ten correlation points for each RI liquid, measured with D-T approach from TFBG spectrum.

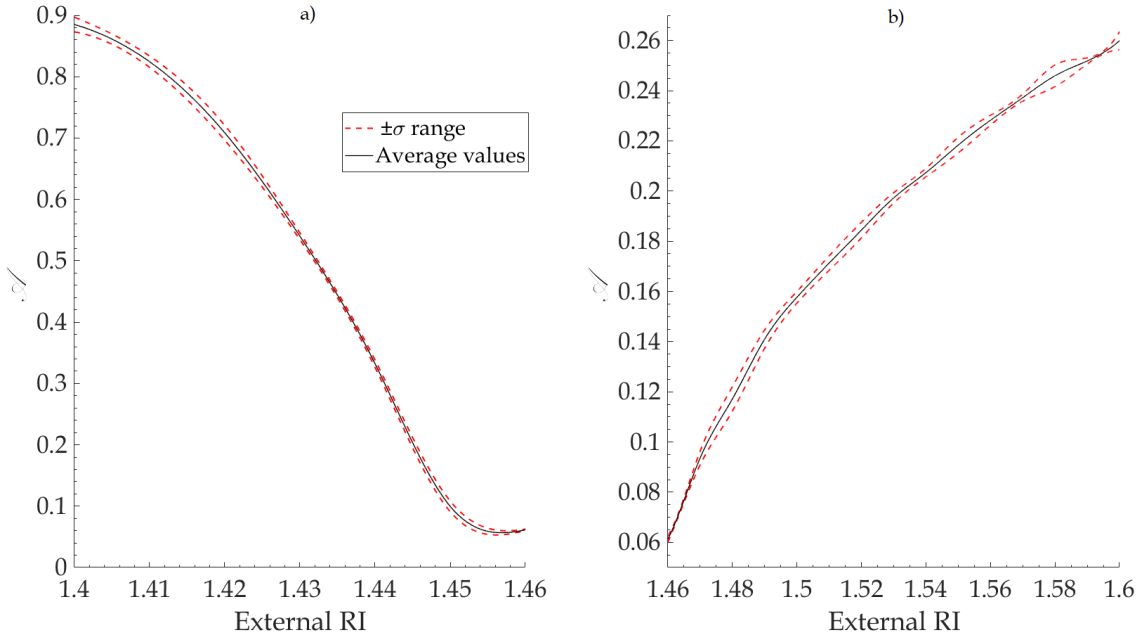


Fig.3-17. Cubic spline interpolation curves of the average, upper and lower standard deviation values in the RI range a) 1.40-1.46 and b) 1.46-1.60.

The inverted behaviour can be observed in Fig.3-17b where, the σ curves are closer to the μ spline for lower RIs and then widen as the RI increases. This trend could indicate that the TFBG spectrum is more stable when the greater part of the cladding resonances is not present in the transmission signal. For clarity, the values of μ and σ used to make the graphs shown in Fig.3-17, are reported in Table.3-6 at each RI of the working ranges. An observation of the values listed in Table.3-6 allows the identification that the standard deviation always fluctuates around the same values when the RIs are greater than 1.46, while the maximum σ is obtained from 1.4 to 1.42. A possible reason for this greater deviation identified at lower RIs may be explained by considering the presence in the spectrum of not well defined peaks generated by high order cladding resonances. These usually appear at lower wavelengths and their shape looks like double or triple peaks. Being created by the coupling between

weakly guided cladding modes, these resonances tend to disappear from the spectrum with increasing ERIs. However, they are still visible in the TFBG signal when the sensor is immersed in RI liquids between 1.40 and 1.42.

Table.3-6. Values of μ and σ for the 10 set points at each RI.

RI	μ	σ
1.40	.8850	.0060
1.41	.8244	.0046
1.42	.7085	.0061
1.43	.5399	.0028
1.44	.3322	.0030
1.45	.0997	.0043
1.46	.0614	.0006
1.47	.0937	.0014
1.48	.1172	.0024
1.49	.1410	.0018
1.50	.1577	.0012
1.51	.1713	.0014
1.52	.1845	.0016
1.53	.1973	.0010
1.54	.2074	.0008
1.55	.2183	.0016
1.56	.2282	.0010
1.57	.2372	.0007
1.58	.2459	.0022
1.59	.2518	.0006
1.60	.2599	.0018

The degeneration of the single peak into multiple peaks is due to the splitting of the vector modes as their electrical propagation field is less confined in the cladding layer, up to the point that the linearly polarized mode approximations are no longer valid to describe the coupling mode theory [9]. The sensing characteristic of these higher cladding modes to the strain and RI variations is such that they have a large irregular wavelength shift and sensitivity coefficients [21]. This means that small external perturbations generate large non-uniform variations of the relative peaks in the spectrum, which are difficult to monitor due to the splitting of the peak. This effect was noted when comparing the TFBG transmission spectra of two subsequent acquisitions by using the same RI liquid, as reported in Fig.3-18 when zooming-in on the higher cladding resonance peaks. These peaks are easily identified in lower wavelengths (1541–1547 nm for the TFBG here used), not only by the irregular shape of the peak but also by the abrupt decay of their amplitude compared to the other peaks in the spectrum. From Fig.3-18, the shapes of the upper and lower peaks between two consecutive spectra, recorded at the same experiment conditions, appear different and not uniform. Therefore, once both the spectra are demodulated with the D-T, the triangulated area regions appear dissimilar between the curves as well (Fig.3-19).

The difference in shape between the convex hulls is irrelevant for the area calculation as different shapes can produce the same area value. However, here, the dashed rectangles indicate zones in which one of the convex hulls incorporates the second. At still lower wavelengths, the peaks are not detectable anymore and become noise in the spectrum because they are already irradiated out of the OF. When the TFBG is surrounded by 1.46 RI, the higher cladding peaks are not visible anymore. Therefore, the curve becomes flatter and the oscillations have smaller amplitudes, in fact, as shown in Fig.3-19, no convex hull incorporates the other one. This demonstrates that, the effect of the higher cladding modes is missing and, the difference between the areas (and hence, the standard deviation) is smaller with respect to when the TFGB was immersed in 1.40 RI liquid.

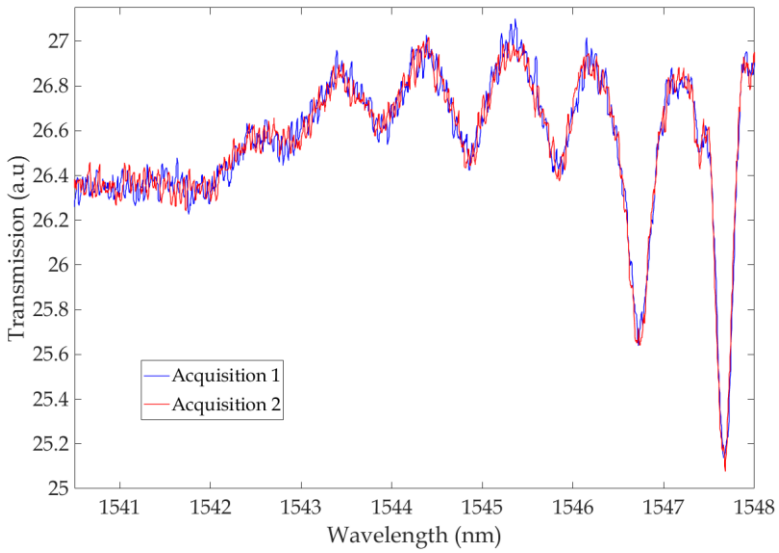


Fig.3-18. Higher cladding resonance peaks in two consecutive acquired TFBG spectra by immersing the sensor in 1.40 RI liquid.

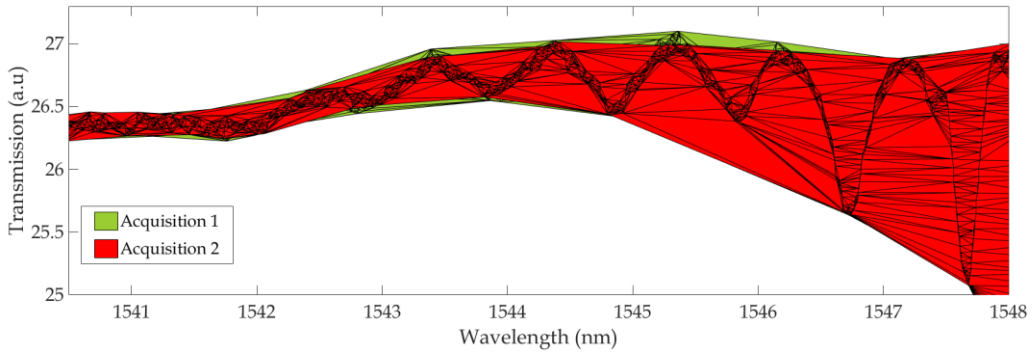


Fig.3-19. D-T area regions of the TFBG spectra of Fig.3-18.

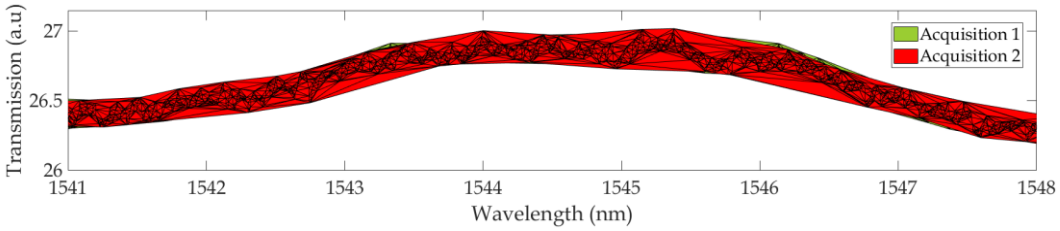


Fig.3-19. D-T areas of two consecutive acquired spectra when the same TFBG is immersed in 1.46 RI liquid.

3.6.2 Influence of the α-parameter on the measurement stability

From the experience gained in the previous section, the higher order cladding modes are assumed to be the reason behind the area differences between two consecutive TFBG spectra recorded during the immersion in the same RI. However, another cause can be the accuracy of the interrogation system in scanning the light wavelength transmitted by the Bragg gratings. In fact, the wavelength scanning and the power detection accuracy of the interrogator determine the exact positioning of the recorded data points in the spectrum, from which D-T returns the envelope area. This means that, when using the same RI at a fixed temperature, two TFBG spectra can have some data points placed at different wavelengths and power transmission range. Consequently, the resulting envelope areas may be different so to increase the standard deviation. Since the D-T demodulation technique depends strongly on the α-shape parameter, which determines the dimensions of the admissible triangles during the spectrum triangulation, in this section, an α-parametric analysis is performed to identify the α-values that reduce the standard deviation at each RI. Therefore, the standard deviation values are reported in Table.3-7 as

a function of the α-parameter used for the D-T and RI liquid. As can be observed from the table, there is no optimum α-parameter to minimize the standard deviation for all the RIs. However, some features can be extracted. Indeed, it is observable that higher α-values have no positive effect on σ. In general, smaller α-values decrease σ as the triangulation is finer due to the use of smaller triangles. This reduces the probability to incorporate, in the area calculation, parts of the spectrum generated by points that are not accurately detected during the interrogation of the TFBG sensor and to take into account small variations. Furthermore, though some α-values make σ smaller than others, the values are closer to make the error negligible when α is between 1 and 4, thus, obtaining a correlation curve or RI measurement with a good approximation.

Table.3-7. σ in function of α and RI for the 10 set points.

α	1	2	3	4	5	6
RI	σ					
1.40	0.0078	**0.006**	0.006	0.0072	0.0084	0.007
1.41	0.005	**0.0046**	0.005	0.0056	0.0047	0.0086
1.42	0.0068	0.0061	**0.0057**	0.0057	0.007	0.0068
1.43	0.004	**0.0028**	0.004	0.0033	0.0048	0.0034
1.44	0.003	0.0030	0.0032	**0.0024**	0.003	0.0028
1.45	0.0048	0.0043	**0.0041**	0.0047	0.0089	0.0071
1.46	0.0009	**0.0006**	**0.0006**	0.0017	0.0015	0.0012
1.47	0.00076	0.0014	0.0011	0.0006	**0.00056**	0.0033
1.48	0.0020	0.0024	**0.0016**	0.0017	0.0023	0.0048
1.49	0.0020	0.0018	0.0019	**0.0016**	0.0027	0.0025
1.50	0.0016	**0.0012**	0.002	0.002	0.0018	0.0013
1.51	0.0013	0.0014	0.0013	**0.0012**	0.0015	0.0026
1.52	**0.0012**	0.0016	0.0023	0.0018	0.0018	0.0027
1.53	0.00087	0.0010	0.0008	**0.0007**	0.0015	0.0035
1.54	**0.00062**	0.0008	0.0008	0.0007	0.001	0.0017
1.55	**0.0008**	0.0016	0.0013	0.0013	0.00177	0.00085
1.56	0.0013	0.0010	0.0011	**0.00082**	0.00114	0.00188
1.57	0.0011	**0.0007**	0.0008	0.0016	0.0015	0.00389
1.58	0.0012	0.0022	**0.0010**	0.0013	0.0014	0.003
1.59	**0.0006**	**0.0006**	0.0007	0.0008	0.0009	0.0028
1.60	0.0015	0.0018	**0.0014**	0.0018	0.002	0.00296

3.6.3 Refractometric resolution and influence of the α-parameter

The last performance parameter remaining to fully characterise the D-T technique is the refractometric resolution. Substantially, the refractometric resolution of the TFBG sensor is strongly dependent on the fitting correlation function obtained from the correlation points once the sensor is calibrated. In turn, the fitting function (and the correlation curve) is tied to the α-value used to perform the D-T. Therefore, a specific value of α can improve the RI resolution of the sensor in relation to the selected fitting correlation function. Also, a further improvement or worsening comes from the *sw*R and minimum power detection of the interrogator device used to acquire the spectra. In this section, the RI resolution is analysed, in the 1.40-1.46 RI range, by considering several fitting function orders obtained with different α values for the same sensing system (TFBG and interrogator) exploited in the previous sections. Initially, several correlation curves are found, based on the applied α values, from the mean points of the 10 correlation points at each RI. A cubic-spline interpolation is then generated through the medians as reported in Fig.3-20, where it is possible to appreciate how a different α causes a different trend of the correlation curve. The wavelength working range is split into two subintervals by exploiting the minimum mean point at 1.46 RI for a better presentation.

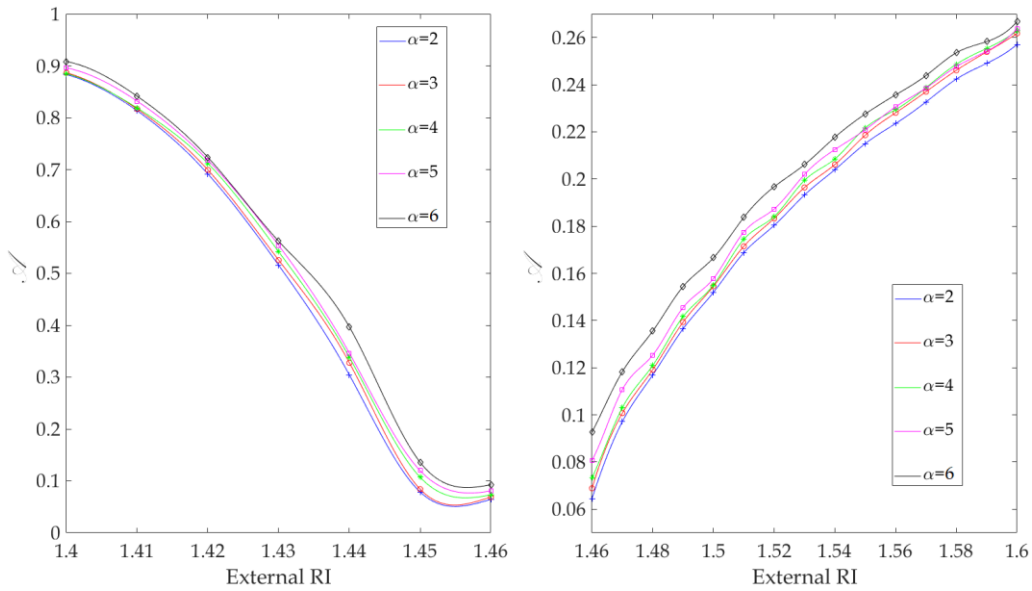


Fig.3-20. Correlation curves of the mean points for several α values.

At this point the study on the RI resolution is initially focused on the correlation curve with the D-T performed with α=2. Successively, the analysis is extended also to other α values. First of all, several orders of fitting functions are obtained from the correlation points. These are reported in Fig.3-21 with ±σ cubic-spline curves. From the fitting functions, the minimum measurable RI step can be calculating through the minimum step amplitude power detection of the FBG interrogator system. However, the here used FBG interrogator has a resolution given in dBm, which is not constant along the dynamic power range once the spectrum is converted into a linear scale. Therefore, to consider the worst measurement condition, the largest interrogator resolution is taken in the entire dBm power range of the TFBG spectrum. Hence, the minimum step area is then calculated and normalised with respect to the reference area value, and the resolution can be obtained along the fitting functions on both the sub-intervals as shown in Fig.3-22.

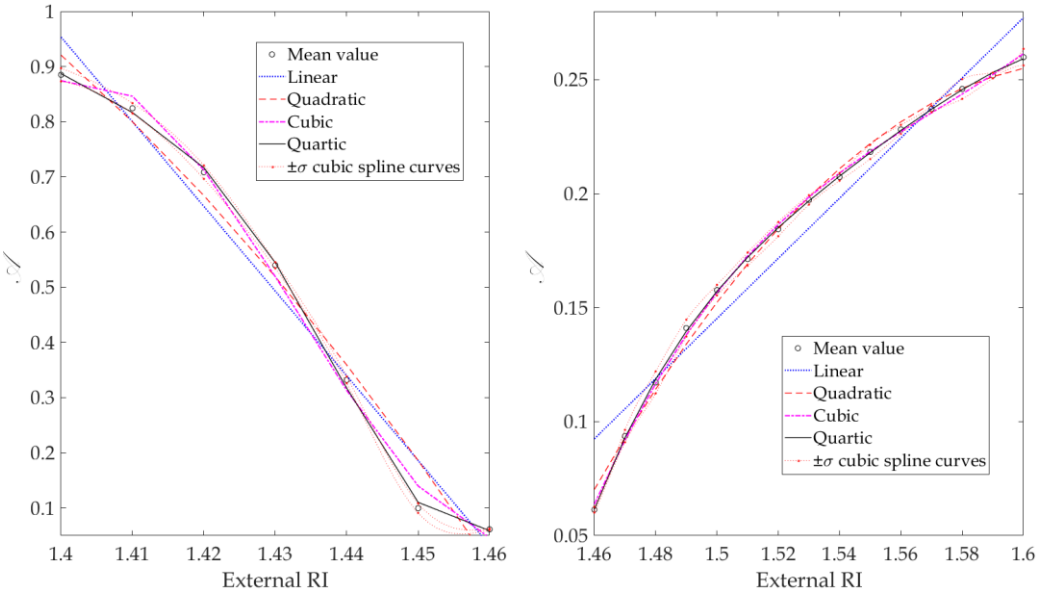


Fig.3-21. Fitting correlation functions with α=2 along the RI range.

Therefore, as observable from the evolution trends of Fig.3-22, a finer resolution makes it possible to achieve certain degrees of fitting function based on the measuring RI range. These variations of resolution along the RIs, are caused by a change in the local slope of the fitting functions. The latter can vary the minimum RI detectable step correlated with the minimum area variation in the spectrum.

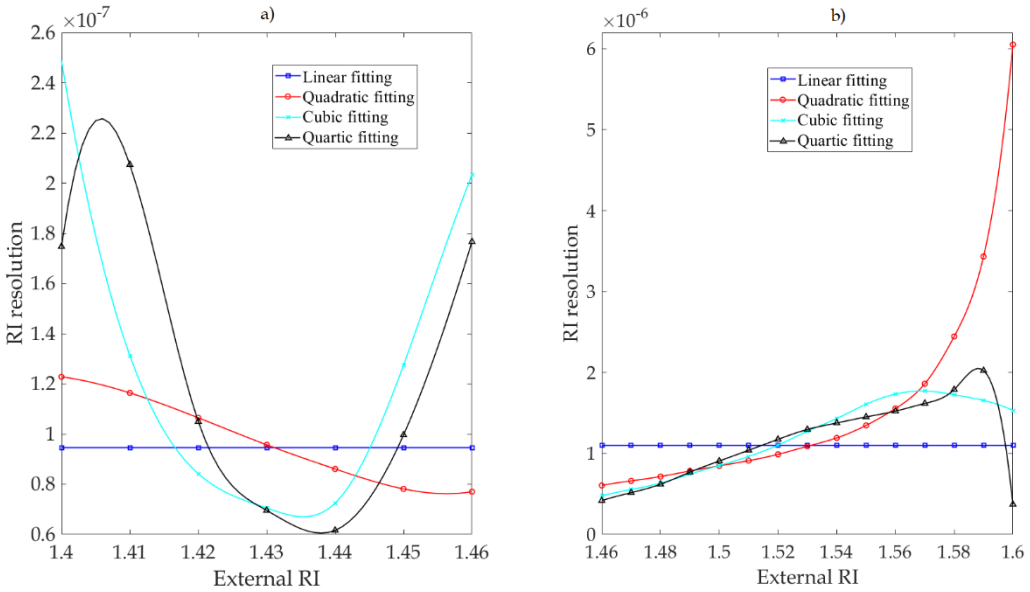


Fig.3-22. Refractometric resolution trends in a) 1.40-1.46 and b) 1.46-1.60 RI range for different fitting functions obtained for α=2.

As expected, linear fitting always offers the same resolution as the slope of the function is constant. The choice of a linear fitting may appear convenient, however, from another side, low-order polynomial functions have a fitting error greater than those at a higher degree. Hence, the measurement would be suffer from a compromised accuracy, though it would result in a more stable and, finer resolution measurement along the entire RI range. Therefore, the choice depends strongly from the application. The same analysis can be performed by considering several α values, and then the curves of Fig.3-20. Therefore, the fitting functions are found for each α (as done in Fig.3-21) and, for a complete point of view, the goodness of the fitting of each function related to the α is reported in Table.3-8 as R^2 error.

Table.3-8. R^2 error of the *i*-th degree fitting functions in relation to the used α for the D-T.

			α				
		RI Range	**2**	**3**	**4**	**5**	**6**
Fitting order function	Linear	1.40-1.46	.9710	.9675	.9697	.9717	.9731
		1.46-1.60	9520	.9554	.9603	.9605	.9656
	Quadratic	1.40-1.46	9763	.9755	.9796	.9867	.9873
		1.46-1.60	.9953	.9963	.9971	.9975	.9983
	Cubic	1.40-1.46	.9952	.9937	.9951	.9952	.9946
		1.46-1.60	.9992	.9993	.9995	.9995	.9995
	Quartic	1.40-1.46	.9993	.9989	.9994	.9983	.9976
		1.46-1.60	.9998	.9998	.9997	.9997	.9997

At the same time the resolution can be extracted for the four orders of fitting in both the intervals. The trends are shown in Fig.3-23 and Fig.3-24 respectively for 1.40-1.46 and 1.46-1.60 RI range. From a first observation, even considering the linear fitting correlation function, the same α does not ensure the finest possible resolution in both the RI sub-ranges. Furthermore, the same conclusion can be asserted also for the other fitting functions by comparing the resolution curve, whose trends are also different when considering the different monotonous nature of the correlation points from which the fitting functions are generated. However, in general, the resolution variation along the RI ranges is restrained, so that an average value can be used. The resolution trend of the quadratic and quartic fitting are the only exceptions as shown in Fig.3-24b and Fig.3-24d. Indeed, in this last figure all the curves have substantially the same amplitude and slope. While, in Fig.3-24b the trends are practically overlapping until 1.57 RI, where they take different exponential growth rates. Of all the graphs, the

highest deviation is achieved for the fitting curve obtained with α= 3 where the resolution at 1.60 is an order of magnitude higher than the same at 1.46.
After this analysis, the TFBG demodulation technique based on the D-T is well characterized for the fundamental measurement performance (stability or repeatability, accuracy and resolution).

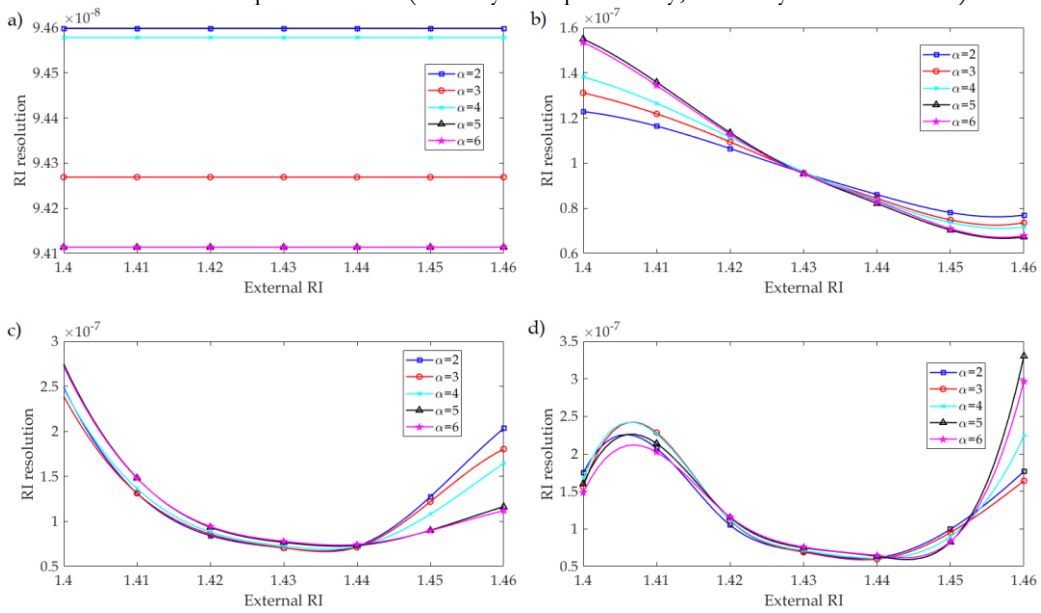


Fig.3-23. Resolution for a) linear, b) quadratic, c) cubic and d) quartic fitting functions with different α along the 1.40-1.46 RI range.

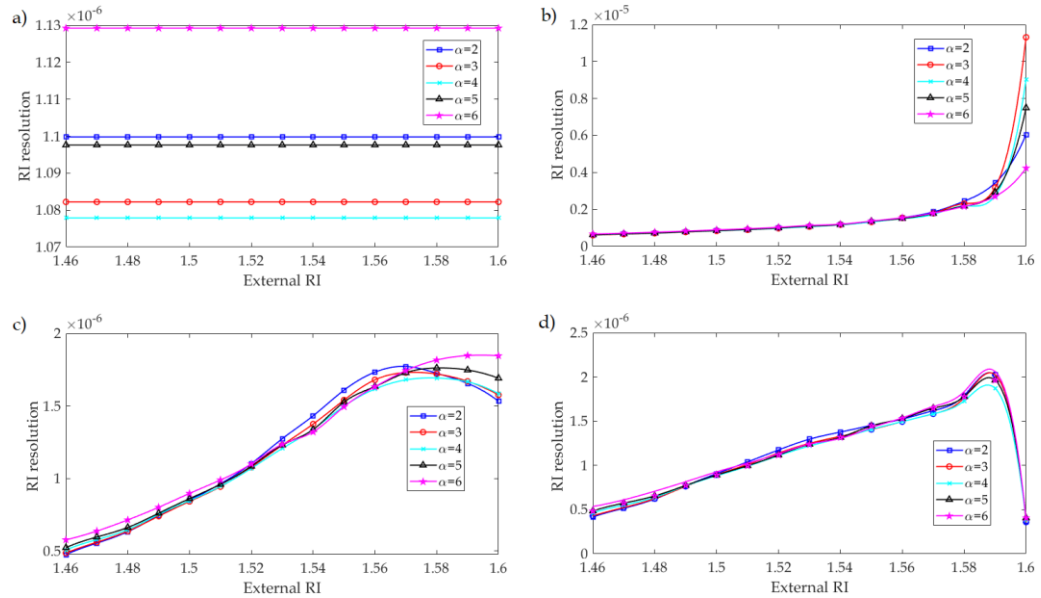


Fig.3-24. Resolution for a) linear, b) quadratic, c) cubic and d) quartic fitting functions with different α along the 1.46-1.60 RI range.

3.7 Partial immersion of the TFBG sensor

This last section is dedicated to the study of the TFBG spectrum behaviour when the sensor is partially immersed in an RI liquid, or in other words, when surrounded by two different RIs. As already mentioned, the cladding modes are irradiated out from the OF when the external RI matches their effective RI. Specifically, the resonance peaks decay is much stronger when the surrounding RI is closer to that of the cladding layer. Therefore, total immersion of the sensor in a RI liquid involves a decrease of the total power transmitted from the TFBG and a drastic change in its spectrum, which are exploited

to use the TFBG as refractometer. However, no study was found in literature regarding the spectrum evolution when the tilted Bragg gratings are partially surrounded by a media with a different RI along its length. This aspect is relevant in applications where the TFBG is used as refractometer for the monitoring of the manufacturing and curing of composite materials. In fact, in these applications, the resin flows gradually around the sensor making unknown changes in its spectrum.
A schematic of this situation is presented in Fig.3-25, where in the partially submerged (by RI_2) TFBG part, the light referred to the cladding modes is irradiated out when its effective RI matches (or it is smaller than) the external one. While, in the second part, the cladding modes are still internally reflected as the RI_1 (of air) is much smaller than the cladding RI.

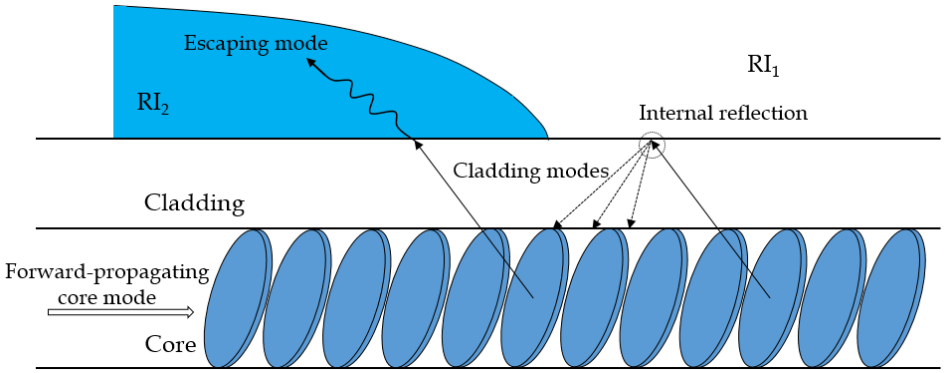


Fig.3-25. Schematic of the cladding modes reflection or radiation during double RI surrounding.

Although the mode-coupling system at the interface between two different materials, as cladding-air or cladding-oil, is much more complex than the one described, the model presented is a simple but effective method which can be useful to understand the behaviour of the TFBG spectrum in this unconventional case. In particular, focusing on the transmitted spectrum, the resonance peaks are obtained for the contribution of each single tilted Bragg grating to the reflection and coupling of the light propagating inside the core of the OF. This can be demonstrated by considering the main Bragg resonance peak of a standard FBG, whose maximum reflectivity (r_{max}) and transmission (t_{max}) is calculated by [22]:

$$r_{max} = \tanh^2(\varkappa L), \qquad \text{(III.6)}$$

$$t_{max} = \tanh^2(\varkappa L), \qquad \text{(III.7)}$$

where $\varkappa$ is the "ac" coupling coefficient (as defined in chapter 2) and L is the length of the TFBG. Hence, from the equations, the peak amplitude increases with the FBG length as more Bragg gratings contribute effectively to the coupling of the light. The same mechanism is valid also for the generation of the cladding resonance peaks. Indeed, as was also mathematically demonstrated during the treatment of the TMM in chapter 2 and in [23], inside the TFBG, each tilted grating gives the same contribution to the cladding resonances amplitude generation in the transmission spectrum. Therefore, longer TFBGs produce greater resonance amplitudes. This aspect is important as when part of the TFBG is surrounded by a medium with a different RI, the local mode-coupling changes and some cladding modes are irradiated out from the OF influencing, in this way, the amplitude and the wavelength of the cladding resonances and, consequently, the shape of the TFBG signal.

Therefore, an investigation about the effects of a possible TFBG partial immersion on the spectrum is performed by considering the situation shown in Fig.3-25. For this purpose, the testing setup of Fig.3-4 was used with a higher frame rate camera (up to 55 fps) positioned in front of the immersion region to record the different degrees of longitudinal immersion. The immersion degree was quantified as a relative length of the TFBG submerged in the liquid. This was measured digitally from the pictures acquired with the camera. A vertical translation stage is necessary to control the dipping rate along the OF axis by inducing the vertical movement of the polycarbonate block respect to the TFBG. Specifically, the combination between the surface tension and the distance of the (1.46) RI liquid from

the OF was used to control the flow along the OF length. The TFBG spectra were recorded every 3 seconds as the liquid gradually enveloped the TFBG. At the same time, pictures were taken every 1 second across each spectrum acquisition. In Fig. 3-26, seven images show the gradual immersion of the OF in the 1.46 RI liquid during the test. Considering the pictures in Fig.3-26, the input light inside the OF was propagating from the left to the right, hence, the transmitted light from the TFBG flows on the right side.

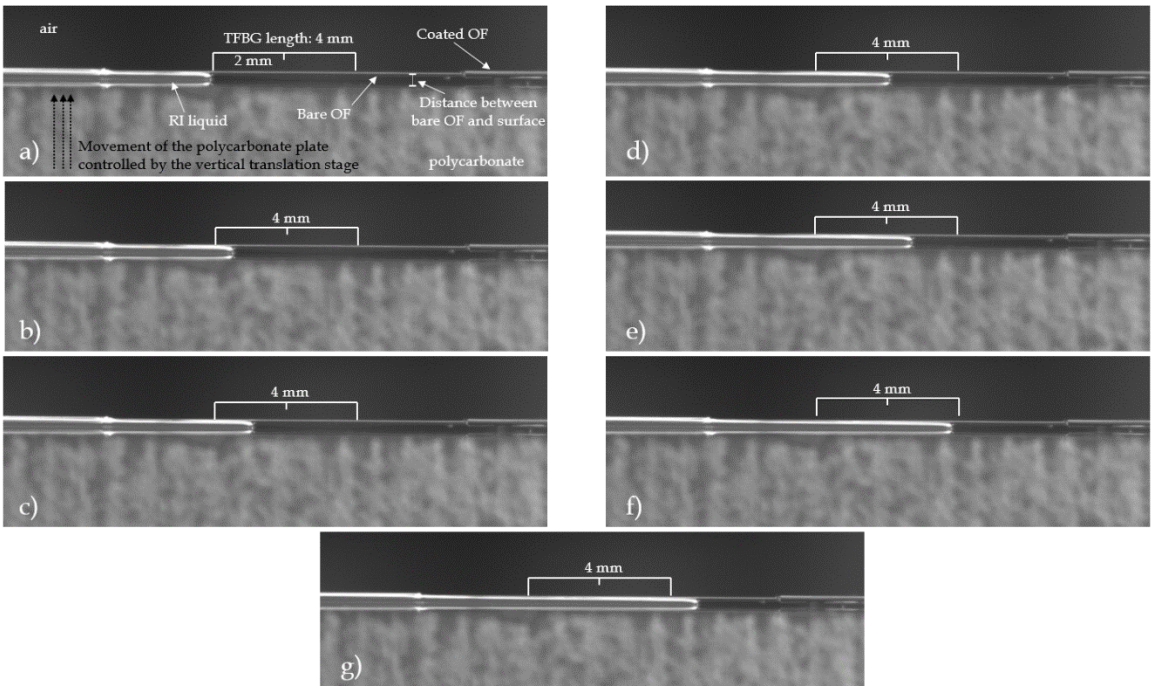


Fig.3-26. Frames sequence (a-g) during the gradual immersion of the TFBG sensor in the 1.46 RI oil.

In the first image Fig.3-26a, the RI liquid is in contact with the OF but not yet with the section where the TFBG is written, for this reason it can be considered as the starting condition. As there is no interaction between liquid and TFBG, the spectrum is the same as that obtained in air. From this moment, the oil is forced to flow toward the TFBG and along its length by exploiting the surface tension and by decreasing the distance between the OF and the polycarbonate block through the vertical translation stage. In this way, a gradual and increasing immersion of the TFBG inside the oil is achieved until the sensor is fully wetted as in Fig.3-26g.

The evolution of the cladding resonance envelope area was analysed with the propagation of the liquid by using the spectra recorded. The calculation of the envelope area was performed with the D-T technique, which demonstrated itself to be very useful for this task. The area values were normalised with respect to the envelope obtained from the spectrum in the situation of Fig.3-26a. In Fig.3-27, the decreasing of the percentages of the envelope area with the forward propagation of oil along TFBG axis, can be appreciated. In this graph, the blue dots are the normalised areas obtained from the spectra of the gradually immersed TFBG and refer to the letters to the images of Fig.3.26. The reference area of 100% corresponds to Fig.3-26a. With the progress of the RI liquid flow front, a higher RI increasingly surrounds the Bragg grating length. Therefore, the envelope area decreases as the cladding modes coupled in those gratings are irradiated out of the OF so that they do not give any contribution to the amplitudes in the spectrum. The blue dot related to Fig.3.26g represents the area when the TFBG is fully incorporated in the liquid, which is considered 0% as all the cladding modes reflections contributing to the spectrum are suppressed.

A linear correlation between the envelope area trend and the submersion length was expected if the proportional relation between the Bragg gratings and the resonance peaks in the TFBG spectrum is considered. Nevertheless, a linear fitting with an unexpected R-square error of 0.9802 is obtained. This means that, although it may be possible to determine the submerged TFBG length digitally by measuring the flow front propagation of the oil from the pictures, the found lengths do not fully

correspond with the real immersion length. As consequence, each estimated immersion length contains an error due to the surface tension and capillarity forces between the RI liquid and the OF.

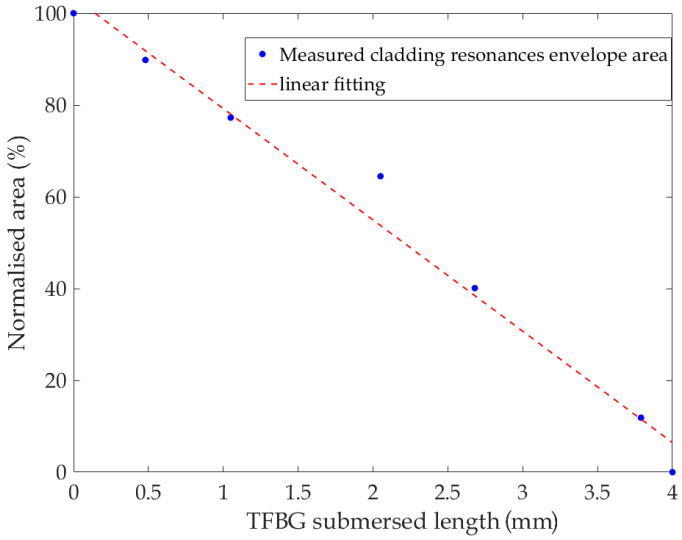


Fig.3-27. Trend of normalised cladding peaks area versus the TFBG submerged length.

An estimation of the immersion length can be accurately performed by using the cladding peaks envelope area. Indeed, as previously described, independently from the local coupling-mode system, the contribution to the resonance peaks amplitudes depends proportionally on the TFBG length. This means that the longer the immersion length is, the greater the decrease of the envelope area is. Especially, as each Bragg peak of the TFBG contributes equally to the spectrum, this decay is linear with the immersion length. Therefore, through the two extreme dipping points along the TFBG length, a linear trend relation between the normalised area and the immersion length can be performed. At this point, by substituting the envelope area value obtained during the immersion on the linear dependence and by solving the equation, the immersion length can be calculated. Therefore, the digitally measured immersion lengths attributed to the envelope areas can be corrected with those calculated by using the envelope area and the linear fitting relation. In Fig.3-28, this correction is reported.

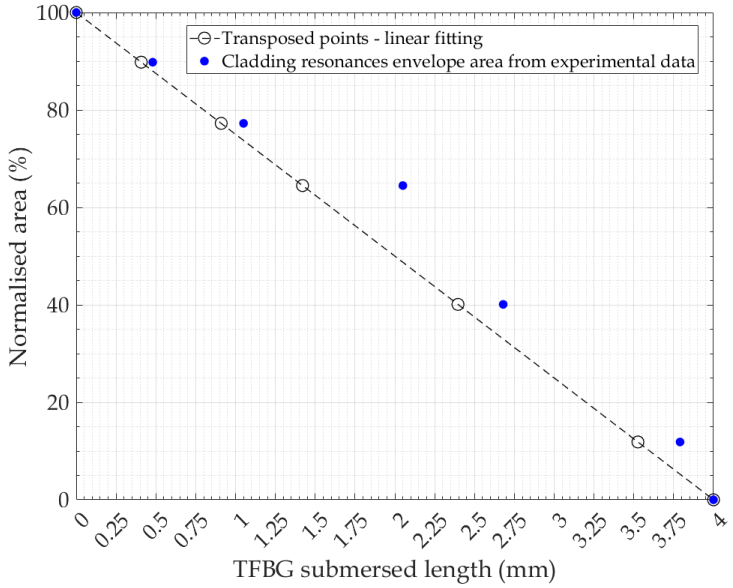


Fig.3-28. Correction of the digitally measured TFBG immersion lengths related to the envelope area values with the linear correlation.

For a better comparison, the immersion length values calculated with both the methods are listed in Table.3-9 in relation to the images of Fig.3-26.

Table.3-9. TFBG immersion lengths estimated digitally and through the envelope areas and linear correlation.

Frame shot		a	b	c	d	e	f	g
TFBG immersion length	Digitally	0	0.48	1.05	2.05	2.61	3.73	≥4
	Envelope area	0	0.408	0.910	1.421	2.396	3.525	≥4

From the values in the table, the digital estimation results are always greater than using the envelope area provided by the TFBG spectrum. The reason is because the digital measurement is performed by observing the flow front of the liquid. However, the flow front does not correspond to the real immersion length as the surface tension forces between the immersed OF and liquid compresses the liquid front in the way to make this one lower than the OF.
The investigation on the experimental data obtained from the progressive immersion of the TFBG sensor, can be concluded by observing the recorded spectra at each submersion length (Fig.3-29).

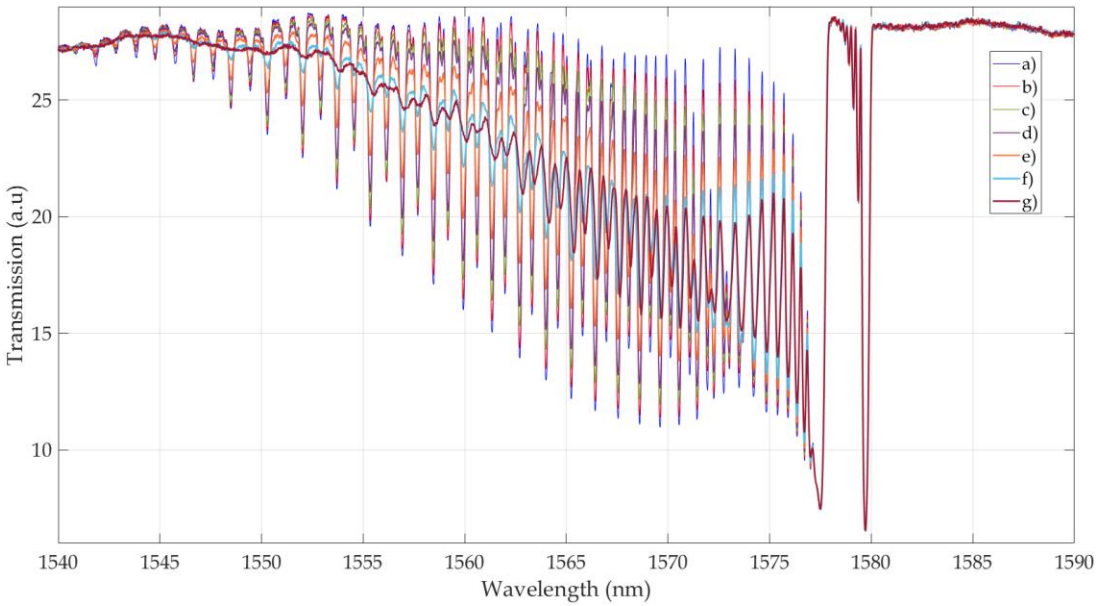


Fig.3-29. TFBG spectra acquired during the gradual TFBG immersion (related to the Fig.3-26 snapshots).

The first observable fact is the change of the upper and lower resonance peak amplitudes along the entire wavelengths window with the increasing of the immersion length. As expected, the Bragg and Ghost peaks do not undergo any changes in amplitude and in wavelength. Therefore, consequently, these results further demonstrate that the coupling mode in the inner OF layer is not influenced by a variation of the external RI around the partial or total length of the TFBG sensor.
A small red shift of the cladding resonance peak wavelengths is observable once the TFBG is fully wetted by the oil, together with the variation of the amplitudes. This behaviour is the base of the wavelength shift demodulation technique [2] introduced in section 3.1. The dynamics of this wavelength variation can be analysed by zooming into a certain upper and lower cladding peaks region of the spectra in Fig.3-29. Therefore, Fig.3-30 is obtained, which shows the evolution of a cladding peak occurring as the liquid flows along the sensor. Specifically, the cladding peak remains substantially at its nominal wavelength (1568.6 nm), but, with the flowing of the oil, it becomes broader, especially on the side of higher wavelengths. Once the TFBG is fully surrounded by the RI liquid, the peak appears completely shifted. This effect may be explained through eq.II.2, which mathematically defines the dependency of the modes from their effective RI during the coupling. When the liquid covers part of the TFBG, the cladding modes still propagating in the OF, have a different effective RI due to the variation of the external one (this is mathematically treated in the three-layers theory mentioned in chapter 2). Hence, their resonance wavelength changes by following eq.II.2, which means that their

contribution to the amplitude is more broadly distributed with respect to when the TFBG is uniformly surrounded.

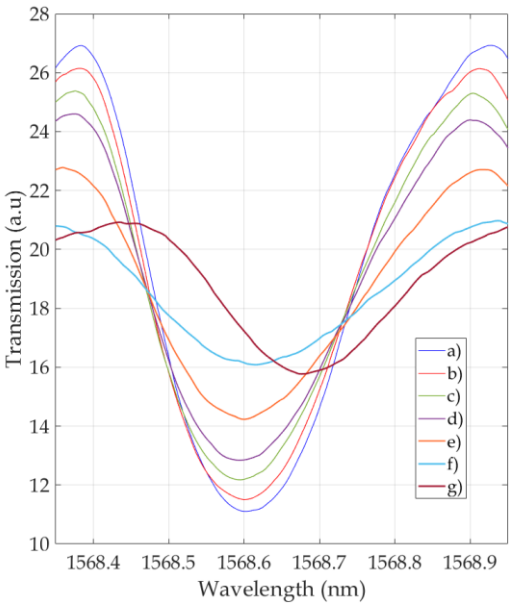


Fig.3-30. Zooming of the TFBG spectra on certain upper and lower cladding resonance peaks.

This dynamic can be further proved by comparing in Fig.3-30 the same peak at the immersion conditions *f* and *g*. In particular, in condition *g* (TFBG fully immersed), the peak is visibly more defined and has a smaller bandwidth with respect to same peak obtained at image *f*. Hence, the complete shifting of the cladding resonance peaks may be used to identify a fully or partial immersion condition of the TFBG sensor.

The D-T can be performed on these spectra to find the envelope areas of cladding resonance peaks, which are shown in Fig.3-31. Since the spectrum associated to the first snapshot has the greatest envelope area, the union of all the underlying areas represents it until the blue. This indicates that the envelope area number two is the overlap of all the areas until the red (removing the blue regions), as well as for each successive area. As expected from the previous descriptions, the reduction of the envelope areas is observable with the immersion of the TFBG, where each subsequent area is gradually contained in the previous ones, so as to create a sort of 'funnel' effect between them.

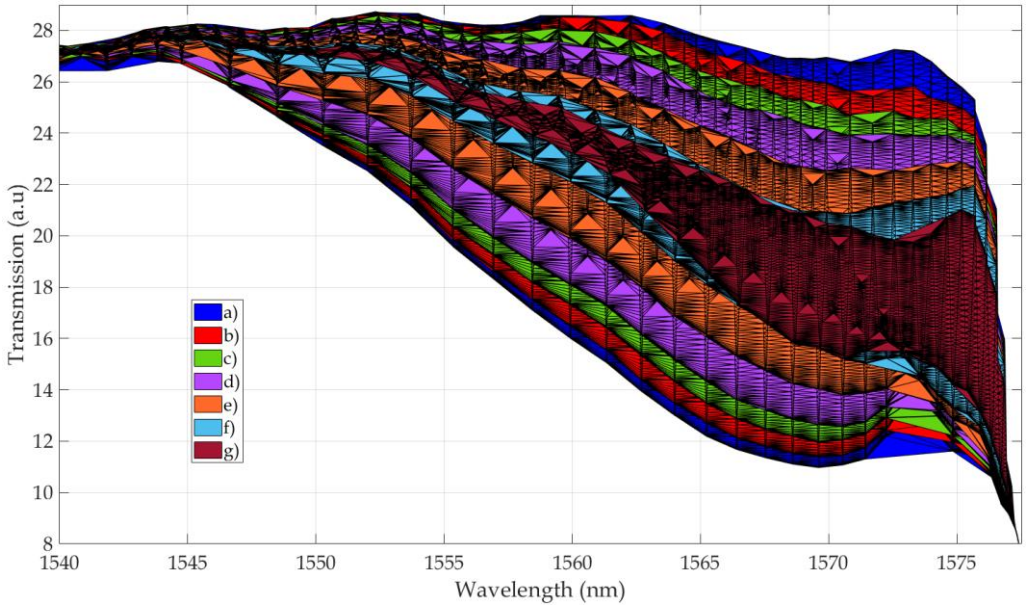


Fig.3-31. D-T envelope areas of the cladding modes resonance peaks of the spectra of Fig.3-29.

3.8 Conclusions

In this chapter a new demodulation technique for tilted FBG sensors has been introduced and demonstrated for refractometric purposes. The development of this approach occurred during the scientific investigation regarding the formulation of an exhaustive response to the second research question. However, considering the benefits of the use of the novel demodulation approach, this latter was exploited, not to analyse the effects of surrounding RI on the cladding resonances (scope of the second research question), but also to verify how the customisation of the TFBG influences the measurement performance which is the aim of the first research question.

In principle, the approach was theoretically defined and based on the use of Delaunay triangulation to obtain the area enclosed between the upper and lower peaks of the cladding resonances in the TFBG transmission spectrum, which are correlated to the surrounding RI. The technique developed is fast and simple to implement, as the triangulation of the set of input data points from the interrogation of the TFBGs is the unique operating step necessary to obtain this area. In this way, the technique does not need the determination of the peaks, the creation of envelope curves and resolution of integrals, or the determination of sensitivity coefficients, saving time and reducing the computational power required. This demodulation technique can be applied for the analysis of a confined part, or for the total length, of the spectrum. Furthermore, since its applicability does not depend on the spectral shape, it can be used for any TFBG customisation, an aspect that allows this novel technique to be used to formulate a response to the first research question about the refractometric measurements. Specifically, a comparison between the correlation curves for TFBGs with standard and thin cladding diameters was performed in order to determine how the cladding thickness affects the refractometric sensing capability of the sensor. Nevertheless, for a complete investigation, also the stability, resolution and accuracy of refractometric measurements were analysed for both the TFBG customisations. Substantially, the analysis of the correlation curves highlighted that the cladding diameter of the OF influences the correlation curves and, hence, the sensing ability and performance of the sensor also when considering the working RI range. This means, the customisation of the TFBG may be a crucial aspect for a well performing and reliable refractometric measurement, even if it regards parameters outside the TFBG sensor such as the cladding diameter.

Initially, the technique was applied substantially to correlate part of the power transmitted by the TFBG with the surrounding RI. Successively, a complete characterisation of the D-T measurement performance was achieved as to better understand its properties and performance. Then, the alteration of the RI measurement performance due to the strain cross-sensitivity was investigated. Specifically, the TFBG was considered as a dual-parameter sensor for simultaneous strain and RI detection. Therefore, a change in the envelope area of the cladding resonance peaks was present due to the applied strain on the TFBG. However, the change of the envelope area was not proportional to the deformation and reached a maximum for lower RI and a particular value of strain due to a special configuration of the peaks in the spectrum. The RI deviation from the unperturbed condition was calculated and corresponded to 0.77% of the RI reference value. However, as previously described, this error includes the strain influence, temperature fluctuation, fitting error and precision of the FBG interrogator device and was calculated in the worst sensitivity range of the TFBG, which represents the worst measurement conditions.

After that, the stability of the measurements and the resolution were widely analysed for several α-values. In certain RI ranges, independently of the α-value and the fitting correlation function, a minimum RI resolution of less than 10^{-7} was achieved. The stability was analysed not only numerically but also by focusing on the higher order cladding resonance peaks, and the reasons for the RI measurement fluctuations were investigated and described.

A last consideration on the Delaunay demodulation technique; the above-described features allow this novel approach to be appropriate also for real-time spectrum monitoring with a moving mesh, and it is besides compatible with other techniques for simultaneous multiple measurements. Furthermore, this technique should be able to operate (in real-time or with data post-processing) even when the spectrum is affected by some disturbances like connector power losses or OF bending due to which the signal could present some ripples.

Once cross-sensitivity, stability, resolution and accuracy of the Delaunay technique were analysed, the investigation continued with the refractometric properties of the TFBG, where the sensor was gradually immersed in the RI oil. This allowed a study of the effects of the surrounding refractive index induced on the cladding resonances and visible in the TFBG transmission spectrum. Therefore, the evolution of the envelope area was observed through correlating the variations with the snapshots of the immersion taken during the experiment. From the area evolution, the real TFBG length wetted by the RI oil was calculated and related to the frames sequence. Therefore, the last section concerned the dynamics of the changes of the spectral signal during the immersion, or on other hand, how the resonance peaks alter in the spectrum due to the gradual immersion in a surrounding media with different RI. Specifically, the sequence of the entire spectrum and a zoomed in view of a certain cladding resonance peak were visualised with the gradual immersion in the oils. This allowed the discovery of the dynamics of the shape and wavelength variation. In particular, based on the wavelength shifting of the cladding peaks, this made it possible to determine independently if the TFBG was fully surrounded by another RI. This result is of considerable importance if the TFBG is applied to monitor the manufacturing and the curing of composite materials during resin transfer moulding (or liquid composite moulding) manufacturing processes. Indeed, in exploiting the TFBG refractometric properties, as described here, it could be possible to measure important parameters, such as: the flow front velocity of the resin during the infusion, the permeability of the reinforcement fibre layers and the detection of eventual voids as well as to evaluate the infusion state of composites.

To conclude, this chapter has provided a better understanding of the TFBG when used as a refractometer sensor and demodulated through the D-T demodulation technique, which improved the RI measurement performance of the entire TFBG sensing system and reports the treatment of how the surrounding RI affects the cladding resonances.

References

[1] L. Fazzi and R.M. Groves, *Demodulation of a tilted fibre Bragg grating transmission signal using a-shape modified Delaunay triangulation*, Measurement, 166, 108197, (2020).

[2] C. Chan, C. Chen, A. Jafari, A. Laronche, D.J. Thomson and J. Albert, *Optical fiber refractometer using narrowband cladding-mode resonance shifts*, Appl. Opt., 46 (7), p. 1142–1149, (2007).

[3] F. Liu, T. Guo, J.G. Liu, X.Y. Zhu, Y. Liu, B.O. Guan and J. Albert, *High-sensitive and temperature-self-calibrated tilted fiber grating biological sensing probe*, Chin. Sci. Bull., 58 (21), p. 2611–2615, (2013).

[4] G. Laffont and P. Ferdinand, *Tilted short-period fibre-Bragg-grating-induced coupling to cladding modes for accurate refractometry*, Meas. Sci. Technol., 12, p. 765–770, (2001).

[5] N.J. Alberto, C.A. Marques, J.L. Pinto and R.N. Nogueira, *Three-parameter optical fiber sensor based on a tilted fiber Bragg grating*, Appl. Opt., 49 (31), p. 6085–6091, (2010).

[6] L.B. Melo, J.M. Rodrigues, A.S. Farinha, C.A. Marques, L. Bilro, N. Alberto, J.P. Tomé and R.N. Nogueira, *Concentration sensor based on a tilted fiber Bragg grating for anions monitoring*, Opt. Fiber Technol., 20, p. 422–427, (2014).

[7] S. Cieszczyk, D. Harasim and P. Kisala, *A novel simple TFBG spectrum demodulation method for RI quantification*, IEEE Photonics Technol. Lett. 29 (24), p. 2264–2267, (2017).

[8] D.T. Lee and A.K. Lin, *Generalized Delaunay triangulation for planar graphs*, Discrete Comput. Geom., 1, p. 201–217, (1986).

[9] L. Fazzi and R.M. Groves, *Refractometric Properties of a TFBG Sensor Demodulated Using a-Shape Modified Delaunay Triangulation*, Optics, 2 (2), p. 113-133, (2021).

[10] J.R. Shewchuk, *Delaunay refinement algorithms for triangular mesh generation*, Computat. Geometry, 22, p. 21–74, (2002).

[11] M. Lamot and B. Zalik, *An overview of triangulation algorithms for simple polygons*, IEEE Intern. Confer. On Inf. Visual., London, UK, 2002.

[12] L.P. Chew, *Constrained Delaunay triangulations*, Algorithmica, 4, p. 97–108, (1989).

[13] H. Edelsbrunner, D.G. Kirkpatrick and R. Seidel, *On the shape of a set points in the plane*, IEEE Trans. Inform. Theory IT-29 (4), (1983).

[14] H. Edelsbrunner and E.P. Mücke, *Three-dimensional alpha shapes*, ACM Trans. Graphics 13 (1), (1994).

[15] Cargille Lab. Available online: https://www.cargille.com/refractive-index-liquids/ (accessed on 5 January 2021).

[16] C. Caucheteur, K. Chah, F. Lhommé, M. Debliquy, D. Lahem, M. Blondel and P. Mégret, *Enhancement of cladding modes couplings in tilted Bragg gratings owing to cladding etching*, Proc. IEEE/LEOS, 8531806, (2005).

[17] C. Caucheteur and P. Megret, *Demodulation technique for weakly tilted fiber Bragg grating refractometer*, IEEE Photon. Technol. Lett., 17 (12), (2005).

[18] https://www.zaber.com/products/linear-actuators/NA/specs?part=NA23C60-T4A (20/03/2022).

[19] S.R. Baker, H.N. Rourke, V. Baker, D. Goodchil, *Thermal Decay of Fiber Bragg Gratings Written in Boron and Germanium Codoped Silica Fiber*, J. Lightwave Technol., 15, p. 1470–1477, (1997).

[20] J. Kumar, G. Singh, M.K. Saxena, O. Prakash, S.K. Dixit, S.V. Nakhe, *Development and Studies on FBG Temperature Sensor for Applications in Nuclear Fuel Cycle Facilities*, IEEE Sens. J., 21, (2022).

[21] T. Gang, F. Liu, M. Hu, J. Albert, *Integrated differential area method for variable sensitivity interrogation of tited fiber bragg grating sensors*, Journal of Lightwave Technology, 37, p. 4531–4536, (2019).

[22] T. Erdogan, *Fiber Grating Spectra*, Journal of Lightwave Technology, 15, p. 1277–1294, (1997).

[23] T. Erdogan, *Cladding-mode resonances in short- and long- period fiber grating filte*, Journal of Optical Society of America 14, p. 1760–1773, (1997).

3

4

Thermomechanical evaluation of a composite plate with an embedded dual-parameter TFBG sensor

"The science of today is the technology of tomorrow."
Albert Einstein

The previous chapters have introduced the TFBG sensor and its theory, and have also described: the importance of TFBG sensor customisation and design before manufacturing, thermomechanical and refractometric calibration of the TFBG sensor, its demodulation techniques and its sensing properties. In summary, the research was motivated by the aim to formulate a response to the first and second research question.
From now on, all these concepts will be exploited to perform real multi-parameter measurements inside materials such as composites and silicones. Therefore, once the sensor is characterised and calibrated, it can be applied to perform reliable evaluations of the internal state of the material in which the sensor is embedded. Specifically, in this chapter, the TFBG is embedded inside a glass-fibre/epoxy composite plate to measure simultaneously and independently the temperature and strain variations induced in the plate by the exposure to heating lamps. During the planning of the research milestone, the argument treated in this chapter, was considered of fundamental importance for the correct development of the experimental steps. Indeed, as anticipated, for the first time in literature, the embedded TFBG sensor simultaneously measures the strain and temperature variations of the material, induced by an external thermal perturbation. The experience obtained from this experiment can be considered a stepping stone for the following chapters and, propaedeutic to the methodology used to carry the next research and response to the third and fourth research questions:

- *How do the several steps of the VARTM process affect the resonance peaks in the transmission signal of the TFBG sensor in combination with the thickness of the composites?*
- *How do the space environmental conditions influence the transmission signal and the sensing abilities of the TFBG sensor even once this is embedded in a space qualified silicone adhesive?*

The success of this research will improve the state-of-art in TFBG sensing technology and will allow the limitations of the current and previous solutions, introduced in section 1.3, to be overcome for simultaneous thermomechanical measurements. The sensorised composite plate was manufactured at the Composite laboratory, TU Delft, and the experimental procedures and set-up were developed and executed at the NDT lab of the Aerospace Structures & Materials department of Delft University of Technology. The research also included the development of a FEM analysis to compare the experimental results with those obtained numerically. The sensorised sample and the experiment were prepared and performed by the TU Delft teamwork. While, the FEA was performed in collaboration

with Stefano Valvano and Andrea Alaimo from the Faculty of Engineering and Architecture of the University of Enna Kore in Sicily. The comparison between the empirical and the FEA results were executed by both the teams. The main part of this chapter has been published in Composite Structures journal [1].

This chapter initially introduces the problem and the technological gap of existing techniques. Then, by exploiting the theory and concepts of the second chapter, the sensorised composite sample and the experimental setup are described. Next, the FEM and experiment are presented in detail and the results are compared and discussed. The TFBG dual-parameter measurements are also compared with the strain obtained by compensating the wavelength shift of the Bragg peak in the TFBG spectrum with the temperature variations detected by an embedded thermocouple close to the OF sensor. This last technique represents a classical approach to uncouple the temperature and strain perturbations in the TFBG signal. The treatment is also focused on the error analysis between the results of the FEA and the measurements with both the techniques.

4.1 Introduction

As introduced in the first chapter (section 1.3), the difficulty of uncoupling easily the temperature and strain perturbations from the signal of a single sensor is a common problem in the SHM technology world. Few sensors are able to provide separate and simultaneous multi-parameter measurements or to self-compensate their measurements from the cross-sensitivity to another parameter. Usually, these solutions use multiple and/or hybrid sensors, so the sensing systems are consequently more complex, expensive and intrusive as the necessary equipment and computational power is larger than with a single sensor. This discussion is valid for any kind of sensor, from strain-gauge to piezo-electric, from magnetic to OF sensors.

Regarding FBGs, the thermomechanical cross-sensitivity has been faced for several years as this drawback is crucial for the monitoring of the health internal state of the composite materials. Specifically, several solutions have been developed during the decades with the aim to overcome this limitation. However, as introduced in section 1.3, the current state-of-art of these technologies is not advanced enough and, sometimes, physically not compatible due to inaccuracy, intrusiveness, non-localised measurements, higher costs, bending cross-sensitivity, hard handling and design complexity. Other drawbacks regard the pre-treatment steps are needed for some external components and the potential of broken of sensors due to embedding. Some of these techniques are the following:

- single OF with double consecutive FBGs [2],
- two consecutive FBGs working at different wavelengths in the same OF [3],
- two FBGs in the same optical fibre, where one is encapsulated in a metallic or plastic capsule [4],
- Fabry-Pérot interferometer in the same OF [5], or
- its hybrid variant called FBG/extrinsic Fabry-Pérot interferometric (FBG/EFPI) technique [6],
- hybrid sensor composed of FBG and Long Period gratings (LPGs) in the same waveguide [7],
- use of thermocouples placed close to the FBG to compensate for temperature effects.

As described in section 2.4.1, a single TFBG can perform the discrimination of the strain and temperature variation through the simultaneous shifting of the wavelengths of two selected peaks (eq.II.26). Therefore, after a preliminary calibration to determine the thermomechanical sensitivity coefficients of the selected peaks, the TFBG can be embedded in composites without another auxiliary sensor. This allows the limitations raised by the use of the other techniques to be overcome while keeping the typical low intrusiveness of the OFs, a simple sensing system and a reduced number of components. As a consequence, the operational costs and computational power are low, there are no time-consuming pre-treatment steps and non-OF components are used. In the past, research has focused on the discrimination of the temperature-strain changes by using the single TFBG sensor [8,9]. However, these works were dedicated to the review of the thermomechanical sensitivity coefficients of

selected peaks. The only literature referring to the embedding of a TFBG in a laminate [10], treats the mutation of the sensitivity coefficients by inducing well-defined mechanical and thermal loading to the composite once the sensor was embedded in the material. Hence, although the theory on the demodulation of the TFBG spectrum to uncouple thermomechanical perturbations is already well known, no proof has been reported as that a single TFBG sensor can effectively measure these parameters in a composite material from an external perturbation. Therefore, this chapter has the aim to prove that a single embedded TFBG is already enough to monitor the internal thermomechanical state of a composite by measuring, at the same time, its temperature and strain variations induced by an external load. In this case the external load is applied through a heat flow from heating lamps. The warming induced in the composite causes simultaneous and a priori unknown variations of strain and temperature, which can be measured via the embedded TFBG.

For a scientific validation of the TFBG measurements, they are compared with the strain obtained by using the classical approach based on the thermal compensation of the Bragg peak wavelength shifting with the temperatures recorded by a K-type thermocouple embedded close to the sensor. Furthermore, a FEA was performed of the partial (only composite) and full FEM (composite + TFBG) cases where the thermal load was modelled by assuming a 3D Gaussian temperature distribution on the top of the plate.

4.2 TFBG sensorised composite plate sample

To achieve the aims described in section 4.1, a glass fibre-epoxy composite plate with an embedded TFBG was heated by infrared heating lamps. The increase of temperature inside the material induces the generation of deformations between the composite layers so that the thermomechanical state of the sample changes. The TFBG sensor has then the task to measure the thermomechanical variations induced by the heating lamps inside the composite so as to evaluate its state. The composite sample selected for this analysis has dimensions 170×75×1 mm with 6 layers of unidirectional (UD) S-glass fibre and Bakelite® Epikote 04908 epoxy + hardener resin system, and was manufactured by using the vacuum assisted resin transfer moulding (VARTM) process. The curing was performed at atmospheric pressure and a temperature of 80°C for 6 hours as suggested by the resin manufacturer. The dimensions of the sample were chosen to function in the test chamber in the experimental setup. The length of the sample was chosen to have a negligible influence on the TFBG coming from the spot bonding points between OF and reinforcement layer applied at the edges during the embedding process of the OF when the sample was manufactured. The sample thickness guaranteed both a good thermal stability during the experiment and ease of manufacture. The embedded OF sensor was a 4 mm long tilted FBG, written in Fibercore PS1250/1500 standard-OF (cladding Ø125 µm) by using the tilted phase mask technique by FORC-Photonics company. The imposed tilt angle was 3° and no coating layer was present for 10 mm across the length of the TFBG. This sensor was placed in the center of the UD composite sample at 0.5 mm height with the OF in the same parallel direction as the fibre reinforcement. This placement design avoided possible bending effects on the sensor caused by a different orientation with respect to the glass fibres. The central location of the TFBG avoids boundary effects in the measurements and it is considered the most affected by the exposure of the heating lamps in the embedding plane. A k-TC (Ø≈0.3 mm) was embedded as close as to the TFBG and in the same plane.

Once the composite was ready and placed on the testing setup, a further three K-type TCs were placed on the top and one on the bottom surface of the composite. All the TCs measurements were used to define the thermal boundary conditions to apply in the FE models. Fig.4-1 provides a schematic view of the sample with its dimensions and sensors.

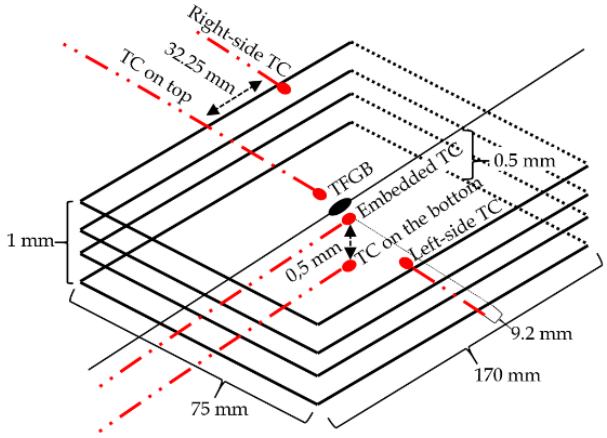


Fig.4-1. Design of the composite sample with the embedded TFBG and placed TCs.

4.3 Finite Element Model and simulation

Two FE models of the tested sample were made: the partial model composed only of the composite plate and the full 3D model where also the embedded OF with the TFBG sensor is present. Stefano Valvano was the lead researcher for the modelling task. The strain values were calculated in both the 3D FEMs by numerical simulation using Abaqus® commercial FEA software. The models were made by considering the composite as an homogeneous material where its thermomechanical properties are obtained from the combined homogenisation of those of the resin and the reinforcement fibres. In the full model, the OF was modelled by considering the dielectric cladding and core layers as a single unique cylindrical material covered by the external coating layer. The numerical simulations were performed by applying a fully coupled thermomechanical analysis. Therefore, the deformations are obtained through a simultaneous solving of the heat transfer and the thermal-stress governing equations with Abaqus®. This can only be achieved by taking into account the thermomechanical properties of the resin, reinforcement fibre, OF and coating at the same time. Hence, the necessary parameters to describe the mechanical behaviour of the elements such as density, Young's and shear modulus and Poisson's ratio are introduced. At the same time, also the parameters which thermally characterise the materials have to be taken such as thermal expansion, conductivity and specific heat coefficient. These properties for the resin and the S-glass reinforcement fibres were provided from their respective manufactures (respectively, [11] and [12]) and are reported in Table.4-1.

Table.4-1. Mechanical and thermal properties of the resin and S-glass reinforcement fibres.

Mechanical properties	**Resin** [11]	**S-glass fibre** [12]
Density (kg· m^{-3})	1150	2490
Young modulus (GPa)	2.9	89
Shear Modulus (GPa)	0.98	37
Poisson's Ratio	0.35	0.22
Thermal properties		
Thermal expansion coefficient (K^{-1})	63.1×10^{-6}	2.85×10^{-6}
Thermal conductivity coefficient (W· K^{-1}· m^{-1})	0.25	1.25
Specific heat coefficient (J· K^{-1} · kg^{-1})	1000	737.5

The first step is the calculation of the thermomechanical properties of the entire composite panel. Since both the fibre reinforcement and resin contributions have to be considered in the homogenisation, the relations of the micro-mechanical theory are applied by starting from the properties indicated by the manufacturer of the resin and glass fibre foil. Therefore, by applying these micro-mechanical relations [13,14] the homogenised composite properties are obtained. These are reported in Table.4-2 with those related to the OF and the acrylate UV-cured coating layer both available in [15].

At this point, since the properties have been obtained, the 3D FEM model of the composite without the OF (called partial-model) was built-up in ABAQUS and meshed with C3D20RT 3D elements with reduced integration and thermo-mechanical capabilities. The reason to use the reduced integration elements for the FEA modelling lies in the fact that, in the case of thin plates, the performance of fully integration elements may occur in a rapidly degeneration during the simulation [16]. Specifically, in FEA simulations, stresses and strains are calculated in integration points of the elements, which are also called Gauss points. Then, the stress, forces and deformations, are successively calculated at the nodes by an averaging technique in order to produce a smooth contour plot between elements that share the same node. Considering that the displacement-based FE formulations over-estimate the stiffness matrix calculated at each integration point, the model would result stiffer than the real one. Therefore, though the solution accuracy may slightly decrease, the application of a lower number of integration points may help, in specific cases as thin plate, to obtain a more reliable real-life model respect with the full integration [17]. The plate model is shown in Fig.4-2a and Fig.4-2b with the boundary conditions applied on the bottom surface and in the corners.
Specifically, each node of the elements in the bottom surface is constrained such that mechanical displacements through the z-direction of the surface are not allowed (w_i=0), which simulates the composite plate resting on a metal support plate during the experiment. Furthermore, since some layers of Kapton®-tape were placed on the corners to hold the composite plate in position, then displacements along these three directions are imposed to be zero (u=v=w=0). While, all the other points of the model are free to move along the three directions as no further constrains are applied on the sample.

Based on the partial model, the full 3D FEM model was made by adding the OF inside the plate (Fig.4-3) and placed along the direction of the glass fibre reinforcement as Fig.4-1 shows. The embedded waveguide is protected by an external coating layer of UV-cured dual-acrylate polymer (Ø≈254 μm). Also in the FEM model, the coating was removed from the OF as in the real TFBG sensor, in this way the thermomechanical perturbations can affect directly the no-recoated dielectric material of the OF as it is in direct contact with the resin (Fig.4-4 and Fig.4-5). The composite material parameters adjacent to the OF are assumed to not vary.

Table.4-2. Mechanical and thermal properties of the materials used in the experiment for the FEA.

Mechanical properties		**Composite** (homogenised)	**OF** [15]	**Coating** [15]
Density (kg· m^{-3})	ϱ	1954	2300	1100
Young modulus (GPa)	E_1	54.56	73.1	3.1
	E_2	13.32		
	E_3			
Shear Modulus (GPa)	G_1	2.356	31.5	1.7
	G_2			
	G_3	3.13		
Poisson's Ratio	υ_{12}	2.72×10^{-1}	0.16	0.36
	υ_{13}			
	υ_{23}	2.584×10^{-6}		
Thermal properties				
Thermal expansion coefficient (K^{-1})	α_1	4.131×10^{-6}	5.5×10^{-7}	7.8×10^{-5}
	α_2	4.131×10^{-5}		
	α_3			
Thermal conductivity coefficient (W· K^{-1}· m^{-1})	$\varkappa_1$	8.5×10^{-1}	1.4	0.189
	$\varkappa_2$	6.679×10^{-1}		
	$\varkappa_3$			
Specific heat coefficient (J· K^{-1} · kg^{-1})	c_v	842.5	703	1360

At the end, the partial model was discretised by using 94064 global elements, with 4 elements through its thickness and, considering the TFBG position (missing in the partial model), 12 elements were

adopted to correspond to the sensor length where the axial deformations were evaluated. Regarding the full model, this was discretised with 300650 elements. Specifically, the section plane (y,z) of the OF was modelled by using 3 elements along it and the coating layer radius. As it can be observed in Fig.4-2, the part in correspondence of the TFBG length was meshed with a denser mesh. In particular, here, the OF section and the composite panel were defined longitudinally (x-direction) with 12 elements from which the axial strains are obtained. While, the remaining sides of the bare OF, in the proximity of the TFBG, were modelled with 4 elements in the same direction.

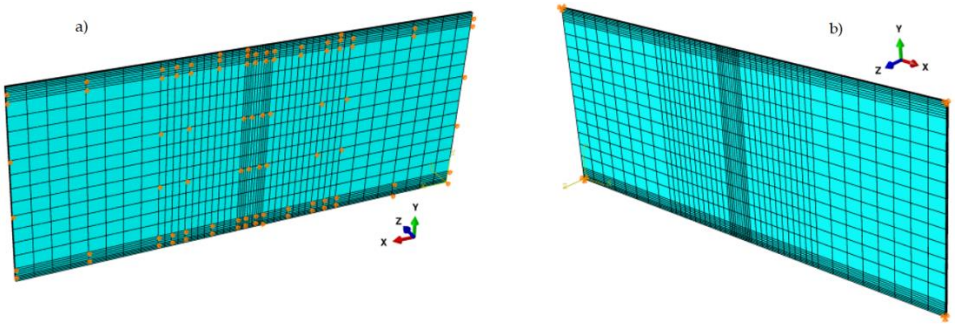


Fig.4-2. Meshed partial model and mechanical boundary conditions on the a) bottom surface and b) corners of the upper surface.

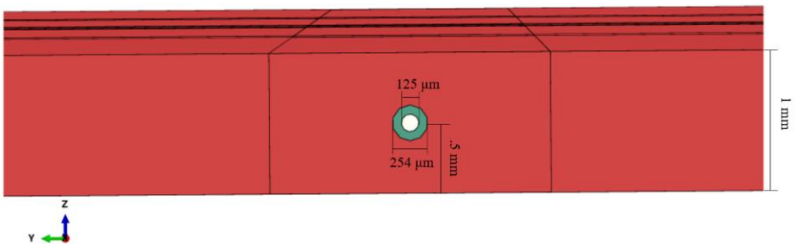


Fig.4-3. Plate section of the full model where the OF (in white) is embedded with the coating layer (in green).

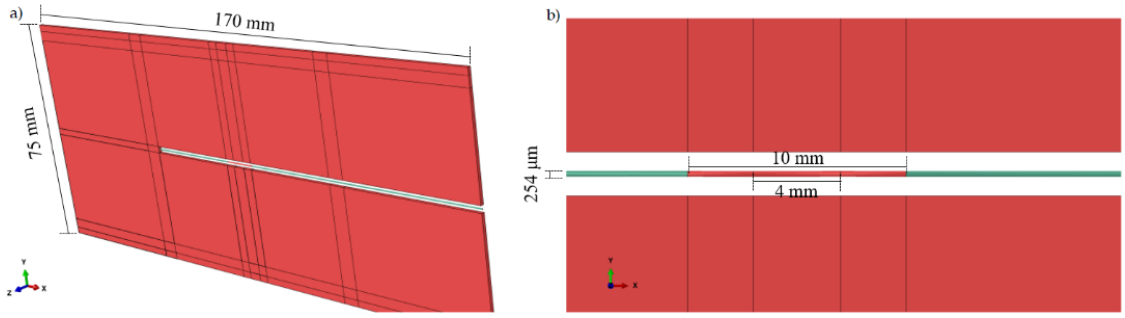


Fig.4-4. Section view of a) the whole plate with the inserted OF with coating and b) zoomed centred region.

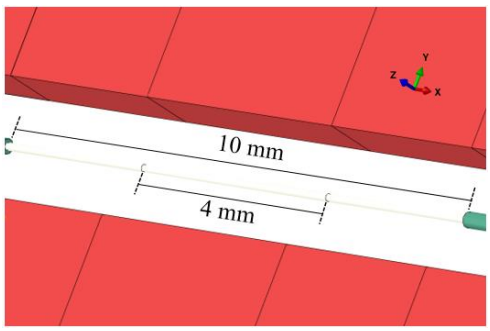


Fig.4-5. No re-coated OF section in the central plate region.

As anticipated in the previous section, the temperatures recorded during the experiment by the TCs placed on top and bottom of the sample and embedded inside, were exploited to define the thermal boundary conditions, which specifically correspond to the temperature profile and thermal gradient through the thickness of both the FEMs. Regarding the temperature profile, though the temperature magnitudes are known every 3 seconds based on the position of the TCs, the spatial distribution of the temperature in the plate is unknown as well as the exposure beam profile of the heating lamps. Therefore, by focusing on the wave nature of the light and taking into account the TCs measurements, the first thermal boundary condition was applied by using a temperature distribution profile on the surface of the modelled plates represented by a Gaussian spatial distribution. This is defined in eq.IV.1 where T_0 is the temperature amplitude obtained from the TCs during each acquisition time:

$$T\left(x,y,z_{top},t\right)=T_0(t)\left(\frac{\Delta T_{max_E}}{\Delta T_{max_C}}\right)+\left(\frac{T_{st}}{\Delta T_{max_C}}\right)e^{-\left(\gamma(x-a/2)^2+2(x-a/2)(y-b/2)+\eta(y-b/2)^2\right)}. \qquad (IV.1)$$

The coordinates x, y and z are the directions along the main axes of the plate and t is the experiment (or exposure) time which can be considered as time increments. While, the coefficients a and b are, respectively, the longer and shorter in-plane dimensions of the sample. The temperature variations ΔT_{max_E} and ΔT_{max_C} are the maximum respectively at the edge and top centre of the plate respect with the temperature of the experiment T_{st}. γ and η are coefficients used to control the shape of the Gaussian profile. Their values were determined through an iteration process which aimed to reach the same temperature values of the Gaussian profile in correspondence of the coordinates of the three TCs on top of the plate. The second boundary condition, which regards the thermal gradient through the sample thickness, is applied by considering the temperatures measured by the TCs embedded inside and on the top and bottom of the plate. Indeed, a negative temperature gradient of 2±0.3°C through the thickness was found when processing the data acquired. Therefore, a 2°C/mm linear temperature gradient was imposed through the thickness of both the 3D FEMs. This could seem to be a weird approach since the thermal properties of the materials are introduced in the models and the temperatures can be calculated in each point of the plate. However, a simple analytical model showed a different trend with respect to those experimentally measured. As treated more deeply in the results section, the explanation of this effect is found by considering the air cooling system of the facility where the experiment was performed. The air vortex effects generated by the fan of the cooling system were not modelled explicitly in the simulations. However, the air flow effect can be implicitly considered by applying the second boundary condition. After applying both thermal conditions, the temperature distribution profile on the upper surface of the FEM composite is shown in Fig.4-6 for the maximum temperature variation which is achieved during the entire test.

From eq.IV.1 the Gaussian profile distribution is dependent from the time t, hence, this evolves starting from the beginning of the experiment at t=0 as the temperature T_0 changes with the time increments during the exposure. The temperature profile evolves also through the thickness due to the second thermal boundary condition. Specifically, it has the same distribution but following a negative gradient of 2°C/mm. The thermal conditions were the last modelling steps. After these, the FEM simulations were solved by using the coupled steady-state thermomechanical analysis at each time increment defined by the TCs acquisition time.

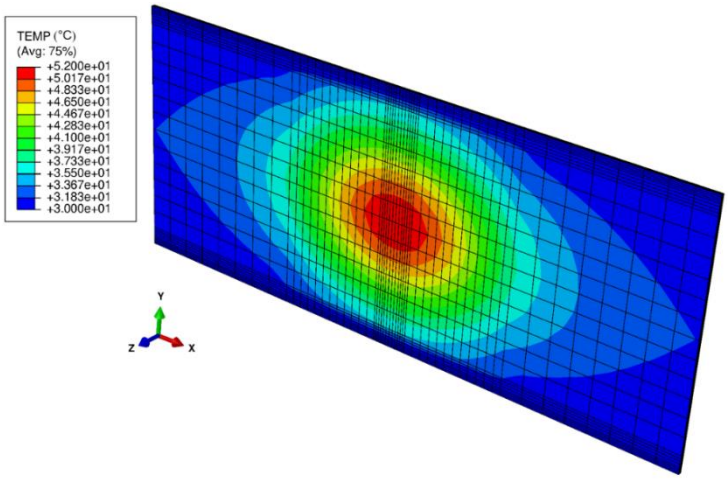


Fig.4-6. Distribution of the temperature on the top surface of the FEM composite at the maximum temperature variation.

4.4 Experiment

The TFBG embedded in the composite panel, was thermomechanically calibrated in a preliminary way as described in chapter 2. Obviously, since the one main scope of the entire chapter research is to demonstrate the performance of the TFBG as a three-parameter sensor, the selected peaks used for simultaneous and separate thermomechanical measurements are the Bragg and the Ghost peak. For the sensor used here, the nominal strain sensitivity coefficient for the Bragg peak is 1.255±0.004 pm/με and for the Ghost resonance 1.255±0.006 pm/με. The linear slopes from which the coefficients are determined have a R^2 of 0.999962 and 0.999968 respectively. From the slope of the thermal calibration, the determined thermal coefficients are 9.114±0.007 pm/°C and 9.6±0.01 pm/°C respectively for the Bragg and Ghost peak, with a respective R^2 of the slope of 0.99888 and 0.99809. The temperature resolution is then $TR \approx 8.23$°C (eq. II.31) by using the same interrogation system. The characterised TFBG was embedded in the composite. After the manufacturing process, the sensorised sample was placed on a metallic plate with threaded holes, then the remaining TCs were mounted on the top and bottom surface as Fig.4-1 shows. The accuracy of the TCs is ±1°C. Specifically, Fig.4-7 shows a view of the top surface where a TC is taped with some Kapton® tape close to the central position of the sample, while the other two TCs were screwed to the side of the sample. The metallic plate with the placed composite sample was sealed inside a test chamber, where it is exposed to light from 2 heating lamps (max 2×1000 W). As anticipated, the chamber is provided with an air cooling system arranged through a fan that introduces fresh air into the cylindrical duct to avoid overheating of the experimental setup components. The airflow propagates through the entire case and streams out through a special duct. A schematic of this setup can be observed in Fig.4-8. The OF enters and exits the test chamber through special holes. Its ends were connected to an optical circulator and, hence, to the same interrogator system, which via a dedicated LabView program, was arranged to acquire the TFBG spectra automatically during the experimental tests.

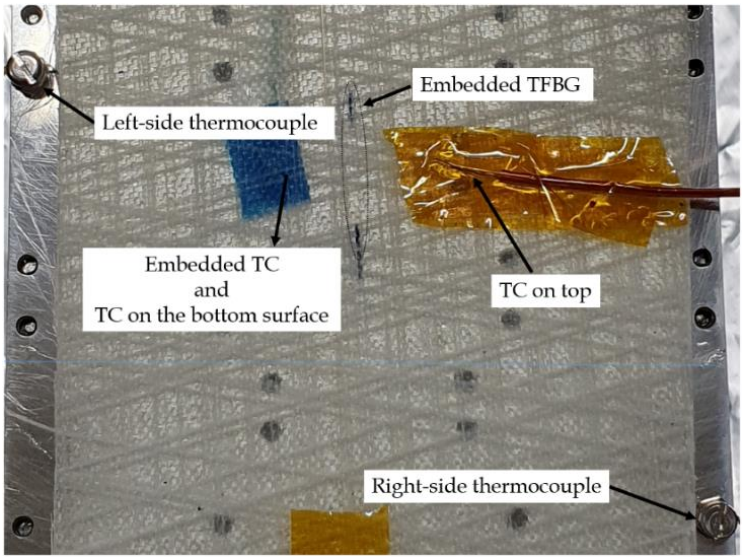


Fig.4-7. Zoomed on the top area of the sample on the metallic plate with all the sensors positions marked.

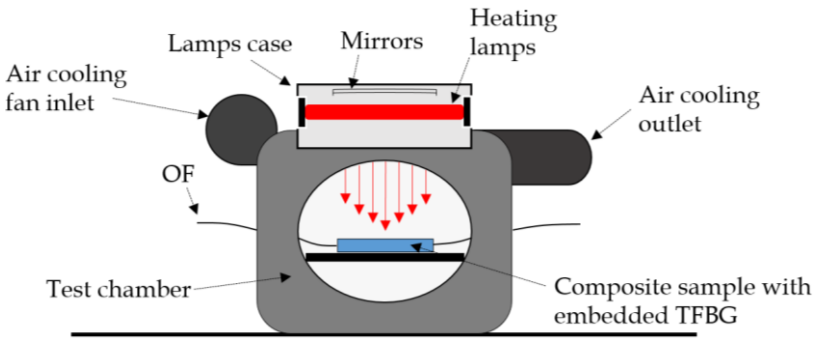


Fig.4-8. Schematic of the experimental setup used to perform the exposure on the composite sample.

4.5 Strain-Temperature measurements: TFBG and classical approach comparison

Once the exposure was performed and the TFBG spectra and TCs readings acquired, the strain and the temperature variations of the composite material can be obtained by applying the demodulation technique already presented (section 2.4.1). In this section, measurements are obtained for the TFBG used as single dual-parameter sensor and as strain-gauge OF sensor compensated with the readings of the embedded TC.

A dedicated algorithm was developed to identify the Bragg and the Ghost peaks in the TFBG spectra, by exploiting their lower marked amplitudes compared to the other peaks. Once these are separated, their corresponding wavelengths can easily be obtained. This process was then applied to each spectrum recorded during the test. Therefore, the wavelength variations of the selected peaks $\Delta\lambda_{Bragg}$ and $\Delta\lambda_{Ghost}$ can be easily calculated between any two spectra recorded during the acquisition time. Here, the starting point is considered to be the switching-on of the heating lamps, which corresponds in the graphs to zero time (t=0). As a consequence, $\Delta\varepsilon$ and ΔT have to be considered as variations in the material with respect the initial condition at t=0. Hence, by recalling the demodulation technique based on the sensitivity matrix **K** and written in eq.II.28, the variations are obtained through the product between $\mathbf{K}^{-1}$ and the vector of the wavelength shifts. In this way, it is possible to calculate $\Delta\varepsilon$ and ΔT between any two different times during the experiment. The strains are evaluated along the axis of the OF across the TFBG length. Since this is the *x*-direction, the deformation is indicated with ε_{xx}.
First of all, since $\Delta\varepsilon$ and ΔT are obtained from $\Delta\lambda_{Bragg}$ and $\Delta\lambda_{Ghost}$ readings caused by the heating lamps, the trends of their wavelength shifts are shown in Fig.4-9 along with the exposure time. The graph starts from t=60 min which corresponds at the end of the heating up phase. As expected, the $\Delta\lambda_{Ghost}$ value is greater than the one of the Bragg peak as its temperature sensitivity coefficient is larger.

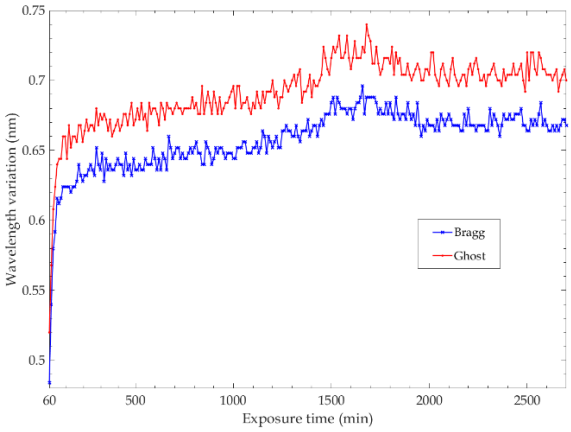


Fig.4-9. Trend of $\Delta\lambda_{Bragg}$ and $\Delta\lambda_{Ghost}$ along the exposure time.

After ~60 minutes, the heating up phase of the sample with the lamps is over and small temperature changes can be detected by the TCs. However, as the TFBG sensing system has a *TR*≈8.23°C, the OF sensor is not able to detect these small temperature fluctuations. Therefore, in these cases, the strain state is determined in isothermal conditions, which in consequence means that the strain evaluation may be over- or under-estimated. For this reason, the TFBG measurements were verified by comparing them with those performed by compensating the Bragg wavelength variation induced by the temperature change through the embedded TC records. This last method represents the classical approach where the TFBG is used as standard strain-gauge FBG compensated with a TC. Therefore, the measurements of the variations of temperature and strain obtained with both the methods are shown in Fig.4.10. Substantially, the comparison between the strain trends reach a better match when the temperature curves are close. This fact is demonstrated by observing Fig.4-11 where the percentage deviation of the strain values is reported after the heating-up step. At the beginning a larger deviation is present when the temperature curves are separated enough. Then, the percentage goes down with the approach of the TC measurement to that of the TFBG. A minimum deviation of 0.098% is measured at the 1240th minute (indicated by the vertical blue dashed line) as at this time the temperature curves intersect with each other. While, between the ~1500th and ~1800th minute, the TC records oscillations of the temperature, and the strain curves move away from each other with an increasing deviation. The last part of the graphs confirms the proportionality between the deviation and the temperature curves. The difference between the strain values obtained by both the methods is due to the temperature resolution of the TFBG sensing system (*TR*). In fact, temperature variations smaller than TR are not visible to the TFBG by using the demodulation technique represented by eq.II.28. As a consequence, the wavelength variations of the selected peaks caused by temperature changes smaller than TR, are mathematically assumed by the algorithm to be strain variations. Hence, the calculation could return an over- or under-evaluated strain state based on the TR and the temperature. Focusing on Fig.4-10, the TFBG strain values result then under-estimated until ~1200 min as the isothermal calculation is performed with a temperature higher than the more accurate one measured through the embedded TC. While, in the interval between ~1500 and ~1800 min, the TC temperature is greater than the one measured with the TFBG. Consequently, the strain values indicated by the TFBG are over-evaluated. In the other intervals time, the strain curves can be considered almost coincident with a deviation below 3%.

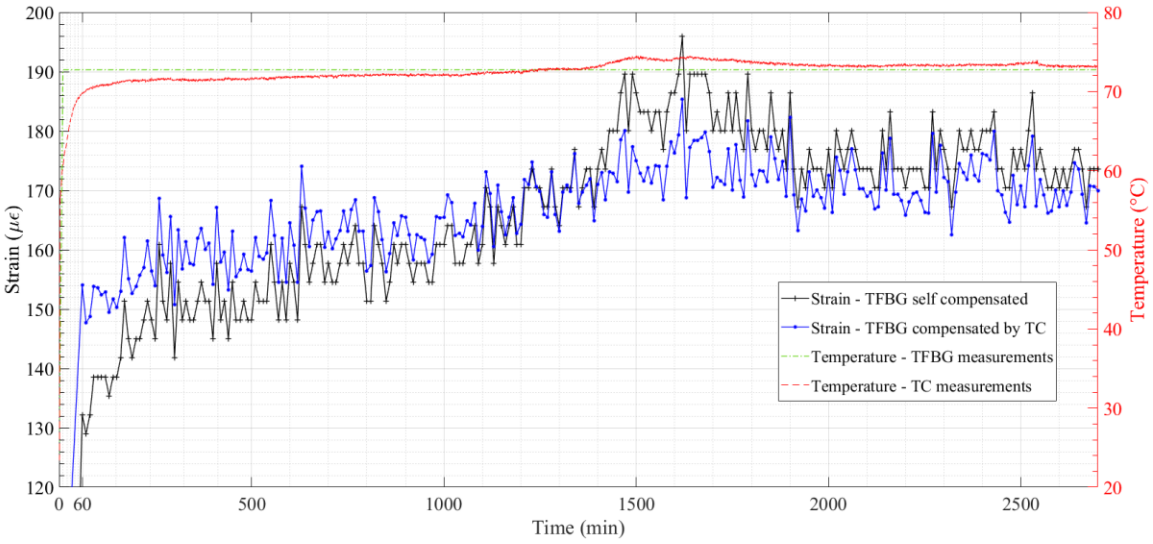


Fig.4-10. Strain and temperature trends obtained for self-compensated TFBG (dual-parameter sensor) and classical approach.

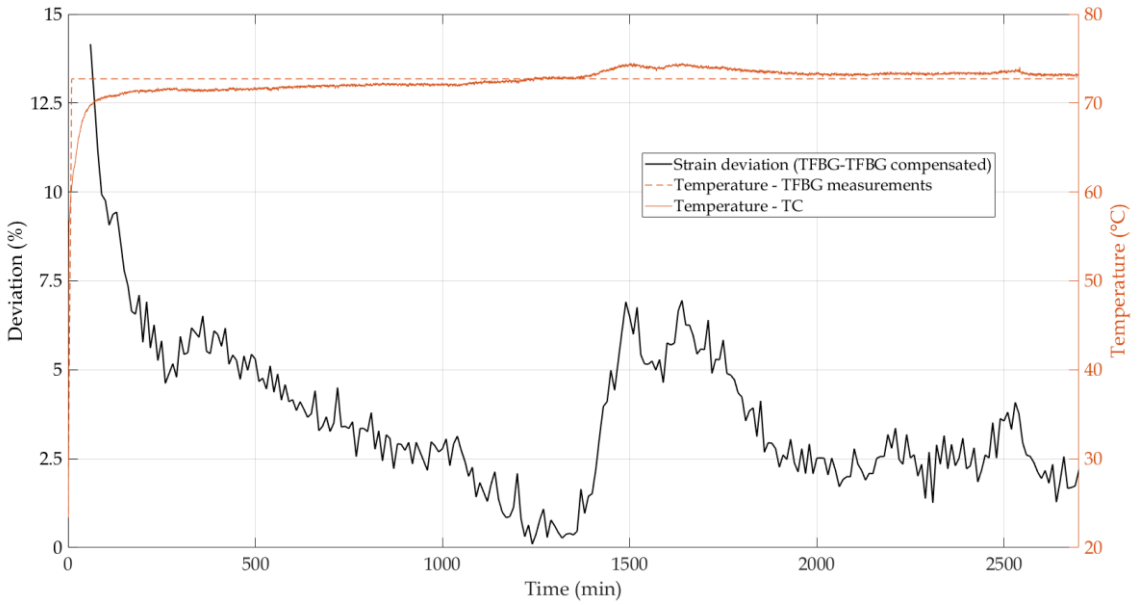


Fig.4-11. Deviation between the strain measured with both the approaches.

4.6 FEA results and comparison with experimental measures

In this section, a comparison between the experimental results and the strain trends from the FEM simulations of the partial and full 3D models is performed. The axial strain ε_{xx} is calculated along the modelled OF axis across the TFBG length. In the case of the partial model, since the OF is not included, ε_{xx} are considered along the same length and position of the TFBG as if the OF was embedded. In Fig.4-12, the strains extracted from the simulation of the partial FEM are reported and compared with those of the self-compensated TFBG. At the beginning of the graph, in correspondence of the temperature rise of the composite due to the heating lamps, a substantial difference can be observed between the reported curves, then they tend to be more similar starting from the 1200th minute.

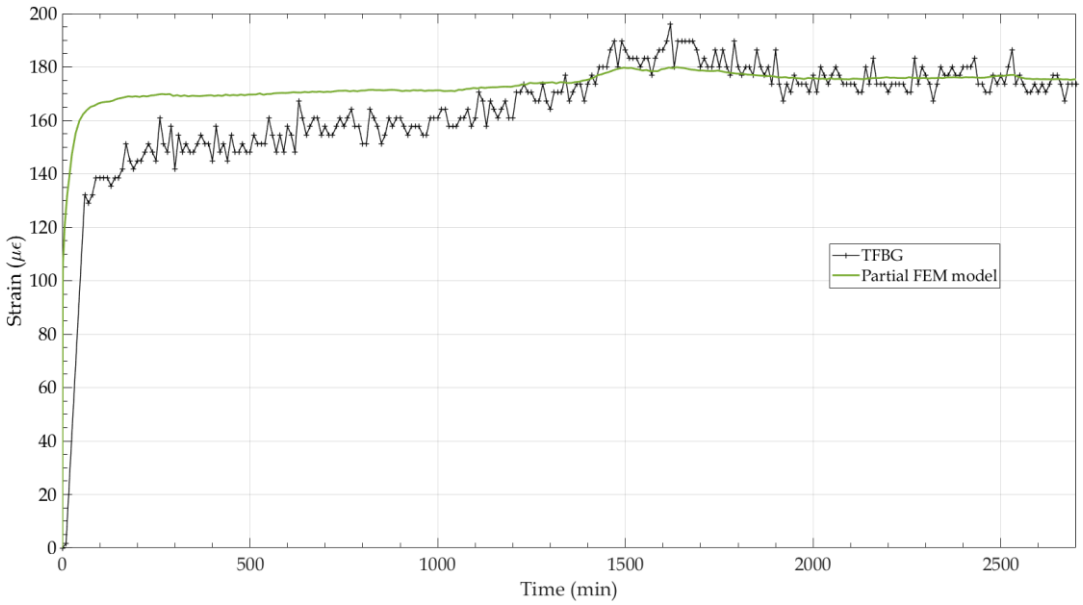


Fig.4-12. Strain comparison between dual-parameter TFBG sensor and FEA of the partial FEM.

However, missing the modelling of the OF in the partial model can slightly influence the local behaviour of the material as demonstrated from the simulation performed on the full 3D FEM. Indeed, the latter includes the embedded OF with the protective coating layer (except across the length of the

TFBG where it is removed). A comparison between the ε_{xx} experimentally measured and those from the FEA results of the FEMs is reported in Fig.4-13.

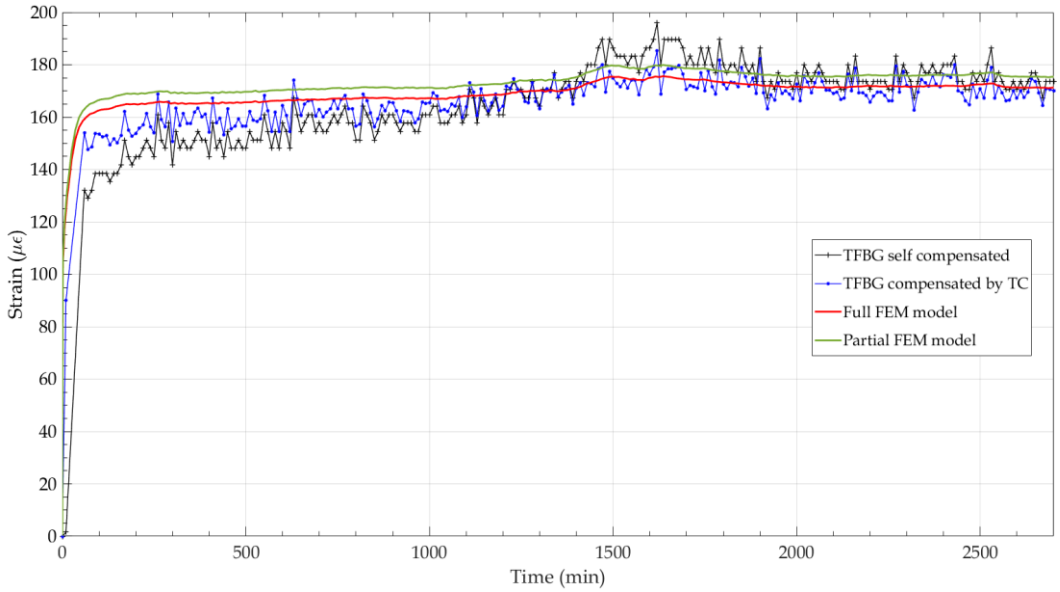


Fig.4-13. Comparison between the numerical and experimental results.

Regarding the calculation error of the numerical simulations, the strain values obtained from the FEAs and reported in Fig.4-13 were compared with those of the same FEMs simulations but discretised by a mesh with 50% of the elements. A strain difference lower than 0.5% was obtained for each time increment. Hence, since the here considered strain values are obtained from FEMs discretised by a higher number of mesh elements, the error was considered negligible.

The strain curves obtained from the two models are visibly different. Specifically, the curve of the full FEM model is lower with respect with to that of the partial FEM. This result is due to the higher stiffness of the full model as consequence of the presence of the embedded OF. Therefore, it has a higher Young's and shear modulus that only the composite plate. For this reason, after the initial heating-up phase, the two curves have the same trend but are constantly separated by ~6με (~3%). This fact proves that the embedding of the OF does not influence negatively the mechanical performance of the composite but, rather, this should be always modelled in the FEM to obtain the correct results from the numerical simulations. The full FEM, being stiffer than the partial one, shows a strain trend closer to the TFBG measurements, especially if the TFBG is compensated by the TC.

4.6.1 Error analysis

The deviation between the experimental and simulation results can be quantified through the percentage error of the FEM models curves with respect the TFBG strain measurements. These are calculated starting from when the heating step is considered over, which corresponds to the 60th minute. Fig.14a and Fig.14b show these deviations, respectively, in the case of comparison with the self-compensated TFBG and the TFBG compensated with TC measurements. As expected from the strain trends shown in Fig.4-13, the lowest strain error trend is obtained when comparing the results of the full 3D FEM simulation with the strain experimentally measured with the classical approach. While, the deviations are slightly higher in the case of comparison with the measurements of the single TFBG. Moreover, at the time interval starting from 1320th minute of Fig.4-14a, the partial model curve reaches lower error percentages than the full model one. This is an unexpected behaviour that could be misleading. In fact, by observing in the graph of Fig.4-13, the increase in the single TFBG measurements (black curve) for the effect of a positive temperature variation at 1320th minute, this is measuring strain values closer to those obtained from the partial model simulation respect with the full model one. This is an inconvenience linked to the *TR* value of the TFBG sensing system. Indeed, since

temperature variations (between any two temporal points) smaller than the *TR* are not counted in the strain calculation by using the demodulation technique represented by eq.II.28, the contribution to the wavelength shifting of the peak is solved as a strain perturbation. For this reason, as anticipated from the comparison between the self-compensated TFBG and the classical approach, the strain trend measured by the single TFBG deviates upwards from the full model and TFBG compensated curves.

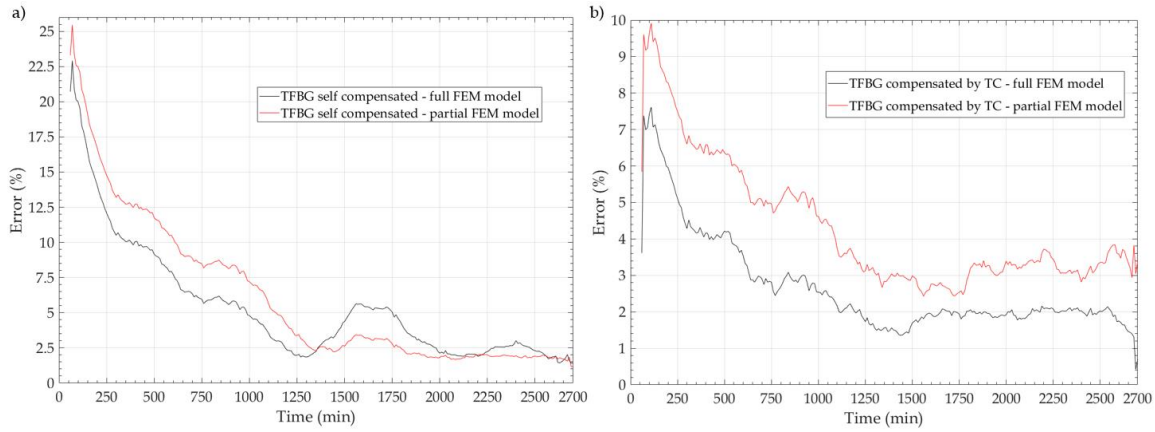


Fig.4-14. Strain error comparison between the full and partial FEM models respect with the TFBG measurements performed as: a) single dual-parameter and b) external temperature compensated sensor.

This once again underlines the importance of reducing the TR value of the TFBG sensing system, and hence, to adopt an FBG interrogator device with a finer *swR* or a particular customisation of the TFBG sensor that increases the difference between the temperature sensitivity coefficients of the selected peaks. These modifications would allow a finer measure of the temperature variation respect with the selected peaks of the TFBG spectra. Consequently, the obtained mechanical response would be more accurate when using the single TFBG as a dual-parameter OF sensor without the compensation of a further sensor. As a last consideration, when considering the error of the FEA full model result with respect to the TFBG measurements in Fig.4-14a and Fig.4-14b, the average deviation along the exposure time is ~5.3% and ~2.7% respectively in the case of single dual-parameter and TC compensated TFBG sensor. Translating these percentages into strain values by considering the maximum deformation obtained from both the TFBG measuring techniques, gives deviations of ~10 με and ~5 με.

4.7 Discussion and conclusions

Some final considerations can be observed by considering the experimental measurements, the simulation results, the spatial distribution of the temperature in the FEAs and the experimental setup. For the comparison between the sensing techniques, the main reason for the difference between the strains obtained with the TFBG as a single dual-parameter sensor and compensated by the TC, was identified as the TFBG thermal resolution (*TR*). This drawback can be overcome by considering an interrogation system with a smaller scanning wavelength step (*swR*) or TFBGs with a special customisation of the Bragg grating structure that can to increase the difference between the thermal sensitivity coefficients (k_{T_i}) of the two selected peaks. A smoother temperature resolution capacity of the TFBG may allow a more accurate thermomechanical separation by removing the need to assume isothermal conditions. However, despite the *TR* limitations achieved, here the maximum strain difference or deviation between the strain (blue and black) curves obtained in Fig.4-10, after the heating-up of the lamps (which is a critical phase), corresponds at ~14.2% (~22 με) at 60 min, while the average strain deviation of all the measurements is 3.4% (~5 με). Therefore, after this comparison, the TFBG used as single dual-parameter OF sensor appears to be a valid tool for embedded sensing of strain and temperature, though its accuracy can be improved decreasing the *TR* value.

Regarding the achieved results from the numerical simulations and their comparison with the experimental results, it seems that the Gaussian spatial temperature distribution assumed in the FEMs properly simulate the thermal conditions of the plate during the heating, but only after the initial warming-up phase. Several factors have to be taken into account as possible physical explanations for this initial deviation. At the beginning, the temperature distribution is different from the assumed profile as the heat generated by the lamps on the composite is partially conducted from the sample to the metallic test plate on which it is placed. Furthermore, each lamp needs a certain time after the switching-on (sometimes even hours, depending from the power level and environmental test conditions) to give stable irradiation power. This lag is not the same and homogeneous among the lights, hence the full operational condition is reached differently for each lamp. This certainly influences the initial spatial distribution of the temperature on the sample. Moreover, also the air cooling system strongly influences the temperature profile as it increases the dissipation of the heat from the composite to the environmental elements (air, metallic test plate and walls). Specifically, as briefly previously introduced, the air cooling system is composed by an external fan that aspirates the air at room temperature and accelerates it in the test chamber. After the interaction with the several elements of the experimental setup, the air is extracted through a special duct. Hence, the air cooling effect is not uniform on the surface of the composite as the air vortex has its own thermal and kinematic conditions from the ingress to the outlet of the chamber. The here performed FEM models do not take into account all of these phenomena, however, the imposed temperature profile is not perturbed or modified during the simulation time. As consequence, the assumed temperature profile distribution in the FEM models may differ from the real one during the exposure time, especially during the delicate heating-up phase. A further consequence of this high heat dissipation concerns the temperature gradient inside the composite plate. In fact, a preliminary comparison between the simulated temperatures (obtained through the thermal properties of the material) and the TC measurements on top, middle and bottom of the composite sample, show a substantial difference. In this case, this effect has been considered in the simulations by imposing a second boundary condition to the FEMs. This was a thermal gradient through the thickness obtained from the TCs temperatures. Although the previously described factors influence the effectiveness of the assumed Gaussian spatial temperature distribution in the FEAs, as Fig.4-14a and Fig.4-14b summarize, the average deviation (or strain error) between the experimental TFBG measurements and the full 3D model is small enough to have a good match for the greater part of the exposure time. As expected from these issues, higher strain errors are detected at the beginning of the exposure in correspondence of the warming-up phase. Moreover, the FEMs were simulated in steady-state analysis, which could be another possible cause of the difference between the numerical and experimental results. Due to the high temperature gradient during the short heating-up phase, a transient analysis may be more appropriate to simulate the model until the 60th minute. However, this interval is very short compared with the total exposure time, hence, unless the transient interval is relevant, the same kind of analysis is not convenient to simulate in the FEM model. In conclusion, a single TFBG sensor embedded in a glass fibre/epoxy composite plate, has been demonstrated to be able to measure simultaneously and separately temperature and strain during exposure to heating lamps. A comparison with the strain variations obtained from the TFBG used as a single self-compensated sensor and an FBG compensated by an embedded TC, show a good match, especially after the warming-up phase. However, this comparison highlights a drawback of the TFBG when used as single dual-parameter OF sensor which is the strong influence of the temperature sensitivity coefficients on its selected peaks, which define the temperature resolution of the measuring system. The *TR* can be improved with some methods already cited, but among these, the use of a higher resolution interrogator system is an easier and more suitable, albeit expensive, strategy.

The numerical simulations demonstrated that they are able to provide the same trends as the TFBG measurements after the warming-up phase. The strain trend of the full FEM model appears to overlap well the strain values measured with the single TFBG sensor (average deviation ~ 5.3%), though, as

the error analysis shown, it returns a lower error when compared with the TFBG compensated measurements (average deviation ~ 2.7%). However, as widely discussed above, the assumed temperature profile used for the simulation is not appropriate during the first phase of the experiment. A comparison of the simulation results of the partial and full FEM with the TFBG measurements proves the low intrusiveness of the sensor and that it does not influence the mechanical performance of the composite. However, as the results demonstrate, it is recommended to model the OF in the FEM composite model to improve the accuracy.

The dual-parameter TFBG technique is specifically useful for dual-parameter measurements in applications where low intrusiveness is required and/or a minimum number of sensors should be used. A suitable example is the TFBG embedding through the thickness of thick composites to monitor their state during the manufacturing process. This allows the strain and temperature level in several points of the thick composites to be obtained without affecting their mechanical performance.

The experience and results achieved in this chapter are exploited and applied in the next chapters, where a further development and improvement of this technique is treated. Specifically, they regard the integration of this technique and simultaneous running with the surrounding RI measurement. As successively demonstrated, the three-parameter measurements allow not only the thermomechanical state of the material surrounding the TFBG to be detected, but also its chemical changes. This is particularly useful for monitoring of: the state of the thermoset composites during their manufacturing and curing process, and the silicone health state during exposure to a simulated space environment.

References

[1] L.Fazzi, S. Valvano, A. Alaimo and R.M. Groves, *A simultaneous dual-parameter optical fibre single sensor embedded in a glass fibre/epoxy composite*, Composite Structures, 270, 114087 (2021).

[2] P.M. Cavaleiro, F.M. Araujo, L.A. Ferreira, J.L. Santos, and F. Farahi, *Simultaneous Measurement of Strain and Temperature Using Bragg Gratings Written in Germanosilicate and Boron-Codoped Germanosilicate Fibers*, IEEE Photonics Technology Letters, 11 (12), (1999).

[3] X. Shu, Y. Liu, D. Zhao, B. Gwandu, F. Floreani, L. Zhang, and I. Bennion, *Dependence of temperature and strain coefficients on fiber grating type and its application to simultaneous temperature and strain measurement*, Optics Letters, 27 (9), (2002).

[4] R. Montanini and L. D'Acquisto, *Simultaneous measurement of temperature and strain in glass fibre/epoxy composites by embedded fibre optic sensors: I. Cure monitoring*, Smart Materials and Structures, 16, p. 1718-1726, (2007).

[5] R. de Olivera, C.A. Ramos and A.T. Marques, *Health monitoring of composite laminates using fibre optic sensors*, Smart Materials and Structures, 86 (3-5), p. 340-346, (2008).

[6] H.K. Kang, D.H. Kang, C.S. Hong and C.G. Kim, *Simultaneous monitoring of strain and temperature during and after cure of unsymmetric composite laminate using fibre-optic sensors*, Smart Materials and Structures, 12(1), p. 29-35, (2003).

[7] H.J. Patrick, G.M. Williams, A.D. Kersey, J.R. Pedrazzani and A.M. Vengsarkar, *Hybrid fibre Bragg grating/long period fibre grating sensor for strain/temperature discrimination,* Photonics Technology Letters, 8(9), p. 1223-1225, (1996).

[8] E. Chehura, S.W. James and R.P Tatam, *Temperature and strain discrimination using a single tilted fibre Bragg grating*, Opt. Commun., 275, p. 344–7, (2007).

[9] B. Dong, J. Hao, C. Liaw, B. Lin and S.C. Tjin, *Simultaneous strain and temperature measurement using a compact photonic crystal fiber inter-modal interferometer and a fiber Bragg grating*, Applied Optics, 49 (32), p. 6232–5, (2010).

[10] D. Kinet, D. Garray, P. Mégret, C. Caucheteur, *Temperature and strain effects discrimination inside composite materials with embedded weakly tilted fibre Bragg grating*, Proceedings of SPIE, 87942R1 – 6, (2013).

[11] Hexion technical information. https://www.swiss-composite.ch/pdf/t-Hexion-Harz-EPR04908.pdf; (last access 22/02/2021).

[12] AZOMaterials. https://www.azom.com/properties.aspx ArticleID=769; (last access 22/02/2021).

[13] C.C. Chamis, *Mechanics of composite materials: past, present and future*, J. Compos. Technol. Res., 11, p. 3–14, (1989).

[14] G. Struzziero, D. Nardi, J. Sinke, J.J.E. Teuwen, *Cure-induced residual stresses for warpage reduction in thermoset laminates*, J. Compos. Mat., 54 (22), p. 3055–3065, (2020).

[15] Fibercore technical information. https://fibercore.humaneticsgroup.com/products/photosensitive fiber/boron-doped-photosensitive-fiber/ps12501500; (last access 22/02/2021).

[16] E. Pugh, E. Hinton, O. Zienkiewicz, *A study of quadrilateral plate bending elements with reduced integration*, International Journal of Numerical Methods in Engineering, 12, 1059–1079, (1978).

[17] T.J.R. Hughes, M. Cohen, M. Horaun, *Reduced and selective integration techniques in the finite element methods*, Nucl. Eng. Des., 46, 203–222, (1978).

4

5

Monitoring of the composite manufacturing process with three-parameter TFBG sensors

"Science is but a perversion of itself unless it has as its ultimate goal the betterment of humanity."
Nikola Tesla

The previously presented treatment was focused on the demonstration of the TFBG sensing capabilities as a dual-parameter OF sensor to monitor the thermomechanical state of a thermally loaded composite. This was to simulate an operational situation which is typically occurs in the application of composite structures.

From now on, the unique TFBG sensing abilities and features are fully exploited by adding a refractometric evaluation to the already treated thermomechanical measurements, when the sensor is embedded in a composite. Specifically, here, the problem of monitoring of the quality of the composite manufacturing process is faced with the help of the three-parameter TFBG sensor.
The aim of this study is to demonstrate the correlation between the parameters measured by the OF sensor and the thermomechanical and curing state of the processed composite. In particular, that the TFBG can simultaneously measure the strain-temperature during several steps of the manufacturing process to inform the user on the internal stress/deformation state and eventual shrinkage generated due to the resin curing. This is of great importance to avoid overheating or insufficient curing temperatures and to forecast unexpected mechanical behaviour caused by residual/unpredicted stress and shrinkage [1]. These phenomena can also influence the dimensional stability of the composite once it is extracted from the mould. At the same time, the refractometric sensitivity of the TFBG allows it to evaluate the resin RI evolution during the manufacturing. In particular, two interesting aspects can be monitored. The first is the flow of the resin during the infusion step between the reinforcement layers when the composite is manufactured with processes based on RTM or resin injection moulding. The second is that through the refractometric abilities and properties of the TFBG, the acquired spectra allow, a check on if some internal locations in the composite could suffer from poor resin impregnation. Furthermore, the infusion times can be observed by considering the decay of the peaks amplitudes. The second aspect is really important for high manufacturing quality and to guarantee the composite's best mechanical performance. It regards the degree of cure of the resin during the processing of the composite. In this context, the RI measurements of the TFBG can be associated to the degree of cure so that the measures can be observed to evaluate the state of cure of the composite.

The above cited arguments and the related research are motivated to the formulation of a response for the fourth research question, which is the following:

- *How do the several steps of the VARTM process affect the resonance peaks in the transmission signal of the TFBG sensor in combination with the thickness of the composites?*

First of all in this chapter, these tasks are demonstrated for a single TFBG sensor embedded in a thin glass fibre/epoxy resin composite sample and manufacturing via VARTM process. Specifically, the aim

here is to demonstrate that the embedded sensor can perform reliable thermo-mechanical-refractometric measurements to evaluate the general state and quality of the composite at each processing step. In this way, each single TFBG may provide a complete sensing of the composite manufacturing quality evaluation. Therefore, several TFBGs were used in thicker composites, composed by the same matrix and reinforcement of the thin one, to analyse the effects of the VARTM production steps on their internal structure. The use of more embedded sensors allows multi-measurements to be performed in more different points of the composite.

The manufacturing of the composite plates was performed at the Composite laboratory, and the experimental procedures and set-up were developed at the NDT lab of the Aerospace Structures & Materials department of Delft University of Technology and executed during the manufacturing process. This research was performed in collaboration with Dr. Giacomo Struzziero (Researcher at the Mechanical Systems Engineering Laboratory, EMPA, Swiss Federal Laboratories for Materials Science and Technology, Duebendorf, Switzerland). The contents of this chapter have been published in the Advanced Manufacturing Polymer & Composites Science international journal [1].

5.1 Introduction

As described in the first chapter, the use of composite materials in primary structures is highly desirable in many technological fields, as it allows to the weight be significantly reduced, which is especially important in the aerospace sector. The benefits are mainly an increase of the payload capacity and/or the reduction of fuel consumption, which is also in line with the new green policies. For these reasons, in the last decades, a significant weight reduction has been achieved by replacing solid metallic parts with composite materials [2]. However, due to the complexity of a composite structure and some poorly designed manufacturing practices, several defects may be introduced in the materials so to bring an unacceptable level of quality. For this reason, around 17% of the parts are rejected causing an increase of the costs and sustainability issues [3,4]. Therefore, inspection techniques can help to obtain a clear investigation of the internal state of composites during the manufacturing process so as to deduce in advance possible inconveniences such as defects, non-compliant stress state, voids, contaminations and premature cracks. Since the first sensing technologies developments were introduced, OFs immediately proved to be a valid option [5]. Especially, FBG sensors are, nowadays, the most used OF sensors for embedded real-time monitoring of composite structures. As manufacturing is a fundamental step to obtain the best mechanical performance [6], since the 2000s, the embedding of FBG sensors has been performed to control the manufacturing quality of the composites [7-10]. Indeed, during the production of composites, due to dominant heat transfer phenomena and low thermal conductivity through thickness, some defects such as voids, temperature overshoots, residual stresses and part deformation can occur [6]. These can significantly lower the mechanical performance of the components, decrease drastically their operational life and cause unexpected and dangerous failures [6,8]. For these reasons, significant efforts on the optimisation of the composite manufacturing [11-15] have been undertaken with the purpose to minimise the occurrence of such issues. As described previously, it is true that the monitoring of a specific manufacturing strategy is necessary to recognise in advance unwanted defects, while, at the same time, a multiple sensor strategy is not desirable as the presence of embedded sensors can influence the material mechanical behaviour or introduce even more defects [1,5,6]. As widely treated previously, several techniques have been developed to perform multi-parameter measurements. However, these possessed many drawbacks, which lead to this study of the application of a TFBG sensor for composite cure monitoring.

Following the road highlighted in the previous chapter, here, the TFBG sensors are used to measure simultaneously and separately the variations of three parameters (strain, temperature and RI) when embedded inside composite samples, during the manufacturing process. Therefore, the thermomechanical evaluation provides information on the deformation caused by the several steps, while the temperature is used to check possible thermal phenomena occurring in the composites. The resin RI measurements performed during the curing stage can be associated with its degree of cure [16], so that the crosslinking rate may be monitored and the completeness of the resin curing is verified. However, though these benefits and promising abilities, no works providing the reliability of the TFBG

for this application, can be found in literature. With this purpose, in this work, a TFBG was embedded in a 2 mm glass-fibre/epoxy composite plate and during its VARTM manufacturing process, the variations of strain, temperature and resin RI were extracted from the recorded spectra. This allows the reliability of the TFBG as three-parameter OF sensor to monitor the thermomechanical and degree of cure of the composite to be demonstrated. After that, these sensing features are used in thicker composites to investigate about the different effects induced by the VARTM process and entities based on the dimensional and curing parameters.
The research scope was investigated by exploiting the concepts already treated in the previous chapters about the thermomechanical and sensing theory, calibration and application.

5.2 Experimental procedure

The following section provides details on the fibre reinforcement, matrix and TFBG sensor used to build-up the sensorised composite panel and perform the measurements. After that, the investigation of the cure kinetics of the resin is presented with the T_g characterisation. This procedure will be useful to obtain the theoretical degree of cure to compare with the resin RI variation due to the crosslinking. The last part of the section is focused on the VARTM process and sensor embedding stage.

5.2.1 Materials and sensors

A number of 12 plies were used to make the 2 mm thick composite plate, manufactured with Interglass™ Unidirectional (UD) S-glass fibre (220 gr/m², 92145) dry plies and epoxy resin. This resin system was a low temperature curing Hexion Epikote™ 04908 epoxy resin mixed with Epikure™ Hardener 04908 with a mix ratio resin : hardener = 100 : 30 parts by weight [17]. This kind of epoxy resin system has been selected as it is really suitable for the infusion stage expected during VARTM, it has mechanical properties compatible for a wide range of applications (from marine to aeronautics) and it was largely available at the Composite Laboratory of Aerospace Structures and Materials department of TU Delft. The VARTM equipment, the vacuum bag setup consisted of a nylon film Wrightlon® 7400, sealant tape Solvay LTS90B, infusion mesh Airtech Greenflow 75, peel ply Airtech Stitch Ply A and release perforated polyolefin foil Wrightlon® WL3700.

The TFBG sensor was manufactured by FORC-Photonics in Fibercore PS1250/1500 OF with a 2° tilt angle, length of 4 mm across 10 mm of uncoated OF. The TFBG signal was acquired using a FBG interrogator NI PXIe-4844, where the maximum sample frequency is 10±0.1 Hz. A k-TC (Ø=0.250 mm, accuracy ±1°C) was also embedded and placed close to the TFBG to provide a temperature measurement reference for comparison with the TFBG measurements. The integration procedure of the sensors and further experimental details are reported in section 5.2.3. Before the embedding of the TFBG, a preliminary thermomechanical calibration was performed as described in chapter 2. The strain and temperature sensitivity coefficients found for the Bragg and the Ghost peaks were $K_{\varepsilon,Bragg}$=1.255±0.004 pm/με and $K_{\varepsilon,Ghost}$=1.255±0.006 pm/με while $K_{T,Bragg}$ =8.686±0.012 pm/°C and $K_{T,Ghost}$=9.2±0.014 pm/°C. The RI calibration procedure of the TFBG was performed as described in chapter 3, with the room temperature kept at 20±1.5°C. Usually the epoxy resins suitable for VARTM processes have a RI range 1.5-1.56 [18] when uncured, which is expected to increase during the curing stage [16]. In this case, the RI of the uncured resin is around 1.54 at 25 °C as provided by the manufacturer [17]. Hence, to obtain the best measurement accuracy, the curved branch in the range 1.46-1.7 was fitted to a fifth-order polynomial function with a fitting square error (R^2) of 0.9996, where the worst RI accuracy is less than 1×10^{-3} at 1.5 RI.

5.2.2 Cure kinetics and T_g characterisation of the resin

The cure kinetics characterisation of the chosen epoxy system was carried out with a TA Instrument Differential Scanning Calorimetry (DSC) 2500. Two isothermal tests conducted at 80°C and 100°C and a further dynamic test at 1°C/min were performed. The glass transition temperature evolution was characterised through Modulated DSC (MDSC), with a ramp rate of 3°C/min and a modulation

frequency of 60 s where the amplitude was 1°C, by observing the evolution of the reversible components of the specific heat. Next to the fully cured and fully uncured samples, four partially cured samples were manufactured starting from the uncured resin samples and by heating them at 1 °C/min up to an increasing final temperature followed by a quick cool down to stop the reaction from progressing. Furthermore, two additional samples have been partially cured to validate the cure kinetics model. The cure profiles used dictated a ramp-up to 80 °C at 1 °C/min followed by an isothermal dwell of 20 min for the first sample and 40 min for the second. After that, the samples have been quickly cooled down to stop the reaction. An MDSC analysis to identify the glass transition temperature of the sample has been subsequently performed. The resin cure kinetics and Di Benedetto equation were fitted to the experimental results to obtain the degree of cure and the glass transition temperatures trend. The experimental data have been fitted with the kinetics model proposed in [19]. This model has been proved to accurately describe similar epoxy resin systems [13]:

$$\frac{d\alpha_r}{dt} = \frac{Ae^{\left(\frac{-E}{RT}\right)}}{1+e^{C(\alpha_r-\alpha_c-\alpha_T T)}}(1-\alpha_r)^n\alpha_r^m, \qquad (V.1)$$

where α_r is the degree of cure, t is time, α_c, α_T, are coefficients controlling the transition of the kinetics from chemical to diffusion, control, C governs the breadth of the transition into the diffusion controlled regime, m and n are reaction orders for the n-*th* order and autocatalytic terms, A is a pre-exponential Arrhenius factor, E is the activation energy of the Arrhenius functions, T is the absolute temperature, and R is the universal gas constant.

The fitting of the experimental data with the proposed phenomenological kinetic model is shown in Fig.5-1a.

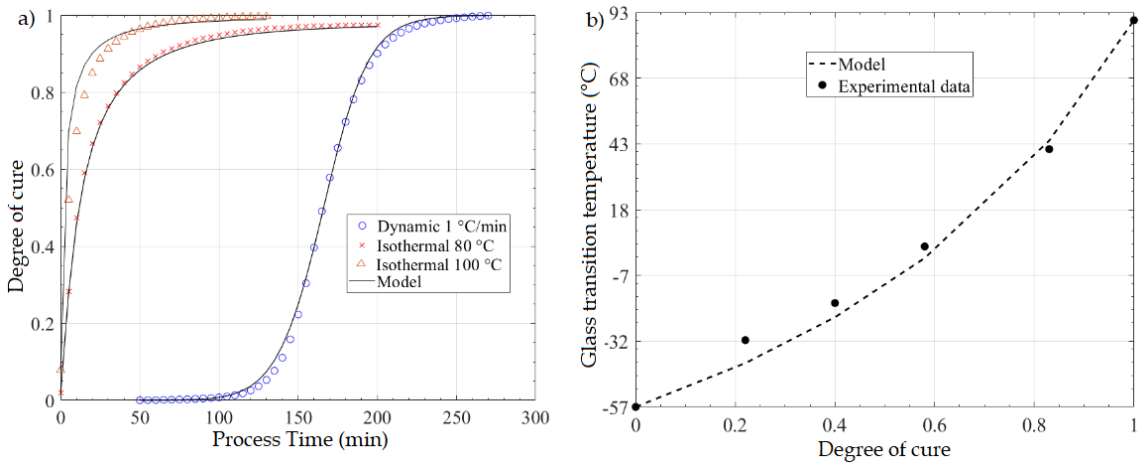


Fig.5-1. EpikoteTM 04908/EpikureTM 04908 system phenomenological models fitting a) Cure kinetics and b) Di Benedetto equation.

The average relative error of the fitting is about 2%. The heat generated (Q) by the exothermic reaction can be calculated through the formula:

$$Q = \varrho_r v_r H_{tot} \frac{d\alpha_r}{dt}, \qquad (V.2)$$

where ϱ_r is the resin density, v_r the volume resin fraction and H_{tot} is the total enthalpy. The glass transition temperature model to fit the experimental data follows the Di Benedetto equation [20]:

$$T_g = T_{go} + \frac{(T_{g\infty}-T_{go})\lambda\alpha_r}{1-(1-\lambda)\alpha_r}. \qquad (V.3)$$

In eq.V.3, $T_{g\infty}$ and T_{go} are, respectively, the glass transition temperatures of the fully cured and uncured material and λ is a fitting parameter governing the convexity of the dependence. Fig.5-1b illustrates the

fitting of the experimental data with the Di Benedetto equation. The fitting parameters of the cure kinetics and glass transition temperature development models are reported in Table 5-1.

Table 5-1. Fitting parameters values for the cure kinetics and glass transition temperature material models of EpikoteTM 04908/EpikureTM 04908 system.

Parameters	A	E	n	m	C	α_c	α_T	H_{tot}	T_{go}	$T_{g\infty}$	λ
Values	21594	49400	1.58	0.05	80	0.44	0.0015	760	-57	90	0.453
Units	s^{-1}	$Jmol^{-1}$					K^{-1}	Jg^{-1}	°C	°C	

The two validation samples resulted in glass transition temperatures of 25 °C and 45 °C and according to the Di Benedetto model developed, this corresponds to degrees of cure of 0.74 and 0.84, respectively. The prediction of the degree of cure by using the cure kinetics model developed is for 0.77 and 0.86 degree of cure, proving that the model predicts the degree of cure development of the resin system analysed within 4% accuracy.

5.2.3 VARTM process

The VARTM manufacturing process was used to produce the samples and consists of an infusion stage followed by a curing stage. The main equipment of this composite manufacturing process is composed of a mould, vacuum bag, vacuum pump, infusion lines (inlet and outlet), infusion layers (described in section 5.2.1), sealant tape and oven. The procedures consist of initially cleaning of the mould with acetone, isopropanol and an adhesive solvent for a deep removal of impurities from the mould's surface. Then, the surface is treated with a realising agent based on hydrocarbons to make the removal of the composite easy after the curing process. The edges of the mould are excluded from this step so that the sealant tape, which must be applied to seal up the mould with the vacuum bag, has a good adhesion with the surface. At this point, the reinforcement foils can be stacked onto the mould and the sensors inserted between the designed layers. In particular, the OF was placed parallel to the UD reinforcement fibres plies of the composite to measure longitudinal strain. This also minimises possible disturbances due to bending or interaction with the glass-fibres during the process. The used mould was a flat aluminium plate (50x50x1 cm). Except for the curing, all the process steps in the resin infusion were at room temperature. The TFBG was embedded by using the same translation stage used for the TFBG mechanical calibration presented in Fig.2-11. This held the TFBG straight and in the centre position of the reinforcement layer by inducing a small pre-tensile (~250 μm) displacement to the OF. Then, the TFBG was spot-glued onto the glass-fibre foil by using a couple of small drops of cyanoacrylate glue close to the edges of the composite layer as shown in Fig.5-2.

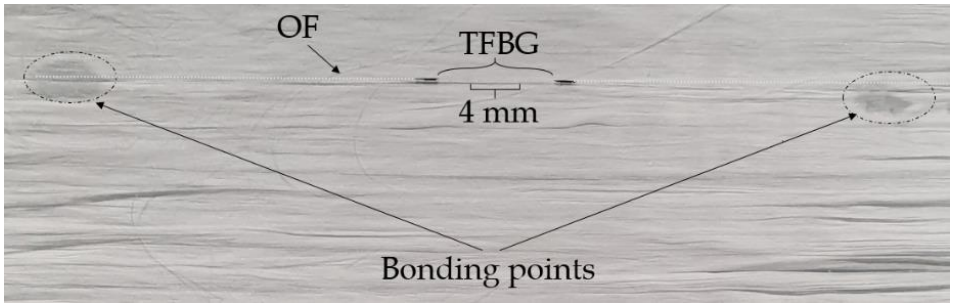


Fig.5-2. Positioning and gluing of a TFBG sensor on a reinforcement ply.

Additionally, a TC was placed as close as possible to each glued TFBG sensor, but in a way so as not to interfere with the material surrounding the OF sensor. Both the sensors, TFBG and TC, were embedded in the middle plane (6th reinforcement layer). After the embedding procedures, the preform was assembled. Fig.5-3 gives a schematic view of the sample with the sensors embedded.

The OFs and the TC wires exiting from the composite were protected with vacuum bag sealant tape so that they are not wetted by the resin flow during the infusion as Fig.5-4 shows. Once, the embedding

of the sensors was completed, the other reinforcement layers were stacked and provided with ventilation and infusion layers. Therefore, the inlet and outlet tubes were inserted in the setup, and the vacuum bag enveloped hermetically the entire mould through the pre-placed sealant tape. At this point, a vacuum test was performed to verify possible leakages coming from the sealed contour and the inlet/outlet points. Hence, once the hermetic seal was verified, the resin infusion was performed at 50 mbar to avoid the evaporation of volatiles. During resin flow, the TFBG sensor was used to provide information on the flow arrival time. This scope has been achieved thanks to the results obtained from the experiment introduced in section 3.7. Indeed, also in this case, the TFBG is partially and increasingly embedded by a medium with a different RI.
After completing the infusion, the inlet line was closed and the panel was cured in an oven provided with an access hole from which the infusion lines, the OFs and the TCs can be externally connected. The applied curing temperature profile is suggested by the resin manufacturer [17]. As no indications have been given by the manufacturer regarding ramp rates, a heating-up of 1°C/min and cooling-down by natural convection were imposed to have a gradual temperature variation. The strain, temperature and RI measurements were performed by demodulating the TFBG spectra acquired during the curing time, with the techniques presented previously. The entire experimental setup is shown in Fig.5-5.

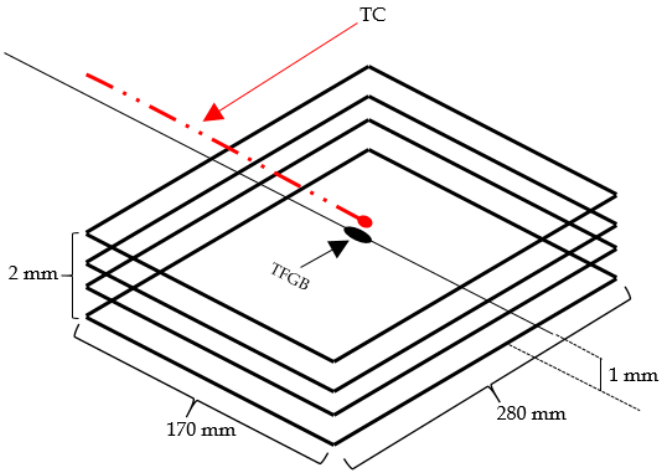


Fig.5-3. Schematic of the composite sample with the TFBG sensor and TC.

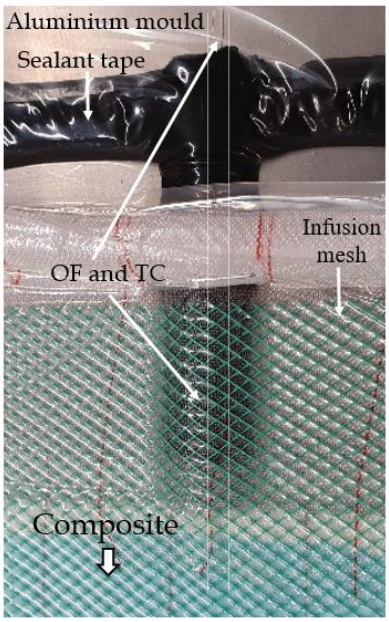


Fig.5-4. Protection of OFs and TCs exiting from the vacuum bag through black tacky tape.

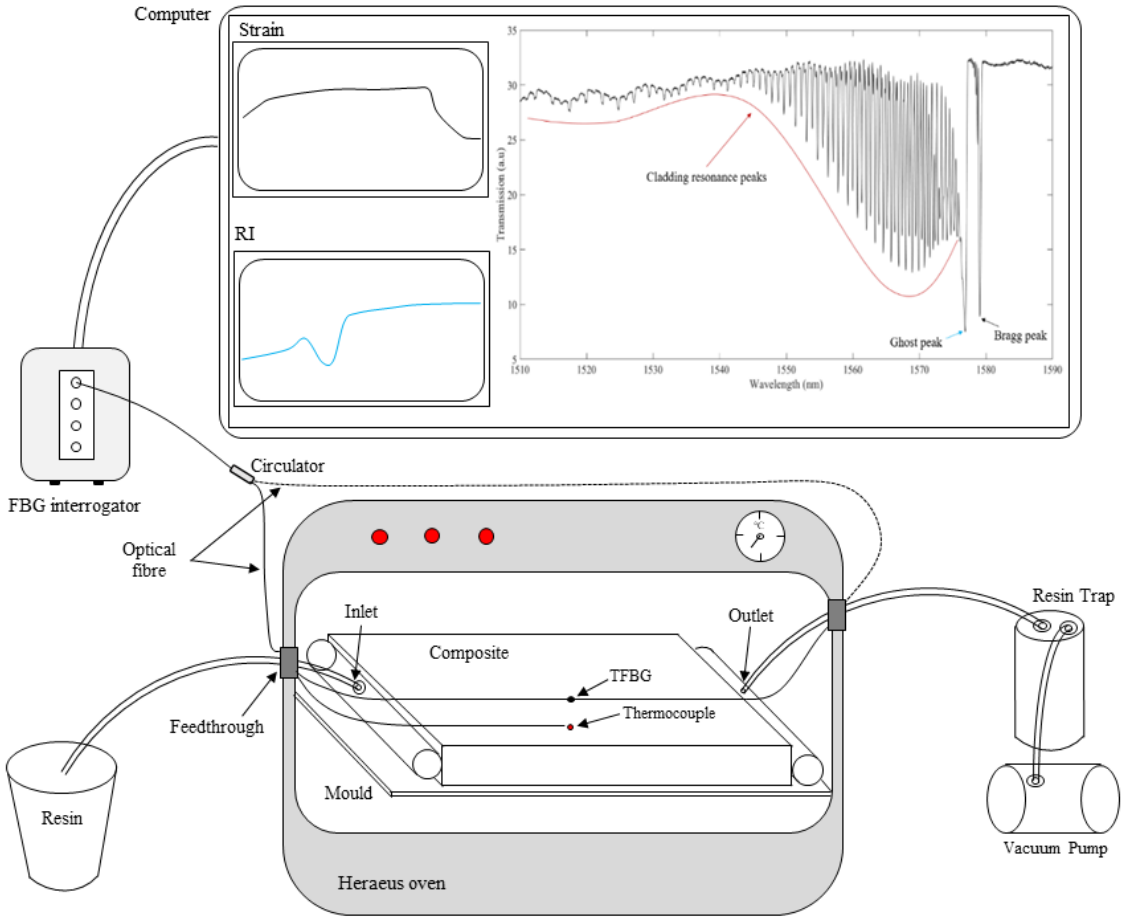


Fig.5-5. Schematic of the experimental setup composed by manufacturing and sensing equipment.

5.3 Results and discussion for 2 mm sensorised composite

After the thermomechanical-refractometric demodulation, the outcomes of the TFBG measurements from the spectra acquired during the several stages of the VARTM process can be observed. In this section, first of all, the results regarding the pre-curing stages and infusion process are presented and then, those about the curing stage of the composite plate.

5.3.1 TFBG measurements during pre-curing stages

The vacuum bag evacuation leads to a through thickness compaction of the layup, including the OF with the TFBG sensor on which a transverse load is generated. As previously demonstrated [21], this causes a reduction of the OF cylindrical section and the initial TFBGs signal changes after the vacuum compaction. Fig.5-5 reports two consequences of the compaction, the distance decreasing in amplitude between two subsequent peaks and the absolute decay of the upper and lower resonance peaks transmission power.

However, despite this signal variation, the vacuum compaction load does not influence the refractometric properties of the TFBG. In fact, as already described, the cladding resonance envelope area evolution depends only on the chemical composition of the OF's layers, the surrounding RI and how the RI modulation is imposed inside the OF's core. Hence, the RI calibration curve is still valid in vacuum compaction, after considering the new reference envelope area as the one obtained after the vacuum compaction. This was confirmed by the RI measurements reported in the results section, where the initial measured resin's RI is similar to the one expected from the manufacturer's datasheet. A further consequence for the resonance peaks is the shifting of their wavelengths. Since the temperature

from the TC was stable, the strain value can be calculated by using $\Delta\lambda_{Bragg}$ or $\Delta\lambda_{Ghost}$ from the initial condition (before vacuum application) and the respective k_ε. As the OF is glued on top of a reinforcement layer, this deformation can be interpreted as that imposed on the i-*th* layer for the compaction effect by the imposed vacuum that makes each layer surface of the laminate flat and is consequently stretching the TFBG. A positive strain of ~29.1 με was detected.

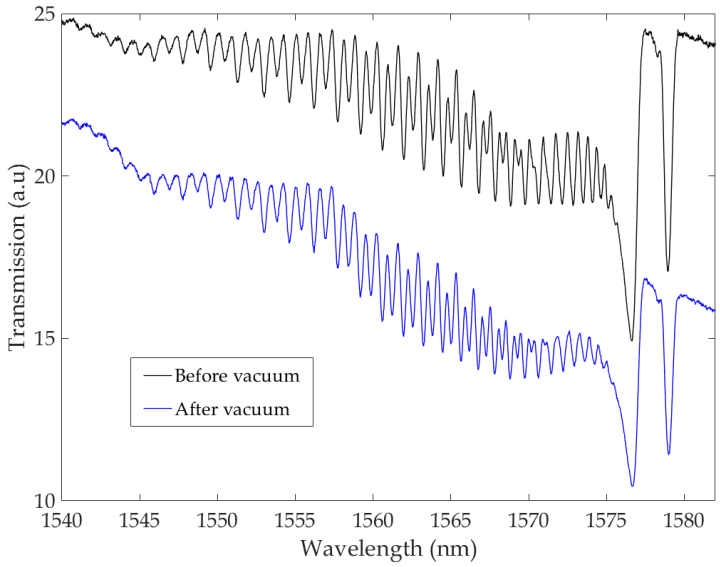


Fig.5-5. Spectrum of a TFBG sensor before and after the vacuum compaction of the laminate.

5.3.2 TFBG detection during resin infusion

The refractometric properties of the TFBG allow the spectra to be used to monitor the resin flow front arrival during the infusion process. Indeed, when the resin reaches the sensor, it starts to wet it and the depth between the upper and lower cladding peaks decreases uniformly until it reachs a stable condition once the TFBG is fully immersed. At this point, the normalised envelope area returns the resin RI by using the fitting correlation function obtained from the calibration. The dynamics of the partial and gradual immersion of the TFBG in a liquid with different RI were deeply analysed in section 3.7. In this context, the differences between the TFBG spectra before and after the resin flows can be observed in Fig.5-6.

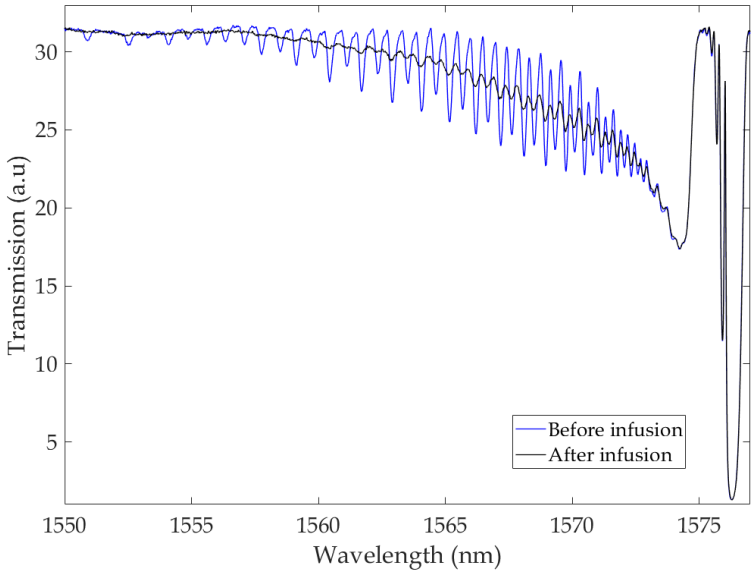


Fig.5-6. Spectrum of the embedded TFBG before and after the resin arrival.

Furthermore, the trend of the cladding resonances envelope area can be observed in Fig.5-7, where the normalised area starts to decrease until it reaches a stable condition when fully immersed in the resin.

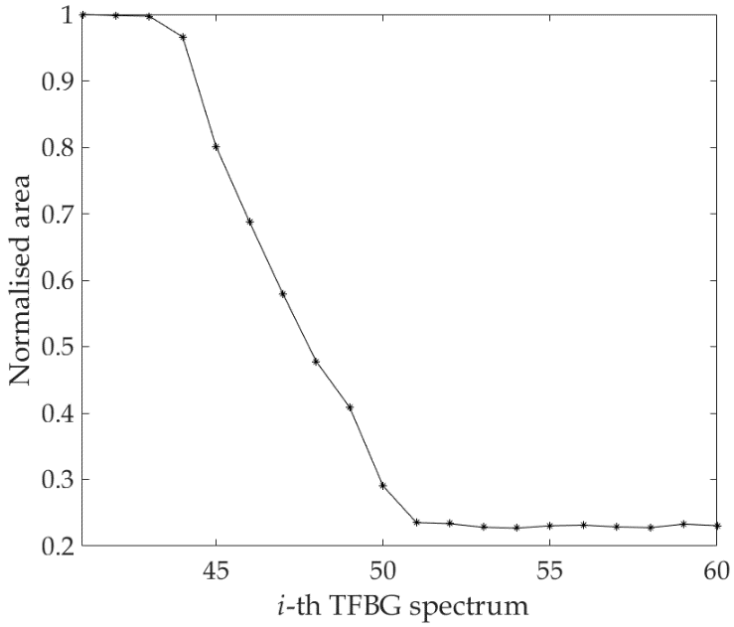


Fig.5-7. Cladding resonances envelope area decreasing trend during the gradual TFBG immersion.

This was clearly expected from the previous conducted studies and description. In Fig.5-7, the normalisation was made by considering the area of the TFBG in vacuum as a reference, while the *x*-axis reports the number of the TFBG spectrum. Since the interval time between each spectrum (~1 s) and the starting acquisition time are known, therefore the required time for the resin to touch the sensor from the start of the infusion was ~50 s whilst to have a stable spectrum at the minimum area, ~9 s were needed. The latter can be considered as the interval needed for the resin flow front to fully cover the TFBG. However, this time should not be confused with the absolute speed in a single direction of the composite. In fact, due to the presence of the flow media on top, the flow front propagation is non uniform through the thickness as its permeation from the flow media is superposed on the in-plane flow. Moreover, small oscillations can be present in the spectrum due to pore migration flowing along the OF surface where the TFBG is present and locally influencing its coupling mode system. Hence, the TFBG spectral signals may be also used to locally identify possible defects due to poor or incomplete wetting. Indeed, in this case, the spectrum would return a different resin RI value from the one expected. This expected value can be obtained from a preliminary measurement by fully immersing the TFBG in a pot of resin at the same infusion boundary conditions. This type of control and monitoring can also occur on-line as the operations to calculate the envelope area are usually fast enough to be completed within the minimum refresh time of the device used to interrogate the TFBG sensors. Furthermore, as the time interval to obtain the spectrum of each single TFBG from dry to fully wet condition, can be calculated with an accuracy of 0.33 s (depending on the interrogator device), these sensors may be used to investigate the local permeability of a fibre reinforcement layer along the embedding direction.

5.3.3 TFBG three-parameter monitoring during composite curing

During the curing stage of the composite in the oven, the sensing abilities of the TFBG are fully exploited to measure simultaneously strain-temperature variations and the resin RI trend. As demonstrated in chapter 4, the thermomechanical state evaluation of the composite can be performed by considering, at the same time, $\Delta\lambda_{Bragg}$ and $\Delta\lambda_{Ghost}$ and the thermomechanical sensitivity coefficients (eq.II.28). From this procedure, $\Delta\varepsilon$ and ΔT can be calculated from the desired moment, which, in this case, is when the oven was switched-on (i.e. 96 min). Hence, at this point, the strain variation is assumed to be zero and the temperature is ~21 °C. Once both the variations are obtained, these are reported in

Fig.5-8 with the temperature recorded by the embedded TC. In the graph, the temperature and strain profiles measured by the embedded TFBG sensor are respectively represented by a dashed red line and a black continuous line, while the TC values are shown as a continuous red line.

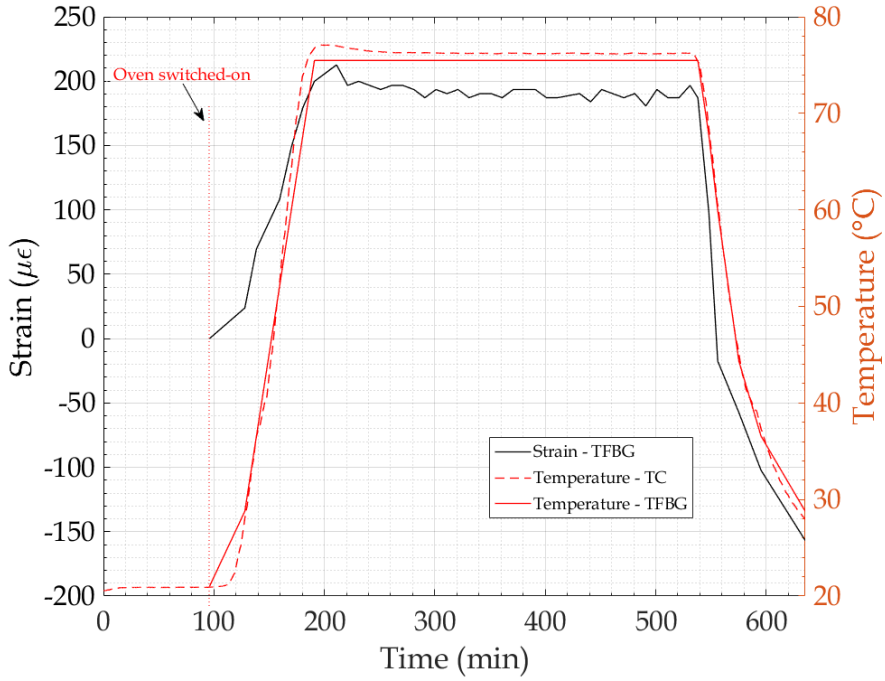


Fig.5-8. Temperature and strain trends during the composite curing time measured trough the embedded TFBG and TC.

It is well known that the TFBG measurements performance are constrained by its thermal resolution (~7.8°C), however, despite this, here the temperature trends measured by the TC and TFBG are similar. Specifically, due to the *TR* of the TFBG, an average temperature difference between the TC and TFBG temperature trends of ~0.78°C is generated, while the maximum difference is ~1.7°C at the 198th minute. As a consequence, since the strains are calculated in isothermal conditions when the temperature measured by the TFBG is at its maximum and is stable, a mean and maximum strain deviation, respectively of ~5 με and ~12 με, can be extracted through the temperature differences. Nevertheless, considering the values of Δε and ΔT involved in Fig.5-8, the previous deviations can be considered negligible. Furthermore, the strain oscillations detected by the TFBG along the entire interval between 200 and 540 min, are caused by temperature fluctuations. During the cooling down step, the TFBG measurements were stopped when the temperature reached 28.8°C as lower temperatures were not detectable due to the *TR* of the TFBG. The deformation measured by the TFBG at this temperature is around -157 με. However, the lowest detected temperature by the TC was 23.7°C. The additional 5.1 °C correspond to about -23 με hence, the maximum Δε is expected to be around -180 με. The compressive strain measured is a combination of compressive strains due to matrix related shrinkage and contraction in the cool down phase due to coefficient of thermal expansion (CTE) [14]. As for the thermomechanical variations, the resin RI can be evaluated through the embedded TFBG at any moment of the manufacturing process. The refractometric measures can be performed simultaneously with the strain and temperature calculations, after which the OF sensor is immersed in the resin flow. The resin RI evolution is clearly obtained from the envelope area trend, and both are shown along with the TC temperature profile in Fig.5-9, where both parameters follow the same trend.

The curves were smoothed with fine averaging (middle points interpolation) to remove the greater part of the oscillations due to possible TFBG signal fluctuations caused by high-heat transfer, transverse strains, OF bending, power detection accuracy and background noise. As the RI is obtained from the envelope area through the correlation fitting function, their trend is very similar. This means that both the envelope area and the RI can provide information about the resin cure state as demonstrated in

Fig.5-10 in the case of the RI variation trend. Therefore, in an on-line monitoring application of the resin curing process, even the envelope area trend provides enough information to determine the resin state without the need to calculate the RI values. Nevertheless, for its physical meaning, the RI is preferred here to base the following discussion on its correlation with the resin cure degree (α_r). In Fig.5-10, α_r and the resin RI curves are compared and, by identifying some characteristic points, three ranges can be identified. The first range goes from the start of the data acquisition until the switching-on of the oven. Here, the sensor measuring the resin's RI has a monotone increase due to the crosslinking of the polymeric chains. Though the initial RI variation is severe, the curve slope becomes milder quickly and this reflects the slow resin crosslinking reaction occurring at room temperature. In particular, the RI value detected from the TFBG at the start of the oven ignition is ~1.552. This value deviates slightly from the one reported in the manufacturer data sheet for three main reasons: different reference temperature (here, ~21°C), the resin was previously mixed with its designated hardener which influences the overall RI, and the resin has already undergone part of the cure stage at room temperature.

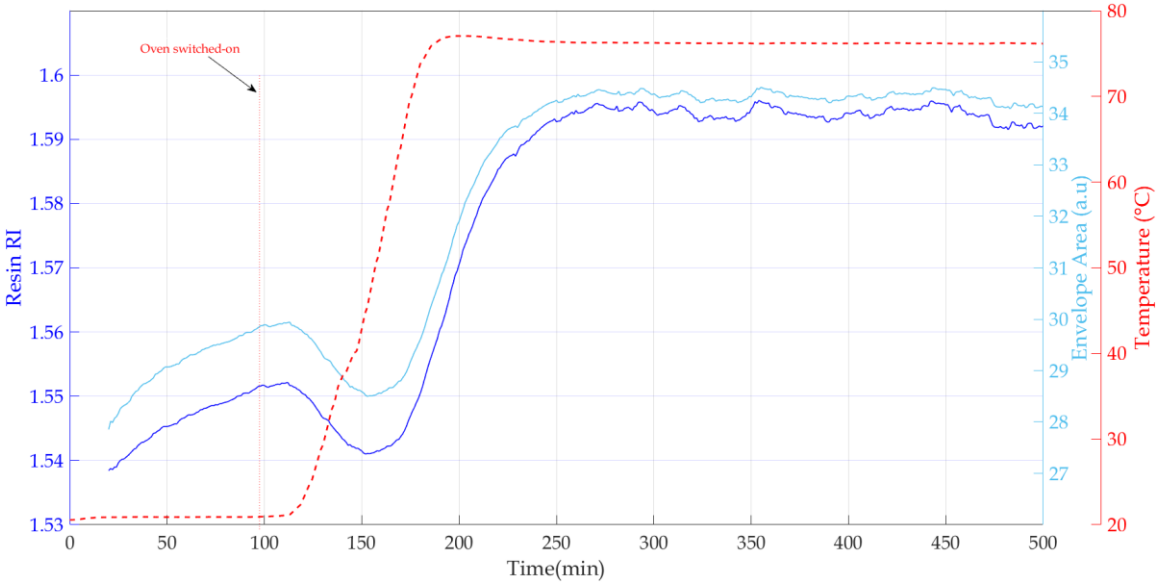


Fig.5-9. Envelope area and resin RI trend during the composite curing time through the TFBG sensor with TC temperature.

In the second range, which is comprised between the oven switching-on and a local minimum point along the RI trend during the oven temperature raising-up, the RI trend changes for the ramp-up of the programmed temperature profile. Specifically, with the switching-on of the oven, the RI tends to flatten, and then decreases as the overall expansion due to the CTE of the mostly uncured resin dominates the shrinkage effect due to the crosslinking. This trend continues until the RI curve reaches a local minimum point, where the third range starts. From this point, the RI trend reverses when the degree of cure is about at 40% which indicates that the resin system might be approaching its gelation point, and starts to increase as shrinkage related effect starts to dominate over the CTE. The competing effects between shrinkage and CTE in composite manufacturing has been discussed and quantified by means of FEA in [14]. The resin's RI converges into a plateau in the last part of the curing stage (observed also in [16,22]), where the great part of the crosslinking reactions (α_r=92%) occurred. The oscillations in the signal are possibly caused by the low crosslinking density occurring in this range, whereby the resin RI changes are too small to be detected from the TFBG with respect to the RI variation caused by the small temperature fluctuations. This demonstrates that the resin RI measurements during its curing (or cladding resonance peaks envelope area), can be used to detect the different cure dynamics even without the help of the α_r curve. Furthermore, since the RI is sensitive to the temperature variations, its measurement can identify also whether the curing occurs at room temperature or in an oven. Finally, as shown in Fig.5-10, the resin's T_g exceeds the curing temperature at about 330 min, leading to a vitrification of the matrix.

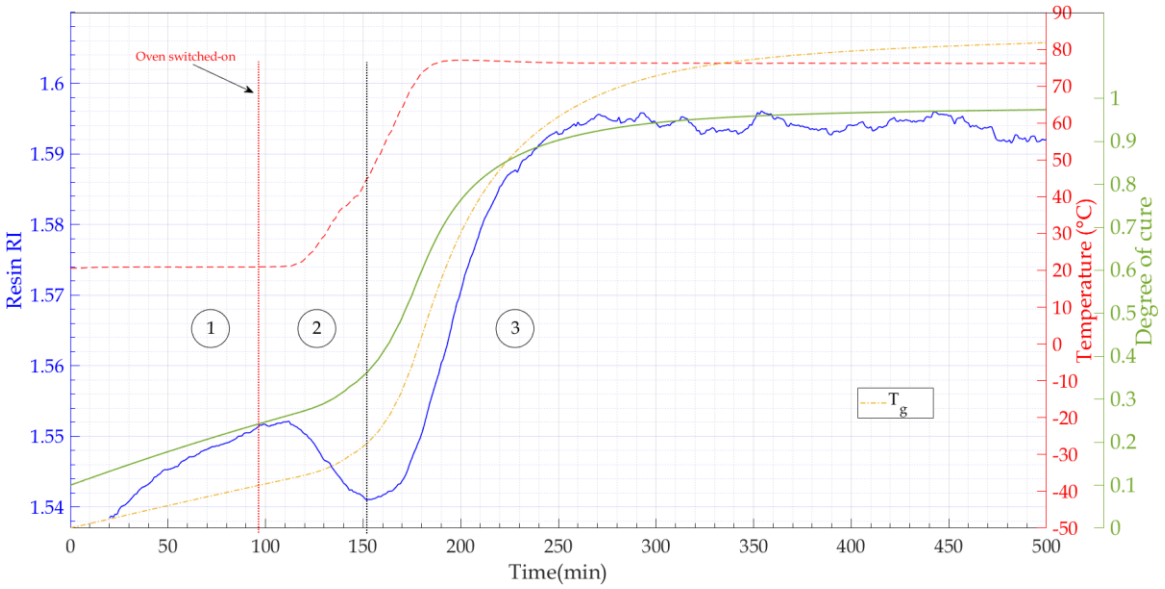


Fig.5-10. Comparison between α_r and the resin RI with TC temperature and T_g evolution.

5.4 Final considerations on the 2 mm thick composite monitoring

In conclusion, the TFBG sensor has been demonstrated to be able to act as a three-parameter OF sensor in monitoring the VARTM manufacturing process of a glass-fibre/epoxy composite. It is able to detect the time needed for the resin flow front to reach the TFBG and the envelope area can be also used to obtain flow information such as resin arrival time, infusion degree and poor resin wetting. The TFBG records simultaneous strain-temperature measurements during the curing in the oven, indicated a relevant development of compressive strains during cool-down. The temperature measured by the TFBG matches well with the one measured by the TC. However, the two profiles deviate due to the TFBG thermal resolution, which influences also the measured strains. This limitation can be easily overcome using a FBG interrogator with a higher *sw*R. The maximum strain deviation calculated corresponds to 2.7% of the average strain for a short time interval of the curing step, and this value can be considered low. At the same time, the TFBG spectra provide the resin RI variation starting from the infusion step. A comparison of the RI trend with the resin degree of cure obtained from its cure kinetics, showed that the RI measurements can detect the resin cure state throughout the process. The monitoring technique could in future be applied to carbon fibre composites made with the Liquid Composite Moulding processes or in an autoclave, and in pre-pregs composites. Furthermore, TFBGs may be suitable for further applications in the composite industry as they could improve the quality and health control of the products by providing information during the manufacturing process and in service. TFBG measurements can be also performed on thicker composites, and potentially in real-time, and for all the three dimensions of the composite by embedding more TFBGs.

To conclude this section, a single minimal by intrusive TFBG sensor was demonstrated as a three-parameter OF sensor embedded in a composite, to monitor the thermomechanical and cure state of the composite during several steps of its manufacturing process after performing a preliminary calibration of the sensor. This improves the state of art of the monitoring and sensing technology and raises the concept of structural health monitoring of a product using a TFBG.

In the next part of the chapter, the sensing properties of the TFBG will be used to perform an overall monitoring of the internal state of thicker composites manufacturing via the VARTM process.

5.5 Monitoring of thicker composites during VARTM

Once the TFBG has been demonstrated to be able to monitor the overall state of a composite plate with 2 mm of thickness during the several steps of the VARTM manufacturing process, the same technique was applied for 5 mm and 10 mm thick composites. The aim was to detect the differences in strain-temperature distribution and RI variations for composites of considerably different thicknesses. Furthermore, 2 TFBGs were embedded between the layers at different heights in the 10 mm composite. This allows the investigation of the thermomechanical-refractometric effects induced in the material during the manufacturing steps at different thickness.

5.5.1 Design, materials, embedded sensors and VARTM equipment

The equipment used for manufacturing with the VARTM process was identical to that used for the 2 mm composite sample, as well as the UD glass fibre reinforcement foils and the epoxy resin system. 60 plies were used to make a 10 mm thick composite sample after the curing stage, while 30 plies were stacked in the case of the 5 mm composite. Regarding the OF sensors, three 3° TFBGs were embedded between the composites (Fig.5-11). Two of them were placed at the middle layer (30th), and at the 6th layer of the 10 mm composite plate. Instead, the last one was centrally integrated in the middle of the 5 mm composite corresponding at the 15th ply. A TC was embedded as close as possible to each TFBG sensor. The OF sensors were calibrated in advance for thermomechanical and refractometric applications as described previously. The thermal and deformation coefficients are in Table.5-2.

Table.5-2. Thermomechanical sensitivity coefficients of the TFBGs embedded in 10 mm thick composite.

Composite thickness		Embedding thickness	$K_{\varepsilon,Bragg}$ (pm/με)	$K_{\varepsilon,Ghost}$ (pm/με)	$K_{T,Bragg}$ (pm/°C)	$K_{T,Ghost}$ (pm/°C)
10 mm	**TFBG1**	1 mm	1.255±0.004	1.255±0.006	8.657±0.007	9.6±0.014
	TFBG2	5 mm			9.068±0.006	9.6±0.006
5 mm	**TFBG3**	2.5 mm	1.255±0.004	1.255±0.006	8.829±0.009	9.114±0.007

In the curing process, the thicker 10 mm composite plate was cured in an oven with the temperature profile indicated by the resin producer as for the 2 mm composite. While, the 5 mm composite was left to cure at room temperature and at the same infusion pressure. This last curing procedure allows an investigation of the curing degree of the resin without the addition of external heat, by using the TFBG refractometric measurements. These results will be shown in section 5.5.2.

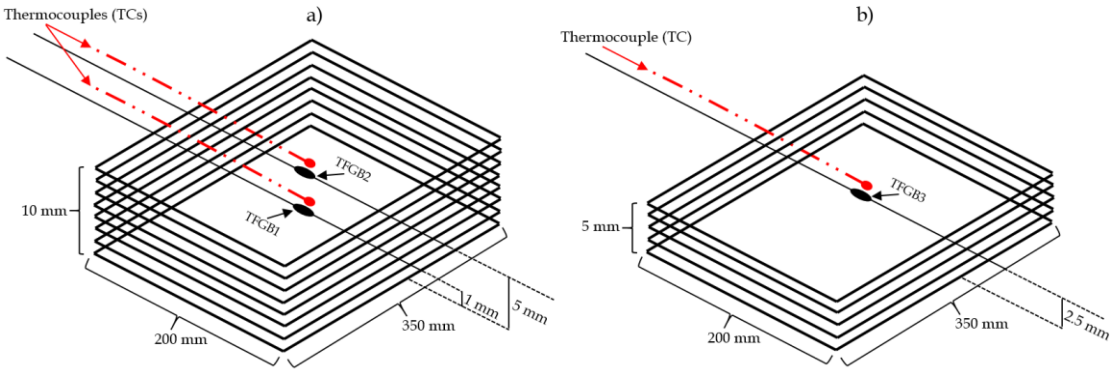


Fig.5-11. Schematic of the a) 10 mm and b) 5 mm composite sample with the TFBG sensors and TCs.

5.5.2 Strain detection during vacuum imposition

As for the 2 mm plate, the strain induced for the application of vacuum can be checked by TFBG monitoring. Hence, once the air was sucked from the composite through the vacuum bag, the TFBG spectrum acquired at room pressure and that recorded after reaching the desired pressure can be compared. As expected from the description of section 5.3.1, the TFBG1 detected a positive

deformation of 38.2±0.2 με, a value that is comparable with the strain measured by the TFBG embedded in the 2 mm composite plate. Here though the strain measured by these last sensors are matching, probably, the small difference may be due to the greater stretching effect in the thick composite due to the higher number of layers.
Unlike the previous sensors, a negative strain (-350.2±3.2 με) was detected by the centre embedded TFBG2 in the composite. This can be explained by observing the composite edges in Fig.5-12, where due to the significant thickness, the vacuum forces the bag to push on the composite sides. This compression effect is enough to compress the composite upper layers, making them rounded and create the compression state that the TFBG2 sensor detected. For the 5 mm composite, even TFBG3 detected a negative strain value of ~20 με, which confirms an increase of the side compression state in the thickness of the composite. While, the other TFBGs, embedded at lower depth (1 mm) in the 2 mm and 10 mm composites, confirm a positive stress state as the stretching generated by the vacuum compaction of the layers is dominant.



Fig.5-12. Rounded down edges of 1 mm thick composite after the manufacturing process.

5.5.3 Resin flow detection

The flow of the resin between the layers of a thick composite is more complex as the propagation direction cannot be considered unidirectional. Indeed, the flow propagates not only along the main direction but also towards the bottom layers due to gravity. In this context, the TFBGs can help in monitoring the flow front arrival and the permeability properties of the composite. Indeed, for the 2 mm composite, if the arrival time to reach and fully wet the TFBG is in order of seconds, for thicker composites the flow can be very slow. In the case of the 5 mm composite, the spectra obtained from the TFBG3 indicates a resin front arrival ~10 minutes the opening of the inlet, and the time interval for the resin flow front to fully cover the TFBG (immersion time) was 97 seconds. While, the time needed by the resin to wet the TFBG1 and TFBG2 embedded in the 10 mm thick composite, were respectively ~53 and ~22 minutes from the beginning of the infusion. Especially in a thick composites infusion setup with flow media, the superposition of through thickness flow and in plane flow is expected to lead to substantial through-thickness flow gradients. Furthermore, as Fig.5-13a shows, the in-plane flow front is not uniform and TFBGs placed in the middle are reached before than sensors embedded on the sides, as the case of TFBGs not being well superposed (in top view). In this context, the TFBG spectral signal can be used to understand the resin infusion degree and identify possible defects deriving from poor or incomplete wetting.
In addition, the thick and thin composites infusion can be regarded as isothermal as the TCs were measuring a constant temperature. However, all the peaks of each TFBG were shifted after wetting with the resin flow, which may be attributed to mechanical strains only, and can be attributed to the flow phenomena. Some previous researchers [23,24] have also reported the generation of a tensile stress state due to the resin infusion between the reinforcement layers. Therefore, the strain values can be calculated, excluding temperature conditions, by using $K_{\varepsilon,Bragg}$ and $\Delta\lambda_{Bragg}$ for each TFBG. The strains induced are reported in Table.5-3 (including the strains measured in the 2 mm composite).

TFBG2 and TFBG3 exhibit small and negative deformations, which means the resin flow dynamics are different with respect to the position through the layers of the same composite and the sample thickness. As portrayed in Fig.5-13b, the resin flows from the inlet to the composite through the flow mesh, into the lower layers. As the resin upper front progresses towards the outlet, a certain amount of resin has already penetrated the lower layers in the part of the composite closer to the inlet. Since the permeability of the reinforcement layers is lower than the flow mesh, the advance of the resin is different through the thickness. This means that the resin flowing slowly inside the layers can meet part of the resin that is penetrating by falling from the upper plies and/or due to capillarity action coming back between the reinforcement fibres. At this point, the impact between the flows with different speed vectors could generate a negative stress, as the TFBG2 and TFBG3 sensors detected in the thicker composites.

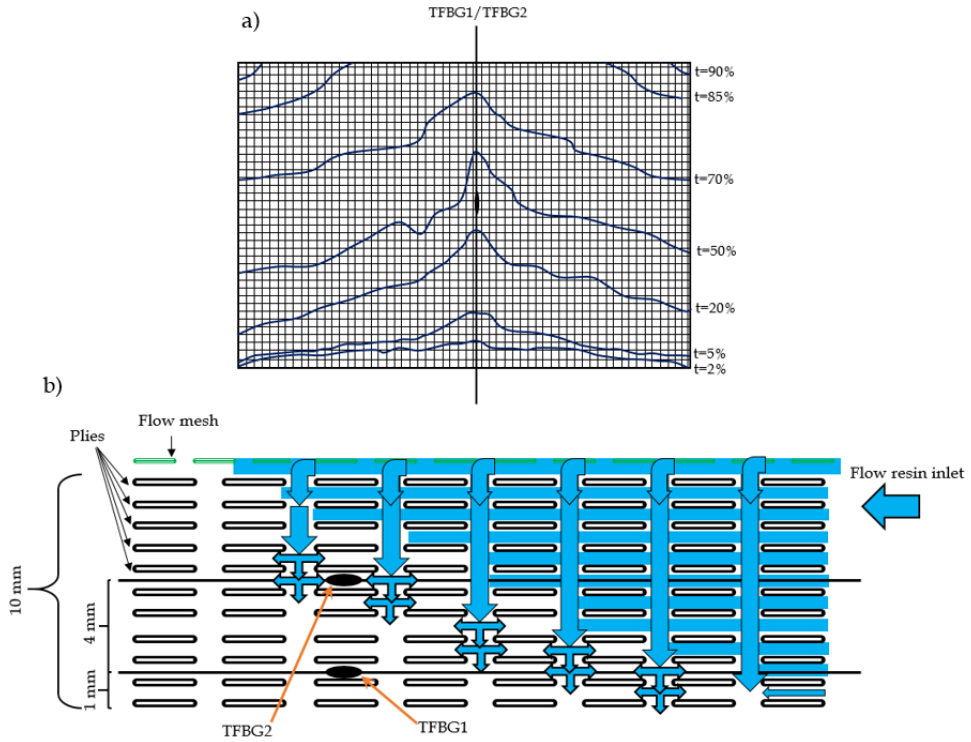


Fig.5-13. a) Schematic of resin flow front (top view) during the infusion time (t) along the 10 mm composite and b) of through thickness section of resin flow front in 10 mm composite.

Table.5-3. Strain values detected by the TFBGs during the resin infusion in 2, 5 and 10 mm composites.

OF sensor	**Composite**	**Strain** (με)
TFBG	2 mm	30.1
TFBG1	10 mm	25.1
TFBG2	10 mm	-20.1
TFBG3	5 mm	-5.02

The same cannot be asserted for the TFBGs embedded at lower thicknesses, which show positive deformations indicating that the flow is induced mainly to propagate along a unidirectional direction. The observation of the TFBGs spectra showed how the same pre-curing manufacturing steps can influence differently the stress/strain distribution state based on the composite thickness. However, the TFBGs allow the evaluation of the composite state and the detection of possible defects, even in real-time developing special demodulation algorithms. These should calculate, for each iteration, the wavelength difference of selected peaks from a reference condition, to obtain the strain value by using eq.II.28. These operations are usually fast enough to be completed within the minimum refresh time of the device used to interrogate the TFBG sensors. This means the strain value is obtained with the same interrogation frequency.

5.6 Monitoring of thicker composites during the curing stage

Here the results of the monitoring with several TFBGs is reported for the thicker composites. Each sensor is able to independently measure the strain, temperature and RI variations, hence the difference in measurements between the TFBGs embedded at different thickness can be observed. Furthermore, unlike the 10 mm composite, the 5 mm sample is cured at room temperature. This allows the mechanical deformation to be assessed and RI trend of the when no heating is applied to the composite during the curing. A comparison with the measurements obtained for the composites cured in oven is reported.

5.6.1 TFBG three-parameter monitoring during composite curing

The 10 mm composite sample was cured in an oven with a temperature profile indicated by the resin producer, hence this raised some thermomechanical variations in the material which can be detected by the TFBGs. Especially, this is interesting to observe, as the measured deformation can vary based on the position of the sensors embedded in the composite thickness. The strain variations detected from the moment in which the oven was switched-on ($\Delta\varepsilon=0$, $t=0$), are reported in Fig.5-14 and Fig.15 respectively, for TFBG1 and TFBG2.

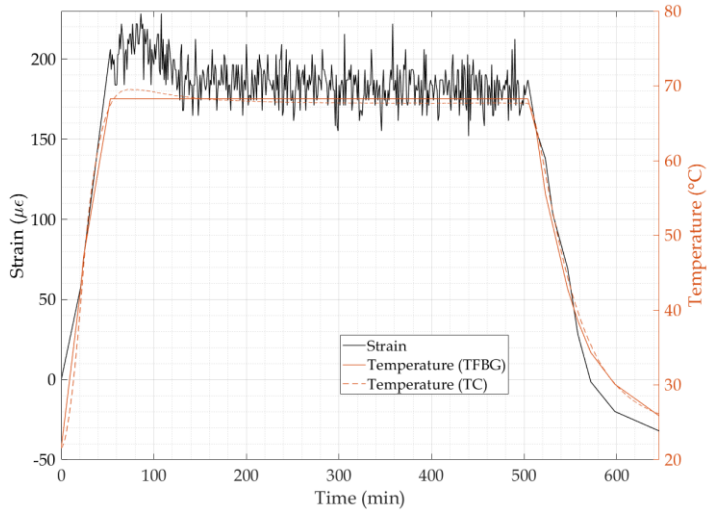


Fig.5-14. Trends of Δε and T during the curing time measured by the embedded TFBG1 and TC.

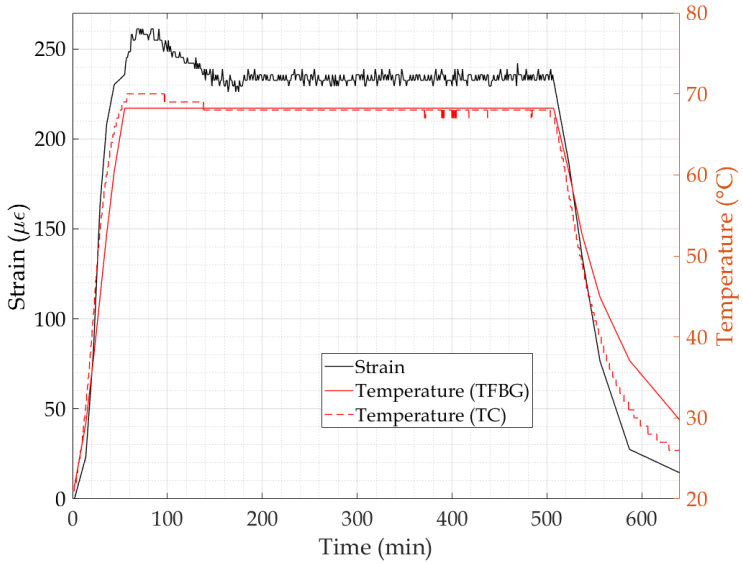


Fig.5-15. Trends of Δε and T during the curing time measured by the embedded TFBG2 and TC.

Both Fig.5-14 and 5-15 show a similar trend for the strain change during the curing. However, the strains detected from TFBG2 are generally higher than those measured with TFBG1. Furthermore, the curve after the heating-up phase of the oven, calculated by supposing an isothermal condition in TFBG1, is characterised by considerable oscillations, while that of the TFBG2 is quite flat. Another consideration regards the final deformation measured by the sensors: TFBG1, embedded deeper, reports a negative strain level at a temperature of 25.5°C, while TFBG2 measures a positive strain at ~30°C. Unfortunately, no lower temperatures were detected by the TFBGs due to their *TR*. The behaviour shown by the strain curves can be explained by considering the embedding position of the TFBGs inside the composite. Specifically, TFBG1 was embedded closer to the aluminium mould at 1 mm, this makes the TFBG more susceptible to the heat flow propagating from the mould toward the composite material. While, since TFBG2 is far from the mould and the materials composing the composite are thermally insulating, the transfer of heat from the external elements is negligible. Furthermore, as demonstrated in section 5.5.2, vacuum compaction inside the bag generates compressing effects through the side surfaces of the composite such that TFBG2 were measuring a strong negative strain. This phenomenon was not noted in TFBGs which were embedded close to the mould such as for the one embedded in the 2 mm composite and TFBG1. Now, considering the temperature rise induced to the entire manufacturing setup, a relaxing of the vacuum bag can release part of the compression imposed to the composite and OF. The result is a return of the tensile stress that holds the OF and the TFBG sensor signal is more stable. Another reason for these oscillations is due to the shrinkage occurring in the resin during the curing [1]. The shrinkage of the resin is also the cause of the negative strain detected by the TFBG embedded in the composites. With an increase of the crosslinking, the molecules of the resin tend to create a more organized semi-crystalline structure which is more rigid than the free polymeric chains characterising the no-cured resin. As consequence, after curing, the composite is restricted, and this shrinkage can be monitored by the TFBGs. In the case of TFBG2, the negative strain induced by the resin shrinkage is compensated by the relaxing of the vacuum bag which releases part of the compressive deformation induced during the vacuum compaction.

In the same way, the strain can be calculated by using the TFBG embedded inside the 5 mm composite. However, unlike the previous composite samples, this specimen was left to cure at room temperature for a longer time (~2 hours). Hence, since the embedded TC was recording approximately the same temperature (22.5°C), the strain variations are calculated in isothermal conditions by considering the temperature oscillations to be negligible (maximum ≤0.8°C). The trend of the deformation is reported in Fig.5-16, where the TFBG strain resolution is ~3 με.

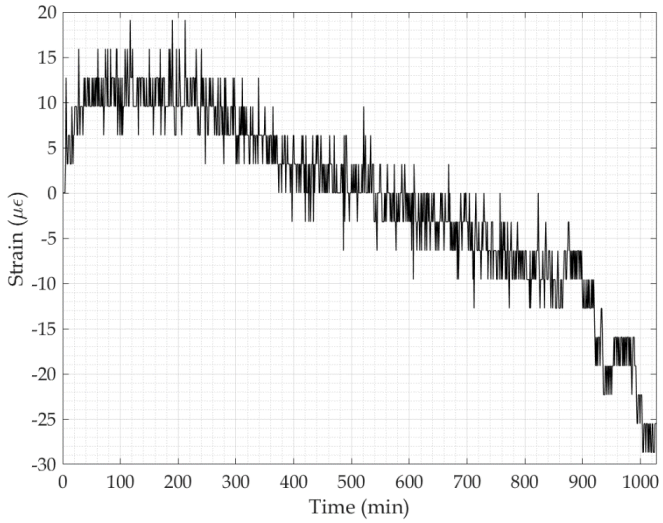


Fig.5-16. Δε of the 5 mm composite during its curing at room temperature measured with embedded TFBG3.

From Fig.5-16, the strain appears to initially increase probably for a local slight exothermic reaction of the resin and/or for the closing of the oven's door. Indeed, although the composite is cured at room

temperature, it was placed inside the oven's chamber to avoid possible fluctuations of the temperature. However, after some hours, the effect of the crosslinking starts to create the shrinking effect on the resin and the deformations measured by the TFBG take a negative slope. Initially the slope looks to be quite smooth, but after 13 hours of curing, the consolidation accentuates the decrease of strain . At the 18th hour of cure, the TFBG measured a negative strain of ~25 με.
The variation of strain induced in the resin during the curing is much strongly lower when curing at room temperature. There is no application of heat is to make the crosslinking process faster. However, the curing process is really long (16-24 hours depending by the external conditions) compared to curing in the oven and, the resin degree of cure does not reach high values making the mechanical performance of the composite poor. A proof of that was noted during the demoulding step of the composite from whose borders, small particles of resin were ripped off with the infusion layers during the removal of these latter. These particles were characterised by solid but sticky surfaces, a signal that the curing degree was not high.
In addition to the thermomechanical measurements, each TFBG was providing also the refractometric condition of the resin during the curing. These trends are reported in Fig.5-17 and Fig.5-18 with the temperatures measured by the TCs embedded close to the TFBGs.

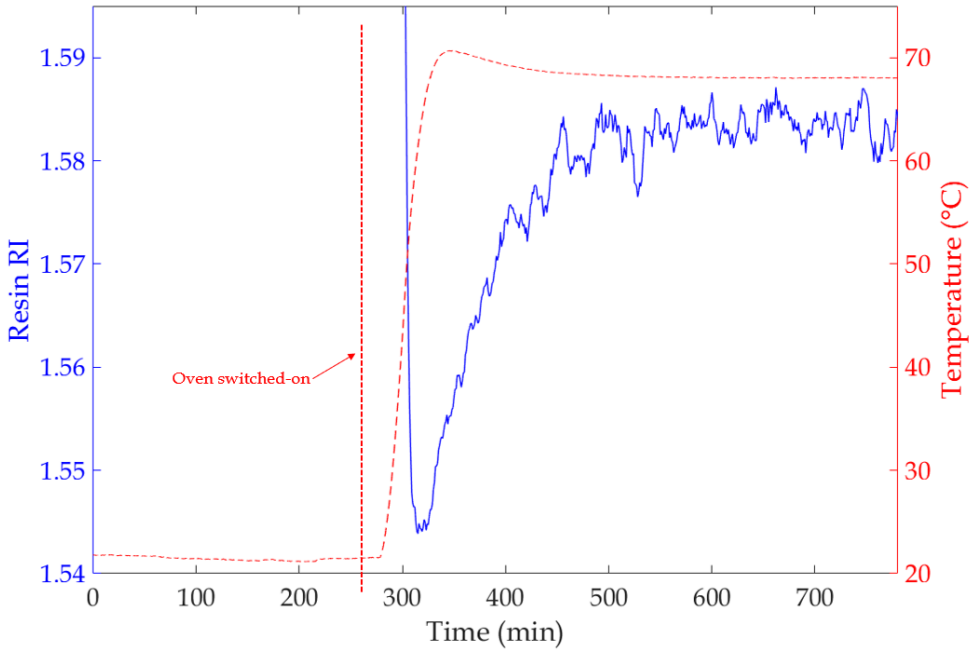


Fig.5-17. Resin RI trend during 10 mm composite curing from TFBG1 with TC temperature.

The first fact is highlighted by the refractometric measurements performed by TFBG1 regards the partial immersion of the resin on the sensor before the switching-on of the oven. Indeed, the RI curve is not present until approximately the 300th minute, which is a signal that the resin did not fully cover the sensor. If this occurs, then the measured RI is much higher with respect with the real one as the envelope area is greater than the one obtained when the sensor is fully immersed. This phenomenon is caused by slow flowing of the resin through the layers of the thicker composites, where the infusion can need hours to be completed. Specifically, in this case, the resin was probably slowly flowing along the axis of the sensor as the trend of the envelope area, obtained before the ~300th minute in Fig.5-19, and was characterised by a sluggish decrease from a constant maximum area. Since the infusion was performed at room temperature, the viscosity of the resin remains high and increases over time due to an increase in the crosslinking, which causes also a positive variation of the RI. However, with the heating-up of the temperature via the switching-on of the oven, the resin starts to flow faster through the layers thanks to a lower viscosity, so that to fully cover the TFBG. In this case, it is not possible to calculate the initial RI of the resin as the TFBG is only partially immersed, and the total immersion occurs during the heating-up phase. However, successively, the sensor is able to report the RI trend until the complete curing of the composite. The trend is similar to the RI curve measured by the TFBG

in the 2 mm composite, where from a minimum point the RI reaches a kind of oscillating plateau around a medium value. The plateau means the resin was fully cured.For TFBG2, the situation is different with respect with TFBG1 as the sensor has been fully covered by the resin a long time earlier. In this way, the resin started the crosslinking when it was surrounding the TFBG which was detecting an increase of the RI.

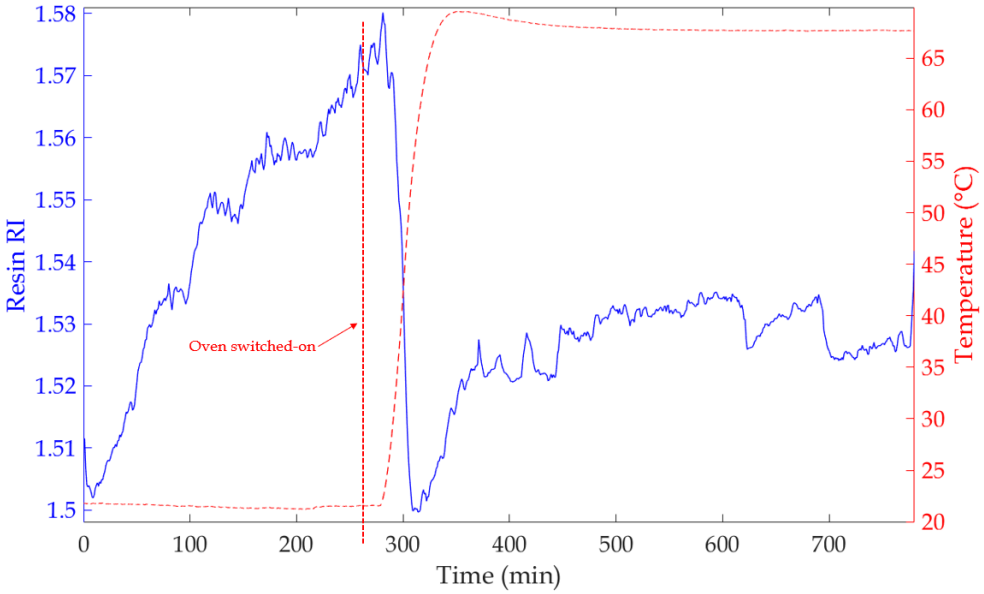


Fig.5-18. Resin RI trend during 10 mm composite curing from TFBG2 with TC temperature.

As in the previous cases, the heat generated by the oven decreases the RI of the resin as the density of the polymer decreases as well. After reaching the minimum local point, the crosslinking dominates the influence on the RI and hence, it starts to increases with the degree of cure. However, for this sensor, the plateau is characterised by large oscillations which were not present in the previous graphs. A possible explanation of this phenomenon might be the influence of bending generated from the shrinkage of the resin during the curing. In fact, as described previously, specifically in thick composites, the material has a different thermomechanical state along the thickness and at the edges due to the boundary effects. The different level of shrinking of the resin and the heat flow passing through the layers of the composite may influence the measuring of the sensor and its position in the composite. Hence, the mechanism of micro-adjustments between the layers of the composite internal structure to reach the dimensional stability can influence the measurement accuracy of the TFBG as they can change its position and orientation.

Regarding the values of RI measured by the sensors embedded in 2 mm and 10 mm composites cured in oven, these oscillate during the curing process between 1.50 and 1.595, with maximum values at the curing between 1.535 and 1.595. The degree of cure, which is related to the refractometric condition of the resin, depends strongly not only on the temperature history but also from the resin mixture ratio, impurities and the dynamics of curing process. Also, the resin, once it is mixed with the hardener is subjected, to a process of degassing to remove any bubbles generated during the mixing process. Furthermore, a time-delay can occur between the end of the degassing and the infusion due to transportation or infusion lines fixing and other technical issues. During these intervals, although slowly, the resin undergoes crosslinking as the molecules react once the mixing is occurred. Hence, different processing times mean different degrees of cure during the resin infusion and, as consequence, different RI values. All these factors make it difficult to compare the refractometric measurements performed with the TFBGs. However, a general observation can be extracted from the results achieved. In fact, the RI seems to reach higher values for a TFBG embedded between reinforcement layers closer to the mould as the TFBG embedded in 2 mm composite and TFBG1 have similar values. This may be explained by taking into account a stronger compression state of the material at a certain depth. Furthermore, the levels of strain detected from both the sensors are widely negative indicating a strong compression state, which can be related to a higher density of the material in those points. While,

TFBG2 measured a positive deformation along its axes and the RI detected is lower with respect with those obtained from the other sensors, indicating maybe a lower density of the material in that point.

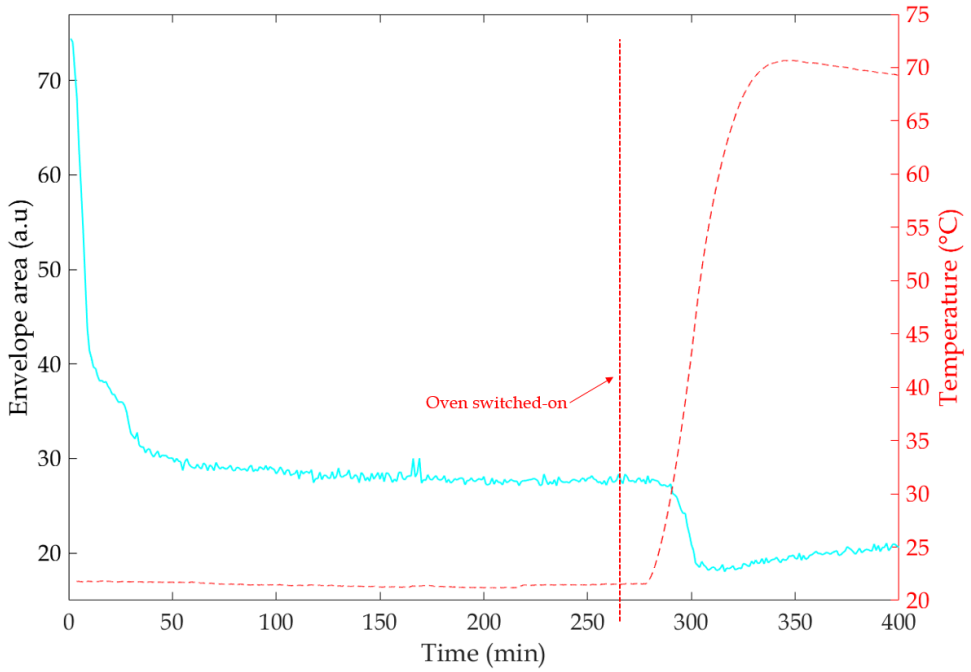


Fig.5-19. Envelope area trend detected in TFBG1 during infusion and heating-up of the oven.

At this point, the last refractometric measurements to present are those obtained from the spectra of TFBG3 embedded in the 5 mm composite. As announced previously, this sample was cured at room temperature. Hence, the RI measurements are not characterised from the typical decreasing/increasing curve with a final plateau seen in the case of samples cured with a temperature profile. In this case, the crosslinking process of the polymeric matrix occurs slowly but constantly and this is reflected in the RI measurements reported in Fig.5-20.

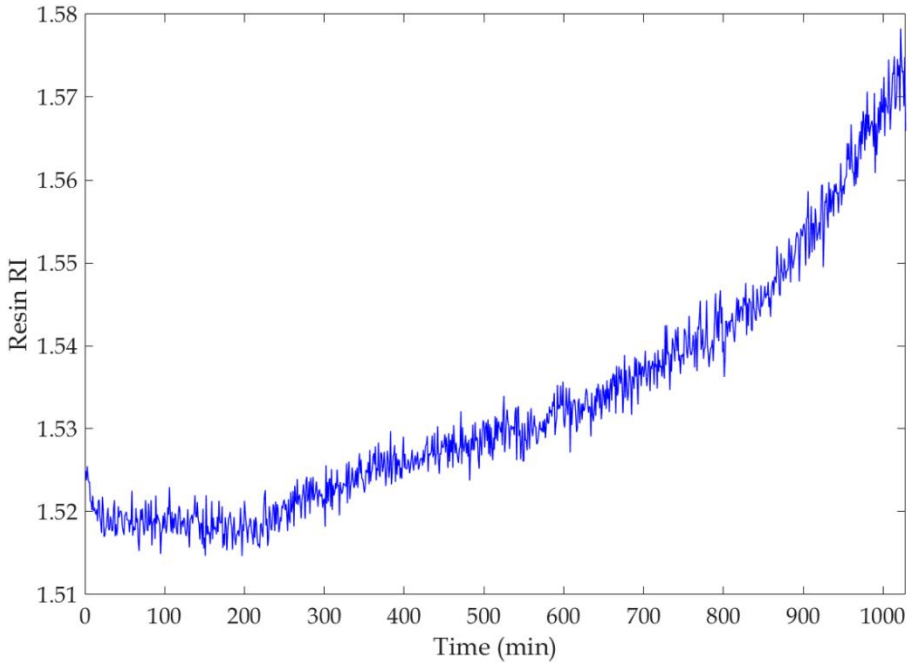


Fig.5-20. Resin RI trend from TFBG3 during 5 mm composite curing at room temperature.

From Fig.5-20, the resin RI can be observed to start from low values after the infusion process and increase to reach an almost-stable oscillating condition after ~18 hours of cure at room temperature. Since, as previously demonstrated, the RI is directly related to the degree of cure, the graph can be associated to the evolution of curing of the composite. In the last part of the graph, the slope of the RI curve becomes almost flat. This is due to the deceleration of the chemical reactions occurring in the polymer. Indeed, when the composite is cured in an oven with a temperature profile suggested by the manufacturer, usually the degree of cure reaches values between 93-98% as in the case of the 2 mm composite reported in Fig.5-10. The reason why α_r=100% cannot reached, is due to not all the reagents reacting to make the products in the crosslinking reaction of the resin. The heating-up in the oven, helps to prioritise the reactions of the reagents as extra energy is provided to the molecules, which can then react much more easily. In this way, higher α_r values are reached. However, when the curing process of the resin is performed at room temperature, the crosslinking rate is not enhanced and the reactions between the molecules occur less frequently. Hence, a greater part of the reagents remains unperturbed and not converted into the product. This means a softer curing slope and lower maximum values of curing degrees (65-70%), which is reflected by the slow increasing of the resin RI during the 18 hours of cure of the 5 mm composite. Regarding the RI values shown in Fig.5-20, the RI reaches maximum values of ~1.57, comparable with those measured from the previous samples. This is unexpected since the cure process was performed without the addition of external heat. However, the level of deformation measured via the same TFBG3, showed a moderate level of negative strain after 18 hours, a signal that the resin shrinkage contributed to increase the density of the composite in the embedding point. From the 1000th minute, the RI seems to remain stable around a certain value, which may mean that the resin has completed the curing and cannot reach higher degree of cure at room temperature.

5.7 Conclusions

In this chapter, the research was moved by the aim to investigate on the effects generated by the VARTM manufacturing process on the TFBG spectrum also considering the embedding of the sensor at different thickness of the composite, which was the focus point of the third research question. The scientific investigation of the phenomena occurred in the spectral signal of the TFBG sensors during the composite manufacturing has brought to several important conclusions.

The final and main result is that each single TFBG was demonstrated as a three-parameter optical sensor able to detect strain, temperature and the RI of the resin during the VARTM manufacturing process of thin and thick glass-fibre/epoxy composite. Indeed, the OF sensor proved to be useful in detecting the strains imposed during the lamination of the fibre reinforcement layers and the resin infusion has highlighted the difference between the thin and thick composites. Furthermore, during the infusion step, the TFBG sensor can be used also to obtain information regarding the propagation of the resin flow through the layers in terms of time, infusion degree and voids. Nevertheless, despite these important outcomes, the more interesting results are obtained by monitoring the curing state of the composites through the TFBGs.

The simultaneous strain-temperature measurements detected the health state of the composites, during curing in the oven when the temperature conditions indicated by the manufacturer were applied. Additionally, one thicker composite was cured at room temperature. Three of the four embedded TFBGs measured strain levels related to a relevant degree of shrinkage, specifically for the composites cured in oven after the cooling-down phase. The temperatures measured through the TFBGs have a good match with respect to the profile measured by the thermocouples. However, the profiles obtained from both the sensors usually deviated due to the thermal resolution of the TFBG sensors, which consequently influences also the measured strain level by the sensors. This limitation can be easily overcome by using FBG interrogator systems with a higher *swR* and/or TFBGs with sensor customisation able to increase the difference between the thermal sensitivity coefficients of the selected

peaks. Nevertheless, the maximum strain deviation calculated during the curing step of the 2 mm composite, corresponds to 2.7% of the average strain, which can be considered quite low.

Furthermore, the demodulation of the TFBGs spectra provides the RI variation of the resin starting from the infusion step. In particular, the comparison of the RI trend with the resin degree of cure performed by taking into account the 2 mm composite, and obtained from the study of its cure kinetics, showed that the RI measurements can detect the cure state of the resin and can identify the several curing phases. Indeed, from the RI trend, a deep qualitative correlation with α_r was described, such that all the cure kinetics are identified until the resin is fully cured. Therefore, the refractometric measurements may be also used to analyse the curing evolution of the other samples.

To conclude, the effects of the VARTM manufacturing steps on a single embedded TFBG, investigated by the third research question, can be exploited to monitor the thermomechanical and cure state of the composite during the several steps of its manufacturing process, easily performing a preliminary calibration of the sensor.

References

[1] L.Fazzi, G. Struzziero, C. Dransfeld and R.M. Groves, *A single three-parameter Tilted Fibre Bragg Grating sensor to monitor the thermosetting composite curing process*, Advanced Manufacturing: Polymer & Composites Science, 8 (1), p. 33-41, (2022).

[2] Y.X. Zhang and C.H. Yang, *Recent developments in finite element analysis for laminated composite plates*, Composite Structures, 88 (1), p. 147-157, (2009).

[3] T.A. Bogetti and J.W. Gillespie, *Process-induced stress and deformation in thick section thermoset composite laminates*, Journal of Composite Materials, 26 (5), p. 626-660, (1992).

[4] N. Patel and L.J. Lee, *Modeling of void formation and removal in liquid composite molding. Part I: wettability analysis*, Polymer Composites, 17 (1), p. 96-103, (1996).

[5] B. Hofer, *Fibre optic damage detection in composite structures*, Composites, 18 (4), (1987).

[6] J.M. Balvares, *In situ strain & cure monitoring in liquid composite moulding by fibre Bragg grating sensors*, Doctoral thesis, TU Delft, 2014.

[7] P. Ferdinand, S. Magne, V. Dewynter-Marty, S. Rougeault and L. Maurin, *Applications of Fibre Bragg Grating Sensors in the Composite Industry*, Materials Research Society, 3, p. 400-407, (2002).

[8] E. Chehura, A.A. Skordos, C.C. Ye, S.W. James, I.K. Partridge and R.P. Tatam, *Strain development in curing epoxy resin and glass fibre/epoxy composites monitored by fibre Bragg grating sensors in birefringent optical fibre*, Smart Materials and Structures, 14 (9), p. 354-362, (2005).

[9] V. Antonucci, M. Giordano, A. Cusano, J. Nasseri and L. Nicolais, *Real time monitoring of cure and gelification of a thermoset matrix*, Composites Science and Technology, 66 (16), p. 3273-3280, (2006).

[10] Y. Blößl, G. Hegedüs, G. Szebényi, T. Tábi, R. Schledjewski and T. Czigany, *Applicability of fiber Bragg grating sensors for cure monitoring in resin transfer molding processes*, Journal of Reinforced Plastics and Composites, 40 (19-20), p. 701-713, (2020).

[11] A.J. Thompson, J.R. McFarlane, J.P.-H. Belnoue and S.R. Hallett, *Numerical modelling of compaction induced defects in thick 2D textile composites*, Materials & Design, 196 (109088), (2020).

[12] G. Struzziero and A.A. Skordos, *Multi-objective optimization of Resin Infusion*, Advanced Manufacturing: Polymer & Composites Science, 5 (1), pp.17-28, (2019).

[13] N. Rai and R. Pitchumani, *Optimal cure cycles for the fabrication of thermosetting-matrix composites*, Polymer Composites, 18 (4), p. 566–81, (1997).

[14] G. Struzziero and J.J.E. Teuwen, *A fully coupled thermo-mechanical analysis for the minimisation of spring-in and process time in ultra-thick components for wind turbine blades*, Composites Part A, 139 (106105), (2019).

[15] M. Li, Q. Zhu, P.H. Geubelle and C.L. Tucker III, *Optimal curing for thermoset matrix composites: thermochemical considerations*, Polymer Composites, 22 (1), p. 118-32, (2021).

[16] S.J. Buggy, E. Chehura, S.W. James and R.P. Tatam, *Optical fibre grating refractometers for resin cure monitoring*, J. Opt. A: Pure Appl. Opt., 9, p. S60-S65, (2007).

[17] https://www.swiss-composite.ch/pdf/t-Hexion-Harz-EPR04908.pdf, *Hexion technical information*, (last access 20/07/2021).

[18] W.F. Sua, Y.C. Fu and W.P. Pan, *Thermal properties of high refractive index epoxy resin system*, Thermochimica Acta, p. 385-389, (2002).

[19] L. Khoun, T. Centea and P. Hubert, *Characterisation Methodology of Thermoset Resins for the Processing of Composite Materials – Case Study: CYCOM 890RTM Epoxy Resin*, Journal of Composite Materials, 44 (11), p. 1397-1415, (2010).

[20] A.T. DiBenedetto, *Prediction of the glass transition temperature of polymers: A model based on the principle of corresponding states*, Journal of Polymer Science Part B: Polymer Physics, 25 (9), p. 1949-1969 (1987).

[21] L. Fazzi, A. Rajabzadeh, A. Milazzo and R.M. Groves, *Analysis of FBG reflection spectra under uniform and non-uniform transverse loads*, Proc. of SPIE., 10970:X-1, (2019).

[22] G. Rajan and B.G. Prusty, *Structural Health Monitoring using Fiber Optic Methods*, CRC Press Taylor & Francis Group, p. 238-243, 2017.

[23] J.P. Hernandez, T. Raush, A. Rios, S. Strauss and T.A. Osswald, *Theoretical analysis of fiber motion and loads during flow*, Polymer Composites, 25, p.1-11, (2004).
[24] R. Montanini and L. D'Acquisto, *Simultaneous measurement of temperature and strain in glass fiber/epoxy composites by embedded fiber optic sensors: I. Cure monitoring*, Smart Materials Structures, 16, p.1718-1726, (2007).

5

6

Silicone adhesive degradation detection via a TFBG sensor in a simulated space environment

"Everything is perfect in the universe - even your desire to improve it."
Wayne W. Dyer

Until the 5th chapter, the sensing properties of the TFBG sensors were exploited on a thermosetting polymeric matrix to detect its health state from the manufacturing process until the beginning of its operational life through the application of a thermal load. All the previous activities were executed in atmospheric environmental conditions, in which the pressure considered was 1 atm and can represent the use of materials on the ground or for aeronautical engineering. From now on, the same monitoring TFBG techniques will be used in the context of silicone elastomers for space applications.

The research question that motivated the investigation carried on in this chapter, and in the next one, was born by a double aspect. The first is related to the aim of providing a sensing technology that may allow multi-parameter measurements even in space environmental working conditions, where any material is undergone to severe degrading operational life. While, the second aspect regards the motivation to raise the bench of the state-of-art of the structural health monitoring by combining the multi-sensing ability of the TFBG with its low intrusiveness to monitor the state of space qualified materials while working in their standard operational environment.
Therefore, the fourth research question is:

- *How do the space environmental conditions influence the transmission signal and the sensing abilities of the TFBG sensor even once this is embedded in a space qualified silicone adhesive?*

As reported in the introduction chapter, the space environment puts any material into harsh environmental working conditions where it is likely to degrade more easily and rapidly both mechanically and chemically. The space environment includes perturbations such as cosmic rays, extreme thermal gradients and cycling loads, and atomic oxygen (ATOX). A factor common to all the space applications is the total or partial absence of the Earth's atmosphere. This means that the effects of the pressure surrounding the material are not anymore negligible as high-vacuum can influence strongly the dimensional stability, degradation state and the chemistry of the materials, as introduced in the first chapter.

Specifically, here, a space qualified silicone adhesive named Nusil® CV16-2500 was tested in high-vacuum under cycling thermal loads while monitored by an embedded TFBG used as a three-parameter sensor. The TFBG was used to measure the thermomechanical variations and refractometric conditions induced by the thermal loads and high vacuum inside the elastomer to evaluate its ageing, degradation level and health state. However, first of all, since the TFBG is composed of several materials, these

were tested for vacuum compatibility via outgassing tests. This verified which components were able to work, without compromising the safety of the equipment, in the absence of atmospheric pressure. For the aims previously described, the Nusil® CV16-2500 silicone was used as an adhesive between two thin cover glasses, and the space environmental ageing was simulated by thermal cycling in high vacuum conditions (better than 10^{-5} mbar). These operational conditions can induce variations in the silicone adhesive with respect to its original properties such as dimensional stability, chemical composition, generated contaminants, discoloration and, mechanical or optical degradation. Therefore, surrounded by the adhesive, in the centre of the cover glass sandwich, a weakly tilted FBG sensor was placed to obtain information from its spectra on the state of the polymer during the test. The three parameters, temperature, strain and RI of the silicone were, simultaneously and independently measured, by performing the thermomechanical and D-T demodulation techniques presented, respectively, in the second and third chapters. These parameters were used to evaluate the "health" state of the silicone during the vacuum thermal cycles. Furthermore, simultaneous TFBG thermomechanical measurements were demonstrated to provide a better understanding of the material behaviour and as a potential solution to non-localized measuring issues when using the classical approach based on fibre optic or electrical strain-gauges and a TC to compensate the temperature. The trends of the measured parameters are reported during the entire testing time, with a comparison between the self-compensated TFBG and the classical method to measure the thermomechanical variations.

The testing activities and the manufacturing of the samples were performed at the Materials and Electrical lab and the TEC-QEE section of European Space Agency (ESA), ESTEC site, while the entire sensing equipment was provided by the NDT lab of the Aerospace Structures & Materials department of Delft University of Technology. This research is the result of a collaboration with Nuno Dias (ESA), Dr. Malgorzata Holynska (ESA), Dr. Adrian P. Tighe (ESA), Riccardo Rampini (ESA) and Dr. Roger M. Groves (TU Delft).

I want to dedicate a special thanks to Nuno Dias and Dr. Malgorzata Holynska for their technical, friendly and constant support during the almost two years of experience at TEC-QEE section of ESA/ESTEC, and for the same reasons to the promotor of the project Dr. Roger M. Groves.

The results of this research have been published in Measurement Science and Technology journal [1].

6.1 Vacuum compatibility of the TFBG components

The OF containing the TFBG sensor was composed of several organic parts in addition to the concentric glass layers, which may show strong outgassing when the working environment is characterised by high vacuum. To avoid high levels of contaminants on the samples and in the testing facilities, a preliminary outgassing test was performed to verify the ability of the organic materials to tolerate the vacuum without incurring in an excessive emission of volatile substances. Therefore, a specimen of each kind of material composing the OF was prepared and tested following the normative ECSS-Q-ST-70-02C [2]. Specifically, the outgassing is also denominated a μ-VCM test and it is performed in a dedicated facility, in which the material is allocated inside a hand-made open aluminium capsule (Fig.6-1) and undergoes a high vacuum at high temperature. Each sample cup must be filled with 100 mg to 300 mg of specimen (tare not included). Three specimens were used for each material. The pieces present in Fig.6-1 were the protectors of the OF



Fig.6-1. Samples in aluminium capsules ready to be tested in μ-VCM facility.

connectors and some pieces of the OF coated by the acrylate coating. Even though not present in this figure, the pin of the connectors was also tested. While, the silicone adhesive was not retested as it is already certified to work in the space environment. The samples were placed in a chamber with controlled humidity levels and they were weighed several times. Once, the samples are ready to be tested, they are placed inside the outgassing facility (Fig.6-2), which, in this case, is a vacuum cylindrical chamber. Inside the chamber, two plates, sliding relative to each other, are present. The specimens were inserted into the cup, which was placed in the holes present on top of the bottom plate, while the holes of the upper surface are provided of so-called collector plates. Once the chamber is closed, each of these latter is placed right above a single specimen with the task of collecting the outgassed material that is flowing out from the specimen. The dimensions of each element of the testing setup are available in [2]. Once all the specimens are inserted into dedicated spaces and the collector plates are allocated, the chamber can be closed and sealed from the surrounding environment.

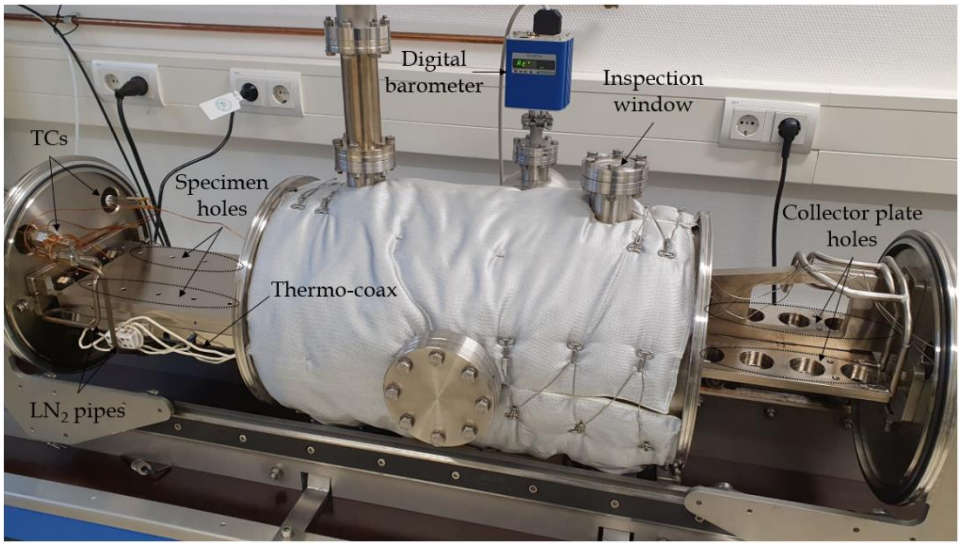


Fig.6-2. µ-VCM facility.

The test was performed by respecting the parameters asserted by the standard ECSS normative:

- Temperature of 125 °C with ± 1 °C accuracy.
- Humidity from 40 % to 80 % RH with ± 1 % RH accuracy.
- Vacuum better than 10^{-4} Pa with ± 10 % accuracy.
- Microbalance from 1×10^{-6} g.

The outgassing test was conducted for 24 hours. After the test, the specimens were weighted and the collector plates were extracted, checked and weighted as well to obtained the mass outgassed from each specimen. The weighing of the specimens and the collector plates allows the percentage of outgassed mass from the materials to be calculated. The standards also provide a procedure to also take into account the water absorption of the specimen after testing due to the humidity present. Indeed, water is not always seen as a critical contaminant in spacecraft materials, hence until certain limits the result may be acceptable. In Fig.6-3, the collector plates corresponding to the protectors of the OF connectors are reported after the test. As their surfaces are full of a liquefied element, this was a terrible outgassing result for the relevant material. In Table 6.1, the outgassing percentage of the materials tested is reported. These percentages are the averages obtained from the values of the three specimens tested for each material. Here, the



Fig.6-3. Collector plates after µ-VCM test corresponding to the material of the OF connector protectors.

values indicate that the protectors of the OF connectors outgassed more than a fifth of their mass, which is a huge amount for a space application. The acrylate coating over the OF and the pin of the connectors showed acceptable values. The acronyms present in Table 6.1 have the following definitions [2]: **TML** is the total mass loss of material outgassed from a specimen that is maintained at a specific constant temperature and operating pressure for a specified time; **CVCM** is expressed as a percentage of the initial specimen mass and is calculated from the condensate mass determined from the difference in mass of the collector plate before and after the test; **RML** is the total mass loss of the specimen itself without the absorbed water, which is basically the TML value that does not include reabsorbed water.

Table.6-1. Percentage of mass loss after μ-VCM test for each specimen.

Specimen	n°	TML (%)	CVCM (%)	RML (%)
OF	1	2.348	0.162	2.237
	2	2.499	0.160	2.384
	3	2.280	0.338	2.178
Average		**2.376**	**0.220**	**2.266**
2σ		**0.112**	**0.102**	**0.106**
Protectors of the OF connectors	1	22.527	8.140	22.480
	2	22.583	8.490	22.537
	3	22.685	8.141	22.638
Average		**22.599**	**8.257**	**22.552**
2σ		**0.080**	**0.202**	**0.080**
Connectors pin	1	0.293	0.023	0.145
	2	0.282	0.011	0.145
	3	0.284	0.018	0.142
Average		**0.286**	**0.017**	**0.144**
2σ		**0.006**	**0.006**	**0.002**

The values reported in the above table confirms what the collector plates were suggesting. Specifically, the elastomeric material that protects the ends of the OF when fitted to the connector, was incurring an excessive outgassing during the test as the total mass loss is 22.599%. This means a fifth of its mass was outgassing outside from itself and depositing on the collector plate. A further consequence of this massive outgassing was noted around the holes of the support plate of the μ-VCM facility, where some deposits were present once the test was completed (Fig.6-4).

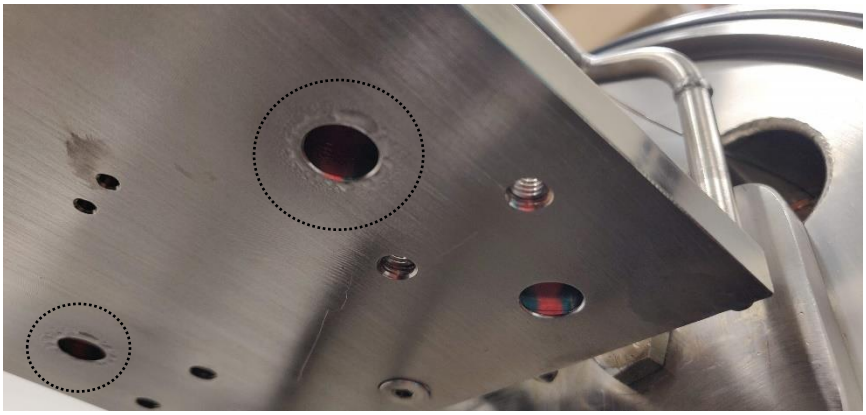
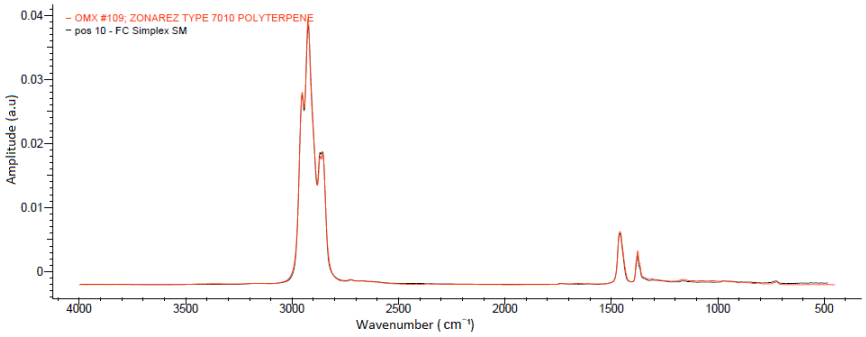


Fig.6-4. Deposits of outgassed material around the holes of the support plate.

Therefore, an analysis of this outgassed material was necessary to perform the right cleaning of the facility and to have a complete analysis of the outgassing test. This task was achieved by using Fourier-transform infrared (FTIR) spectroscopy, which allows the detection of organic contamination on surfaces. The procedures, requirements and specifications were performed by following the dedicated standards ECSS-Q-ST-70-05C [3]. Briefly, the material on the surface of the collector plate was

collected and mixed with an easily volatile chemical solution when exposed to air. Therefore, a thin layer of this solution is applied with a pipette onto special circular lenses of a rotation system of the FTIR. Once the lenses were filled, the rotational system was placed inside the spectrometer and a vacuum was created inside the chamber. A light beam, with wavelength from the near-infrared (NIR) to the far IR, is then sent from a laser through each lens and received from a detector placed on the other side. The detector analysed the light transmitted by passing through the lens and returns a graph such as the one reported in Fig.6-5. At this point, the transmitted spectrum was compared with an online database of spectra shared in the ESA laboratories. In particular, the software returns the percentage of compatibility between the materials, since some contaminants can deviate the results. In the case of the material outgassed from the OF ends protectors, the comparison returned a compatibility of ~99% with polyterpene; in Fig.6-5 the comparison between the spectra can be observed.



Name	Value
Name	ZONAREZ TYPE 7010 POLYTERPENE
Chemical Description	POLYTERPENE
Classification	POLYTEREPENE AND NAPHTHENE RESINS
Density	(Specific Gravity)= 0.980
Saponification Number	~0
Softening Point	(RING & BALL) 10C
Solution Data	Acid Number= ~0
Source of Sample	ARIZONA CHEMICAL COMPANY, PANAMA CITY, FLORIDA
Technique	NEAT

Fig.6-5. Result of the FTIR analysis and comparison with spectra of the materials of the database.

This component was banned from the use in vacuum chambers and removed from each OF.

FTIR spectroscopy is an important tool to detect the nature of organic elements, as this allows an easy investigation into the consequences contamination present on the surfaces of the components. Furthermore, another important point is the cleaning of the facilities, a knowledge of the contaminants nature allows to choose the best cleaning strategies to reduce to a minimum the contamination level before a new testing campaign.

6.2 Importance of silicone monitoring in space applications

As previously described in section 1.1.2a, the space environment will expose materials to harsh operational conditions such as high vacuum, ultra-violet (UV) and ionizing radiations, thermal cycles, micro-gravity, atomic oxygen (ATOX), high accelerations, vibrations and space debris. It is then easy to understand that the original state and properties of the used materials can be influenced and modified due to the effects of each of these perturbations or by their combination [4]. Although silicone adhesives have excellent environmental compatibility properties (such as low outgassing, good thermal stability and excellent elastomeric properties over a wide range of temperatures [5]), a high vacuum still induces anyway polymer outgassing of additives and low-molecular weight residues. This affects the original dimensional stability and composition of the material as well as depositing contaminants on nearby cold surfaces. Furthermore, the interaction of the contaminant layers with UV or ionizing radiation, thermal cycles and ATOX can cause their fixation causing severe issues [6].

Other important factors of many space missions are the rapid thermal excursions and cycles. For example, in LEO space missions, spacecraft and satellites switch from sunlight to shadow cycling based on their orbit. The typical temperature fluctuations range is between -100°C to over 300°C [7], which

can strongly influence the polymers' mechanical performance during the mission lifetime. In addition, this large temperature excursion generates a further issue when the silicone is used as an adhesive to bond elements of different nature. Indeed, if the CTEs between the elements do not match each other, cracking may be induced which weakens the bond strength.

From the chemical point of view, high temperatures or severe thermal variations can induce new chemical reactions in organic molecules including undesirable post-curing or ageing, rupture of bonds and discolouration of the material [8]. This has the possible consequence of the silicone adhesive losing its optical properties, which originally made it extremely useful in space solar cells or other applications. These effects mentioned above can be caused only by high-vacuum and thermal cycles, however, their combination with other space environment factors makes the operational working conditions even more severe. Since these working conditions exist, the possibility to have a premature failure and a degradation of the efficiency must be taken into account. For this reason, the normative legislates that the space materials are required to undergo strict testing campaigns to determine their suitability for space applications and to evaluate their behaviour and the consequences of space environment exposure [9]. In this way, premature failures and efficiency degradation can not only be avoided or minimised, but even characterised and analysed to provide the best countermeasures that limit losses. In this scenarios, the multi-parameter weak TFBG is here proposed to detect and monitor simultaneously the thermomechanical and chemical state of a silicone adhesive operating in a space environment simulated high vacuum thermal cycling test. Specifically, as the TFBG sensor satisfies the embedding requirements of low intrusiveness (Ø125 µm) and mass (~65 g/km), it was embedded in the Nusil® CV16-2500 silicone used as adhesive between two cover glasses. Therefore, the strain-temperature measurements were used to monitor the change in the thermomechanical state of the silicone material induced by the thermal cycles. These data were also used to correct and compare with the deformation trend obtained by using the TC temperature compensation of the TFBG spectrum, which is the classical strain-gauge approach.

As already demonstrated in chapters 3 and 5, at the same time, the TFBG can measure the surrounding RI. Then, in this chapter silicone RI variations were observed, which enabled an understanding of possible changes of the original refractometric properties of the silicone material. In particular, the RI variations occurring in a polymeric material can be caused by curing and post-curing [10,11], ageing and degradation [12,13] with the temperature variation. Hence, the silicone RI variation might indicate an evolution of the material, during the thermal cycles. To investigate further, Differential Scanning Calorimetry (DSC) measurements were also performed.

6.3 Methodology

In the next section the TFBG, the tested sample and the testing facility are presented in detail. Specifically, in section 6.3, the TFBG embedded in the cover glass sandwich is described in detail along with reporting the thermomechanical and refractometric calibration. Next, section 6.3.2 is dedicated to the cover glass sandwich sample and testing facility description, specifically the materials, the dimensions and the components are described. The final section 6.3.3 details the parameters used to perform the thermal cycles under high vacuum environmental conditions.

6.3.1 TFBG specifications and calibration

The TFBG sensor embedded in the silicone adhesive was manufactured by FORC-Photonics in not-recoated (~20 mm across the TFBG length) Fibercore PS1250/1500 OF by using the rotated phase-mask technique. The sensor has a 3° tilt angle and is 4 mm long. The coating comprises a layer of UV-cured acrylate. The TFBG was certified by the manufacturer to operate in a temperature range between -40°C and 85°C without degradation of the spectrum or the coating layer for a long exposure time. During the entire calibration and testing stage, the TFBG spectra were always acquired by using, as for the previous works, the NI PXI-4844 interrogator. Before embedding the sensor, the sensitivity coefficients and of the Bragg and Ghost peaks were determined by performing the thermomechanical calibration as described in sections 2.4.1a and 2.4.1b. The calculated coefficients are

$K_{\varepsilon,Bragg}$=1.255±0.008 pm/με and $K_{\varepsilon,Ghost}$=1.255±0.01 pm/με where the accuracy of the coefficients takes into account also the repeatability of the measurements more specifically each deformation level was repeated 5 times. The thermal calibration resulted in the following thermal sensitivity coefficients: $K_{T,Bragg}$ =8.96±0.22 pm/°C and $K_{T,Ghost}$=9.53±0.27 pm/°C, with a *TR* of the TFBG sensor of ~7°C. The refractometric calibration was also performed by using the setup shown in Fig.3-4 and the procedure described in section 3.2. Specifically, a set of RI oils (range: 1.3-1.7 ±0.0002 between 18°C and 30°C, produced by Cargille laboratories) was used on top of a polycarbonate flat surface to immerse the sensor. Once the TFBG spectra acquisition was completed, the spectra were demodulated using the D-T technique described previously in chapter 3. The envelope areas were then normalised with respect to the one obtained by immersing the TFBG in 1.32 RI liquid. In this way the correlation points are found along the RI range and, several fitting functions can be taken into account based on the correlation points trend by considering different degree of polynomial regression. For the silicone adhesive used in this study, the RI is around 1.43 [14], and considering the temperature range and the duration of the test, the minimum and maximum expected variations are within the 1.4-1.45 RI range. Hence, to optimise the RI measurement performance of the TFBG, the fitting correlation function was obtained inside this RI range. A study of the RI measurement performance was made as presented in chapter 3. Indeed, as a strain variation induces a shifting of the cladding peaks wavelength, it can comprimise the accuracy of the measured RI by influencing the value of the envelope area. Therefore, an analysis was performed to calculate a standard deviation that also considers this kind of error. The R^2-error of the fitting is 0.9999 by using a 4th degree polynomial function, with a maximum normalised area standard deviation of 0.0016 and a mean RI resolution of 2×10^{-7}.

6.3.2 Sensorised cover glass sandwich and testing facility

The cover glass sandwich sample was composed of transparent optical silicone adhesive Nusil® CV16-2500 which was used to bond together two layers of Cerium Doped Microsheets (CMX) cover glass (20×20×0.05 mm). These materials are typically used for space solar arrays to protect the solar cells from the space environment (for solar arrays, a single sheet of cover glass is bonded onto the cell surface). Therefore, the TFBG sensor was embedded centrally inside the adhesive during the manufacturing of the sample as shown in Fig.6-6. A k-TC (Ø≈100μm) sensor was also embedded in the silicone adhesive to monitor the temperature trend during the test and to compare it with that measured by the TFBG sensor. Once the TFBG and the TC sensors were embedded and the silicone adhesive cured, the final thickness of the sample was about 0.5 mm. The recommended temperature curing profile of the silicone adhesive is 4 hours at 65°C [14]. Curing was performed in an oven once the cover glass sandwich was assembled with the embedded sensors.

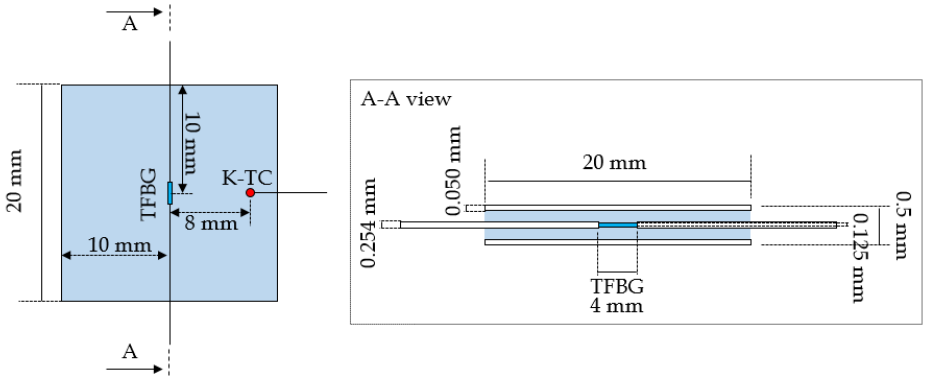


Fig.6-6. Schematic of TFBG sensorised cover glass sandwich sample design.

High vacuum thermal cycling was performed at the European Space Research and Technology Center (ESTEC) with the MCross facility. This is a high vacuum testing chamber used to simulate the space environment, such as UV/VUV radiation, thermal cycling (fatigue) and long-term temperature ageing exposure of materials. Since this research was focused on the high vacuum thermal cycles effects on the silicone adhesive, a test chamber connected with a Pfeiffer Turbo Molecular pump and a membrane

pump was used to create a high vacuum down to 10^{-6} mbar. A metallic sample plate is placed on top of a resistance heating plate (thermocoax), which is mounted on a liquid nitrogen coolable plate (Fig.6-7a and Fig.6-7b). The chamber is also equipped with Kapton®-coated K-type TCs, which can be attached to the sample or the plate for temperature monitoring. Furthermore, to acquire the spectra of the OF sensors, the facility was also upgraded with two hermetic polarization-maintaining fibre optic feedthroughs manufactured by SQS. Each of these feedthroughs has two input/output FC/APC connectors, which are externally connected with two optical circulators, and hence, to the interrogator system.

A Differential Scanning Calorimetry (DSC) test was also performed on the silicone adhesive to investigate exothermic or endothermic reactions within the temperature range. The DSC test detects all processes with thermal flow (as for example phase transition), however, these not necessarily are related to chemical reactions. This test was conducted by using a TA Instruments DSC 2500 machine at the thermal lab at ESTEC. The temperature range used for the DSC test was between -150°C to 250°C with a heating-up/cooling-down ramp of 10°C/min in nitrogen atmosphere.

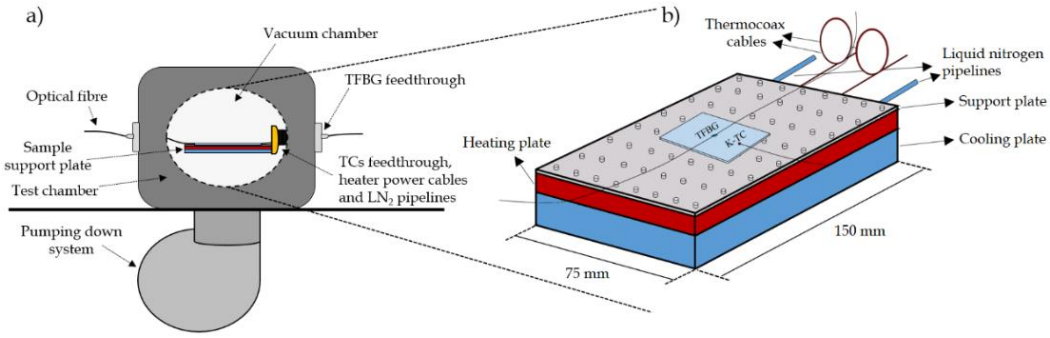


Fig.6-7. Schematic of a) the MCross facility and b) the support, heating and cooling plates.

6.3.3 High vacuum thermal cycling test parameters

The sample was clamped on the support plate using a few layers of Kapton® Polyimide tape to ensure good thermal contact between the elements. Indeed, since the test was performed in a vacuum environment, it was important to control the contact quality for the heat transfer between the heating/cooling plate and the sample. Once the cover glass sandwich was mounted on top of the sample support plate (Fig.6-7b), a vacuum was applied inside the chamber through the pumping down system. The data acquisition system of the TFBG sensor and the mounted TCs recorded the spectra and the temperature values during the entire exposure time. When the pressure inside the chamber reached ~2×10^{-6} mbar, the heating plate was switched-on so that the thermal cycling started. At a certain time, after the stabilisation of the temperature, the heater was switched off and the cooler was activated to cool-down the sample. Through this cyclic temperature inversion, the sample was exposed to thermal ageing cycles between ~-20°C and ~85°C, as shown in Fig.6-8.

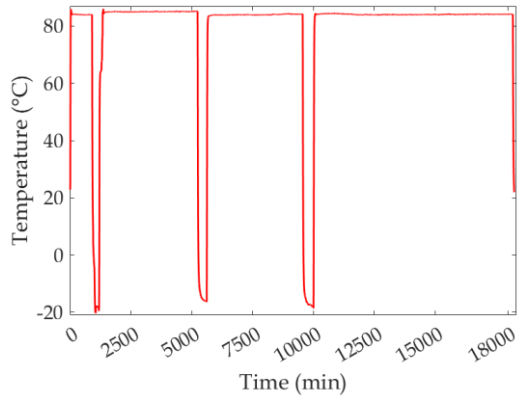


Fig.6-8. Temperature profile measured by the embedded TC during the test.

6.4 Results

In this section the strain-temperature and the RI measurements detected from the TFBG sensor in the silicone adhesive during the thermal cycle test are presented and commented on. An interesting aspect is the comparison between the strain values measured with the single self-temperature compensated TFBG and those obtained using a classical approach by compensating the temperature effects on the TFBG spectrum using the TC measurements. Indeed, one of the most used previous techniques to compensate the cross temperature sensitivity on the standard FBG sensors comprises the removal from the total Bragg wavelength shift of the part due to the temperature variation recorded with TC measurements [15]. While the TFBG measurements of the silicone RI highlighted a variation compared to the initial condition, which may be due to a physical properties evolution of the adhesive.

6.4.1 Strain measurements with classical TC compensation approach

From Fig.6-9, it can be seen from the recorded Bragg peak wavelength variation and the TC temperature profile, it is possible demonstrate these have some delays at different times. Hence, the compensation of the TFBG cross-temperature sensitivity by using the TC measurements suffers strongly from non-localized measurements, specifically in a vacuum environment. This is due to the different location of the two sensors and an extremely non homogeneous distribution of the temperature in vacuum. This implies that conduction can be considered as the only heat transfer mode, and this consequently, results in a delay in the sensitivity of sensors placed in different points. The delay can increase with the distance between the two sensors.

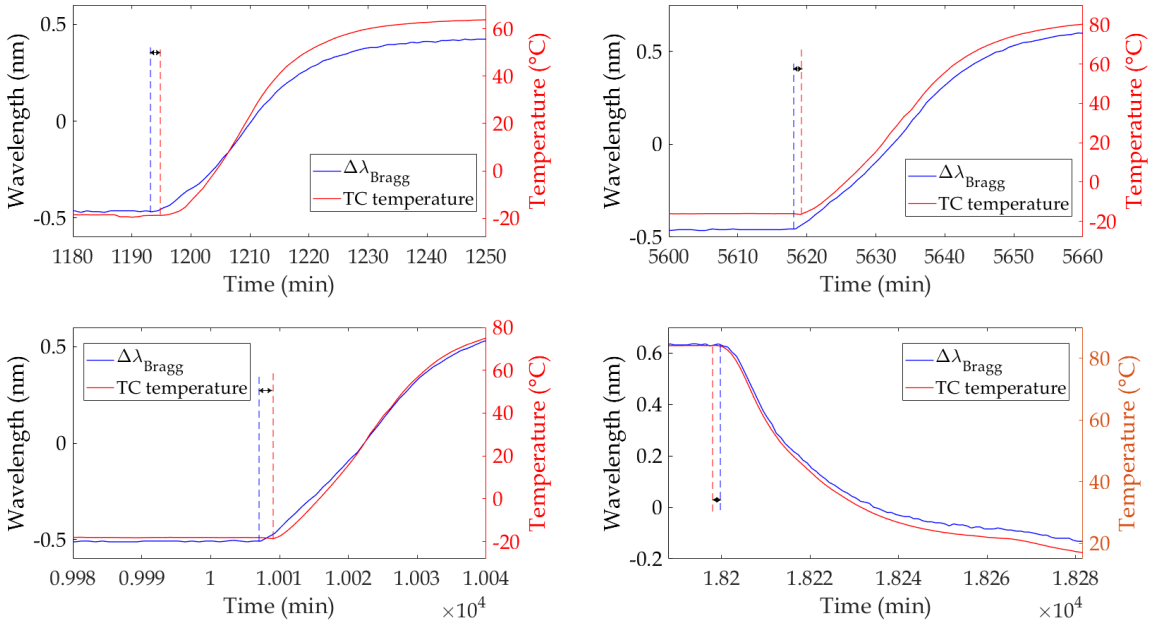


Fig.6-9. Bragg wavelength variations and TC temperature trend during the testing time.

As a consequence, since the Bragg wavelength shift is not properly compensated in same range, the measured deformation curve has unexpected trends or inaccurate values as observed in Fig.6-10. Moreover, since the test is performed in vacuum, the two different locations can experience different temperatures which means an error in the evaluation of the strain.

These issues can be overcome by using the TFBG as a dual parameter single sensor because, being self-compensated, the measurement is point-localized removing the delay between two different devices. The next section reports the results of the simultaneous strain-temperature measurements of the TFBG, showing that this sensor is promising for space environmental measurements under vacuum.

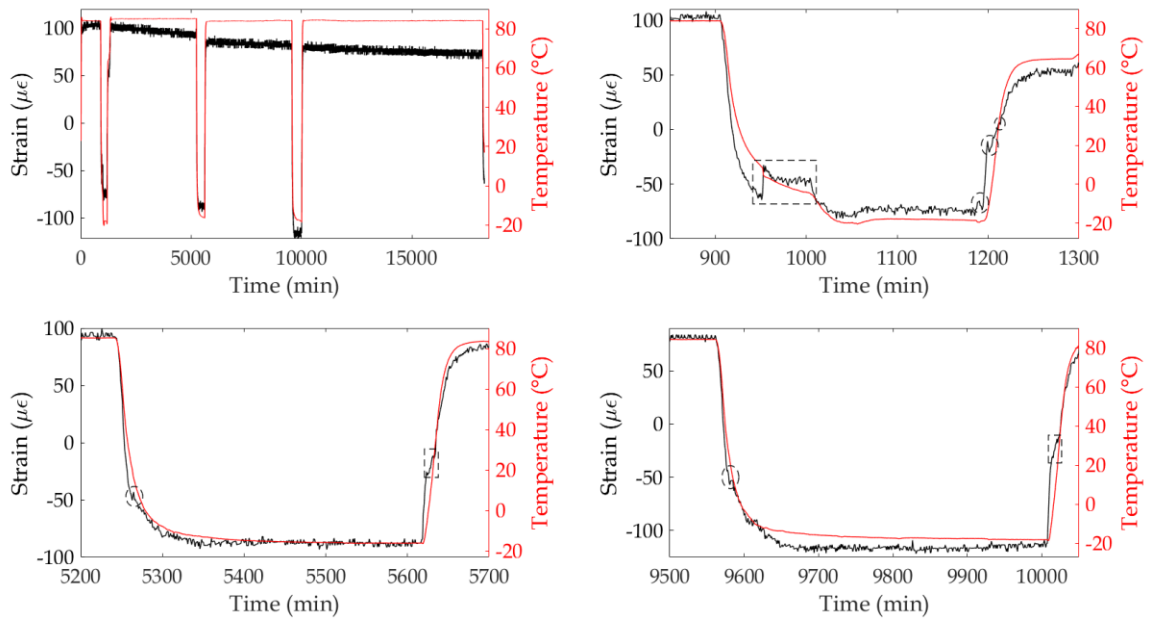


Fig.6-10. Strain values measured by compensation of the TFBG through TC temperature measurement.

6.4.2 Strain-temperature measurements with self-compensated TFBG

As made previously for the thermally loaded composite plate (chapter 4) and the monitoring of the composite curing (chapter 5), by using the demodulation technique represented by Eq.II.26, the strain-temperature variations can be calculated starting from a reference condition. This latter is considered as the switching-on moment of the heating plate. In Fig.6-11, the strain and temperature trends measured with the single TFBG are reported, in blue and red, respectively, and compared with the curves obtained from the compensation of the Bragg wavelength shift with the TC measurements.

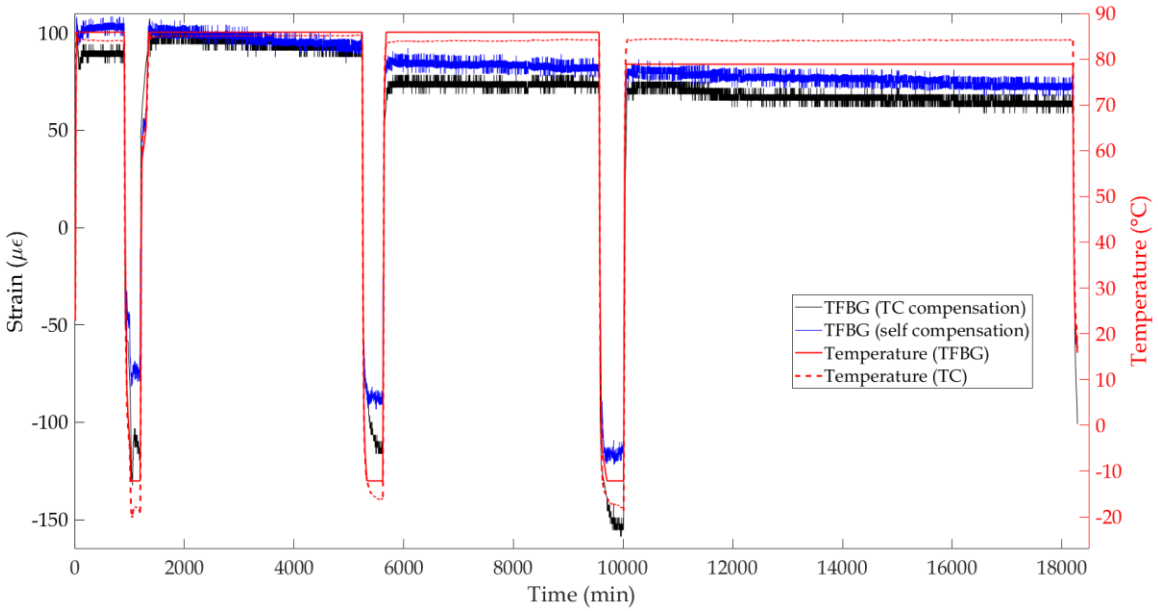


Fig.6-11. Strain values measured by self-compensated TFBG and comparison with those of Fig.6-10.

From Fig.6-12, the silicone strain trend, measured with the self-compensated TFBG, does not show the unexpected spike or behaviour which was seen using only the TC compensation (Fig.6-10). Although the strain trends of the two different techniques are similar, the measured TFBG strains have a smoother and continuous trend, underlining the effectiveness of the self-compensated TFBG. The

difference in strain and temperatures, even after the transient of thermal excursion, is due to the TR of the TFBG and the different embedding positions of the two sensors. In fact, as introduced in section 2.4.1, the measurements of the strain are performed in accordance with the sensor's TR, this causes a strain accuracy of ±12.8 με. Regarding the thermomechanical state of the silicone adhesive during its ageing, the TFBG measurements suggest a permanent shrinkage of the material following the thermal cycles. Using both techniques, there is a consistent negative deformation state of 60.8 με at the same initial temperature (22.8 °C). This means that the silicone adhesive has undergone a change of its mechanical state, which could be due to a combination of factors such as the variation of its physical state (due to post-curing, ageing) and the different CTEs of the several materials that compose the sample.

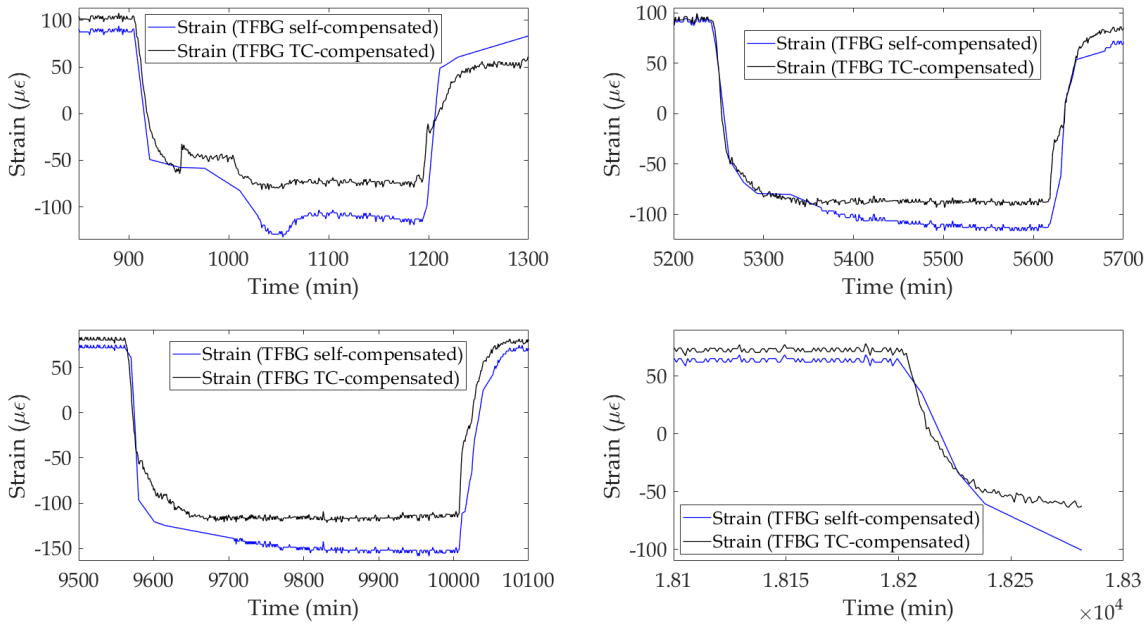


Fig.6-12. Strain curves during heating-up, cooling-down and final phases of Fig.6-11.

6.4.3 Silicone RI measurements detected by the TFBG

Simultaneously to the strain and temperature measurements, from the envelope area of the upper and lower cladding peaks in the TFBG spectrum, the silicone RI can be determined by applying the D-T demodulation technique (as for the epoxy resin in chapter 5). However, the same envelope area can also give an indication of the surrounding RI as it is dependent on this. The measured trends of the envelope area and RI of the silicone adhesive are reported, respectively, in Fig.6-13 and Fig.6-14 during the entire testing time. From the typical trend of the TFBG refractometric calibration curve (as in Fig.3-7), it is evident that the envelope area increases with increasing temperature, while it decreases during the cooling-down phase (Fig.6-13). The RI range given from the envelope area excursion is between 1.4 and 1.45, as expected. The evolution of the silicone RI shows the expected behaviour with changing temperature. The initial silicone RI measured by the TFBG sensor was 1.42648 at 22.6°C, which is close to the value declared by [14]. From this value, the RI changes according to the thermal and physical properties of the material where the TFBG is embedded [16]. At the end of the test, the envelope area and the RI were different with respect to their initial value at the same temperature. In particular, the envelope area reached a final variation of -2.1%, which in terms of RI means a value of 1.42744 at the same initial temperature. Now, considering the level of strain of the tested silicone at the same time, the error induced on the RI measurement is in the order of 10^{-5} [17], while that linked to the temperature is negligible. This implies that the silicone RI variation is fully induced by some physical or chemical processes generated in the material during the high vacuum thermal cycles.

For a more accurate investigation, a DSC test was also performed on a sample of pure cured silicone material to detect eventual absorption or release of heat due to chemical reactions or physical processes

(such as phase transitions) induced by temperature variations. The heat flow as a function of temperature variation during the DSC test is shown in Fig.6-15. The heat flow rate detected in the silicone during the DSC test, shows the exothermic (positive y-axis) and endothermic (negative y-axis) processes occurring in the elastomer with the temperature variation. This heat flow trend suggests that the thermal characteristics of the silicone may change due to temperature excursions. Furthermore, as it is possible to note in Fig.6.15, although the heat flow trend is reversible, some small spikes and bumps are present at several temperatures. These may suggest the generation of volatiles which release or absorb heat during the test due to different thermal conditions. The effect of volatiles evolution is expected to be even stronger in simulated space environments due to Le Chatelier's principle [18]. However, another aspect to consider regards the emission of volatile acetic acid from the silicone adhesive during the (post-) curing process [19]. These phenomena cause an evolution of the material, and this change may be detected by the TFBG in refractometric terms by measuring small changes in the RI.

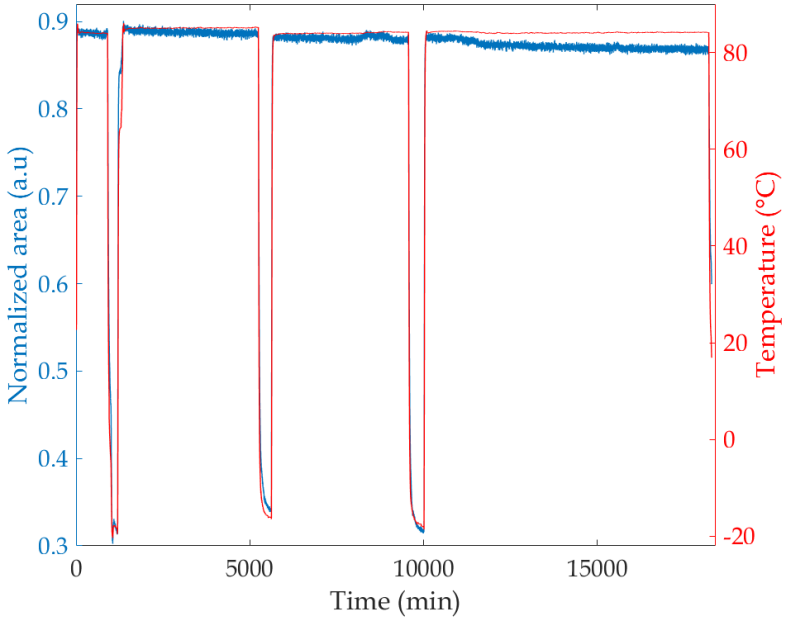


Fig.6-13. Cladding resonance peaks envelope area trend.

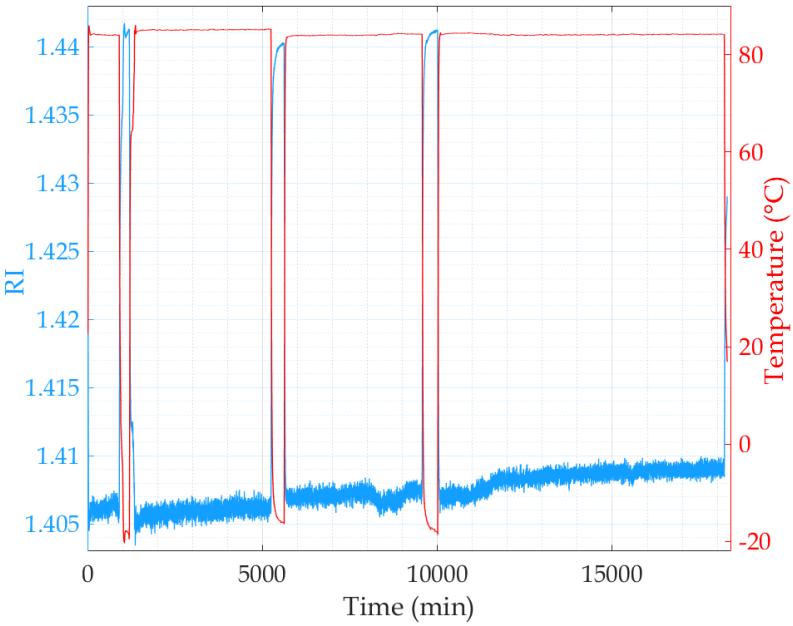


Fig.6-14. Silicone adhesive RI trend measured with the TFBG sensor.

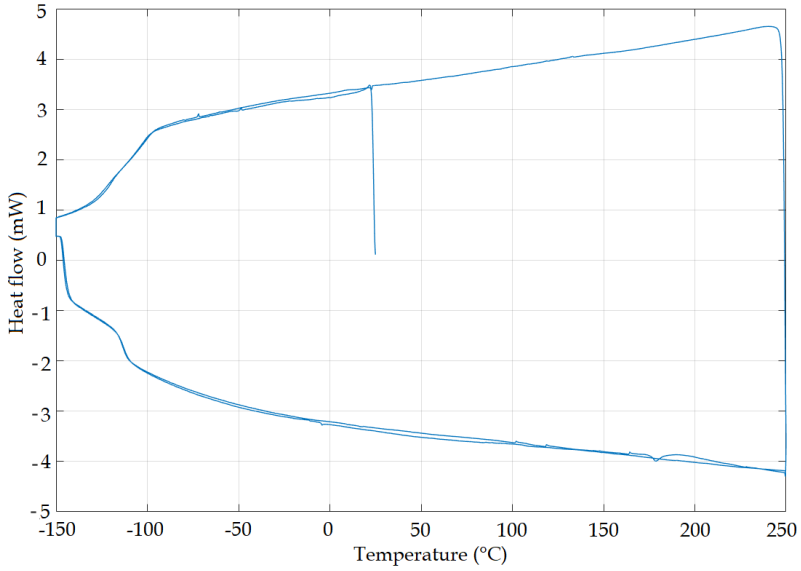


Fig.6-15. Heat flow and temperature measured during the DSC test on the silicone sample before thermal cycling test.

6.5 Conclusions

The investigation motivated by the research question has concluded at two important results. The first regards the compatibility of the OF layers to the vacuum that characterizes the space environment. Indeed, the low outgassing rate of the glasses composing the dielectric layers makes the OF a potential candidate for applications in space field. The second result regards the TFBG sensor, which, once embedded in the silicone adhesive of a cover glass sandwich sample, was demonstrated to be able to detect simultaneously strain-temperature and RI variations of the silicone material when the tested sample was exposed to high vacuum thermal cycles. The TFBG sensor had a TR of 7°C, a strain resolution of 5.02 $\mu\varepsilon$, a RI resolution of 2×10^{-7} and a normalised envelope area accuracy of 1.6×10^{-3}. Silicone strain variations may be calculated, avoiding the inconsistencies obtained from the temperature compensation of the TFBG spectrum through the TC measures due to the non-localized measurements for the different position of the two sensors. A substantial permanent negative strain (~100 $\mu\varepsilon$) was measured by the self-compensated TFBG at the end of the test, implying the possibility of shrinkage effects due to the post-curing/ageing reactions occurring in the silicone during the thermal cycles. Another effect causing the occurrence of negative stress may be the difference between the CTEs of the used materials in contact and the sample, in particular the cover glass and the silicone adhesive. The sensor was able to detect also a variation of RI of the adhesive, suggesting that the thermal cycles performed in high vacuum induced an evolution of the silicone. Specifically, at the beginning, the silicone RI was 1.42648, while after the test it was 1.42744 at the same temperature. To specifically investigate this aspect, a DSC test was performed on a cured silicone sample, where the presence of volatiles released during the heating-up and the cooling-down was detected. The same phenomenon, but enhanced, is expected to occur during the vacuum thermal cycles test, which can be considered as the main cause of the silicone RI changing.
Therefore, in conclusion, the fourth research question allowed demonstrating that an embedded TFBG sensor can provide information on the thermomechanical and refractometric state of the silicone during exposure to standard space environmental conditions. Specifically, in this chapter, it was proved by applying the high vacuum thermal cycles. Nevertheless, these multi-sensing abilities can be also performed in real-time as described for the composites in chapters 4 and 5.

In chapter 7, the investigation on the compatibility between TFBG sensor and perturbations of the space environment will bring to advanced sensing possibilities offered by the embedding of the TFBG inside silicone adhesives.

References

[1] L.Fazzi, N. Dias, M. Holynska, A. Tighe, R. Rampini and R.M. Groves, *Monitoring of silicone adhesive in space solar cells with an embedded multi-parameter TFBG sensor in a simulated space environment*, Measurement Science and Technology, 33 (8), p. 085108, (2022).

[2] ECSS-Q-ST-70-02C - *Thermal vacuum outgassing test for the screening of space materials*, 15/11/2008, https://ecss.nl/standard/ecss-q-st-70-02c-thermal-vacuum-outgassing-test-for-the-screening-of-space-materials/ (last access: 06/05/2022).

[3] ECSS-Q-ST-70-05C – *Detection of organic contamination surfaces by IR spectroscopy*, 6/03/2009, https://ecss.nl/standard/ecss-q-st-70-05c-detection-of-organic-contamination-surfaces-by-ir-spectroscopy (last access: 06/05/2022).

[4] E. Grossman and I. Gouzman, *Space environment effects on polymers in low earth orbit*, Nuclear Instruments and Methods in Physics Research B, 208, p. 48-57, (2003).

[5] H.R. Fischer, C. Semprimoschnig, C. Mooney, T.Rohr, E.R.H. van Eck and M.H.W. Verkuijlen, *Degradation mechanism of silicone glues under UV irradiation and options for designing materials with increased stability*, Polymer Degradation and Stability, 98, p. 720–726, (2013).

[6] B.A. Banks, S.K. Rutledge, E. Sechkar, T. Stueber, A. Snyder, K.K. de Groh, C. Haytas and D. Brinker, *Issues and effects of atomic oxygen interactions with silicone contamination on spacecraft in low earth orbit*, Proceedings of the 8th International Symposium on Materials in a Space Environment, 5th International Conference on Protection of Materials and Structures from the LEO Space Environment, (2000).

[7] M. Kutz, *Handbook of environmental degradation of materials*, William Andrew Applied Science Publishers, p. 736, (2018).

[8] J.A. Dever, E.J Bruckner, D.A. Scheiman and C.R. Stidham, *Contamination and space environmental effects on solar cells and thermal control surfaces*, 18th Aerospace Ground Testing Conference, 94-2627, (1994).

[9] D.L. Edwards, A.P. Tighe, M. Van Eesbeek, Y. Kimoto and K.K. de Groh, *Overview of the natural space environment and ESA, JAXA, and NASA materials flight experiments*, MRS Bulletin, 35, p. 25–34, (2010).

[10] Q.G. Gu and Q.L. Zhou, *Preparation of high strength and optically transparent silicone rubber*, European Polymer Journal, 34 (11), p.1727-1733, (1998).

[11] L.Y. Tyng, M.R. Ramli, M.B.H. Othman, R. Ramli, Z.A.M. Ishak and Z. Ahmad, *Effect of crosslink density on the refractive index of a polysiloxane network based on 2, 4, 6, 8-tetramethyl-2, 4, 6, 8-tetravinylcyclotetrasiloxane*, Polymer International 62 p. 382-389, (2013).

[12] K.R. McIntosh, J.N. Cotsell and J.S. Cumpston, *The effect of accelerated aging tests on the optical properties of silicone and EVA encapsulants*, Proc. Eur.PVSEC, p. 3475–3482, (2009).

[13] C. Huber, B.Stein and H. Kalt, *Plasma-enhanced chemical vapor deposition of amorphous silicon carbonitride: Deposition temperature dependence of bonding structure, refractive index, mechanical stress and their aging under ambient air*, Thin Solid Films, 634, p. 66–72, (2017).

[14] https://www.avantorsciences.com/nusil/en/product/CV16-2500/controlled-volatility-silicone-elastomer, (last access: 21/09/2021).

[15] L.Fazzi, S. Valvano, A. Alaimo and R.M. Groves, *A simultaneous dual-parameter optical fibre single sensor embedded in a glass fibre/epoxy composite*, Composite Structures, 270, 114087 (2021).

[16] J. Dugas, P. Michel, L. Martin and J.M. Cariou, *Behavior of the refractive index and of the coefficient of thermal expansion of silicone with temperature*, Appl. Opt., 25, p. 3807-3808, (1986).

[17] L. Fazzi and R.M. Groves, *Refractometric Properties of a TFBG Sensor Demodulated Using a-Shape Modified Delaunay Triangulation*, Optics, 2 (2), p. 113-133, (2021).

[18] J. De Heer, The principle of Le Châtelier and Braun, Journal of Chemical Education, 34 (8), p. 375, (1957).

[19] C. White, K.Tan, A. Wolf and L. Carbary, Advances in structural silicone adhesives, Woodhead Publishing Series in Welding and Other Joining Technologies, Chapter 4, p. 66-95, (2010).

7

Multi-parameter single sensor for space silicone adhesive monitoring under hi-vacuum ultra-violet exposure

"The universe seems neither benign nor hostile, merely indifferent to the concerns of such puny creatures as we are."
Carl Sagan

The previous chapter demonstrated that a TFBG sensor can be a suitable sensor to monitor the thermomechanical and refractometric evolution of a space qualified silicone adhesive when this has undergone thermal cycling in a high vacuum environment. Specifically, not only silicone temperature and strain variations can be monitored at the embedded TFBG sensor location but also chemical aging as the RI is a parameter which depends on the chemistry of the silicone, as described in the previous chapter.

At this point, a step forward regards the application of the TFBG also as sensor to monitor the state of silicone adhesive even when other typical effects present in space environment, as UV radiation, affect the elastomer. In fact, UV radiation is widely present in any space mission and, as described in chapter 1, they can cause severe damage to silicone adhesives.
However, this desire collides with the effects that the UV beam perturbation of space environment may have on the dielectric layers of the OF and/or also on the same internal structure of the TFBG. In fact, the TFBG is manufactured by using a UV laser beam with a specific wavelength, which means that an external UV radiation may influence the photosensitive doped layer of the OF. Hence, the external UV beam may modify the well-defined RI modulation in the core of the OF, inducing a variation of the TFBG transmission spectrum and its sensing properties. Therefore, an investigation of these effects is needed starting from the analysis of the transmission spectrum of the TFBG sensor when this is exposed in simulated space environment to UV radiation. Once the possible consequences are defined and understood, the research is then focused on the sensing abilities of the TFBG embedded in silicone adhesive sample to in-situ monitor the state and the degradation of the material exposed to UV radiation.
The research question that motivated this investigation is the fourth:

- *How do the space environmental conditions influence the transmission signal and the sensing abilities of the TFBG sensor even once this is embedded in a space qualified silicone adhesive?*

In a space environment with high vacuum and extreme thermal cycling loads, the materials of the space vehicles have to resist other forms of perturbations such as electromagnetic or cosmic radiation rays. Indeed, high-energy particles such as photons, protons and atomic nuclei moving through space at nearly the speed of light, generate different forms of radiation depending on their carried energy, such

as Ultra-Violet (UV), Infrared, x-rays and gamma rays [1]. The long exposure of materials to these types of radiation can cause severe failures and damage to the elements and structures of a spacecraft (as anticipated in section 1.1.2). Specifically, silicone adhesives are largely used in the solar arrays of telescopes and spacecraft, which are components directly exposed to solar radiation in order to convert the light waves in electrical energy. This means that silicone adhesives are exposed for long time to different radiation, particularly to UV radiation. As explained in section 1.1.2a, light with wavelengths between 200 and 400 nm (which corresponds to UV radiation) is particularly dangerous for silicones. The reason lies in the fact that the organic chemical composition of silicone is photochemically susceptible to these light wavelengths [2]. The absorption of the UV light generates photochemical reactions which cause the rupture of the original bonds and, consequently, the colouration of the transparent silicones which means a higher solar absorbance capability. This degradation causes a variation of the original thermo-optical properties and efficiency, with a deterioration of the silicone mechanical performance and shorter operational life. Moreover, the combination of UV radiation with other space phenomena, can bring even worse consequences such as micro-cracking, loss of efficiency and premature failures [2-6].

Therefore, considering the effects described before which represent the working conditions in the space environment, a technique able to monitor and detect the state of the silicone adhesive during its operational life may be convenient to avoid possible failures and decay of performance by evaluating its degradation. In the previous chapter, embedded Tilted Fibre Bragg Grating (TFBG) sensors were demonstrated to be able to simultaneously measure the thermomechanical and refractometric state of Nusil® CV16-2500 during high vacuum thermal cycles. In this work, for the first time, TFBGs are investigated for three-parameter monitoring of the space qualified Nusil® CV16-2500 silicone operating during high vacuum Ultra-Violet exposure. The first part of the work is focused on the Ultra-Violet effect on the TFBG spectrum, when the sensor is: (i) directly exposed to the radiation, (ii) covered by a thin cover glass and (iii) with a Kapton-layer on top. Successively, the silicone was used as an adhesive in a sandwich structure in which the TFBGs are embedded and exposed under high vacuum to various UV/Vacuum UV intensities radiation and durations. The sensors' spectra were acquired and demodulated to detect the silicone strain-temperature-refractive index variations and correlate the silicone refractometric changes with the equivalent exposure solar hours.

The second part of the chapter is on silicone degradation state evaluation using the embedded TFBG, but during a direct exposure of the adhesive to the radiation. This allowed the UV effects on the silicone to be enhanced but needed a method to compensate for the damaging effect of UV radiation on the TFBG spectrum.

The testing activities and the manufacturing of the samples were performed at the Materials and Electrical lab and the TEC-QEE section of European Space Agency (ESA), ESTEC site, while the entire sensing equipment was provided by the NDT lab of the Aerospace Structures & Materials department of Delft University of Technology. This research is the result of a collaboration with Nuno Dias (ESA), Dr. Malgorzata Holynska (ESA), Dr. Adrian P. Tighe (ESA), Riccardo Rampini (ESA) and Dr. Roger M. Groves (TU Delft). This work was published in Journal of Spacecraft and Rockets [7].

I want to dedicate a special thanks to Nuno Dias and Dr. Malgorzata Holynska for their technical, friendly and constant support during the almost two years of experience at TEC-QEE section of ESA/ESTEC, and for the same reasons to the promotor of the project Dr. Roger M. Groves.

7.1 Predicting UV degradation of polymers for space applications through embedded TFBGs

Although space qualified silicones have been studied for many years and have been developed to be resistant to the harsh space working conditions, they must coexist with ultra-high-vacuum, ultra-violet (UV) and ionizing radiations, an extreme thermal range and cycles, thermal shock, micro-gravity, atomic oxigen (ATOX), high accelerations, vibrations and space debris for their entire functional life. The combination of these effects may cause severe damage, decreasing of mechanical and specific

performance, change of the original material properties and even premature failure of the components [6]. The organic chemical composition of polymers is photo-chemically susceptible to degradation at light wavelengths between 200 and 400 nm [2]. Indeed, organic molecules absorb UV light initiating photochemical reactions which cause the rupture of the original bonds. The radical reactions released due to the cleavage of homolytic bonds induce discoloration of the transparent silicones with the unwanted consequence of producing a much stronger solar absorbance capability. This effect is especially high when volatiles are released and non-saturated bonds are present in the remaining material, or even if there are impurities contained in the polymer. All these effects will increase the absorption of UVs contributing to the photochemical reactions [3-5]. Apart from the discoloration/coloration, this degradation process changes the original thermo-optical properties and efficiency, as well as decreases of the silicone mechanical performance and durability. Even worse consequences may occur when UV effects are combined concurrently with other space phenomena, in particular micro-cracking, severe degradation and premature failures [2-6]. In addition, an ultra-high-vacuum can affect the original dimensional stability and composition of the polymer as it induces silicone outgassing of additives and low-molecular weight residues. In this way, as asserted in [8], contaminant layers may deposit on nearby cold surfaces and their interaction with UV or ionizing radiation, thermal cycles and ATOX can induce their fixation. This might compromise quality, efficiency or even cause severe issues. Therefore, taking into account these harsh operational conditions and the consequences of their combined actions on the materials, the materials and the components for space flight undergo strict development, qualification, acceptance and protoflight test campaigns to verify and certify their suitability for space applications, to evaluate their degradation state after the space environment exposure, and to minimize the risk of premature failure [9]. However, testing campaigns are very time consuming and expensive in terms of resources, equipment, apparatuses and personnel, so intermediate verification methods are necessary to estimate the sample condition. Hence, with the evolution of the space industry, several non-destructive evaluation techniques (NDET) have been developed to monitor the health state of the materials during ground testing and in service [10-15]. However, although many technologies might be used for in-situ evaluation/remote/real-time monitoring [16], the sensors and the support apparatus must match the space compatibility [17] and embedding requirements [18]. Another issue regards the need to perform multi-parameter measurements to evaluate the overall state of a material or for simple cross-sensitivity compensation of some sensors to a determined parameter (as in the case of temperature for strain-gauges). This involves the integration of more sensors inside the materials and apparatuses in the spacecraft, with a consequent increase of the weight and complexity of the overall system, costs and reduction of the volume available for the payload.

TFBG sensors address these issues by being minimally intrusive and able to simultaneously measure many parameters such as strain-temperature and RI variations [19]. In chapter 6, the TFBG sensor has been demonstrated to be compatible with vacuum applications and able to measure the desired parameters inside the silicone adhesive. In the work presented in this chapter, some TFBGs were embedded inside the silicone adhesive of the cover glass sandwiches to evaluate the thermomechanical and refractometric state of the elastomer during high vacuum UV exposure. Of particular interest is the RI trend as the equivalent solar hours (esh) of exposure to the UV light are increased. As previously introduced the test methodology was conducted by performing, on different kinds of samples, several grades of severity of the exposure to the UV radiation.

In summary, the aim of the chapter is to demonstrate that the TFBG sensor can provide reliable information on the fundamental parameters (as strain, temperature and RI) of the tested silicone adhesive, which may in future be consulted to investigate its mechanical and chemical degradation degree.

7.2 Samples

To achieve a proper and complete investigation of the UV effects on silicone adhesive through the three-parameter measurements performed by the embedded TFBGs, the experimental campaign has been divided into three different parts. First of all, the TFBG is tested under UV light to investigate

the effects of the radiation on the spectrum of the sensor. In the second part, samples composed of cover glasses and silicone adhesives are prepared with embedded TFBGs and a K-type thermocouple (TC). The third experiment investigates the aging in the silicone due to UV exposure when the cover glass is not blocking the radiation.

The first group of samples are bare TFBGs where the OF coating has been removed in the region of the sensor. The TFBGs were tested under (i) direct exposure to UV light, (ii) covered by a thin cover glass and (iii) covered by a thin Kapton® layer. The aim of these measurements was to prove that the sensor works as intended and to confirm its reliability in the specified working conditions. These samples were tested in high vacuum with increasing esh (equivalent solar hours) values of UV exposure. TFBG spectra were recorded to investigate the thermomechanical and refractometric state of the silicone adhesive and a compensation procedure was performed on the TFBG spectrum to obtain the real RI value of the aged silicone.

Descriptions of the samples used during the testing campaigns are presented in this section. For these experiments, three TFBGs were used. The first one was directly exposed to the UV radiation (Fig.7-1a), the second was covered by a layer of cerium doped microsheets of cover glass (30 × 20 × 0.05 mm) (Fig.7-1b) and the third was exposed but protected by a layer (~200 µm) of Kapton® foil (Fig.7-1c). All the TFBGs had a TC placed as close as possible.

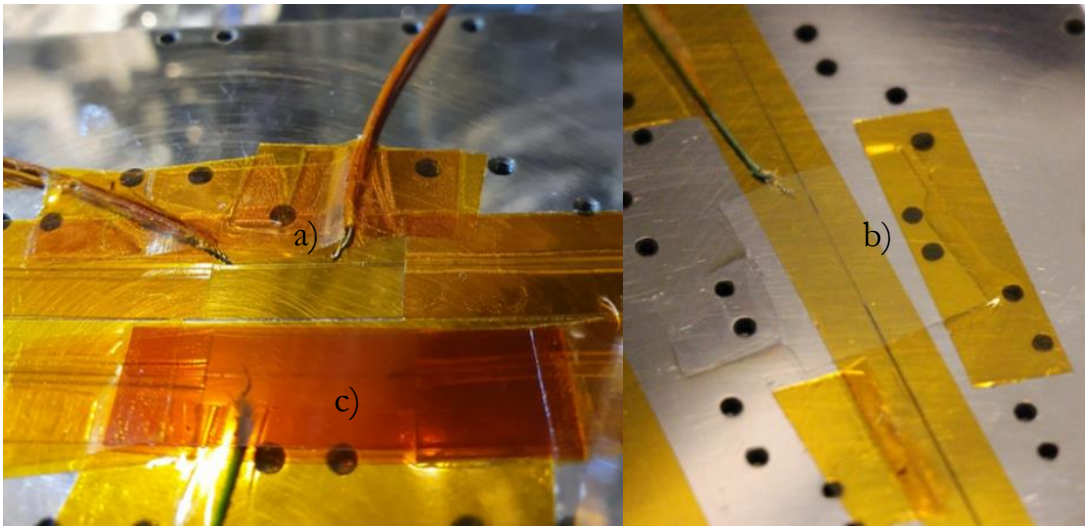


Fig.7-1. Sensorised sample on test plate of MCross: a) bare TFBG, b) cover glass sandwich, c) single cover glass with directed exposure of silicone to UV radiation.

The second type of sample was the cover glass sandwiches sensorised with TFBGs and TCs. Each sample is composed of two layers of cerium doped microsheets cover glass (30 × 20 × 0.05 mm) bonded together with the silicone adhesive NusilTM CV16-2500 in which a bare TFBG sensor and a TC are embedded. The dimensions of the samples and the embedding distances of the sensors are reported in Fig.7-2.

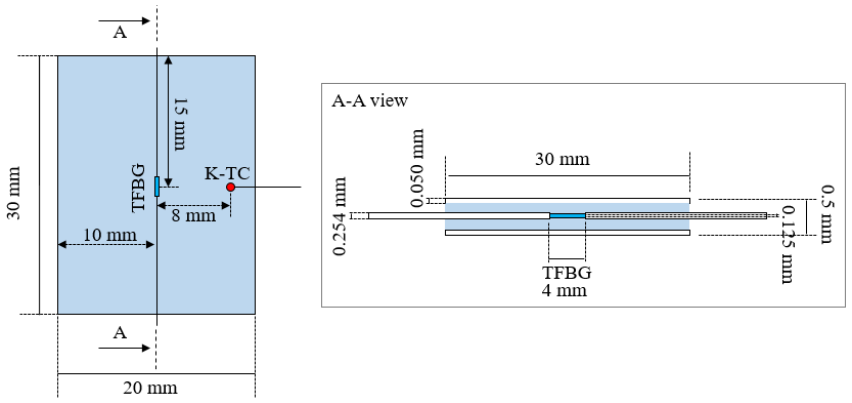


Fig.7-2. Schematic of the sample 2 (Fig.7-2b): sensorised cover glass sandwich samples.

The last sample is composed of similar components to experiment

two but the cover glass on top is removed to directly expose the silicone to the UV radiation. The details of this sample are reported in Fig.7-3.

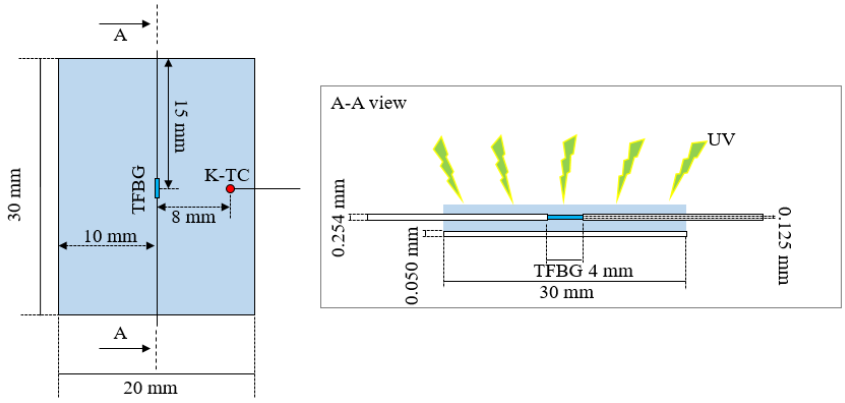


Fig.7-3. Schematic of the sample 3 (Fig.7-1c): sensorised assembly cover glass and silicone adhesive.

7.3 Equipment

All the TFBG sensors used in this work were manufactured by FORC-Photonics in Fibercore PS1250/1500 OF by using the rotated phase-mask technique. All the sensors have a 3° tilt angle and are 4 mm long. The sensors are uncoated for approximately 20 mm of length and the remaing OF is coated by a layer of UV-cured acrylate. The TFBGs were certified by the manufacturer to operate in a temperature range between −40 °C and 250 °C without degradation of the spectrum for a long exposure time (more than 720 hours). The K-type TCs used have a diameter of ~200 µm and ±1°C of accuracy. As described at each use of the TFBG in this thesis, before embedding the sensors, a preliminary thermomechanical and refractometric calibration was performed on the TFBGs in order to obtain the sensitivity thermomechanical coefficients of eq.II.8 and the fitting correlation function between the envelope area and the surrounding RI. The TFBGs were calibrated before testing, as described, thermomechanically in section 2.4.1a and 2.4.1b ([20]) and refractometrically in chapter 2 ([21,22]) . During the entire calibration and testing stage, the TFBG spectra were always acquired by using the NI PXI-4844 interrogator (scanning wavelength resolution = 4 pm, scanning accuracy ±1 pm and minimum power detection 6.103×10^{-4} dBm). The sensing system apparatus was provided by the Aerospace NDT lab of TU Delft, while, the high vacuum UV radiation tests were performed using the MCross facility at the Materials & Electrical components laboratory of ESTEC/ESA.

The MCross (Fig.7-4a) is a vacuum chamber provided with an Agilent scroll pump and a Pfeiffer Turbo Molecular vacuum pump with Electronic Drive Unit TC360 (vacuum better than $<10^{-5}$ mbar), 2 vacuum UV (VUV) deuterium and 2 high pressure discharge UV lamps (reaching a maximum of 6 solar constants). Inside the test chamber, a metallic sample plate (Fig.7-4b) was placed on top of a resistance heating plate (thermocoax), which was mounted on a liquid nitrogen coolable plate. The chamber is also equipped with Kapton-coated K-type TCs, which can be attached to the sample or the plate for temperature monitoring. To acquire the spectra of the OF sensors, the facility was also upgraded with two hermetic polarization-maintaining fibre optic feedthroughs manufactured by SQS, each of which has two input/output FC/APC connectors, externally connected with two optical circulators, and hence, to the interrogator system. Before each test, the UV intensity (in solar constant) was measured at different sample positions. The solar constant is an internationally recognised unit used to quantify unequivocally the intensity of electromagnetic radiation that falls on a unit area of surface normal to the line from the Sun at one astronomical unit (1AU), outside the atmosphere, per unit time [22]. Specifically, the solar flux mean value at 1AU is defined as 1366.1 W/m² which corresponds to 1 solar constant. This value can be measured on the surface of the support plate in correspondence to the sample positions through a UVpad spectral radiometer Opsytec Dr. Gröbel which measures the radiation intensity in the UVA (315-400 nm), UVB (280-315 nm) and UVC (100-280 nm) wavelengths. These values are converted to solar constant [23]. This value is then multiplied by the exposure time to obtain the esh, which is the acceleration factor.

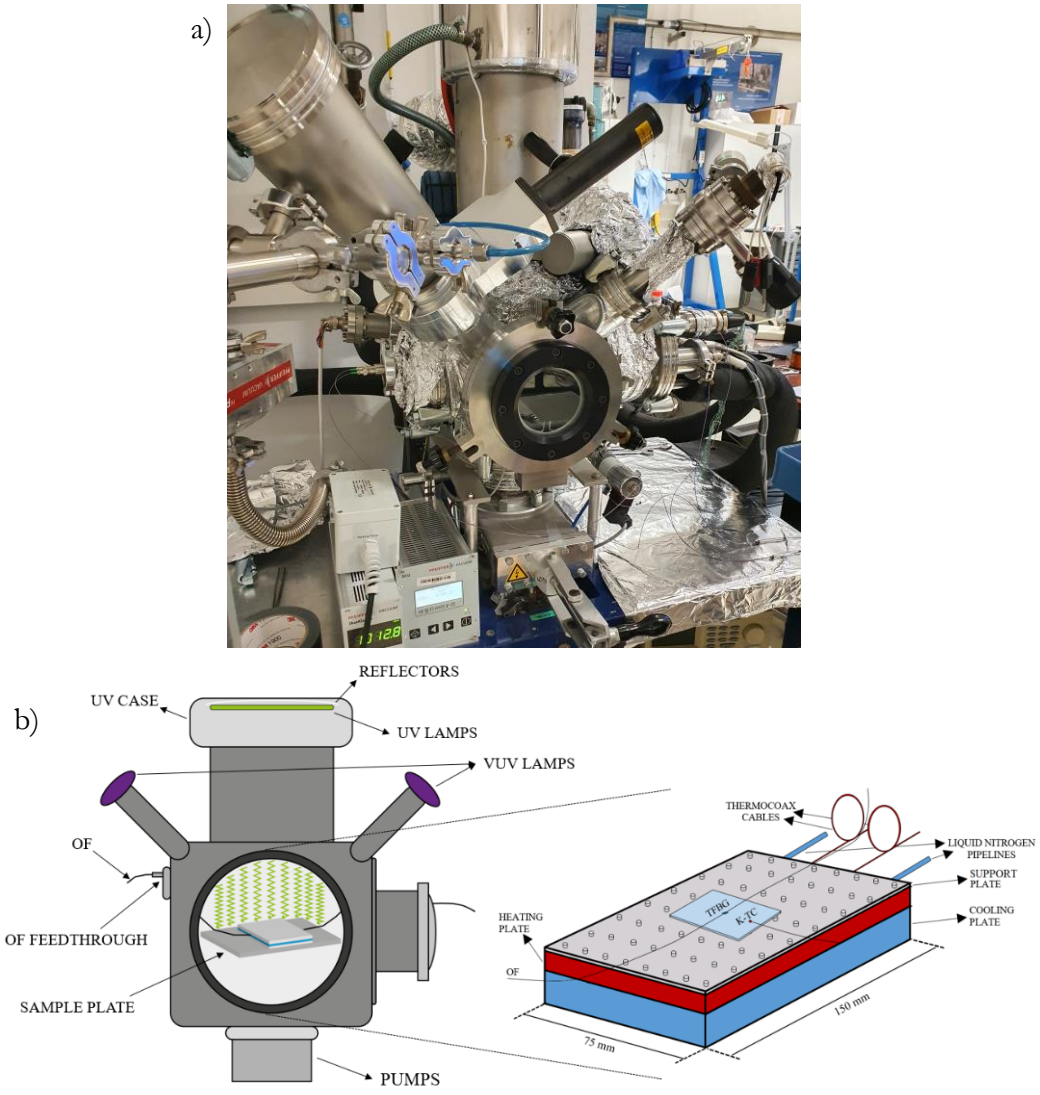


Fig.7-4. a) MCross and b) schematic of sample plate in the MCross.

7.4 UV effects on the TFBG sensors

In this section, the effects of the UV radiation on the TFBG spectrum for sample 1 are treated. Indeed, since the TFBGs are made by inducing a modulation of the core RI with UV light interference, an external UV radiation incident on the photo-sensitive silica layers of the not-recoated OF may modify the RI profile imposed during the manufacturing. In fact, usually for photo-sensitive OFs, such as the one used here (Boron-Germanium Doped Fibercore PS1250/1500), the RI core is modulated, during FBG production, using an UV excimer laser with wavelengths between 193 nm and 296 nm [24,25]. Hence, considering that the UV radiation from the MCross includes these wavelengths, this may influence or modify the original modulation of the RI core. This would bring unexpected changes in the spectrum of the TFBG during the test, which could lead to erroneous measurements. To avoid these drawbacks, the TFBGs have been preliminary tested under UV light to verify their compatibility with the determined operational conditions. As mentioned previously, three kinds of samples were tested: (i) a directly exposed TFBG (Fig.7-1a), (ii) a TFBG covered with a cover glass sheet (Fig.7-1b) and (iii) a TFBG shielded by a Kapton® layer (Fig.7-1c). All the exposures were performed in high vacuum (1.6×10^{-6} mbar, accuracy of the MKS pressure sensor declared by the manufacturer: ±0.5%) and with a solar constant of ~3. While the lamps were emitting the UV radiation, the TFBGs were

connected to the external interrogation system via feedthroughs to acquire and record TFBG transmission spectra during the test. Once the test had been completed, the spectra were processed and analyzed by considering the envelope area of the upper and lower cladding resonance peaks. Hence, the degradation of the TFBG was measured by considering the trend of the envelope area. For this reason, the acquired spectra were demodulated by using the D-T technique that returned the envelope area values, which were normalized with respect to the original area value before of the experiment (Fig.7-5, 7-6 and 7-7).

The trend of the envelope area in Fig.7-5, referred to as the TFBG directly exposed to the UV light, clearly shows a decrease of the envelope area with exposure time. Specifically, at the end of the test, all the resonances in the spectrum of the sensor, analysed via the envelope area, have resulted in a smaller amplitude than the one at the beginning. If no influence was induced by the UV radiation, they could be expected to have the same area at the end of the test. This means the RI core modulation has undergone a modification due to determined wavelengths of the incident radiation. In particular, since the envelope area (and also the spectrum) were reduced (Fig.7-8), a possible explanation is that the UV beams are reducing the depth of the RI modulation in the OF core created during the TFBG manufacturing. Indeed, this parameter is fundamental to obtain a consistent amplitude of the resonance peaks in the spectrum [26]. Furthermore, as shown in Fig.7-8, the comparison between the original and the spectrum after the exposure raises another consequence: all the resonance peaks of the spectrum after the exposure, are red-shifted even while at the same temperature. This could maybe be explained by considering a tensile force induced by the tapes used to hold the OFs, however, as the comparison was made in the absence of external supports, this shift is probably more likely to be due to a change of the original RI core modulation caused by UV radiation.

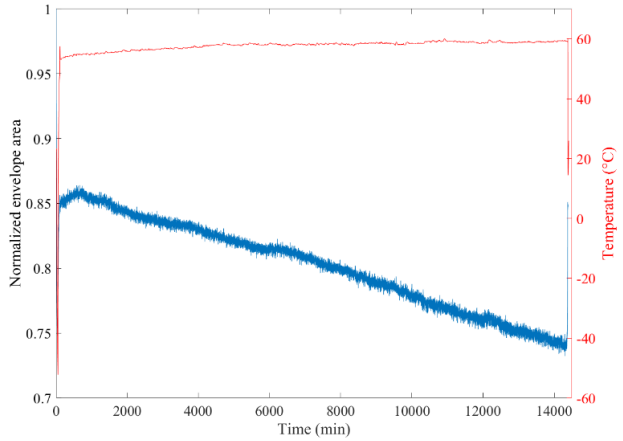


Fig.7-5. Normalized envelope area obtained from the directly exposed TFBG

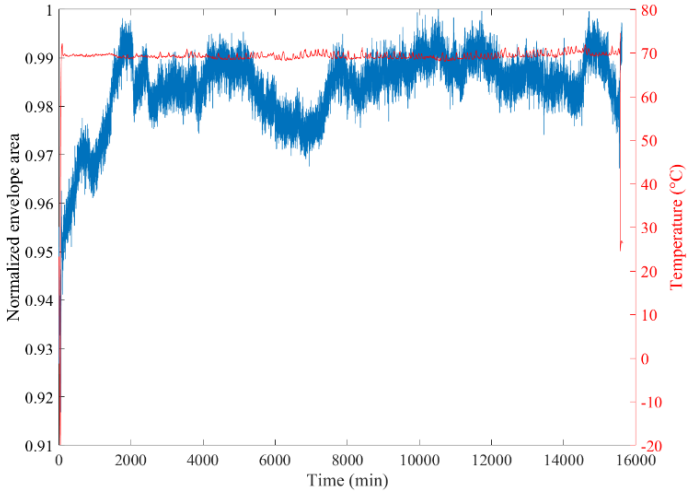


Fig.7-6. Normalized envelope area obtained from the TFBG exposed to UV through a cover glass layer.

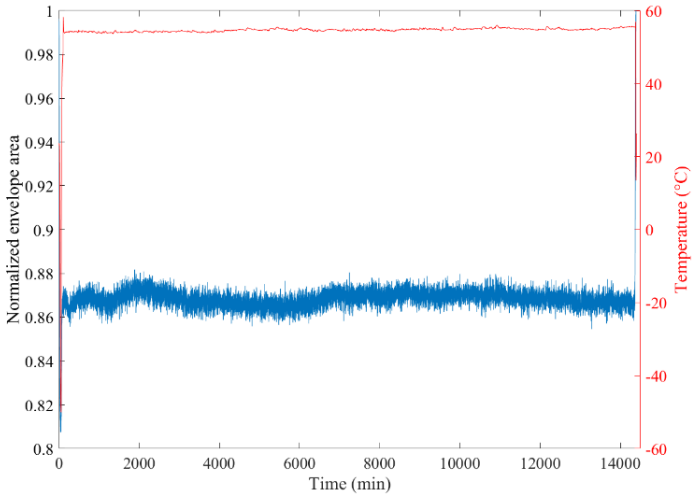


Fig.7-7. Normalized envelope area obtained from the TFBG exposed to UV and shielded by the Kapton® layer.

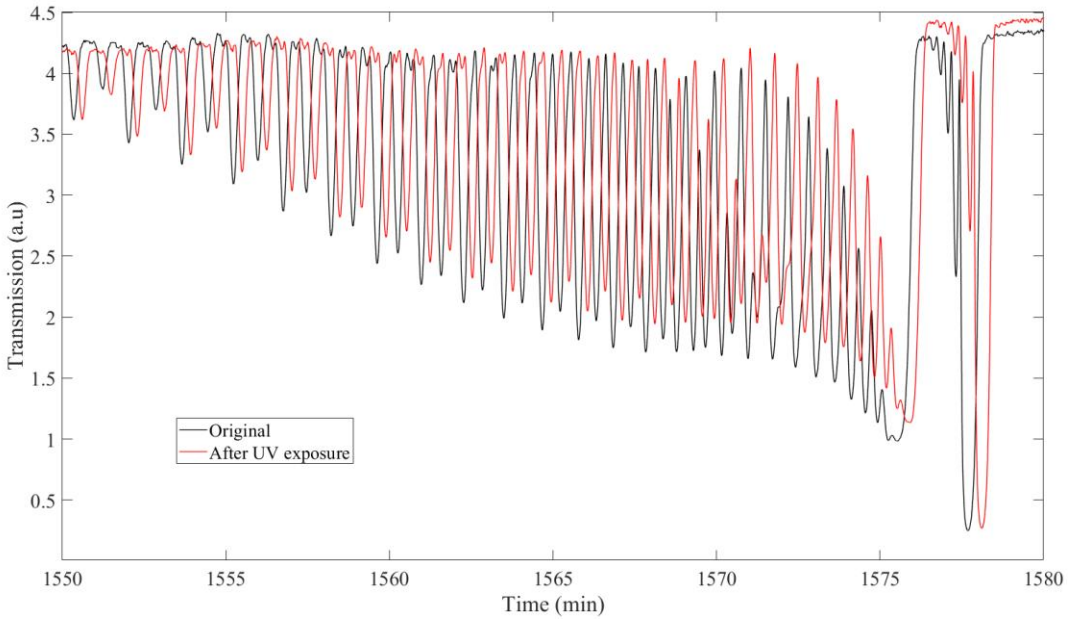


Fig.7-8. Comparison between the TFBG transmission spectrum before and after the test.

In the case of the TFBGs shielded by the cover glass (Fig.7-6) or the Kapton® layer (Fig.7-7), the reaction of both sensors to the UV radiation is different from the previous one. In fact, in both cases, the envelope area returns to the original value (or almost, due to the temperature effect [22]) and the original spectra are identical after the UV exposure. This means that the TFBGs were not influenced by the shielding of the layers between themselves and the UV radiation. The reason of this result can be discovered by investigating the wavelengths of the light allowed to pass through the media. Each material possesses an absorption power of light based on its wavelength. Therefore, an Agilent Cary 5000 UV-Visible-Near Infrared spectrophotometer was used to obtain the percentage of light, along the wavelengths range, transmitted through the shielding layers, see Fig.7-9.

Fig.7-9 shows the transmission spectra as a function of the wavelength. In the case without a shielding layer, the curve referred to is that for the quartz glass which divides the vacuum chamber from the UV case, which transmits all the wavelengths associated with the UV radiation by >90%. Different situations are presented for the case of the cover glass and the Kapton® foil. They block the light starting from, respectively, ~340 nm and ~490 nm. In this way, the TFBG internal structure cannot be modified as it is not sensitive to the transmitted wavelengths.

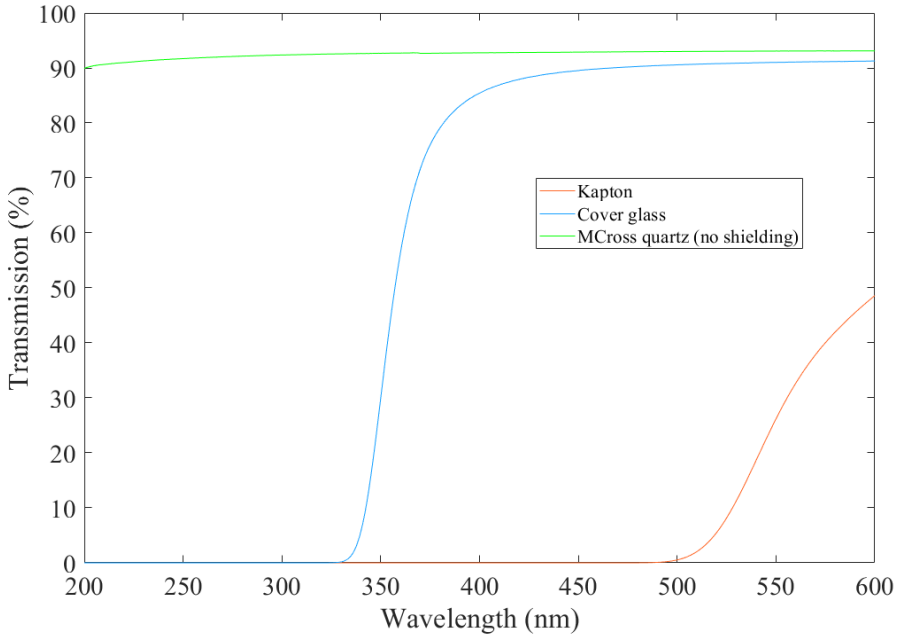


Fig.7-9. Transmission percentages of the light through different materials in the range 200 nm – 600 nm.

The reason why the Kapton® foil was tested regards the initial hypothesis of the need to protect the TFBG sensor with a narrow (~150 μm) piece of this material, in case of the cover glass was not able to shield the sensor from the radiation. Taking into account these results the sensorised sandwich was realized with the cover glass, as shown in Fig.7-10a.

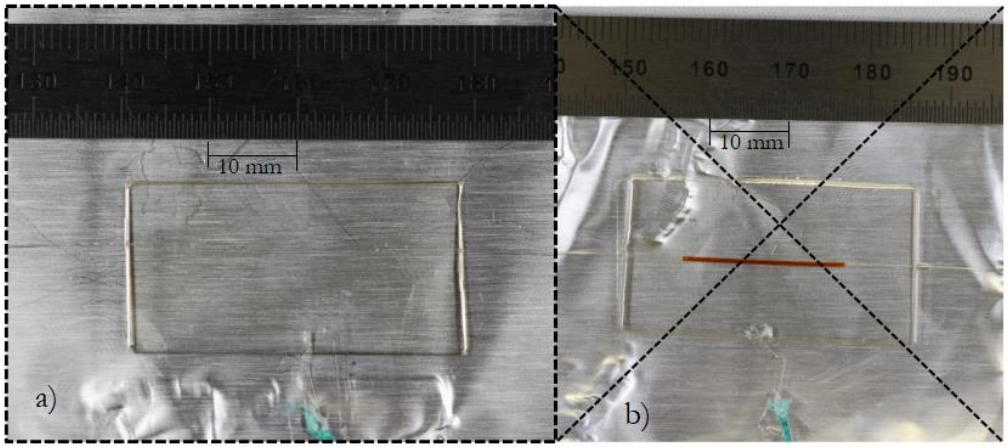


Fig.7-10. Configurations of sensorised cover glass sandwich samples with a) free embedded TFBG and b) Kapton shielding embedded TFBG.

7.5 UV effects on silicone adhesive monitored via TFBG sensor

Once the TFBGs were ready to be embedded, the cover glass sandwich samples (sample 2) were made with the embedded TFBG and TC as Fig.7-2 shows. In this section, the results and discussion are about the effects of UV radiation in vacuum on the silicone adhesive as detected through the simultaneous thermomechanical-refractometric TFBG measurements. Eight samples were tested under the UV lamps each with increasing esh. This value was obtained by multiplying the solar constant by the number of hours of exposure. The TFBG spectra were acquired and then demodulated to calculate the strain-temperature variations and the silicone RI.

In Fig.7-11, the strain and temperature variations are reported for a TFBG embedded in a cover glass sandwich and exposed for 808.18 esh. Although the TFBGs offer a TR which is much coarser that the TC, the temperature trend measured by the OF sensor is close to the variation measured by the TC. The maximum difference between the two trends is achieved during the radiation at constant lamp power. This is due to the TFBG TR which does not allow small temperature oscillations to be read however, the maximum difference is ~2°C, which corresponds to a strain variation of 15 με. At the beginning of the test, the TFBG measured a consistent level of negative strain (reaching to more than -850 με) due to the slow cooling-down caused by the liquid nitrogen cooling plate. Once the lamps were switched-on, the strain variation started to increase, then the compressive deformation was recovered until reaching a stable value of ~+130 με in 358th minute. From this point, since the TFBG is not able to detect thermal oscillations lower than its resolution, the strain calculation was performed by considering isothermal conditions.

From Fig.7-11, it is possible to note some spikes, such as at the ~950th, 13000th and 16500th minutes and oscillations of the strain levels, which follow the temperature changes detected by the TC. Unfortunately, the TFBG cannot take into account these thermal fluctuations due to its resolution, indeed the temperature trend measured by the OF sensor is flat. This means the strain measured in this condition is overestimated as part of the wavelength shift that is used to calculate the strain should be compensating thermal variation. The exposure was performed for around 330 hours, and at the end of the test, once the lamps were switched off, the TFBG measured a final negative deformation of ~160 με at 24.2°C. This means that the UV radiation in high vacuum caused a compressive state inside the silicone adhesive. Thermomechanical measurements can be performed by using this technique on all the samples and also in real-time, in this way the state of the material can be detected in any moment of the test.

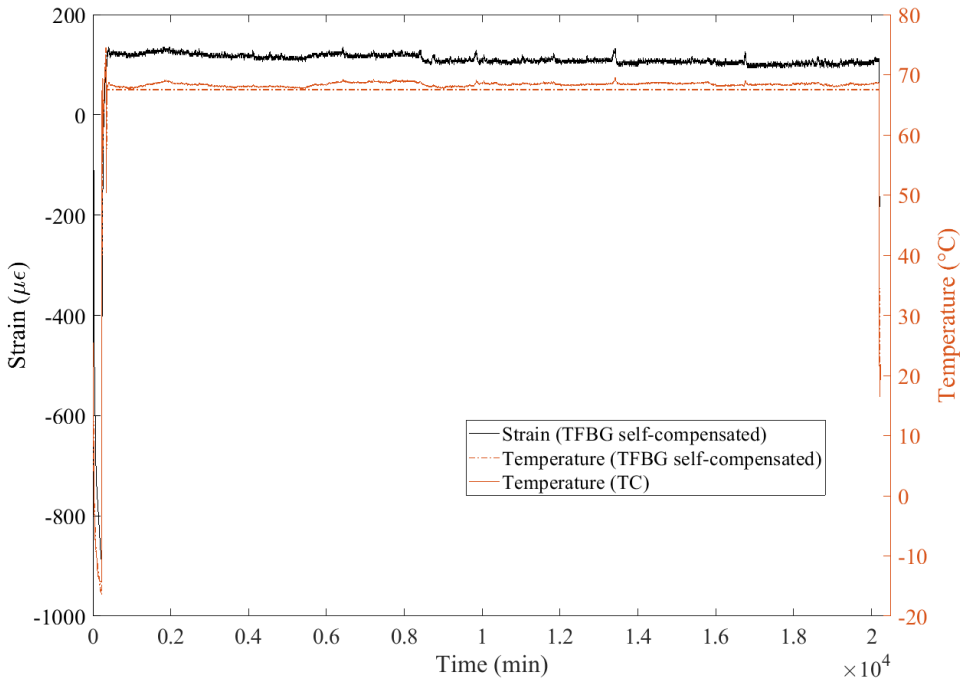


Fig.7-11. Thermomechanical measurements performed with the single TFBG and TC temperature trend.

Simultaneously to the strain-temperature measurements, also the refractometric state of the silicone was evaluated with the embedded TFBG. In particular, the RI depends on many material factors such as thermal, physical (density) and chemical composition. Hence, the monitoring of this parameter can provide a global indication of the state of the material. Therefore, the spectra are demodulated to obtain the normalized envelope area as explained in the second chapter, and the RI is calculated from the fitting correlation function. In Fig.7-12, the silicone adhesive RI trend is reported from the spectra of the TFBG previously used for the thermomechanical evaluation.

At the beginning of the experiment, the RI of the silicone adhesive measured by the TFBG, was at a value of 1.42506195 (the TFBGs used here has a resolution of ~10^{-8}). This started to increase when the cover glass sandwich was cooled down by the cooling plate due to the increase of the elastomer density generated by the negative temperature variation. When the UV lamps were switched on, the temperature increases and the material undergoes a positive deformation, which corresponds to a decrease in its density and, consequently, a reduction of the RI. However, when a stable range of exposure was achieved, the RI slowly increased during the hours of exposure, the consequence of which can be observed at the end of the exposure. Indeed, when the lamps were switched-off, the temperature was redirected with the help of the cooling plate, toward values which were close to the initial values. The silicone RI then decreased, and at the same initial temperature (24.2°C), an RI value of 1.42606481 was determined, which means an RI variation of more than 1×10^{-3} RI with 808.18 esh of UV exposure. These measurements were performed on all eight tested samples, which were exposed to the UV radiation with increasing esh. Specifically, it was noted that the silicone RI variation was greater the higher the esh. Therefore, the RI variations of all the cover glass sandwich samples are reported in Fig.7-13 with the corresponding esh values, while the values related to the refractometric measurements are reported in Table 7-1.

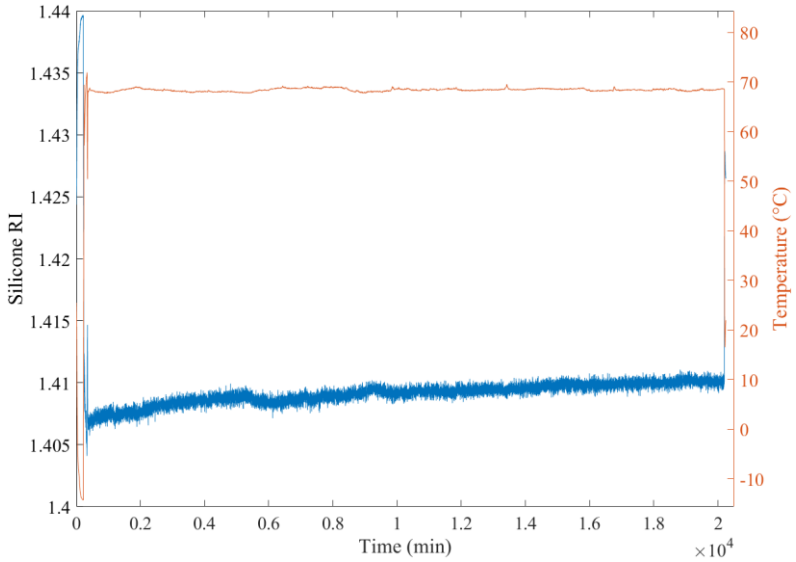


Fig.7-12. Silicone RI measurements performed with the embedded TFBG during UV exposure.

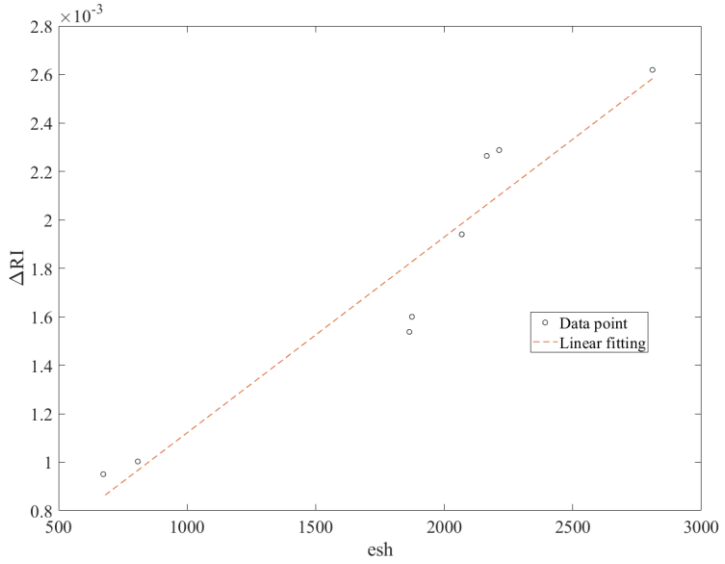


Fig.7-13. RI variation of the silicone adhesive of the eight samples tested with increasing esh.

Table.7-1. Values of the silicone refractometric measurements after the UV exposure with increasing esh.

esh	Temperature (°C)	Initial RI	Final RI	ΔRI (×10^{-3})
673.89	24.3	1.42479304	1.42574317	0.95013
808.18	24.2	1.42506195	1.42606481	1.00286
1864.3	24.8	1.42448586	1.42602337	1.53752
1874.21	24.5	1.42490283	1.42650266	1.59983
2068.16	27.1	1.42383392	1.42577389	1.93997
2165.21	24.4	1.42482412	1.42708795	2.26383
2213.46	25.4	1.42447117	1.42675870	2.28754
2809.75	25.3	1.42439906	1.42701765	2.61859

In Table 7.1, the temperatures reported are those recorded at the initial and final refractometric measurements. From Fig.7-13, an increase of the RI variation can be observed when increasing the esh and this trend seems to have a good fitting with a linear regression as the resulting square error (R^2) of the fitting is 0.92 with a standard deviation of 9.76×10^{-5}. The RI grows from the initial value with increasing esh, which means that a longer exposure and/or higher solar constant, produces a different physical and/or chemical condition of the material after the radiation, at the same temperature. Specifically, as noted in [7], the shrinking of the silicone due to the environmental conditions can cause an increase of the RI as the compressive stress compacts the material and increases its density. However, here, the effect of the UV must be taken into account as, although the cover glass can shield part of the UV (Fig.7-9), the silicone elastomer absorbs and is photo-chemically sensitive to the wavelengths of the light passing through [2,4]. For this reason, some chemical reactions may occur inside the silicone due to photoexcitation which is generated by the radiation. These reactions are favored by the high temperature. The consequences on the adhesive are easily visible and recognizable as the sample undergoes an amber discoloration (Fig.7-14), which is more intense the higher the esh is. Furthermore, this is the main reason for the silicone RI variation, which, at this point, may be used as a parameter to detect and evaluate the degradation state of the elastomer during or after the high vacuum UV exposure. Indeed, a greater RI variation indicates a larger deviation of the material from its original condition, and hence, it may be used as a degradation/aging index of the silicone adhesive.

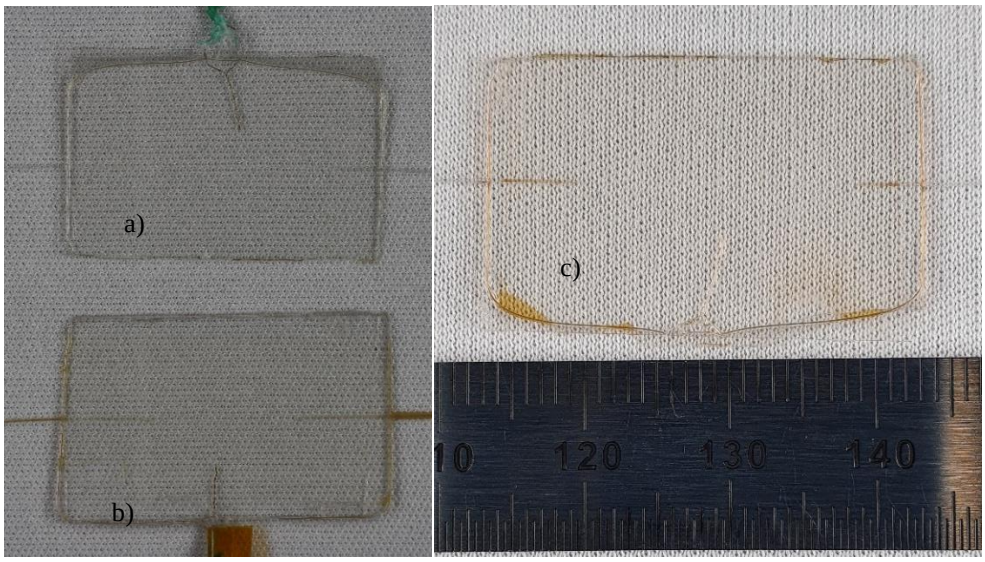


Fig.7-14. Inspection of the samples at a) original state, b) after 808.18 esh and c) 2068.16 esh of UV exposure.

7.6 Sensorised silicone adhesive directly exposed to UV radiation

In this section, the results and discussion regarding the high vacuum UV exposure of sample 3, reported in Fig.7-3 are presented. In this case, one single sample was tested, in which the silicone, with an embedded TFBG, was directly exposed to the UV radiation (Fig.7-15). The aim of this experiment was to enhance the degradation effects on the silicone adhesive, especially regarding the RI variation using higher levels of UV radiation. The high vacuum UV exposure was performed for 601.72 hours at 5.11 solar constant which means 3074.79 esh of exposure.
The silicone RI trend measured by the TFBG is reported in Fig.7-16. As previously, the RI changes with the temperature and is higher at the end of the test. This RI increases much more than the RI variations detected in the previous samples as the lack of the cover glass on top of the sample causes the silicone to absorb a larger wavelength range and amount of UV radiation. A visible consequence of this fact is a stronger discoloration of the sample at the end of the test, as shown in Fig.7-17. A comparison between Fig.7-17b and Fig.7-14b or Fig.7-14c, makes evident the stronger effect of the UV on the silicone.

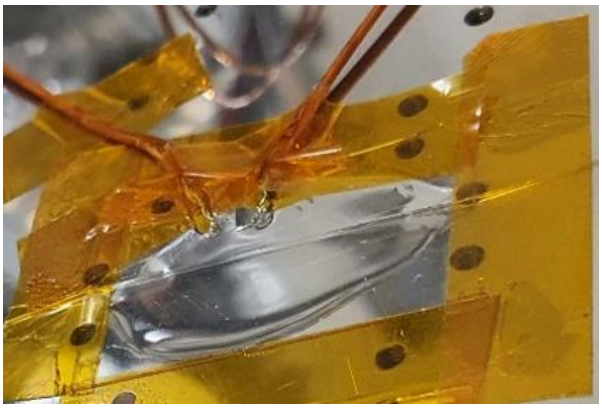


Fig.7-15. Sample of silicone directly exposed to the UV radiation on the test plate.

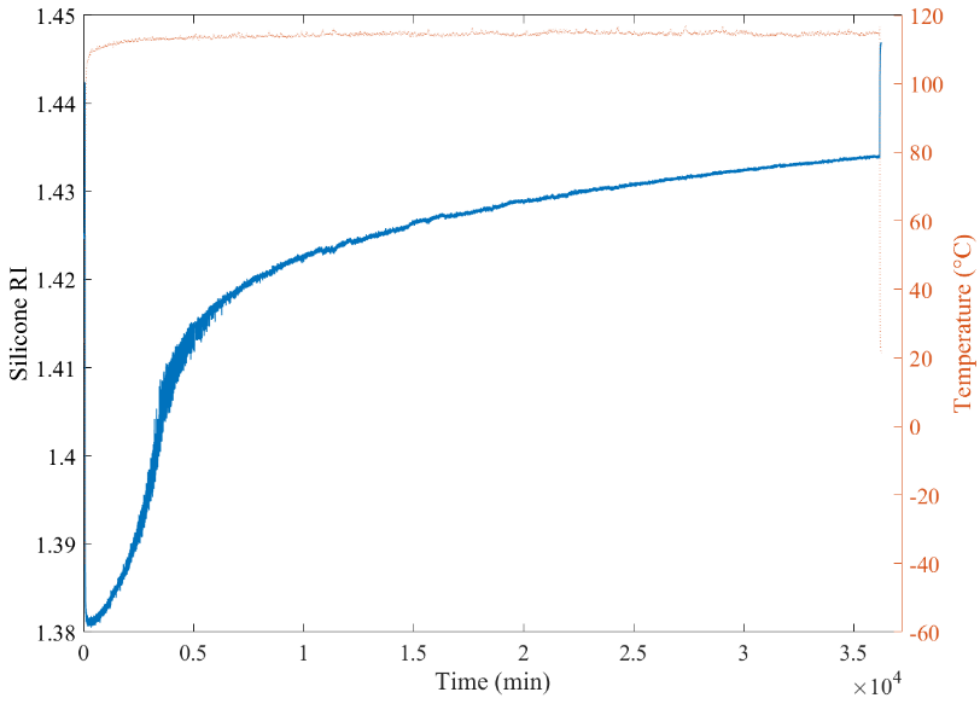


Fig.7-16. RI trend of the silicone directly exposed to the UV radiation.

However, although the RI measurements shown in Fig.7-16 performed with the TFBG may seem reliable and reasonable considering the conditions of samples after the test (Fig.7-17b), after a check of the spectra, a degradation of these was noted during the test. The reason is that the silicone adhesive was not able to effectively shield the TFBG as in the case of the cover glass. This was further investigated by performing UV-Vis-NIR spectroscopy with an Agilent Cary 5000 spectrophotometer on a sample of not exposed of pure silicone adhesive of the same thickness. The transmission spectra are reported in Fig.7-18.

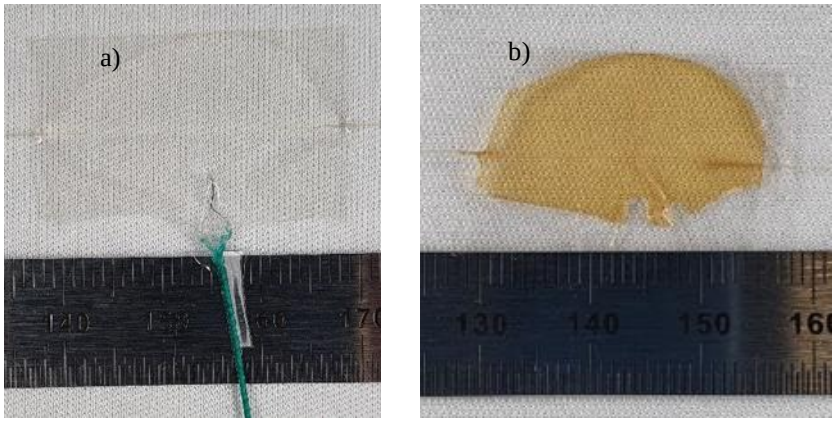


Fig.7-17. Silicone sample a) before and b) after UV exposure.

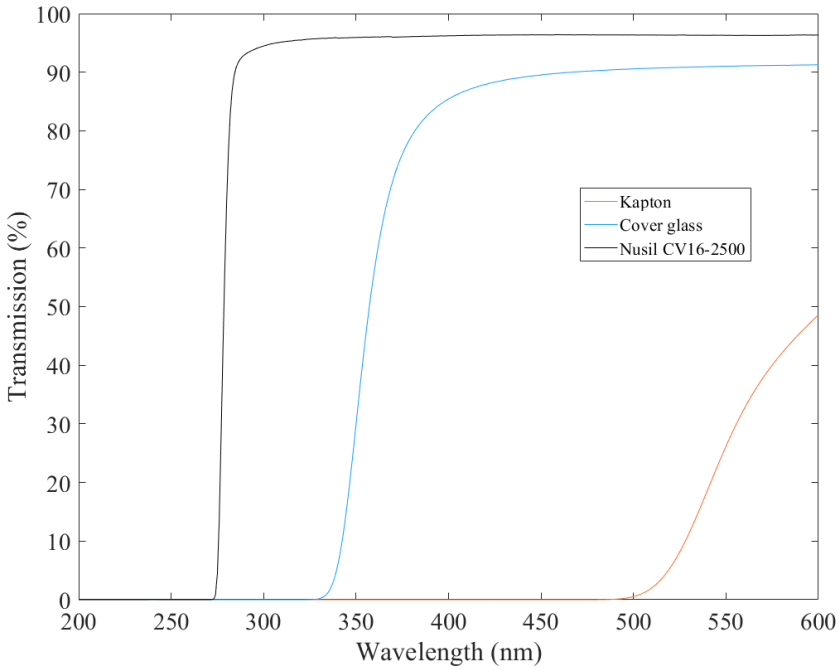


Fig.7-18. Transmission light spectrum through Nusil CV16-2500 with those of cover glass and Kapton®.

From Fig.7-18, it is clear that the tested silicone lets a broader bandwidth of UV light pass in comparison to the cover glass and Kapton® foil. These wavelengths may influence the RI core modulation inside the OF and this is clearly detected in the TFBG spectra, the consequences of which are similar to those reported in Fig.7-8. This makes the TFBG measurements not reliable at this stage. However, the TFBG spectra can exploited by performing a compensation of the TFBG spectra using the decay trend of the bare TFBG under UV light (Fig.7-5) and the transmission light spectrum of the silicone adhesive sample tested in the spectrophotometer before and after the UV exposure (Fig.7-19). Specifically, from the ratio of the areas obtained by performing the integral of the transmission curves in Fig.7-19, the transmission decay percentage trend of the silicone adhesive can be calculated at the

end of the experiment in the wavelength range 200 nm – 400 nm with respect to its initial condition. Considering the starting transmission to be 100%, this results in decay to 20.92% at the end of the exposure. At this point, by supposing a linear decay rate of the silicone transmission and taking into account the linear decrease of the envelope area due to UV in air along the exposure time (Fig.7-5), a compensation can be applied on this latter trend by considering the decreasing silicone transmission of the UV light at each moment of the exposure. The linear trend of the percentage of the Nusil transmission is approximated by the following equation:

$$P(esh) = a\,t + b, \tag{VII.1}$$

where the coefficients *a* and *b* depend on the linear fitting. The decay percentage P depends on the esh minute at which it is calculated and can be written respect to this unit. At the same way, the linear trend of the envelope area can be obtained and, hence, its percentage of decay along the exposure time.
The Nusil decay variation is then obtained as P_{var}=1-P. Hence, the shielding effect of the silicone can be introduced on the envelope area trend and a new linear fitting function describing the degradation of the envelope area due to the UV radiation but partially protected by the silicone adhesive, can be found. This process is made by calculating the compensated decay of the envelope area:

$$P_{comp} = P_{Area} \times P_{var}, \tag{3}$$

where P_{Area} is the unitary envelope area decay obtain at each moment of the exposure from the linear fitting between the initial area and the final area after the exposure over the testing time. Hence, successively, the compensated unitary envelope area variation is obtained:

$$P_{a} = P_{var} - P_{comp}. \tag{4}$$

This value is used to calculate the variation of the envelope area,

$$A_{var} = A \times P_{a}. \tag{5}$$

At the end, the compensated area A_{new} value obtained by using the non-compensated area value (A) added to the variation A_{var} from the compensation.

At this point, the envelope areas from the spectra of the sample used for the refractometric measurements of the silicone sample (Fig.7-16), are corrected and a new RI trend for the silicone is calculated and is reported in Fig.7-20.

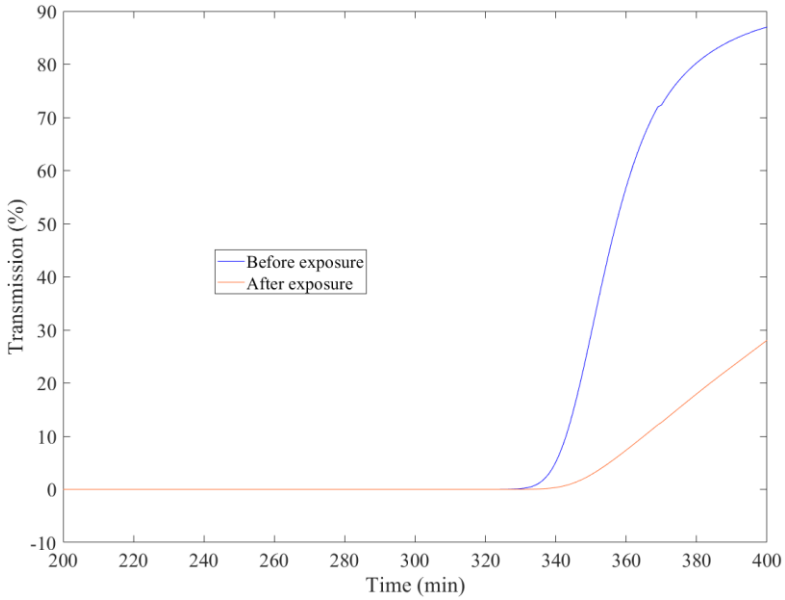


Fig.7-19. Transmission light spectrum through the silicone adhesive sample (Fig.7-17) before and after UV exposure.

The compensation of the RI measurements allowed the degradation effects on the cladding envelope area to be isolated and removed from those caused by the RI variation of the surroundings. Although the compensation reduced the positive RI variation measured by the TFBG, it is still possible to detect a consistent variation with respect to the initial value as Fig.7-20 shows. In particular, at 24.2 °C, an initial RI of ~1.424 was measured corresponding to the sample in Fig.7-17a, while, after the UV exposure, the final RI measured was ~1.440 at the same temperature, which is a variation of 1.6×10^{-2} (around one order bigger than the RI variation reported in table 7-1). This underlines that the TFBG refractometric measurements can detect the operational conditions of the material and the evolution of its degradation during harsh working environmental conditions.

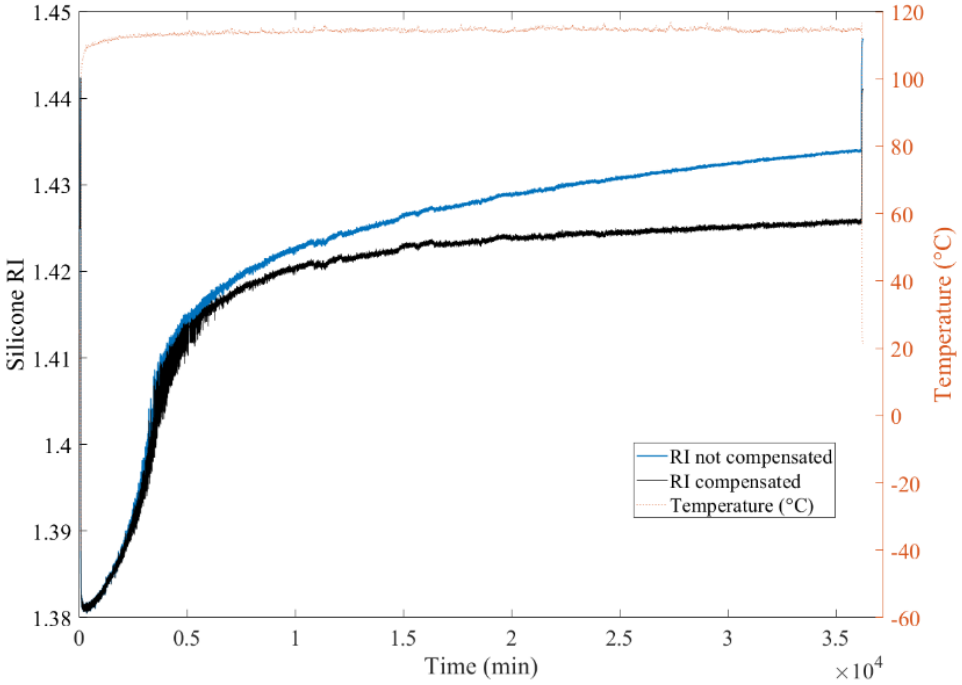


Fig.7-20. Silicone RI measurements performed with the TFBG spectra with compensated UV degradation.

7.7 Conclusions

Motivated by the interrogatives induced by the fourth research question, in this chapter, TFBG sensors have been demonstrated to be able to detect the thermomechanical and refractometric state of a silicone adhesive, used to bound two thin cover glasses, during a simulated space environmental test characterized by high vacuum and UV exposure. Nevertheless, as anticipated at the beginning of this chapter, first of all, the TFBGs were tested under UV light to prove their performance in working under the testing simulated space conditions. The result of this specific investigation was the need to shield the OF sensors with at least a cover glass to avoid the degradation the spectrum during the measurements. This condition was perfectly fitting the subsequent test methodology where each TFBG was embedded in the silicone between the cover glasses.

Then, at this point, the second part of the research question was scientifically treated taking into account the perturbation generated by the UV radiation. Therefore, several cover glass sandwiches were exposed in high vacuum and under UV radiation for different times, and in the meantime, the spectra of each TFBG were acquired. Through the demodulation of the spectra, the thermomechanical variations and the RI of the material were measured along the entire testing time. Specifically, a consistent level of negative deformation (~160 με) after the test was found, which means a shrinking of the material due to the outgassing and UV radiation. The RI measurements also reported interesting information on the material state. Indeed, the D-T demodulation allowed the silicone RI value of all

the samples to be obtained during the test time. In particular, an increasing RI variation was calculated with an increase of the esh value, which means with the severity of the testing conditions (solar constant and/or exposure time). This proved the ability of the TFBG to monitor and also detect the state of the material based on its operational conditions. Specifically, the detected silicone RI variations were from ~0.95×10^{-3} RI for 673.89 esh until ~2.62×10^{-3} RI at 2809.75 esh, following a linear line.

A further experiment was performed on a sample of TFBG sensorised silicone adhesive directly exposed to the UV radiation without the shielding of the top cover glass. This experiment aimed at enhancing the effects of the radiation on the silicone so to investigate the reaction of the TFBG to more severe damage. The consequence was the necessity to perform a compensation of the TFBG spectrum to remove the sensor degradation due to the UV beams from its spectrum and to obtain the RI values. This compensation was achieved by exploiting the light transmission percentages obtained with the UV-Vis-NIR spectrophotometer testing on the silicone sample before and after the UV exposure, and finding the linear degradation trend of the cladding envelope area in the TFBG spectrum. In this way, a reliable RI variation of 1.6×10^{-2} RI was found along ~3074 esh of exposure. The substantial ΔRI difference of one order of magnitude between the longest tested cover glass sandwich sample and the directly exposed silicone sample (with similar exposure time) demonstrates two aspects: the shielding effect of the cover glass and the ability of the TFBG to detect the degradation state of the material.

In conclusion, the investigation pushed by the fourth research allowed to demonstrate that the TFBG sensors can be a potential valid solution for in-situ sensing of space qualified polymers as in the case of the silicone adhesive used in the solar arrays. Indeed, these sensors are minimally intrusive, compatible with operating in a space environment and provide reliable measurements useful for the monitoring of the thermomechanical and refractometric state of the material during its operations in space environment.

A future research might be focused on the correlation between the RI variation occurring in the silicone during the UV exposure and the thermal optical properties of the silicone adhesive.

References

[1] T.K. Gaisser, R. Engel and E. Resconi, *Cosmic Rays and Particle Physics*, Cambridge University Press, p. 1-11, 2016.

[2] C.G. Zimmermann, *On the kinetics of photodegradation in transparent silicones*, Journal of Applied Physics, 103, 083547, (2008).

[3] A.C. Tribble, *The Space Environment: Implications for Spacecraft Design*, Princeton University Press, (1995).

[4] H.R. Fischer, C. Semprimoschnig, C. Mooney, T. Rohr, E.R.H. van Eck and M.H.W. Verkuijlen, *Degradation mechanism of silicone glues under UV irradiation and options for designing materials with increased stability*, Polymer Degradation and Stability, 98, p. 720-726, (2013).

[5] W. Schnabel, *Polymer Degradation: Principles and Practical Applications*, Macmillan Publishing Co. Inc., Chapter 4, (1981).

[6] M. Kutz, *Handbook of Environmental Degradation of Materials*, William Andrew Publishing, Chapter 23, (2005).

[7] L. Fazzi, N. Dias, M. Holynska, A. Tighe, R. Rampini, and R.M. Groves, *Multi-parameter Single Sensor for Space Silicone Adhesive Monitoring Under Hi-vacuum Ultra-violet Exposure*, Journal of Spacecraft and Rockets, Vol. 33, No. 8 (085108), 2022.

[8] B.A Banks, S.K. Rutledge, E. Sechkar, T. Stueber, A. Snyder, K.K. de Groh, C. Haytas and D. Brinker, *Issues Effects of Atomic Oxygen Interactions with Silicone Contamination on Spacecraft in Low Earth Orbit*, in: Proceedings of the 8th International Symposium on Materials in a Space Environment, 5th International Conference on Protection of Materials and Structures from the LEO Space Environment, France, 2000.

[9] D.L. Edwards, A.P. Tighe, M. Van Eesbeek, Y. Kimoto and K.K. de Groh, *Overview of the Natural Space Environment and ESA, JAXA, and NASA Materials Flight Experiments*, MRS Bulletin, 35, 2010, p. 25–34.

[10] R.O. Claus, K.A. Murphy and K.D. Bennett, *Smart Skins and Structures overview*, SEM Spring Conference on Experimental Mechanics, Proceedings A91-16751, 04-39, 1989, p. 528-533.

[11] R.S. Rogowski, J.S. Heyman and M.S. Holben Jr., *Sensor Technology for Smart Structures*, International Instrumentation Symposium, Proceedings A91-1965106-35, 1989, p. 177-181.

[12] R.S. Rogowski, *On-orbit Structural Health Monitoring Fiber Optic Smart Structures and Skins III*, Proceedings of SPIE, 1370, 1990.

[13] M.D. Aggarwal, B.G. Penn and J. Miller, *Triboluminescent Materials for Smart Optical Damage Sensors for Space Applications*, NASA/TM-2008-215410, 2008.

[14] S.G. Hang, D.H Kang and C.G. Kim, *Real-time monitoring of transverse thermal strain of carbon fiber reinforced composites under long-term space environment using fiber optic sensors*, NDT&E International, 42, 2009, p. 361-368.

[15] A.J. Osei, *Monitoring of Structural Integrity of Composite Structures by Embedded Optical Fiber Sensors*, Journal of Emerging Trends in Engineering and Applied Sciences, 5 (7), 2014.

[16] T. Savill and E. Jewell, *Techniques for In Situ Monitoring the Performance of Organic Coatings and Their Applicability to the Pre-Finished Steel Industry: A Review*, Sensors, 21, 6334, 2021.

[17] B. Hufenbach, S. Habinc and P. Vuilleumier, *Space Applications For Smart Sensors*, European Space Agency, Proceed. Eurosensors XIII, 13th European Conference On Solid-St. Transducers, 1999.

[18] G. Dumstorff, S. Paul and W. Lang, *Integration Without Disruption: The Basic Challenge of Sensor Integration*, IEEE Sensors Journal, Vol.14, No.7, 2014.

[19] L. Fazzi, G. Struzziero, C. Dransfeld, and R.M. Groves, *A single three-parameter tilted fibre Bragg grating sensor to monitor the thermosetting composite curing process*, Polymer & Composites, Vol. 8, No. 1, 2022.

[20] L. Fazzi, S. Valvano, A. Alaimo and R.M. Groves, *A simultaneous dual-parameter optical fibre single sensor embedded in a glass fibre/epoxy composite*, Composite Structures, Vol. 270, No. 114087, 2021.

[21] L. Fazzi and R.M. Groves, *Demodulation of a tilted fibre Bragg grating transmission signal using a-shape modified Delaunay triangulation*, Measurement, Vol. 166, No. 108197, 2020.
[22] L. Fazzi and R.M. Groves, *Refractometric Properties of a TFBG Sensor Demodulated Using a-Shape Modified Delaunay Triangulation*, Optics, Vol.2, No.2, 2021, p. 113-133.
[23] European Cooperation for Space Standardization, ECSS-E-ST-10-04c – Space Environment, 15/06/2020.
[24] N. Singh, S.C. Jain, A.K. Aggarwal and R.P. Bajpai, *Fibre Bragg grating writing using phase mask technology*, Journal of Scientific & Industrial Research, Vol. 64, 2005, p. 108-115.
[25] X. Hu, Y. Liu, J. Jiang, W. Lin, H. Qua and C. Caucheteur, *Tilted Fiber Bragg Grating Inscription in Boron Co-Doped Photosensitive Optical Fiber Using 266 nm Solid State Laser Pulses*, IEEE Sensors Journal, Vol. 22, No.3, 2022, p. 2229-2236.
[26] T. Erdogan, *Fiber grating spectra*, Journal of Lightwave Technology, Vol.15, No.8, 1997, p. 1277-1294.

8

Conclusions and future developments

"The best way to predict the future is to create it."
Alan Kay

The path traced in this doctorate dissertation started from the Tilted FBG theoretical knowledge and its manufacturing, in order to determine the effects of the tilted Bragg structure on the sensing abilities of the sensor, which were deeply studied in relation to the sensor customization. Then, the scientific steps continued focusing on its embedded monitoring applications for different advanced engineering materials, widely employed in aeronautical and aerospace industry as composite materials and space-qualified silicone adhesives. As highlighted at each chapter, the treatment of this research can be collected in four milestones, which are the research queries that motivated the entire investigation. These are the following:

- *How can the customization of the Bragg gratings influence the capability of the sensor for measuring a certain parameter?*
- *How does the surrounding refractive index variation affect the cladding resonance peaks in the transmission signal of the TFBG sensor?*
- *How do the several steps of the VARTM process affect the resonance peaks in the transmission signal of the TFBG sensor in combination with the thickness of the composites?*
- *How do the space environmental conditions influence the transmission signal and the sensing abilities of the TFBG sensor even once this is embedded in a space qualified silicone adhesive?*

After the analysis of the results reported at each chapter, the final important achievement remaining to the reader of this thesis is the awareness to have strengthened the knowledge about several aspects of the TFBG sensors such as: manufacturing, applications, sensor embedding methods, measurements, environmental working conditions, demodulation techniques and numerical modelling.

The special Bragg grating structure imposed to the core refractive index of the OF makes the transmission spectrum rich of resonance peaks. The concept behind the possibility to perform simultaneously multiple measurements with a single sensors presented in several publications, have been definitely here demonstrated. However, as treated, to obtain determined measurements abilities, some preliminary considerations must be conducted on the Bragg grating structure of the TFBG, before of the manufacturing process.

Therefore, studies motivated by the first research question have specifically proved that the modulation of the core RI, its saturation and length, must be made in the way to create a Bragg grating structure with a certain tilt angle. The reason lies in the generation of a TFBG transmission spectrum with specific characteristics such as the presence of Bragg, Ghost and Cladding resonance peaks. Furthermore, as proved in the second chapter, the fundamental TFBG internal structure parameters, can also influence the measurement performance and accuracy of the sensor. The strong dependence of the TFBG sensor on its internal structure offers the possibility to engineering the manufacturing process and obtain the best TFBG customisation by starting from the manufacturing parameters to

induce an exact internal Bragg structure which has the designed shape. The estimation of the TFBG spectrum starting from the internal parameters is a hard and long challenge. Nevertheless, in chapter 2, the Transfer Matrix Method has been demonstrated to be a good time-saving tool to solve the coupled-mode equations and obtain the resonance amplitude of the Bragg peak based on the TFBG customisation of its internal structure. This method can be potentially used to numerically simulate also other peaks in the spectrum such as the cladding resonances. However, some efforts should be still spent for a rigorous mathematical formulation of the Ghost peak, which modelling is more complex with respect with the other resonances due to its coupling nature between the low-order cladding modes and forward-propagating core mode.

Once the TFBG has been customised and produced, its spectrum can be demodulated to obtain the measurements of strain-temperature variations and the absolute RI measure of the surrounding medium. Therefore, the investigation moved by the first research question links with the second research point. Hence, in chapter 3, a novel demodulation technique based on the Delaunay triangulation has been presented with the purpose to increase the external RI measurement accuracy and performance and, at the same time, making shorter the calculation times respect to the other methods.
The technique uses the TFBG spectrum as a set of data-points and develops a triangulation between them by following the Delaunay triangulations laws. In this way, a sort of "mesh" is created which discretises the spectrum in a certain number of triangles. Since, only the maximum dimension of the triangles is constrained through the α-shape parameter, these can be small enough to detect each minimum change in the TFBG spectrum. The RI is then measured by performing a preliminary calibration of the TFBG and obtaining a correlation function between the envelope triangles area and the RI values in the working range. The application of the D-T technique allowed a resolution to be reached down to 8×10^{-8} RI, with an accuracy of 8.05×10^{-3} RI in the most disadvantageous measuring range which includes also the temperature and strain cross-sensitivity deviation. The technique has been compared with the previous most common used global demodulation methods, and is 10 times faster than the Envelope method and 17 times respect with the Area method, which reflects also a low computational power and easier implementation.
With this novel technique, the refractometric sensing abilities of the TFBG are studied in relation to the customisation of the TFBG. Nevertheless, in meantime, the effects of the surrounding RI are analysed on the transmission spectrum.
It is right at this point of the research that, since the D-T demodulation can be performed on any spectrum without any wavelength and shape limit, it was hypothesised that the TFBG may be used also to monitor the flow of a liquid along its optical axis by observing the change of the triangulated envelope area. This property has then been exploited in the fifth chapter to measure the flow times of resin between the composites layers during the infusion process of the composites manufacturing. The same can be done to have an estimation of the interlaminate flow speed of the resin during the infusion along multiple directions, the permeability of the reinforcement fibre layers and the detection of eventual voids as well as to evaluate the infusion state of composites.

In chapter 4 and 5, the three-parameter measurement abilities of the TFBG sensor have been demonstrated when this was embedded in composite materials.
Nevertheless, as described during the treatment, the fourth chapter was not only realized for composite material monitoring, but it is a propaedeutic chapter of fundamental importance for a correct development of the rest of the research motivated by the third and fourth research question. Indeed, in this chapter, for the first time in literature, an embedded TFBG sensor performed simultaneous thermomechanical measurements induced by an external perturbation, inside an engineering material.
In particular, a TFBG sensorised glass fibre/epoxy composite was exposed to the light of heating lamps and, in meantime, the sensor was measuring simultaneously the strain-temperature variations occurring in the material. The dual TFBG measurements were compared with the thermocouple compensated FBG sensor measures and the results obtained from the FEM analysis of the sample with and without the embedded TFBG. The comparison between the two empirical techniques has shown an average deviation around 3%, and a maximum of 7% in correspondence of 2 °C variation. This difference is

due to the poor thermal resolution of the self-compensated TFBG and the different embedding position of sensor and thermocouple.
The results from the FEM simulations and the comparison with the strains measured by the sensing methods have highlighted several points. First of all, the presence of the embedded OF is necessary for a correct modelling of the sensorised composite sample as the glass of the waveguide contributes and enhances the mechanical properties of the plate. This demonstrates also that the embedding of a OF in glass-fibre composite does not decrease the mechanical performance of the material. A second result regards the better matching of the strain trend obtained with the full FEM analysis and the thermocouple compensated TFBG sensor with respect to the self-compensated TFBG. Although the difference deviation between the methods is small, this indicates the necessity to improve the thermal resolution of the sensor so that to make finer the calculation of deformation in the materials. Nevertheless, although the technique can be improved, the self-compensated TFBG has been proved to be valid for the simultaneous strain-temperature measurements.

The next research query point regarded the effects generated by a composite manufacturing process on embedded TFBG sensors. Therefore, the scientific argumentations raised by the third research question are fully treated by taking also experience from chapter 4.
Specifically, in chapter 5, each single TFBG was proved as a three-parameter sensor so that the strain-temperature variations and the RI of the resin were calculated where the TFBGs were embedded in several composites during their manufacturing process. This result was possible by performing also the demodulation of the cladding resonance peaks through the Delaunay triangulation demodulation technique treated in the third chapter.
The simultaneous TFBG measurements performed during the VARTM manufacturing process and curing of three glass-fibre/epoxy composites with 2, 5 and 10 mm thickness demonstrated the great utility of this sensor in the deformation detection and cure evaluation during the composite manufacturing steps. Specifically, the thermomechanical measurements detected the different deformation states induced in the composite along the manufacturing steps, while the refractometric sensing was used to correlate the evolution of the resin RI with the cure degree trend. The correlation has highlighted a similar trend between the two curves. Specifically, the RI trend increases with the cure rate of the resin until reaching a plateau once the resin can be considered cured. This is really convenient in the composite industry as the TFBG offers the possibility to do not perform expensive and time consuming thermal analysis to extract the degree of cure model of the used resin and have an estimation of the cure through the refractometric measurements.
Furthermore, the variation of the triangulated cladding peaks envelope area was observed during the resin infusion so that the infusion times were calculated at the embedding points of the TFBGs in the composites. This allowed to have an idea of how the resin flow changes between the reinforcement layers based on the thickness of the composite. As anticipated in chapter 3, also defects, such as voids or poor resin wetted regions, can be detected through the cladding peaks area monitoring. This further ability added to the three-parameter measurements, makes the TFBG sensor a complete and accurate tool, not only for the monitoring of the composite health state, but also for its quality evaluation.
These operations can be potentially performed in real-time, hence, the information may be available during each step of the manufacturing process. Therefore, during the manufacturing, another possibility may be to apply a specific pre-deformation state to the composite by observing the measures of the TFBG sensor.

Once the special abilities of the tilted FBG have been demonstrated in the composites world, these appeared to be potentially interesting also in the case of polymers for space applications. The question in then shifted to the effects that the working conditions of the space environment can have on the transmission spectrum of a TFBG and, hence, on the sensing abilities of the sensor.
Therefore, in this last section of the thesis, the fourth research question motivated the investigation, also considering the case in which the TFBGs are embedded inside widely used space qualified materials as the silicone adhesives.
In particular, chapter 6 and 7 were dedicated to demonstrate that the multi-measurements are possible and reliable when the TFBG is embedded in space qualified silicone adhesive even operating in harsh

space environmental conditions. Therefore, in chapter 6, a sample of TFBG sensorised silicone adhesive between two layers of thin cover glass sheet, was placed in a vacuum chamber at ~10^{-6} mbar and loaded with a thermal cycling load between ~-20°C and ~85°C. The compatibility of the OF containing the TFBG sensor to high vacuum, was preliminary tested and verified according to ECSS normative.
The comparison between the trends of the recorded shifts of the Bragg and Ghost peaks in the spectrum and the temperature measured by the thermocouple highlighted some differences. This means that, if the calculation of the strains induced by the thermal cycles in the silicone is performed by thermally compensating the TFBG with the thermocouple, these values are affected by errors due to the delay between the curves. Therefore, the classical approach to compensate the thermal cross-sensitivity with the thermocouple from the peak shifting in the TFBG spectrum is an inaccurate method which brings serious mistakes due to the different location of the sensor in the silicone. Indeed, in high vacuum (hence in space environment), the absence of air makes the conduction the only way to transfer the heat inside a body, which (depending from the thermal conductivity of the material) this results in much slower heat transfer compared to a body in air. As demonstrated, the self-compensated TFBG solves this problem as it does not need any external sensor to measure simultaneously the thermomechanical changes. Furthermore, at the end of the exposure, the strain value reported a negative deformation state of the silicone, which means a change of the original silicone dimensional properties. The refractometric measurements also detected a change, specifically the final silicone RI result was higher than the starting value at the same temperature. This variation may be caused by two effects: the compressive deformation state detected also from the strain measurements and a chemical evolution of the silicone due to the heating/cooling cycles in high vacuum environment. A Differential Scanning Calorimetry test was then performed on a sample of pure cured silicone adhesive, which highlighted the realising of volatiles during heating-up and cooling-down phases of the test.
This means the TFBG provided important information on the silicone thermomechanical and refractometric state from which it was possible to deduce what was happing inside the silicone adhesive during the thermal cycles.

At this point, a further step was implemented by studying the effect of UV/VUV radiation on the TFBG sensor and sensorised cover glass sandwich sample. Some TFBG sensors were then exposed to the light of UV/VUV lamps in high vacuum chamber and, in meantime, their spectra were recorded. The TFBGs were tested in three ways, directly exposed to the radiation, covered by a thin cover glass (the same used to make the sample sandwich) and protected with a Kapton® layer. An analysis of the spectra at the end of the experiment, showed the necessity to protect the TFBG with the cover glass layer. Indeed, from the analysis of the TFBG spectra is emerged that the UV radiation can modify the RI core modulation of the OF imposed during the TFBG production process. The consequences are the modification of the Bragg internal structure of the sensor and, then, a change of the transmitted spectrum and original sensing properties (thermomechanical sensitivity coefficients and refractometric correlation). Of course, this is an undesirable drawback for measurement which cannot be accepted. Therefore, for this kind of applications, the TFBG should be always protected by a layer able to block the UV wavelengths that can modify the sensor's internal structure. This study guaranteed that the variations resulting in the spectrum of the TFBG, embedded in the silicone, are not caused by the direct influence of the UV radiation on the sensor but from the change of conditions of the elastomer.
At this point, several TFBG sensorised cover glass sandwiches have been tested by increasing, at each exposure, the UV radiation power, and hence, the equivalent solar hours. For this study, more space has been left to the silicone refractometric measurements and analysis respect with the thermomechanical calculation.
For one of the samples, the thermomechanical measurements during the test has been reported, where a final negative deformation can be noted. Hence, as expected from the previous chapter, the application of the vacuum and heat to the elastomer creates a compressive deformation in the elastomer.
Instead, the RI variation has been obtained and evaluated for all the exposed samples. The results have highlighted the increasing of the silicone RI variation with the equivalent solar hours. Specifically, the

trend between these two parameters seems to be linear, hence, the silicone RI grows linearly with the increasing of the UV radiation power and/or exposure time. The increasing of the RI is also coupled with a progressive yellow coloration of the silicone, as noted from the observation of the specimens after the exposure. This means that photochemical reactions were happening during the experiments which may cause the variation of the silicone RI. Therefore, the TFBG refractometric measurements can be related to the aging/degradation undergone by the silicone during the UV exposure.
A further step consisted in increase the UV effect on the silicone by removing the upper cover glass and expose the elastomer directly to the radiation. However, this experiment raised some issues for the TFBG because, as verified through the UV-Vis-NIR spectrophotometer, the silicone adhesive is not able to shield the UV wavelengths that cause the RI core modulation changes. Specifically, the silicone is initially transparent to the radiation but it starts to absorb more and more with its degradation. Hence, the internal RI core modulation of the TFBG is initially hardly influenced, while this effect fades along the silicone aging. Therefore, the RI measurements were influenced by the degradation of the original Bragg internal structure. In this paper, a method to remove the variation in the RI measurement due to the UV radiation was presented by considering the decreasing of the silicone UV transmission and assuming linear this decay.
The final result is a bigger variation of the silicone RI due to the aging of the UV exposure according to the linear trend found previously between RI and esh of exposure, while the curve related to the uncorrected measurement resulted to substantially converge after a certain exposure time.

8.1 Final considerations on TFBG sensing technology and future perspective

The several applications of the TFBGs embedded in composites and space qualified silicone adhesive reported in this thesis, have demonstrated that the sensor can provide reliable and accurate multi-parameter measurements for different purposes and operating environmental conditions. Furthermore, these special sensing abilities are still more appreciated if the TFBG characteristics are taken into account, such as: low weight, cost and intrusiveness, high mechanical performance, resistance to chemicals and corrosion, immunity to electromagnetic fields and high possibility of customization.
However, as any technology, there some weak points that should be improved in future to make more robust and reliable a multi-parameter monitoring system based on only TFBG sensors:

- First of all, improving the sensor thermal resolution during simultaneous thermomechanical measurements which can be achieved in two ways:
  - by using an interrogator system with finer scanning wavelength resolution,
  - a dedicated customisation of the TFBG able to separate better the thermal sensitivity of the Bragg and Ghost peaks.

A finer thermal resolution would also improve the strain accuracy as demonstrated in chapter 4.

- A second aspect to improve would be to reduce the dimensions of the equipment dedicated to the acquisition of the TFBG signal, record, demodulation and processing.

This is a fundamental aspect particularly for space applications. Indeed, although the TFBG sensor and equipment can be easily used during the testing campaign of the components, the application of a sensing network based on TFBGs and embedded in a spacecraft would be improbable due to the weight of the devices used to interrogate the sensors and acquire the signal. Payload is a fundamental aspect of the space missions, therefore, the equipment dedicated to this task should be extremely light and miniaturized. Only once this aspect is achieved, the advantages of the TFBGs may be fully exploited. Nevertheless, the same is valid for aeronautics composite structures, where the embedded monitoring system should guarantee accurate and reliable information without increasing the total weight of the airplane.
Furthermore, another important point regards the distribution and the placing of the sensors in a component or structure. Since the TFBGs are really versatile, as they can provide information at any

stage of the material (from manufacturing to the end of its operating life), their positioning inside the materials should be optimized and studied. This argument should be, in future, studied in deep, also considering the path of the OFs so that: the waveguides can be protected at the edge minimizing the risk of cutting, the parts can be joined to others without incurring in damaging the OFs, the light flows inside the waveguides without small bending radii.

Notwithstanding, the novel developed technique based on the Delaunay triangulation of the spectrum provided a fast and easy calculation method to obtain the external RI measure, the demodulation technique related to the thermomechanical measurement from the Bragg and Ghost shifts may also be an important item to improve in the next future. Indeed, recognizing of the peaks may sometimes be difficult due to the distortion of the spectrum due to the embedding of the OF inside the material. An erroneous reading of the wavelength shift brings an error in the matrix calculation and, hence, in the output. Furthermore, the demodulation technique based on the sensitivity matrix is dependent from many factors such as thermal resolution of the TFBG, individuation of the wavelength peak shifting and matrix condition number. So far, it has been noted that these aspects may bring to the failure of the calculation specifically for real-time monitoring.

In conclusions, although some drawbacks, which are present in any technology, the TFBG sensors seem to have the features and flexibility to potentially overcome the limits of the state of art of the monitoring and sensing technologies. An embedded network of TFBGs inside the materials may represent a complete and reliable method to constantly monitoring the health state of the components, from the manufacturing, through the operating life and even once the piece is decommissioned from the service.
A further future step would be to study and test the TFBGs also to detect, in the materials, damages induced from other types of sources such as impact for aerospace applications and ionizing radiation in spacecraft.
Furthermore, certainly, it has to be considered that the special features of the TFBGs and the related researches for their application in aerospace and space engineering are attractive. Also for the use of these sensors in other fields such as biology, chemistry, medicine, infrastructures and in any field where the accurate detection of a single- or multi-parameter is required with minimal intrusiveness and special or harsh environmental conditions.

Appendix A

In this appendix, the drawings regarding the components of the calibration system used for the thermomechanical and refractometric characterisation of the TFBG sensors are reported.

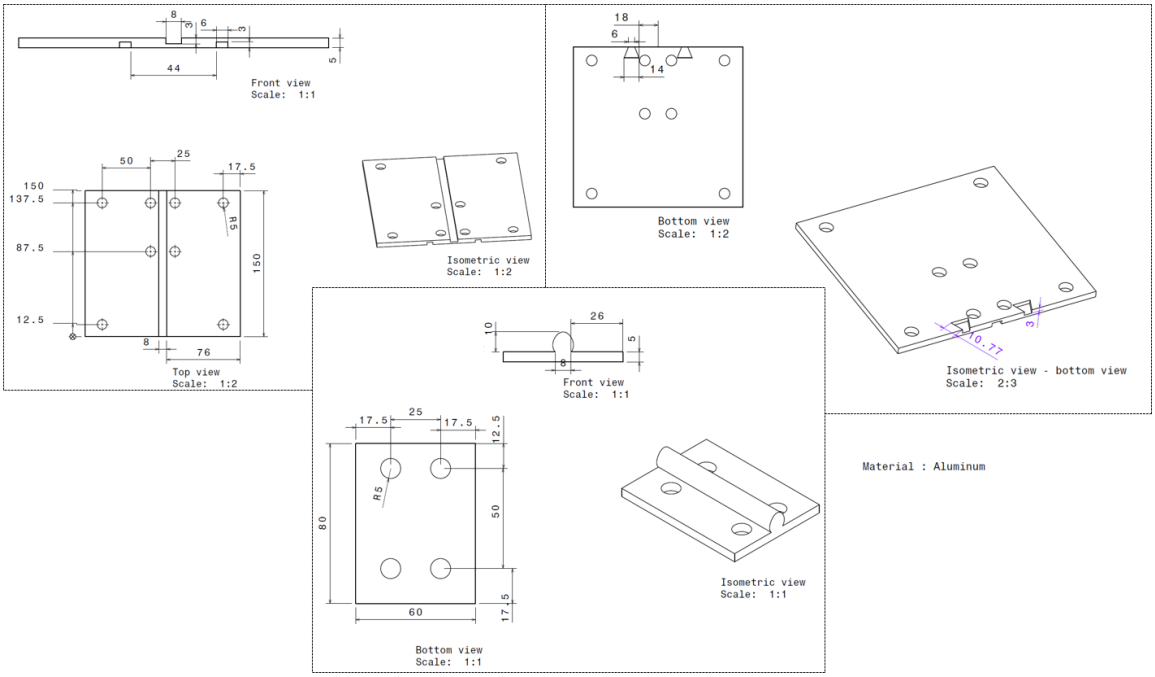


Fig.A-1. Drawings of the components to manufacture the fixed block of the translation stage setup.

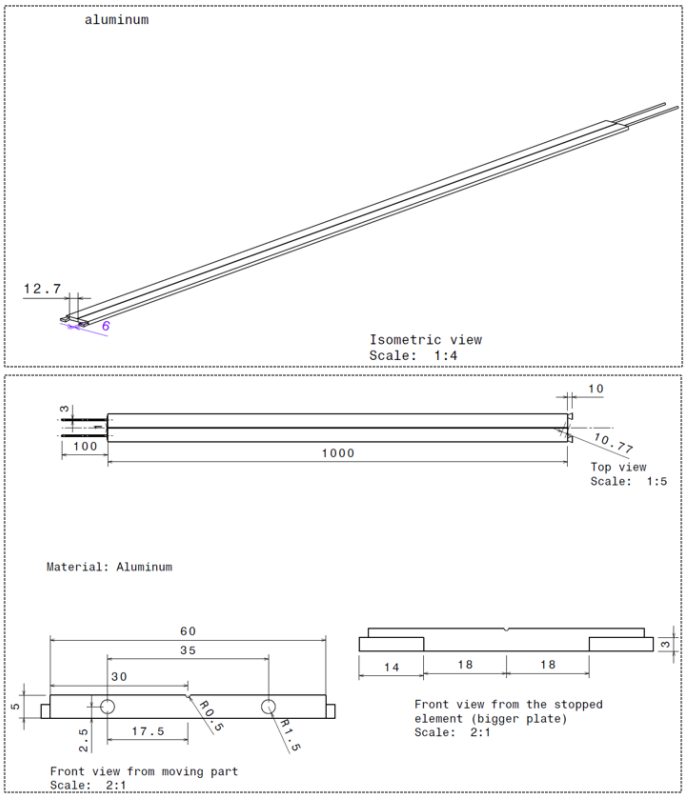


Fig.A-2. Drawings of the guide element.

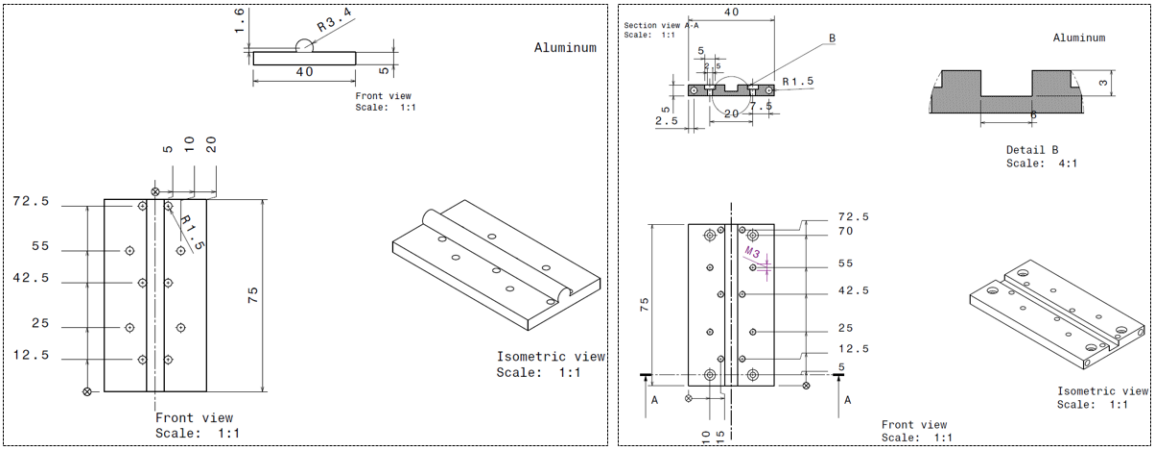


Fig.A-3. Drawings of the components to reproduce the moving element block.

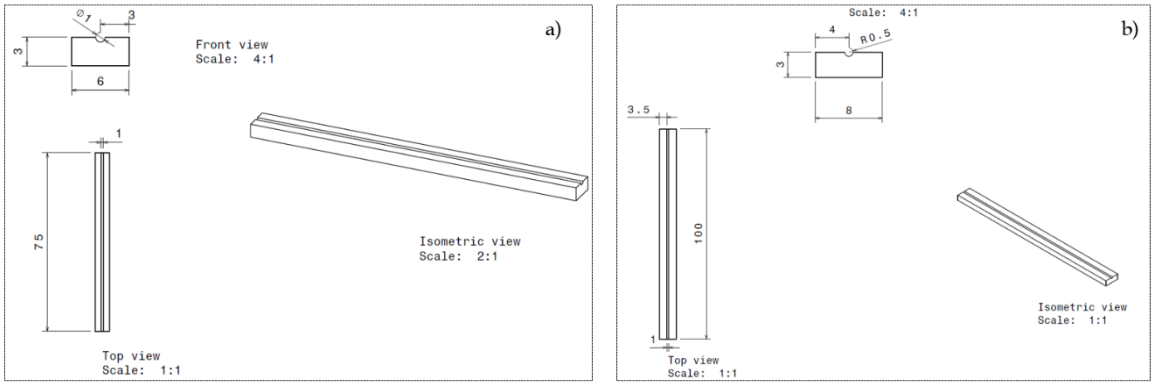


Fig.A-4. Drawings of the slots components for a) moving element and b) fixed block element.

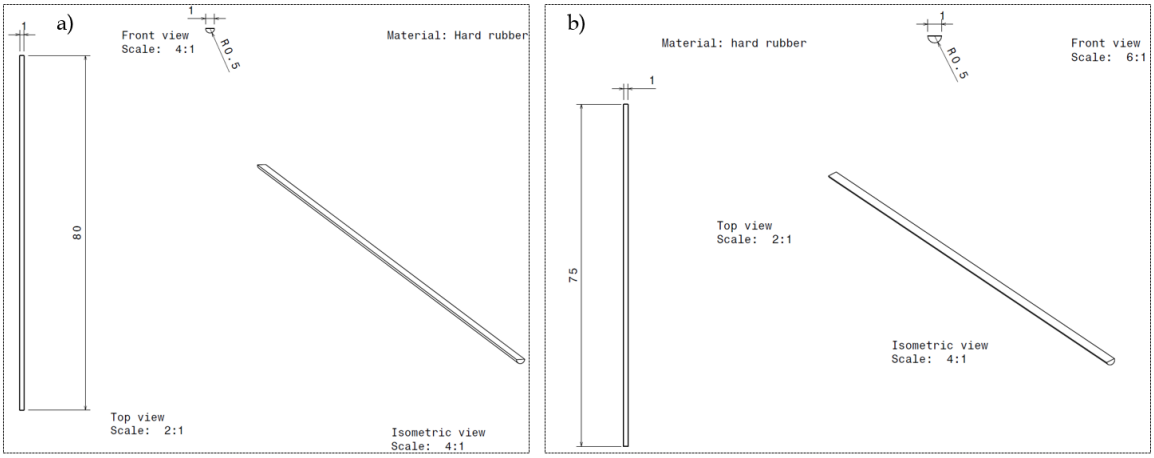


Fig.A-4. Drawings of the rubber slices for the closing element of the a) fixed part and b) moving element.